Experimental Investigation of Inertial Particle Transport in a Turbulent Boundary Layer

Suhaimi Haji Abdul Wahab

A thesis submitted in partial fulfillment for the
degree of Doctor of Philosophy

in the

School of Mechanical and Systems Engineering
University of Newcastle upon Tyne

April 2018

Declaration of Authorship

I, **Suhaimi Haji Abdul Wahab**, declare that this thesis titled, '**Experimental Investigation of Inertial Particle Transport in a Turbulent Boundary Layer**' and the work presented in it are my own. I confirm that:

- This work was done wholly or mainly while in candidature for a research degree at this University.
- Where any part of this thesis has previously been submitted for a degree or any other qualification at this University or any other institution, this has been clearly stated.
- Where I have consulted the published work of others, this is always clearly attributed.
- Where I have quoted from the work of others, the source is always given. With the exception of such quotations, this thesis is entirely my own work.
- I have acknowledged all main sources of help.
- Where the thesis is based on work done by myself jointly with others, I have made clear exactly what was done by others and what I have contributed myself.

Signed: _____

Date: _____

Abstract

The first major part of the work was to commission and test the newly built 3 meter open-channel experimental rig. Various development stages have been carried to improve the design specifications to meet experimental requirements. The original 2 meter open-channel working section was replaced with a new 3 meter channel working section enabling measurements to be taken further downstream allowing the boundary layer to develop. The original bell mouth inlet was replaced with a hyperbolic tangent profile 3:1 contraction with a honeycomb, coarse and fine gauzes fitted upstream. 25% porous perforated plates were installed at the channel exit and also within the inlet plenum tank to reduce the turbulence level. LDV measurement in the free-stream revealed that the turbulence level is below 1% and the boundary layer profile collapses well with DNS data of Schlatter (2010). A dip in the outer wake region of the velocity profile can be observed throughout the measurements and is attributed to the aspect ratio of the channel which is 1.7 at Fr = 0.33. Nevertheless, boundary layer profile and turbulence intensity profile collapse well with published DNS data. Good agreement was obtained between measurements carried out using the available LDV and time-resolved PIV systems.

Time-resolved PIV measurements were performed in a dilute particle-laden flow, tracking nearly neutrally buoyant polymer microspheres within the measured velocity field of a near wall turbulent boundary layer. Data were taken 2100mm downstream of the inlet, in a vertical light-sheet aligned in the streamwise direction on the centerline of the horizontal, open-channel channel facility. High frame-rate measurements were taken to temporally and spatially track particle motion and instantaneous visualization clearly reveal a link between particle movement and near-wall coherent structures. Structures having 2D vorticity signatures of near-wall hairpin vortices and hairpin packets, directly affect particle motion. Statistical and instantaneous results agree well with published experimental and numerical work.

Conditional statistics were investigated for the particles using the Quadrant method. Particles moving outwards from the channel floor are influenced by the Quadrant 2 ejection events and those that moves inwards towards the wall are influenced by the Quadrant 4 sweeps events.

Particle-fluid velocity correlations, r_{pf} were calculated for each particle trajectory and averaged of all the particle-fluid velocity correlations, R, were determined for the whole dataset for Re=1000. This value is estimated to be 0.0261 and 0.000643 respectively for the particle-fluid streamwise and wall-normal velocity correlation.

Acknowledgements

First and foremost, I would like to thank Dr. Ian Potts for his unwavering support, guidance, inspiration throughout the years I have spent at Newcastle University. I would like to thank Dr. Richard D. Whalley whom has given me advice, support and encouragement, and to Dr. David Swailes for his continuous support and thoughtful ideas.

Secondly thanks to Dr. Xiohua Wu who helped us with the lasers, to Dr. Oana Bretchanu for the help with fluorescent particles. Although the bright fluorescent resin was a nuisance when it comes to cleaning, nevertheless, that has all been an enjoyable and worthwhile experience. Also thanks to Dr. John Hedley who help us to realign the LDV lasers, which was a great relief for us. Also thanks to Dr. Lian Gan for patiently accompanying me during our lengthy LDV experiments down at the lab.

I would also like to convey my greatest appreciation to all the technical support staffs under the lead of Mr. Ken Madden. This appreciation goes to Michael Foster, Brian Stoker, Stephen Charlton, Frank Atkinson, Paul Harrison, Jamie Hodgson, Lewis Sholder and others.

My colleagues and fellow postgraduate students in the school have been nothing but kind and supportive in all my experience, and I thank you to all. In room T4, they were Chunyu Jin, Andy Bragg, Mahyar Mahinzaeim, Yuan Gao, Mohit Katragadda, Dipal Patel, Şahin Yiğit, Pavlo Doichyk, David Butz, Jiawei Lai, Bruno de Souza Machado and Johannes Sellmann. In M22 they were Naif Alharbi, Ricardo da Conceicao Ribeiro and Eseoghene Etowe.

I would never have made it this far without the consistent love and unconditional support of my mother, in-laws, brothers and sisters and my wife and three children, Danish, Aisha and newborn Arya.

Contents

Declaration of Authorship iii

Abstract iv

Acknowledgements vi

List of Figures xi

List of Tables xvii

Abbreviations xix

Nomenclature xxi

1 Introduction 1
1.1 Thesis outline . . . 2

2 Literature Survey 5
2.1 Introduction . . . 5
2.2 Turbulent boundary layer . . . 6
2.2.1 Boundary layer structure . . . 6
2.2.1.1 Near-Wall Structure . . . 6
2.2.1.2 The Logarithmic Region and Outer Region . . . 8
2.2.1.3 Very Large-Scale Coherent Motions . . . 9
2.2.2 Hairpin vortex . . . 10
2.3 Structure identification in boundary layer PIV . . . 12
2.3.1 Two-dimensional visualization of vortices . . . 16
2.3.1.1 Vorticity . . . 17
2.3.1.2 Swirling strength . . . 18
2.3.1.3 Second invariant of the velocity-gradient tensor (Q-criterion) 19
2.4 Boundary Layer PIV . . . 20
2.5 Two-phase flow . . . 25

3 Experimental Facilities and Instrumentation 35

3.1 Newcastle open-channel facility . . . 35
3.1.1 New 3m Working Section . . . 39
3.1.2 New Profiled Inlet . . . 41
3.1.3 Design of inlet and outlet plenum tank . . . 43
3.1.4 Boundary layer tripping - via Zig-zag strip . . . 46
3.1.5 Summary description of upgraded Newcastle flow channel . . . 47
3.2 Instrumentation . . . 48
3.2.1 Time-resolved particle image velocimetry system . . . 48
3.2.2 Target plate and target traverse system . . . 52
3.2.2.1 Particle image velocimetry . . . 54
3.2.2.2 Principle of PIV . . . 55
3.2.2.3 Imaging of small particles . . . 56
3.2.2.4 Seeding . . . 59
3.2.3 Laser Doppler velocimetry System . . . 60
3.3 Laser Doppler velocimetry . . . 61
3.3.1 Data acquisition and analysis . . . 61
3.4 Water channel boundary layer calculations . . . 63

4 Commissioning and testing of Newcastle open-channel facility. 65
4.1 Introduction . . . 65
4.2 Turbulence level in the free-stream of the open-channel experimental rig . . . 67
4.3 LDV measurement of velocity profiles and boundary layer thickness . . . 69
4.4 Effects of fine, coarse and perforated pressure drop screen (Back-plate) . . . 70
4.5 Effects of zig-zag strip on the boundary layer profile and thickness . . . 76
4.6 Velocity dip phenomenon . . . 78
4.7 Effect of Reynolds number . . . 79
4.8 Comparison of LDV and PIV measurements . . . 82
4.8.1 Spectra . . . 86
4.9 Mean and turbulence statistics of the flow in the channel . . . 89
4.9.1 Two-dimensional visualization of PIV data . . . 96

5 Two-phase flow in turbulent boundary layer 103
5.1 Introduction . . . 103
5.2 Experimental setup and methodology . . . 107
5.2.1 Two-phase flow image processing and phase-separation . . . 111
5.3 Fluid mean velocity and turbulence profiles . . . 112
5.4 Inertial particle mean and RMS velocity profiles . . . 118
5.5 Inertial Particle Tracking . . . 122
5.5.1 Particle track lengths . . . 124
5.6 Conditional statistics for inertial particles . . . 127
5.6.1 Particle-fluid velocity correlation . . . 141
5.7 Conclusions . . . 146

6 Discussion and Conclusions 149

6.1 Discussion and Conclusion 149
6.2 Recommendation for Further Work 155

A Phase-separation of two-phase image **157**
A.1 MATLAB script for tracer particles image separation 158
A.2 MATLAB script for inertial particle image separation 160

B MotionPro X5PLUS Standoff Distance for 60mm, 105mm and 200mm AF Micro Nikkor lens **163**

C Depth-of-Field for 60mm, 105mm and 200mm AF Micro Nikkor lens **167**

D PIV laser power requirements **171**

E Investigation into DynamicStudio tracking anomalies **173**
E.1 How does the code works? 181
E.2 MATLAB script for image frame separation and renaming 183
E.3 MATLAB script for particle tracking 183

F Particle tracking **195**
F.1 MATLAB script for processing DynamicStudio PIV cross-correlation data output 195
F.2 MATLAB script for loading PIV data for conditional sampling 197
F.3 MATLAB script for particle tracking 198

References **207**

List of Figures

2.1 Representation of the "*bursting*" process in which a low-speed streak develops into a hairpin vortex. From: Smith (1984). 13
2.2 Quadrant analysis to detect and sort events (ejections or sweeps)(Bigillon and Garcia, 2002). 15
2.3 Rrms contour plot representing ejections or sweeps, and inwards or outwards (Bigillon and Garcia, 2002). 16
2.4 a) Schematic of a hairpin vortex attached to the wall and the induced motion. b) Signature of the hairpin vortex in the streamwise wall-normal plane (Adrian, Meinhart and Tomkins, 2000). 17
2.5 (a) Hairpin vortex heads, reproduced from Adrian, Meinhart and Tomkins (2000). 21
2.6 (b) Layers of approximately constant streamwise momentum for the $Re_\tau = 872$ boundary layer, reproduced from Adrian, Meinhart and Tomkins (2000). 21
2.7 Conceptual scenario of nested packets of hairpin or cane vortices, growing from the wall, reproduced from Adrian, Meinhart and Tomkins (2000). 22
2.8 Packets of hairpin, viewed in a plane parallel to the wall at $y^+ = 92$, reproduced from Ganapathisubramani et al. (2003). Positions indicated by letter B, C, and D are region having uniform velocity momentum. 23
2.9 Influence of particle relaxation time on particle trajectory. Small inertia particles follow precisely the flow; large inertia particles filter the space changes of velocity; intermediate inertia particles respond to the flow structure (Soldati, 2005). 26
2.10 Quadrant analysis around all beads, with distribution of the turbulent events in clear water flow for $Re = 24,000$ (Lelouvetel et al., 2009). 31
2.11 Quadrant analysis around beads with a positive vertical velocity ($V_p > 0$), with distribution of the turbulent events in clear water flow for $Re = 24,000$ (Clear) (Lelouvetel et al., 2009). 32
2.12 Quadrant analysis around beads with a negative vertical velocity ($V_p < 0$), with distribution of the turbulent events in clear water flow for $Re = 24,000$ (Lelouvetel et al., 2009). 32
2.13 Comparison between the mean streamwise velocity of the fluid, ascending and descending bead (fluids □, PS beads masked: ◆ $V_p < 0$ m/s, ◇ $V_p > 0$ m/s) (Van Hout, 2011) 33
2.14 Comparison of the normalised rms values of the streamwise and wall-normal bead and fluid velocity fluctuations. Closed symbols: beads; Open symbols: fluid (Van Hout, 2011) 34

3.1 The original water-channel, as supplied by Dantec and re-assembled at Newcastle. 36
3.2 New axial flow propeller pump, drive shaft tube, seal and motor on vibration isolation cradle. . . . 37
3.3 Floor boundary layer with original bellmouth inlet and 2m working section. . . 38
3.4 The original water-channel, with propeller drive system with proposed light-sheet setup. . . . 39
3.5 The Newcastle 3 m open-channel flow rig. . . . 40
3.6 Laser setup at channel bottom. . . . 41
3.7 New hyperbolic tangent profile channel inlet design. . . . 42
3.8 New hyperbolic tangent profile channel inlet design. From left, 1) Honeycomb, 2) 3 pc Coarse gauze, 3) 2 pc Fine gause, and 4) Channel inlet. . . . 42
3.9 Inlet plenum tank design with 4 perforated plates at different height. . . . 44
3.10 Exit plenum tank design with a perforated plate secured immediately after channel exit. . . . 44
3.11 Schematic diagram showing all components of the water channel rig (Not to scale). . . . 45
3.12 LDV velocity time trace plot showing the reduction of the low frequency undulation with the use of a perforated plate at the channel exit. . . . 46
3.13 Zigzag strip (design following (Elsinga and Westerweel, 2012)). . . . 47
3.14 Newcastle University PIV System. . . . 49
3.15 Pulse energy vs. repetition rate for LDP-100MQG laser. . . . 49
3.16 Vertical light-sheet, reflected from under floor of channel. . . . 50
3.17 IDT Redlake's MotionPro X5PLUS high-speed camera. . . . 52
3.18 DantecDynamics target plate. . . . 53
3.19 DantecDynamics target plate and custom traverse system. . . . 53
3.20 The velocity vector field of a jet flow measured by two-dimensional PIV. . . . 54
3.21 Elements and processes in a planar two-dimensional particle image velocimetry system (Adrian, 2005). . . . 56
3.22 Peak widths for 12μm particles imaged with MicroNikkor 60mm lens at f/2.8 . 58
3.23 Peak widths for 12μm particles imaged with MicroNikkor 60mm lens at f/4. . 58
3.24 Velocity histogram plot for $10\mu m$ S-HGS ($M = 0.17$, $f_{\#} = 2.8$, at $25\,W$) jet flow experiment clearly exhibiting pixel-locking behaviour. . . . 59

4.1 Mean velocity profile for various back-plate porosity level (perforated plate, 25%, fine gauze, 45 %, and coarse gauze, 60 % porous). . . . 71
4.2 Dimensionless mean velocity in the Newcastle open-channel with various back-plate porosity levels (Perforated plate, 25%, fine gauze, 45 %, and coarse gauze, 60 % porous). . . . 72
4.3 Turbulence intensity u'/u_τ for various level of back-plate porosity (Perforated plate, 25%, fine gauze, 45 %, and coarse gauze, 60 % porous). . . . 73
4.4 PIV time-averaged velocity contour plots along the channel from 2115mm up to 2515mm. . . . 74
4.5 Time-averaged velocity profile plotted at central position of frames in Figure 4.4, i.e. 2115mm, 2215mm, 2315mm, 2415mm and at 2545mm. . . . 75

4.6 Time-averaged velocity profile at 2115mm with and without zig-zag tripping device. . . . 76
4.7 Time-averaged velocity profile at 2115mm with and without tripping device - magnified view. . . . 77
4.8 Effect of the channel aspect ratio on the wake region of the boundary layer profile plotted against the data of (Nezu and Rodi, 1986). . . . 78
4.9 Velocity profile at 0.11m, 1.2m and 2.1m corresponding to x^+ = 2079, 22680 and 39690. . . . 80
4.10 Boundary layer profile at 0.11m, 1.2m and 2.1m corresponding to x^+ = 2079, 22680 and 39690. . . . 80
4.11 Turbulence profile at 0.11m, 1.2m and 2.1m corresponding to y^+ = 2079, 22680 and 39690. . . . 81
4.12 Boundary layer profile profile at 2075mm downstream of zig-zag strip (Newcastle LDV data). . . . 83
4.13 Turbulence intensity profile at 2075mm downstream of zig-zag strip (Newcastle LDV data). . . . 83
4.14 Velocity profile at 2075mm downstream of zig-zag strip (Newcastle LDV data). 84
4.15 Turbulence profile at 2075mm downstream of zig-zag strip (Newcastle LDV data). . . . 84
4.16 Turbulence profile at 2075mm downstream of zig-zag strip (Newcastle LDV data). . . . 85
4.17 Spectra at y ≈ 10mm at x = 2.1m downstream of channel inlet. . . . 87
4.18 Spectra at y ≈ 30mm at x = 2.1m downstream of channel inlet. . . . 87
4.19 Spectra at y ≈ 60mm at x = 2.1m downstream of channel inlet. . . . 88
4.20 Spectra at y ≈ 95mm at x = 2.1m downstream of channel inlet. . . . 88
4.21 LDV Velocity profile at 2075mm downstream of zig-zag strip without inertial particles. . . . 90
4.22 LDV Boundary layer profile at 2075mm downstream of zig-zag strip without inertial particles. . . . 91
4.23 LDV turbulence intensity profile at 2075mm downstream of zig-zag strip without inertial particles. . . . 92
4.24 Velocity profiles at Re = 730, 1420, and 2660 for LDV and PIV. . . . 93
4.25 Time average velocity profile from the PIV measurements. Colorbar in m/s. . . . 94
4.26 Velocity histogram plot (in m/s and pixels). . . . 95
4.27 Galilean decomposed revealing ramp like structures close to the wall following Adrian, Meinhart and Tomkins (2000). . . . 96
4.28 Velocity and velocity fluctuations profiles plot. . . . 98
4.29 Iso-surface of $|\lambda_{ci}|$ swirling strength and Q-criterion and vorticity profile plot. 99
4.30 Examples of velocity profile for frame 200 up to 220 showing hairpin structure propagating across the FOV (Part 1). Colorbar in m/s. . . . 100
4.31 Examples of velocity profile for frame 230 up to 250 showing hairpin structure propagating across the FOV (Part 2). Colorbar in m/s. . . . 101
4.32 Examples of velocity profile for frame 260 up to 270 showing hairpin structure propagating across the FOV (Part 3). Colorbar in m/s. . . . 102

4.33 Velocity profile plot indicating the presence of regions of constant velocity momentum across the measurement region following the work of Adrian, Meinhart and Tomkins (2000). 102

5.1 Schematic layout of experimental setups, (a) top view, (b) PIV setup (channel cross-section), (c) coordinate system and field-of-view (FOV). 109
5.2 Separation of particle images for two-phase flow (FOV x=100mm × y = 71 mm) 113
5.3 Fluid mean velocity profile for boundary layer with particle volumetric loading of $\phi = 0$, 1.4×10^{-5} and 2.8×10^{-5} 114
5.4 Fluid mean velocity profile for boundary layer with particle volumetric loading of $\phi = 0$, 1.4×10^{-5} and 2.8×10^{-5} in wall law form. 115
5.5 Normalised rms of streamwise and wall-normal velocity fluctuations for boundary layer with particle volumetric loading of $\phi = 0$, and 2.8×10^{-5} in wall law form. 116
5.6 Normalized Reynolds stresses profile at particle volumetric loading of $\phi = 0$, and 2.8×10^{-5}. 117
5.7 Histogram of particle count for all runs vs. distance from wall ($\Delta y^+ = 10$). . . 119
5.8 Comparison between the mean streamwise velocity of the fluid (particle image masked), and inertial particle streamwise velocity (bin size: $\Delta y^+ = 10$ for volumetric loading $\phi = 2.8 \times 10^{-5}$) - Small FOV. 120
5.9 Rms of fluctuating velocity components of open-channel at two particle volumetric loading ($\phi = 0$, and 2.8×10^{-5}), particle rms plot for u'_p/u_τ, and v'_p/u_τ. 121
5.10 Example of particle trajectories (Part 1) 123
5.11 Example of particle trajectories (Part 2) 124
5.12 Pdf of particle tracks for Re_θ = 730, 1420 and 2660 at volumetric loading, $\phi = 1.4 \times 10^{-5}$ (Figure 5.12(a), 5.12(b), 5.12(c)), and 2.8×10^{-5} (Figure 5.12(d), 5.12(e), 5.12(f)) 126
5.13 Particle samples sorted by quadrant of local fluid velocity perturbation (after Willmarth and Lu (1972)). Figure 5.13(a) Raw data, Thresholded data: 5.13(b) H=0.1, 5.13(c) H=0.2, Figure 5.13(d) H=0.3, 5.13(e) H=0.4, and 5.13(f) H=0.5 128
5.14 Plot of particle trajectories for the 10 longest tracks. 130
5.15 Plot of particle trajectories for the 10 greatest y^+ movement. 131
5.16 Plot of a) Particle trajectory near the channel wall, $y^+ \approx 21$ down to $y^+ \approx 7$ at the end of the FOV. b) Plot of stream-wise fluid and particle velocity along particle track, and c) plot of wall-normal fluid and particle velocity along particle track. 131
5.17 Plot of a) Particle trajectory near the channel wall, $y^+ \approx 21$ down to $y^+ \approx 7$ at the end of the FOV, b) Plot of fluid velocity perturbation along particle track, and 3) Quadrant number along the particle track with Q4 sweeps event along the particle trajectory. 132
5.18 Plot of a) Particle trajectory near the channel wall, $y^+ \approx 7$ up to $y^+ \approx 36$ at the end of the FOV, b) Plot of stream-wise fluid and particle velocity along particle track, and c) plot of wall-normal fluid and particle velocity along particle track. 133

5.19 Plot of a) Particle trajectory near the channel wall, $y^+ \approx 7$ up to $y^+ \approx 36$ at the end of the FOV, b) Plot of fluid velocity perturbation along particle track, and 3) Quadrant number along the particle track with Q2 ejection event along the particle trajectory. 134
5.20 Plot of a) Particle trajectory near the channel wall, $y^+ \approx 7$ along the trajectory, b) Plot of fluid velocity perturbation along particle track, and 3) Quadrant number along the particle track with Q2 ejection event along the particle trajectory. . . 135
5.21 Plot of a) Particle trajectory near the channel wall, $y^+ \approx 36$ up to 72, b) Plot of fluid velocity perturbation along particle track, and 3) Quadrant number along the particle track with Q2 ejection event dominating the particle trajectory. . . 136
5.22 Plot of a) Particle trajectory near the channel wall, $y^+ \approx 72$ down to 28, b) Plot of fluid velocity perturbation along particle track, and 3) Quadrant number along the particle track with Q4 sweep event dominating the particle trajectory. 137
5.23 Plot of a) Particle trajectory near the channel wall, $y^+ \approx 86$ up to 130, b) Plot of fluid velocity perturbation along particle track, and 3) Quadrant number along the particle track with Q2 ejection event dominating the particle trajectory. . . 138
5.24 Plot of a) Particle trajectory near the channel wall, $y^+ \approx 86$ down to 65, b) Plot of fluid velocity perturbation along particle track, and 3) Quadrant number along the particle track with Q4 sweep event dominating the particle trajectory. 139
5.25 Plot of a) Particle trajectory near the channel wall, $y^+ \approx 58$, b) Plot of fluid velocity perturbation along particle track, and 3) Quadrant number along the particle track affected byQ1, Q2, Q3 and Q4 event along the particle trajectory. 140
5.26 Plot of a) Particle trajectory near the channel wall, b) Plot of stream-wise fluid and particle velocities along particle track, and c) plot of wall-normal fluid and particle velocity along particle track. 142
5.27 Plot of a) Particle trajectory near the channel wall, b) Plot of stream-wise fluid and particle velocity along particle track, and c) plot of wall-normal fluid and particle velocity along particle track. 143
5.28 Histogram plot of particle-fluid velocity correlation for run 1, and 2. 144
5.29 Histogram plot of particle-fluid velocity correlation for run 3 and 4. 145

B.1 AF Micro Nikkor 60mm standoff distance. 165
B.2 AF Micro Nikkor 105mm standoff distance. 165
B.3 AF Micro Nikkor 200mm standoff distance. 166

D.1 The percentage of valid velocity vectors as a function of laser power for 10–μm S-HGS, Interrogation: Adaptive correlation using 32 by 32 pixels IW, 50% overlap and local-median abd moving-average validation based on 100 single-exposure double-frame images without image pre-processing. 172

E.1 Particle track and corresponding streamwise velocity for fluid and particle showing spikes at x = 500, 750, 1000, 1250, 1500 and 1750 pixels 173
E.2 DynamicStudio particle tracking data output A 174
E.3 DynamicStudio particle tracking data output (Continue from Figure E.2). . . . 175
E.4 DynamicStudio particle tracking data output for frame 251. 176
E.5 Two-phase image showing inertial particles (Frame 1) 177

E.6 Two-phase image showing inertial particles (Frame 2) 177
E.7 New particle tracking algorithm output for particle velocities. 179
E.8 Fluid and inertial particle velocities using DynamicStudio particle tracking algorithm showing velocity spikes. 179
E.9 Distorted particle image after filtering and binarization process. 180
E.10 Fluid and inertial particle velocities using in-house particle tracking algorithm showing the absence of velocity spikes. 181

List of Tables

3.1 MotionPro X5PLUS sample frame rates (@ Max. Horizontal resolution of 2352 (Horizontal resolution does not affect frame rate performance) 51
3.2 MotionPro X5PLUS Performance Specifications 52
3.3 Effect of diffraction on image size for 12 μm particle. 57
3.4 Theoretical estimates of boundary layer characteristics 64

4.1 Plenum tank and channel inlet configuration. (* High-pass filtered data, ** With perforated plate at channel exit; subscript represents the number of items installed) Perf.Plate = Perforated plate in inlet plenum tank, HComb = Honeycomb 69

5.1 Comparable 2-phase experimental data. (* Based on δ_{99}; + Based on depth = 35.36mm; ++ Based on half-height = 25mm). 116
5.2 Average track lengths in t^+ and x^+ for large FOV (M=0.16) at $\phi = 1.4 \times 10^{-5}$. . 125
5.3 Average track lengths in t^+ and x^+ for small FOV (M=0.34) at $\phi = 2.8 \times 10^{-5}$. 127
5.4 Average track lengths in t^+ and x^+ for large FOV (M=0.16) at $\phi = 2.8 \times 10^{-5}$. . 127
5.5 No. of particles recorded in each fluid velocity perturbation quadrant. 130
5.6 Streamwise particle-velocity correlation coefficient, Ru, and wall-normal particle-velocity correlation coefficient, Rv, and the average particle-fluid velocity correlation, R, for streamwise and wall-normal velocities. 146

B.1 AF Micro Nikkor 60mm standoff data at $f/2.8$ 164
B.2 AF Micro Nikkor 105mm standoff data at $f/2.8$ 164
B.3 AF Micro Nikkor 200mm standoff data at $f/2.8$ 164

C.1 Theoretical and experimental depth-of-field for AF Micro Nikkor 60 mm lens ($M_0 = 0.2$). 169
C.2 Theoretical and experimental depth-of-field for AF Micro Nikkor 105 mm lens ($M_0 = 0.22$). 169
C.3 Theoretical and experimental depth-of-field for AF Micro Nikkor 200 mm lens ($M_0 = 0.6$). 169

Abbreviations

CMOS	**C**omplementary **M**etal-**O**xide-**S**emiconductor
DNS	**D**irect **N**umerical **S**imulation
FOV	**F**ield **O**f **V**iew
FFT	**F**ast **F**ourier **T**ransform
LDV	**L**aser **D**oppler **V**elocimetry
LES	**L**arge **E**ddy **S**imulation
LSM	**L**arge **S**cale **M**otion
PDA	**P**hase **D**oppler **A**nemometry
PDF	**P**robability **D**ensity **F**unction
PIV	**P**article **I**mage **V**elocimetry
PTV	**P**article **T**racking **V**elocimetry
S-HGS	**S**ilver-coated **H**ollow **G**lass **S**phere
TRPIV	**T**ime **R**esolved **P**article **I**mage **V**elocimetry
TR	**T**ime **R**esolved
TBL	**T**urbulent **B**oundary **L**ayer
VLSM	**V**ery **L**arge **S**cale **M**otion

Nomenclature

B	Constant
Cd	Drag coefficient
d_e	Diameter of diffracted image of particle, $d_e = \sqrt{d_s^2 + M_0^2 d_p^2}$
d_{geom}	Geometric diameter of particle, $d_{\text{geom}} = \sqrt{M_0^2\, d_p^2}$
d_p	Diameter of particle
d_r	Pixel size
d_s	Diffraction limited spot size of particle, $d_s = 2.44\,(1 + M_0)\; f^{\#}\,\lambda$
$f^{\#},\, f$	f-number of camera, f-stops
Fr	Froude number, Fr = $\frac{\mathrm{U}}{\sqrt{dD}}$
H	Threshold value
M_0	Image magnification
N(k)	Number of lagged product
Q1, Q2, Q3, Q4	Quadrants of instantaneous Reynolds stress uv
r_{pf}	Fluid-particle velocity correlation for particle trajectory
R	Fluid-particle velocity correlation for particle trajectory average over all particle trajectories
Re	Reynolds number
Re_θ	Reynolds number based on momentum thickness, $\mathrm{Re}_\theta = \frac{\rho_p\, U_\infty\, \theta}{\mu}$
Re_δ	Reynolds number based on displacement thickness
Re_p	Particle Reynolds number, $\mathrm{Re}_p = \lvert u - u_p \rvert \frac{d_p}{\nu}$
Re_τ	Reynolds number based on wall friction velocity, $\mathrm{Re}_\tau = \frac{\delta\, u_\tau}{\nu}$
Re_x	Reynolds number based on distance from leading edge, $\mathrm{Re}_x = \frac{\rho\, \mathrm{U}_\infty\, x}{\mu}$
Re_{XX}	Autocorrelation function

St	Stokes number, St = $\frac{\tau_p}{\tau_f} = \frac{\rho_p d_p^2 u_\tau^2}{18 \rho_f \nu^2}$
St^+	Non-dimensional Stokes number
St_K	Stokes number based on Kolgomorov length scale
S_Q	Detection function
t	Time
t^+	Non-dimensionless time, $t^+ = \frac{t u_\tau^2}{\nu}$
u, v, w	Fluctuation velocity component
$-uv$	Reynolds shear stress
u_f	Fluid velocity
u_p	Inertial particle velocity
u_{rms}, v_{rms}	Root mean square of the velocity fluctuation
u_τ	Wall friction velocity, $u_\tau = \sqrt{\tau_w / \rho}$
u', v', w'	rms velocity components
U, V, W	Streamwise, wal-normal and spanwise velocity
U_m	Mean bulk velocity
U_∞	Free-stream velocity
w_i	Weighting
x, y, z	Streamwise, wall-normal and spanwise coordinates
x^+, y^+, z^+	Instantaneous velocity based on u_τ
δ	Boundary layer thickness
δ_0	Boundary layer thickness at trip position
δ_{99}	Boundary layer thickness based on 99% of free-stream velocity
κ	Von Kármán constant
λ	Wavelength of light
λ_{ci}	Swirling strength
μ	Dynamic viscosity
ν	Kinematic viscosity
ϕ	Volumetric loading
ρ	Density of water
ρ_p	Density of particle
σ	Variance

τ_i	Transit time
τ_p	Particle response time, $\tau_p = \frac{\rho_p d_p^2}{18\mu}$
τ_f	Viscous time scale, $\tau_f = \frac{\nu}{u_\tau^2}$
τ_w	Wall shear stress, $\tau_w = \frac{0.0288\rho U_\infty^2}{\mathrm{Re}_x^{1/5}}$
θ	Momentum thickness, $\theta = \int_0^\infty \frac{\rho u}{\rho \mathrm{U}_\infty}\left(1 - \frac{\mathrm{U}}{\mathrm{U}_\infty}\right)\mathrm{d}y$
ω	Vorticity
ω_i	Weighting
$+$	indicates viscous scaling or inner scaling
Δ	indicates a change in quantity

Dedicated to my mother,

my wife, son (Danish) and

our two lovely daughters, Aisha and Arya,

&

to the memory of my father and brother . . .

Chapter 1

Introduction

Particle-laden turbulent flows are involved in a wide variety of fields. Interactions of particles (solids, droplets or bubbles) with turbulent flows occurs in a large number of industrial and environmental processes such as chemical reactors and combustion chambers,

Prediction of the transport and deposition of inertial particles in turbulent boundary layers is of significant importance in a number of engineering situations. Important examples are (see Crowe et al. (1998) books and papers by J.B. Young and A. Dehbi).

Early experimental work on deposition by Liu and Agarwal (1974) and Papavergos and Hedley (1984) still provide the benchmark for particle deposition. Mathematical models for the process involved were developed, and a notable advance in modelling the actual physics involved was the seminal paper of Kallio and Reeks (1989). Various refinements of this, all make use of stochastic models of turbulence.

In parallel with this progress, fundamental investigations of turbulent boundary layers from the 1960s onwards began to reveal the existence of coherent structures within what was previously thought to be purely chaotic turbulent boundary layer.

As separate line of research into the possible effects of these structures on inertial particle transport was thus also begun, with notable early contributions by Willmarth and Lu (1972)

More recently, attempts have been made to incorporate modelling of turbulent structures in particle transport and deposition prediction models, e.g. by Guingo and Minier (2008) and by Jin et al. (2015), but the models lack verification by direct experimental observation of the transport phenomena.

Computational advances have led to Direct Numerical Simulation (DNS) of boundary layers, and this has been developed to include particle transport, notably by Soldati (2005); Soldati and Marchioli (2009) among others. The limitation here is that current computer resources only allow simulation at relatively low Reynolds numbers, so there is some doubt about the generalisation of these results.

Against this background, the recent commercial availability of time resolved Particle Image Velocimetry (TRPIV) in the mid 2000s was seen, at that time, to be a potential tool for detailed experimental investigation of particle transport in turbulent boundary layers by direct observation. This was the genesis of the present project. A detailed review of the literature is provided in the following chapter.

1.1 Thesis outline

The principal objective of this thesis is to investigate the transport of heavy particle suspended in turbulent boundary layers as a dilute second dispersed phase in an experimental channel flow.

Chapter 2 report the background literature review on turbulent boundary layers, structure identifications, boundary layer particle image velocimetry and two-phase flow.

Chapter 3 describes the design and construction of the Newcastle open-channel facility and the stages of improvement and modification that it has undergone to meet experimental requirements. This include the extension of the channel length, a new inlet section, inlet and outlet plenum setup, light beam reflection facility, calibration target facility and the tripping device used in the experiment. A detail description of particle image velocimetry and laser Doppler velocimetry system used in the experiment are also presented.

Chapter 4 details the vigorous testing to characterize and validate the experimental rig prior to two-phase measurements. Both PIV and LDV were used to characterize boundary layer profile, to determine the level of turbulence in the free-stream at different inlet and outlet configurations, to investigate the effects of Reynolds number on boundary layer profile and the detection of coherent structures within the boundary layer. Experimental testing of the channel using both LDV and PIV has proven that the characteristic behaviour of the flow was sufficient and meets the two-phase experiment requirement.

Chapter 5 details the two-phase measurements where 200μm secondary phase particles that are neutrally buoyant were used. Two series of experiments were done, both with two particle loadings of $\phi = 1.4 \times 10^{-5}$ and 2.8×10^{-5}. These tests were carried out at a single Reynolds number of $\mathrm{Re}_\theta = 3000\,(\mathrm{Re}_\tau = 890)$. The second series of experiments, carried out at the same two volumetric loadings, and at three Reynolds numbers, Re_θ = 730, 1420 and 2660, concentrated on tracking the inertial particles in real time. Inertial particle mean and RMS velocity profiles were plotted together with the tracking of inertial particles and their track lengths. Conditional statistics for inertial particles were also carried out to investigate quadrant statistics and particle-fluid velocity correlation coefficient.

Chapter 6 summarizes these investigations and discusses in general, features of future work.

Chapter 2

Literature Survey

2.1 Introduction

Many industrial and environmental processes involve turbulent dispersed two-phase flows, such as gaseous flows laden with solid particles or liquid drops and liquids containing solid particles or bubbles. In such flows, discrete particles, i.e., drops or bubbles constitute a disperse phase, whereas the carrier liquid or gas represents the continuous phase. The disperse phase can move differently from the continuous phase and the motion of both phases can be very complicated, especially in turbulent flow and in particular in a turbulent boundary layer.

It has been found that turbulence may be characterized by semi-organized structures (Robinson, 1991) and researchers have been trying to understand the flow phenomena employing different techniques to deconstruct the complex disorganised turbulent flow field into a set of atleast quasi-organised motions. These are called "coherent structures". In addition, the presence of particles and their interactions with these coherent structures are now actively being studied by various researchers, see for example the works of Kallio and Reeks (1989); Kaftori et al. (1995*a*,*b*); Kiger and Pan (2002); Khalitov and Longmire (2002); Soldati (2005); Van Hout (2011); Lee and Lee (2015) among others.

This chapter is drafted to review both the historical and latest advances in the area of two-phase boundary layer flow, and is broken down into sections that include a brief introduction

to boundary layer flow, boundary layer structure covering the near wall region, the logarithmic and outer regions, and very large-scale coherent motions, and this is followed by a review of the available methods of identifying structures. Further, a review of the literature in the area of boundary layer measurement using particle image velocimetry is given, and finally this is extended to include the topic of two-phase flow.

2.2 Turbulent boundary layer

2.2.1 Boundary layer structure

The underlying structure of the turbulent boundary layer has been extensively studied because of its importance in many practical engineering applications. The properties of turbulence in wall-bounded flows have been in the past investigated, both experimentally and numerically, with the use of a variety of techniques and methods. Statistical descriptions and models of boundary-layer turbulence constituted the earliest approach, but these ignore the presence of more recently observed repeating quasi-periodic patterns in the flow. It has also been discovered that the coherent motions are responsible for the maintenance of turbulence in the boundary layer, therefore the study of these underlying structures is very important for fundamental understanding of turbulent boundary layer dynamics. Equally, the existence of coherent structures must have a significant effect on turbulent transport of particles within the boundary layer.

In the following sub-sections, boundary layer structures are systematically categorized and described in greater detail in accordance with their locations within the boundary layer, expressed in terms of non-dimensional distance from the wall, y^+.

2.2.1.1 Near-Wall Structure

In this sub-section, we discuss events that reside within the first 100 wall units from the surface ($y^+ \lesssim 100$, where y is the wall-normal distance and $y^+ = yu_\tau/\nu$). Coherent motions within this region are dominated by near wall low-speed streaks (Kline et al., 1967; Robinson, 1991) and quasi-streamwise vortices.

These streaks consists of elongated spanwise alternating regions of low and high-speed streamwise velocity fluctuations. Quasi-streamwise vortices, approximately centered at $y^+ = 15$ accompany the streaks.

Experimental observations over a range of Reynolds numbers (Kline et al., 1967; Smith and Metzler, 1983; Robinson, 1991) have confirmed that the spacing and length of the near-wall streaks scale with the viscous length-scale (average spanwise spacing of $100\,\nu/u_\tau$ and streamwise length in the range 400 - 1,000 ν/u_τ).

Reynolds number is the ratio of inertial forces to viscous forces. Flow perturbations tend to preserved by inertia forces leading to instability. Counteracting this effect is the viscosity of the fluid which as it increases, progressively inhibits turbulence as more kinetic energy is absorbed by the fluid. The Reynolds number quantifies the importance of these two forces for a given flow condition, and as a guide when turbulent flow will occur. The momentum thickness Reynolds number is given by

$$\mathrm{Re}_\theta = \frac{\rho \mathrm{U}_\infty \theta}{\mu} \tag{2.1}$$

where the momentum thickness, θ is calculated by evaluating the integral

$$\theta = \int_0^\infty \frac{\rho u}{\rho \mathrm{U}_\infty}\left(1 - \frac{\mathrm{U}}{\mathrm{U}_\infty} dy\right) \tag{2.2}$$

The momentum thickness is chosen as the outer variable to scale wall-normal distance because it can be determined accurately from experimental data than boundary layer thickness.

In wall bounded flow studies, the friction Reynolds number is often used as a common Reynolds number to compare Reynolds number effects among different types of flow. It is defined as the ratio of the inner and outer length scales.

$$\mathrm{Re}_\tau = \frac{\delta\, u_\tau}{\nu} \tag{2.3}$$

where δ is the boundary layer thickness.

The near-wall structures only exist over smooth to moderately rough surfaces. In early visualization experiments (for example Kline et al., 1967), the streaks were often observed

to undergo an oscillation and break-up referred to as 'bursting'. Inflows of high-speed fluids towards the wall and ejections of low-speed fluid away from the wall were termed 'sweeps' and 'ejections', respectively. Subsequent studies have suggested a self-sustaining near-wall cycle of break-up and regeneration in which the streaks and vortices mutually self-sustain without the need of external influences or triggers (Jiménez and Pinelli, 1999; Schoppa and Hussain, 2002).

2.2.1.2 The Logarithmic Region and Outer Region

The logarithmic region is approximately defined as the region $100 < y^+ < 0.15\,Re_\tau$ for turbulent boundary layers. The logarithmic region is given by

$$\frac{U(y)}{u_\tau} = \frac{1}{\kappa}\ln\left(\frac{y u_\tau}{\nu}\right) + B \tag{2.4}$$

where U(y) is the instantaneous velocity along the wall-normal direction, u_τ is the friction velocity, κ is the von Kármán constant, μ is the kinematic viscosity, and B is a parameter that depends on the roughness of the surface, and is a constant for a smooth wall. The von Kármán constant can range between 0.35 and 0.42, but it is considered to be universal at $\kappa \approx 0.41$.

The existence of much larger structures in the logarithmic and outer regions of the flow has long been indicated by single-point statistics. Two-point correlation measurements (e.g. Kovasnay et al., 1970; Nakagawa and Nezu, 1981; Mclean, 1990; Wark et al., 1991) revealed the existence of elongated regions of streamwise momentum deficit with length scales that approximately scale on δ. The advent of particle image velocimetry (PIV) and higher Reynolds number DNS studies, provided the first quantitative instantaneous views of the logarithmic region structures, starting a renewed interest in these larger scales. One of the most interesting results from PIV studies involved observations of hairpin vortex structures arranged into groups or 'packets'. As early as the 1950s, hairpin vortices had been postulated as possible boundary-layer structures (Theodorsen, 1952; Townsend, 1956). Flow visualization (Head and Bandyopadhyay, 1981) suggested that the turbulent boundary layer was extensively populated by hairpin vortices. Laboratory-based PIV studies, initially from Adrian's group at Champagne-Urbana, provided evidence that these hairpin vortices are preferentially arranged into packets

(Adrian, Meinhart and Tomkins, 2000; Christensen and Adrian, 2001; Tomkins and Adrian, 2003). These packets form ramp-like structures, with hairpins at the downstream end of the packet extending further from the wall than hairpins at the upstream end (Ganapathisubramani et al., 2003; Hambleton et al., 2006; Wu and Christensen, 2006; Dennis and Nickels, 2011*a*, and others) and numerical investigations (Zhou et al., 1999; Wu and Moin, 2009; Lee and Sung, 2011, and others). Adrian (2007) provides an excellent review and overview of hairpin packet literature.

2.2.1.3 Very Large-Scale Coherent Motions

In streamwise/spanwise planes within the logarithmic region, the packet structure appears as pronounced large-scale "stripes" in streamwise velocity fluctuations. The region within the hairpin packet is characterised by negative streamwise velocity fluctuations and upwash. When a structure is sliced by streamwise/spanwise planes, highly elongated regions of negative streamwise velocity fluctuation are evident, with similarly elongated high-speed regions present to each side (e.g. Tomkins and Adrian, 2003; Ganapathisubramani et al., 2003; Hambleton et al., 2006). In the PIV experiments described in these references, these elongated stripes often exceeded the field of view.

Energy spectra measured in the past have hinted that these structures in the logarithmic region could be very long. Peaks in pre-multiplied energy spectra were known to occur at wavelength of $\approx 6\delta$ in the logarithmic region. Kim and Adrian (1999) had shown that for turbulent pipe flow the pre-multiplied spectra had a bi-modal appearance with peaks occurring at 3δ and $14-20\delta$ that they termed large-scale motions (LSM) and very-large-scale motions (VLSM), respectively (see also Guala et al., 2006). In DNS of channel flow, Del Álamo et al. (2004) found similar large-scale contributions in energy spectra. Hutchins and Marusic (2007*a*) used hotwire probes arranged as spanwise rakes in the logarithmic region of the turbulent boundary layer and discovered meandering regions of highly elongated negative and positive velocity fluctuations occasionally exceeding 15δ in length. They termed these events "superstructures". Similar experiments performed in channel and pipe flows by Monty et al. (2007) have shown the existence of similar events in fully developed turbulent flows. In pipes and channel, these events appear to be on average slightly longer, and with slightly greater spanwise spacing and dimension than

those found in the turbulent boundary layer. It has been shown that the superstructures/VLSM are responsible for a high proportion of the Reynolds shear-stress (Ganapathisubramani et al., 2003; Guala et al., 2006). Additionally, Hutchins and Marusic (2007*a*,*b*) have shown that the magnitude of the streamwise fluctuations associated with the superstructure events increase in comparison to those of the near-wall cycle with increasing Reynolds number. (i.e. as Re increases, velocity fluctuations with wavelength equal to or greater than δ become increasingly energetic as compared to the smaller scale fluctuations arising from the near-wall cycle, see also Hutchins et al. (2009). As the Reynolds number increases, the large and very large scale events appear to dominate the turbulent structural landscape.

Superstructures/VLSM have been observed to maintain a footprint all the way down to the surface, and thus they strongly influence the near-wall flow. In addition to a clearly observed large-scale superposition (Abe et al., 2004; Hutchins and Marusic, 2007*a*,*b*) the large-scale events appear to modulate the amplitude of the small-scale activity (Hutchins and Marusic, 2007*a*,*b*; Marusic and Hutchins, 2008; Mathis et al., 2009). This modulation has also be observed in LES of turbulent channel flow (Chung and McKeon, 2010). The ideas of large scales interacting with small-scales in such a way is not new and has been extensively discussed in relation to shear flow (Bandyopadhyay and Hussain, 1984) and intermittency of fine scale turbulence (Sreenivasan, 1985; Kholmyansky et al., 2007).

2.2.2 Hairpin vortex

A simple structure that explains many of the observed features of wall turbulence is the hairpin vortex (Theodorsen, 1952; Head and Bandyopadhyay, 1981). Following Adrian, Meinhart and Tomkins (2000), in this thesis the term “hairpin” is used to describe a variety of structures including the classic, double legged hairpin, omega-shaped, horseshoe, or asymmetric cane vortices, all of the same generic family, but at different stages of evolution, exhibiting different degrees of deformation, aspect ratio and symmetry, depending on age and size. Thus, in this thesis, “hairpin” will be taken to include all such structures, narrow or wide, with or without symmetry, of this generic type.

In Robinson's (1991) modification of Theodorsen's original model structure (Theodorsen, 1952), vortex "necks", inclined at approximately 45 degrees to the wall, connect the head of the hairpin to long, quasi-streamwise, trailing vortices. With this simple model, viscous low speed fluid is induced by the quasi-streamwise vortices to move up from the wall, providing an explanation of the low speed streaks observed in the wall region.

The inclined "neck" (or "legs") and head of the hairpin induce low speed fluid through the inclined loop of the structure, resulting in a so-called "ejection" region of fluid, with upward wall-normal velocity perturbation and negative streamwise velocity perturbation. A countering "sweep" event, with negative wall normal velocity perturbation and positive streamwise velocity perturbation may be explained if the hairpin propagates more slowly than the surrounding fluid, or if it lies in the downwash of an upstream hairpin. When an ejection meets a sweep at the back of a hairpin, a stagnation point flow occurs, generating a shear layer inclined at less than 45 degrees to the wall, as observed in the experiments of Liu et al. (1991). According to Adrian, Meinhart and Tomkins (2000), these shear layers are associated with regions of high Reynolds stress, and terminate in regions of rolled-up spanwise vorticity, which they interpreted as the heads of hairpin vortices. Many of these features are illustrated in Figures 2.4 and 2.7, reproduced from Adrian, Meinhart and Tomkins (2000).

Researchers have proposed that hairpin vortices move in groups (see Bandyopadhyay, 1980; Head and Bandyopadhyay, 1981). Adrian, Christensen and Liu (2000) have observed the existence of "vortex packets" employing planar PIV measurements in streamwise-wall-normal flow planes in turbulent boundary layers. Their experimental results correspond well with the DNS simulation of Zhou et al. (1999). The existence of packets helps explain the long tails observed on streamwise velocity auto-correlations in boundary layers (see Townsend, 1976; Marusic, 2001). Longmire et al. (2001) made stereoscopic PIV measurements slicing through streamwise-spanwise planes within a turbulent boundary layer, which revealed signatures of vortex packets within the logarithmic region at $z^+ = 92$ ($z/\delta = 0.09$). The near-wall model of Smith (1984) as shown in Figure 2.1, shows that hairpins move in groups of two or three, and grow as they travel downstream with their heads inclined at $15 - 30^\circ$ to the wall. Adrian, Meinhart and Tomkins (2000) associate bursting events with a group of hairpins, explaining the

existence of the long extension of near wall low-speed streaks and the occurrence of multiple ejections.

DNS data of Wu and Moin (2009) and Schlatter (2010) supports the existence and domination of hairpin vortices in the turbulent boundary layer. Further, analysis of Wu and Moin (2009) data and of Schlatter (2010) shows that the presence of classical symmetrical hairpin structures are only transitional (i.e. only a low Reynolds number effect). At higher $\mathrm{Re}_\theta > 2,500$, these vortices becomes rare; instead they are inclined, formed as a cane or arch. Recent experiment by Dennis and Nickels (2011*a*,*b*) among others clearly show the presence of hairpins and hairpin packets and long structures within the turbulent boundary layer.

2.3 Structure identification in boundary layer PIV

The random locations of structures in both streamwise and spanwise directions in the boundary layer makes the interpretation of planar velocity vector fields more complex. In the context of experimental measurements, this difficulty can be resolved by relating hypothetical three-dimensional structures with observed planar data and the data of other researchers. For a better understanding of boundary structure, the reader is directed to Section 2.2.1 where these structure has been reviewed. In the context of the present experiment, both two-dimensional and three-dimensional structure identification will be addressed.

Decomposing the velocity field by subtracting the time-averaged velocity field from instantaneous velocity data (Reynolds decomposition) is a natural approach for the analysis of turbulent signals. This is the basis in all two and three-dimensional visualization of structures from which contours and iso-surface plots are generated.

To understand the structured, coherent elements of the flow, methods of visualisation that leave the large structures intact may be more appropriate. The Galilean approach proposed by Adrian, Meinhart and Tomkins (2000), is to decompose the velocity field into a constant streamwise convection velocity plus a deviation field. The deviation vectors are equivalent to the velocity vectors seen in a frame of reference moving with the convection velocity, and this technique provides the best visualization of the vector field as shown by Adrian, Meinhart

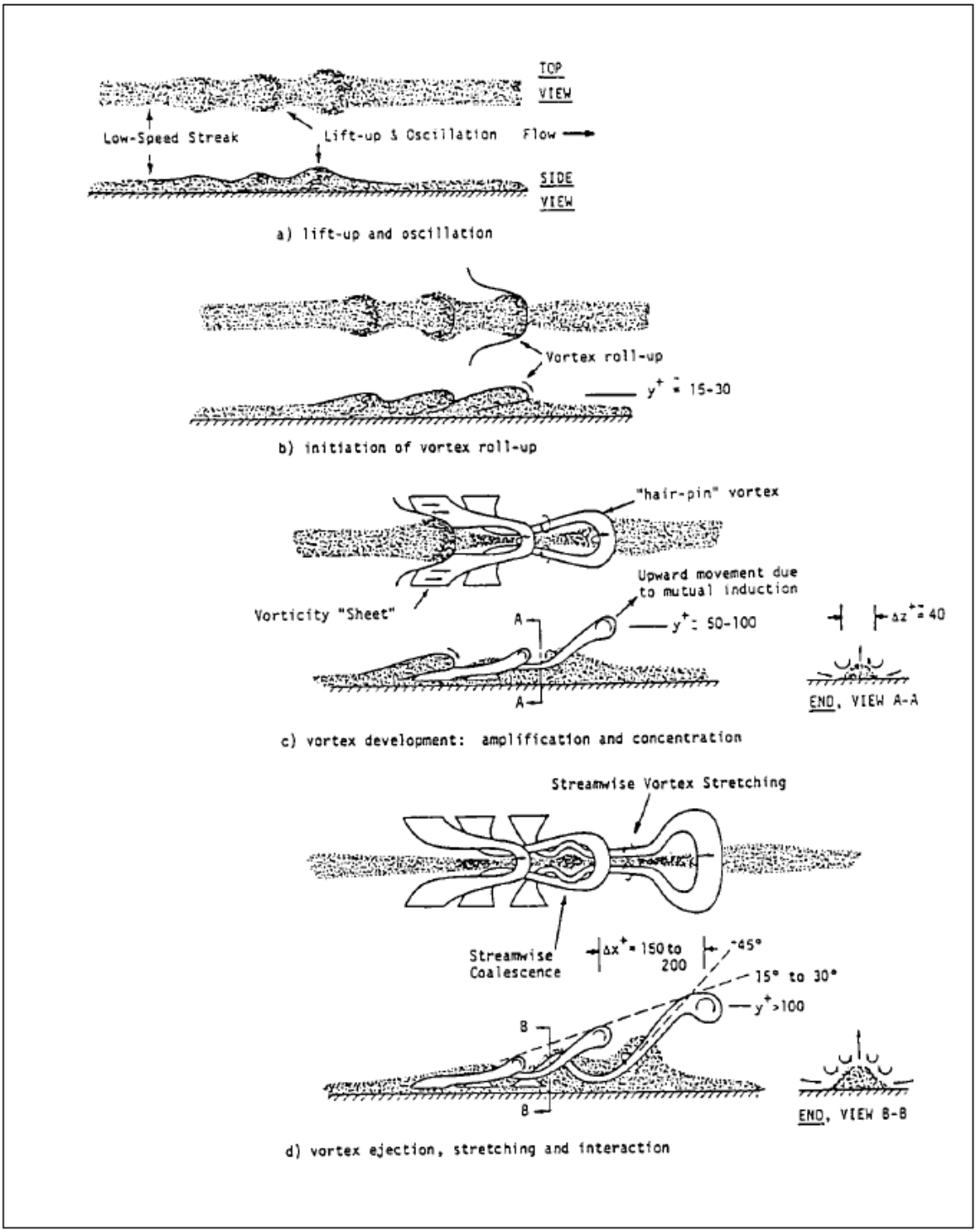

FIGURE 2.1: Representation of the "*bursting*" process in which a low-speed streak develops into a hairpin vortex. From: Smith (1984)

and Tomkins (2000). Selecting the appropriate streamwise convection velocity is somewhat arbitrary, and may require some "trial and error".

Kline and Robinson (1989) and Robinson et al. (1989) define a vortex as: "A vortex exists when instantaneous streamlines mapped on to a plane normal to the core exhibit a roughly circular or spiral pattern, when viewed in a reference frame moving with the center of the vortex core". From this definition, firstly the velocity field should be viewed in a reference frame that moves at the same velocity as the vortex core. Secondly, the vorticity is concentrated in a core. Since a turbulent field consists of large-scale motion with many small-scale vortices embedded within it, to recognize a vortex the convection velocity at the center of the each small vortex must be removed. An important function of decomposition by scale is to do exactly this. Galilean analysis can also reveal most of the vortex cores in a flow field if one systematically cycles thorough a range of convection velocities.

Identifying vortices in a velocity field, and calculation of vortex statistics can be accomplished by identifying isolated regions of significant vorticity. This is relatively straightforward with simple flows with minimal shear. In complex flows, such as those very close to the wall, vortices are often masked by regions of significant shear. Although this technique is excellent for identifying two-dimensional structures such as for example shear layers and signatures of hairpins, three-dimensional iso-surface contours have been more effective in visualizing three-dimensional structures. Two-dimensional contours of similar quantities do help in identifying rotation in planar-PIV. Determination of vorticity, swirling strength or Q-criterion for two-dimensional visualisation by contour plotting requires the computation of velocity gradients from the measured velocity field.

The quadrant classification, dividing the (u, v) velocity perturbation plane into four quadrant according to the sign of the fluctuations u and v, was first proposed by Willmarth and Lu (1972). Each quadrant is associated with a specific event type: outward or Quadrant 1 events have ($u > 0$ and $v > 0$), ejections or Quadrant 2 events have ($u < 0$ and $v > 0$), inwards or Quadrant 3 events have ($u < 0$ and $v < 0$) whilst sweeps or Quadrant 4 events correspond to ($u > 0$ and $v < 0$). The quadrant technique was applied to PIV data for a particle laden turbulent boundary layer by Bigillon and Garcia (2002), using a detection function S_Q and a threshold H.

$$S_Q(H) = \begin{cases} 1 & \text{if } u' < 0,\ v' > 0 \text{ and } |R_{rms}| > H \\ 0 & \text{otherwise} \end{cases} \tag{2.5}$$

with $R_{rms} = u'v'/u_{rms}v_{rms}$. The quantities u_{rms} and v_{rms} are the root mean square values of the velocity fluctuations.

The function S_Q is used to sort the events u; v into the four quadrants. An event is detected when the corresponding point is located outside a hyperbola as shown in Figure 2.2. A threshold H defines this hyperbola and is used to sort events into different ranges of intensity.

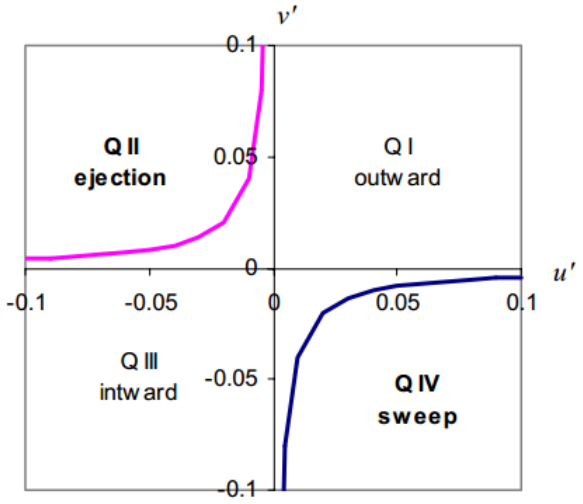

FIGURE 2.2: Quadrant analysis to detect and sort events (ejections or sweeps)(Bigillon and Garcia, 2002).

Coherent structures can be identified using the detection function S_Q or, in other words, analysing both the velocity fluctuation field and the perturbation intensity value R_{rms}. This method can be applied to detect such structures and quantify them in terms of intensity, spatial scale and dynamic characteristics. An example of such plot is shown in Figure 2.3 where the blue regions ($R_{rms} < 0$) correspond to ejections or sweeps whereas red regions ($R_{rms} > 0$) correspond to inwards or outwards.

Figure 2.4 schematically depicts the qualitative signature of the velocity field induced by a hairpin vortex on a streamwise wall-normal plane through the centre of the hairpin. The various parts of the idealised, three -dimensional hairpin can clearly be identified as shown

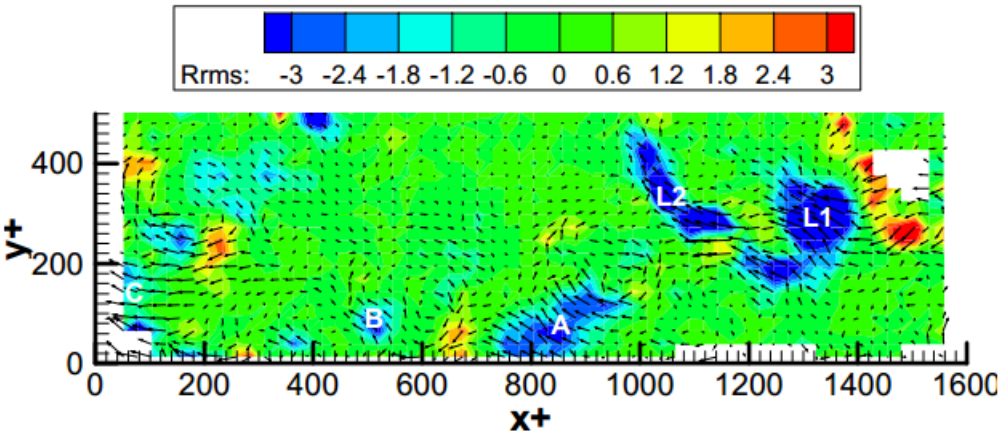

FIGURE 2.3: Rrms contour plot representing ejections or sweeps, and inwards or outwards (Bigillon and Garcia, 2002).

in Figure 2.4a, whilst the corresponding two-dimensional velocity pattern of a cross-section view of the hairpin structures is also shown in Figure 2.4b. Evident in the 2-D sectional slice are the clockwise rotating hairpin head, the low momentum of the fluid near the wall, below and upstream of the vortex head, the second quadrant ejection flow, roughly normal to the hypothesized hairpin necks at 45 degrees to the wall, the fourth quadrant inward sweep flow, and the shear layer where sweep and ejection meet, inclined at around 15-20 degrees from the wall.

A two dimensional or planar PIV slice through the turbulent boundary layer proposed for the present study would be expected to show a pattern similar to that in Figure 2.4b, enabling the identification of the underlying 3-D hairpin structure, as done by previous researchers such as Adrian, Meinhart and Tomkins (2000).

2.3.1 Two-dimensional visualization of vortices

There are numerous technique to visualize two-dimensional contours of the flow that can indicate the presence of flow structures within the turbulent boundary layer. A plot of Galilean decomposed velocity vectors, Reynolds decomposed velocity components, vorticity, swirling strength, or the second invariant of the velocity-gradient tensors can reveal vortex cores.

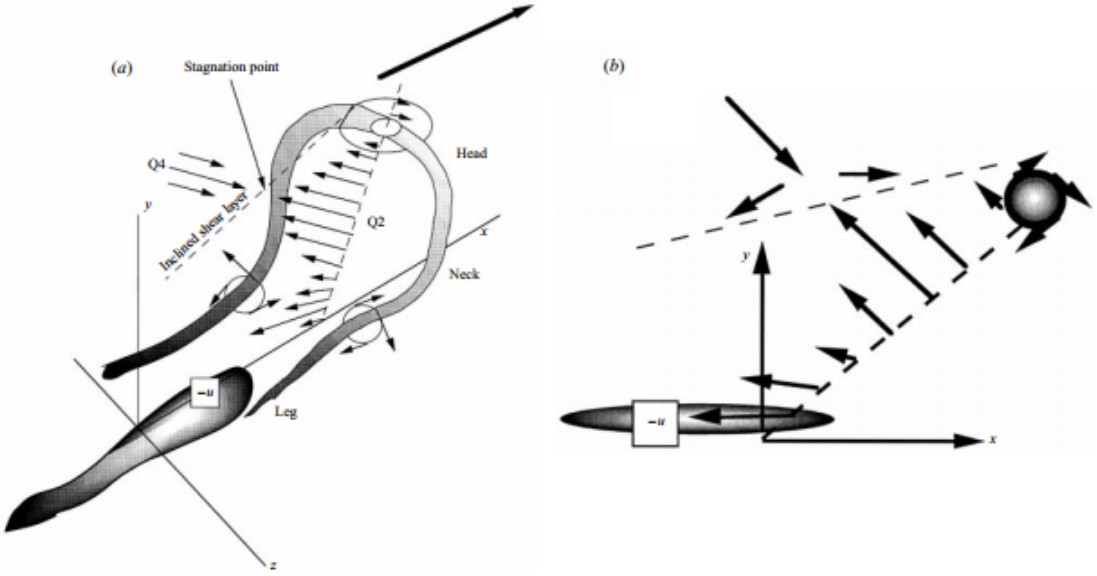

FIGURE 2.4: a) Schematic of a hairpin vortex attached to the wall and the induced motion. b) Signature of the hairpin vortex in the streamwise wall-normal plane (Adrian, Meinhart and Tomkins, 2000).

2.3.1.1 Vorticity

An essential feature of turbulent flow is that they are rotational, thus they have non-zero vorticity. The vorticity at a point is defined as the local rotation or curl of the three-dimensional velocity field.

$$\overline{\omega} = \mathrm{rot}\left(\overline{\mathrm{U}}\right) = \mathrm{curl}\left(\overline{\mathrm{U}}\right) = \nabla \times \overline{\mathrm{U}} = \left(\frac{\partial \mathrm{W}}{\partial y} - \frac{\partial \mathrm{V}}{\partial z}\right)\overline{i} - \left(\frac{\partial \mathrm{U}}{\partial z} - \frac{\partial \mathrm{W}}{\partial x}\right)\overline{j} + \left(\frac{\partial \mathrm{V}}{\partial x} - \frac{\partial \mathrm{U}}{\partial y}\right)\overline{k} \tag{2.6}$$

For planar data in the x-y plane, gradients in the z-direction could not be calculated, therefore only rotation about the z-axis can be determined

$$\omega_z = \frac{\partial \mathrm{V}}{\partial x} - \frac{\partial \mathrm{U}}{\partial y} \tag{2.7}$$

$$\omega_z\left(i, j\right) \cong \frac{v(i+1, j) - v(i-1, j)}{2\delta x} - \frac{u(i, j+1) - v(i, j-1)}{2\delta y} \tag{2.8}$$

The vorticity in this thesis were calculated using the filtered second-order difference scheme (Westerweel, 1993). The second-second order difference scheme is expected to amplify the noise in the measured velocity data. Landreth and Adrian (1990) proposed the use of low-pass filter with Gaussian kernel to attenuate the noise while retaining the velocity signal. This technique was implemented for calculating the vorticity.

$$\widetilde{u}(i,j) = \frac{1}{2}\left[u(i,j) + \frac{1}{2}\left\{u(i-1,j) + u(i+1,j)\right\}\right] \tag{2.9}$$

$$\widetilde{v}(i,j) = \frac{1}{2}\left[v(i,j) + \frac{1}{2}\left\{v(i,j-1) + v(i,j+1)\right\}\right] \tag{2.10}$$

2.3.1.2 Swirling strength

Swirling strength, λ_{ci} is the imaginary portion of the complex eigenvalue of the local velocity gradient tensor, J and is a measure of rotation (Zhou et al., 1999). Unlike vorticity, swirling strength does not highlight regions of intense shear and is an effective technique for identifying vortex cores (Adrian, Meinhart and Tomkins, 2000). The technique yield similar pattern to the λ_2 identification technique of Jeong and Hussain (1995). The velocity gradient tensor, J is given by

$$\mathrm{J} = \nabla\overline{\mathrm{U}} = \begin{bmatrix} \partial\mathrm{U}/\partial x & \partial\mathrm{U}/\partial y & \partial\mathrm{U}/\partial z \\ \partial\mathrm{V}/\partial x & \partial\mathrm{V}/\partial y & \partial\mathrm{V}/\partial z \\ \partial\mathrm{W}/\partial x & \partial\mathrm{W}/\partial y & \partial\mathrm{W}/\partial z \end{bmatrix} \tag{2.11}$$

For planar PIV data in the x-y plane, the gradient in the z-direction could not be calculated, and setting it to zero simplifies the eigenvalue calculation, and thus the square of the imaginary part can be computed using

$$\lambda_{ci}^2 = \frac{1}{4}\left(\frac{\partial\mathrm{U}}{\partial x}\right)^2 + \frac{1}{4}\left(\frac{\partial\mathrm{V}}{\partial y}\right)^2 - \frac{1}{2}\frac{\partial\mathrm{U}}{\partial x}\frac{\partial\mathrm{V}}{\partial y} + \frac{\partial\mathrm{V}}{\partial x}\frac{\partial\mathrm{U}}{\partial y} \tag{2.12}$$

For good visualization of vortices, a threshold value could be set up to eliminate background noises. Alternatively, the threshold value could be set to zero to highlight all areas of swirl,

however this would not provide good visualization and vortices would be indistinguishable from the background noises. In reality, a small positive value could be use to highlight areas with significant swirls only but exact choice is subjective. Zhou et al. (1999) shows that the threshold value does not affect the vortex characteristics except for the diameter of the vortices, and thus should not affects the results and conclusion presented in this thesis.

2.3.1.3 Second invariant of the velocity-gradient tensor (Q-criterion)

Vortices of an incompressible flow are identified as connected fluid regions with positive second invariant of the velocity-gradient tensor ∇u, ∇u = S + Ω, S is the strain-rate tensor, Ω is the vorticity tensor (in tensor notation below the subscript comma denotes differentiation),

$$\mathrm{Q} \equiv \frac{1}{2}\left(u_{i,i}^2 - u_{i,j}\,u_{j,i}\right) = -\frac{1}{2}u_{i,j}\,u_{j,i} = \frac{1}{2}\left(\|\Omega\|^2 - \|\mathrm{S}\|^2\right) > 0 \tag{2.13}$$

When the value of Q is positive, it represent locations in the flow where the rotation dominates the strain and shear. Negative values indicates areas where shear are present without swirling motions. To emphasize this, one could return only the positive value and set all negative values to zero. The second invariant of Q for a 3 × 3 velocity gradient matrix, J is given by

$$\mathrm{Q} = \left(\frac{\partial \mathrm{U}}{\partial \mathrm{x}}\frac{\partial \mathrm{V}}{\partial \mathrm{y}} - \frac{\partial \mathrm{V}}{\partial \mathrm{x}}\frac{\partial \mathrm{U}}{\partial \mathrm{y}}\right) + \left(\frac{\partial \mathrm{V}}{\partial \mathrm{y}}\frac{\partial \mathrm{W}}{\partial \mathrm{z}} - \frac{\partial \mathrm{W}}{\partial \mathrm{y}}\frac{\partial \mathrm{V}}{\partial \mathrm{z}}\right) + \left(\frac{\partial \mathrm{U}}{\partial \mathrm{x}}\frac{\partial \mathrm{W}}{\partial \mathrm{z}} - \frac{\partial \mathrm{W}}{\partial \mathrm{x}}\frac{\partial \mathrm{U}}{\partial \mathrm{z}}\right) \tag{2.14}$$

For planar PIV data in the x-y plane, the gradient in the z-direction could not be calculated, and by setting it to zero, the expression in Equation 2.14 can be simplified to

$$\mathrm{Q} = \frac{\partial \mathrm{U}}{\partial \mathrm{x}}\frac{\partial \mathrm{V}}{\partial \mathrm{y}} - \frac{\partial \mathrm{V}}{\partial \mathrm{x}}\frac{\partial \mathrm{U}}{\partial \mathrm{y}} \tag{2.15}$$

2.4 Boundary Layer PIV

Adrian, Meinhart and Tomkins (2000) performed 2D-PIV on a zero pressure gradient flat plate boundary layer at three Reynolds number, Re_θ = 930, 2370 and 6845 in a wind-tunnel at velocities of 1.6, 3.8, and 10.9 ms^{-1} at the free-stream. The free-stream turbulence intensity was less than $0.2\,\%$ for free-stream velocities below 10 ms^{-1}. Measurements were taken 5.33 m downstream of the leading edge, corresponding to 64 times the maximum boundary layer thickness of 82.8 mm. The middle Reynolds number Re_τ = 872 corresponds most closely to the Newcastle rig, and was chosen because a significant number of published results were available for similar conditions. A large format film camera was used for the steady state PIV, resolving an area in the streamwise / wall-normal plane of x/δ = 1.4 by y/δ = 1.3, with 12,500 vectors at a vector pitch of 20 wall units. Mean and rms velocity profiles were measured and verified to show excellent agreement with previous experimental and DNS results. The main focus of the work was in visualisation of the instantaneous x, y plane velocity field, with the preferred method being to display vector maps with the streamwise convection velocity subtracted from the field to reveal convected vortical structures. Values of convection velocity between 0.8 and 1.0 times the free stream velocity were subtracted to best reveal cross-stream vorticity at different distances from the wall. Circular patterns of vectors were shown to correspond closely to circular patches of cross-stream vorticity in vorticity contour plots. Adrian et. al. found that, because this form of Galilean transformation preserves the relative shear in the flow, interpretation of the structure is much easier and more accurate than with Reynolds decomposition. Although the technique only yields a planar slice through the three-dimensional turbulent structures, Adrian et. al. was able to discern the form as a 2-D "signature" of hairpin vortex head, Q2 and Q4 flow, and region of low momentum fluid located below and upstream of the vortex head, as shown in Figure 2.5 and Figure 2.6 .

These visualisations provide evidence for packets of hairpin vortices, with many vortex heads being evident in the range between y^+ = 100 and y^+ = 250, corresponding to the outer range of the logarithmic layer, but with similar vortex heads occurring around y^+ = 500 and beyond for the Re_τ = 872 boundary layer.

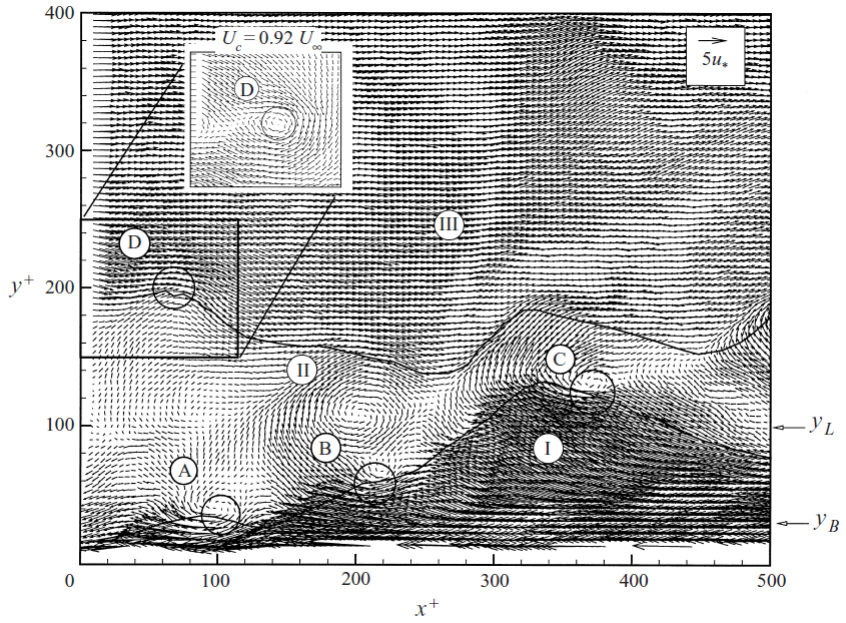

FIGURE 2.5: (a) Hairpin vortex heads, reproduced from Adrian, Meinhart and Tomkins (2000).

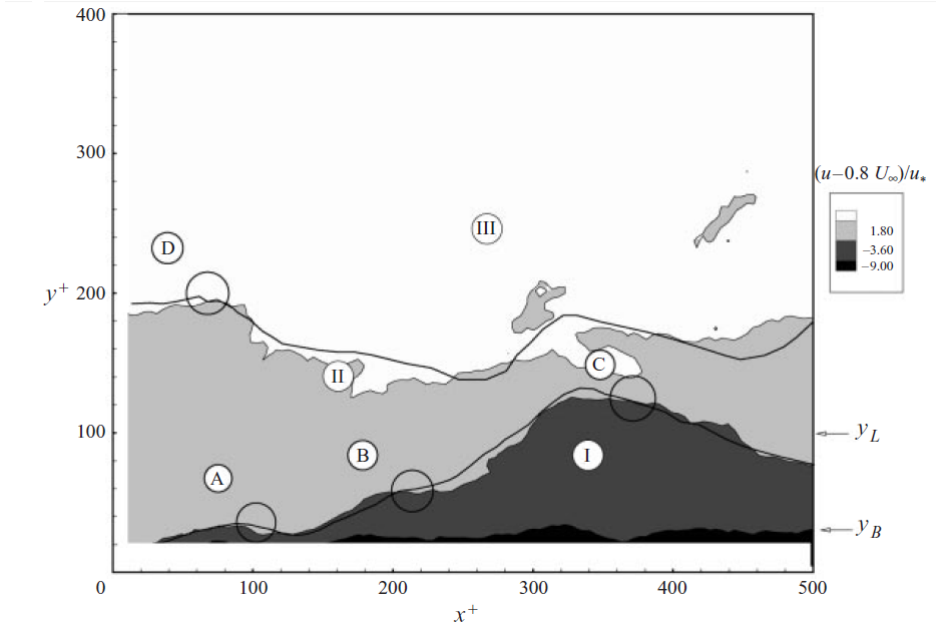

FIGURE 2.6: (b) Layers of approximately constant streamwise momentum for the Re_τ = 872 boundary layer, reproduced from Adrian, Meinhart and Tomkins (2000).

From these results, Adrian, Meinhart and Tomkins (2000) postulated a conceptual model of nested packets of hairpin, giving rise to extensive layers of almost constant fluid momentum, with increasing streamwise velocity with the displacement of the "layer" from the wall, as illustrated by Figure 2.7 .

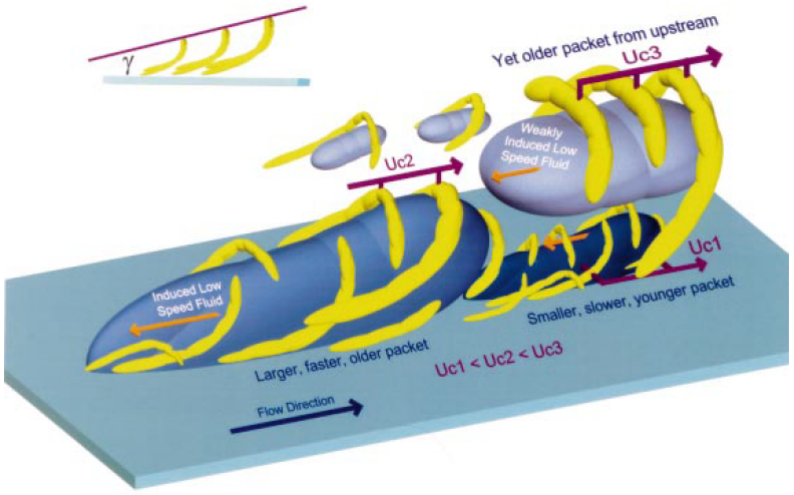

FIGURE 2.7: Conceptual scenario of nested packets of hairpin or cane vortices, growing from the wall, reproduced from Adrian, Meinhart and Tomkins (2000).

Ganapathisubramani et al. (2003) used stereoscopic PIV to measure the instantaneous velocity field in the streamwise/cross-stream plane of a zero pressure gradient flat plate boundary layer with $Re_\tau = 1060$. Measurements were made in a suction wind tunnel with free stream velocity and turbulence intensity of 5.9 ms^{-1} and $0.2\,\%$ respectively, giving a boundary layer of thickness 69 mm 3.9 m downstream of a boundary layer trip. The objective was to determine if hairpin vortex packet signatures could be detected in the streamwise/cross-stream plane within the outer region of the boundary layer and, if so, to determine their contribution to the Reynolds shear stress. Measurements were made for planes at $y^+ = 92$, $198\,(y/\delta = 0.2)$ and $530\,(y/\delta = 0.5)$ using Kodak Megaplus 1 megapixel cameras, and at $y^+ = 150$ using TSI PowerView 4 megapixel cameras, all using Nikon Micro Nikkor 60 mm f/2.8 lenses. The resulting field of view was $1.2\delta \times 1.2\delta$ for the 1 megapixel cameras and $2.4\delta \times 2.4\delta$ for the 4 megapixel cameras, yielding a vector pitch of 0.65 mm or 10 wall units in each case. In the streamwise / cross-stream plane, the near wall-normal section of the legs of a hairpin vortex would appear as neighbouring cores of positive and negative wall-normal vorticity, whilst packets of

hairpins would appear as a streamwise train of such features. The authors devised a special algorithm to automatically identify such features, based on the strength of wall normal vorticity and Reynolds shear stress in combination and seeking streamwise linking of detected features.

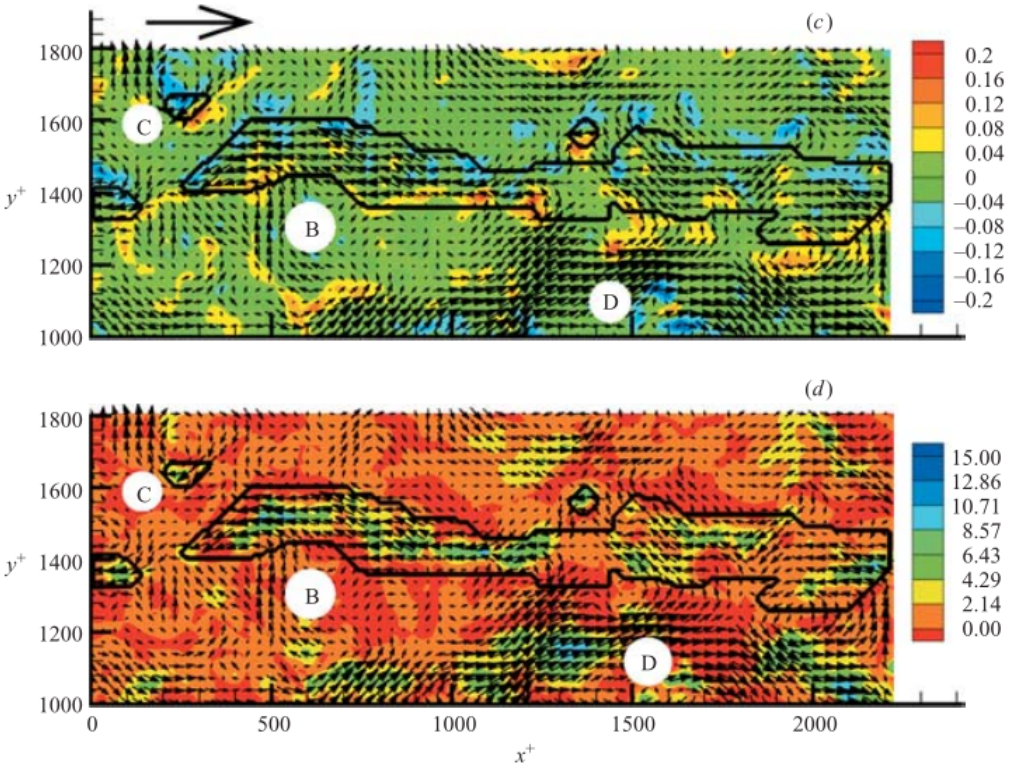

FIGURE 2.8: Packets of hairpin, viewed in a plane parallel to the wall at $y^+ = 92$, reproduced from Ganapathisubramani et al. (2003). Positions indicated by letter B, C, and D are region having uniform velocity momentum.

Figure 2.8 shows a typical measurement plane 92 wall units from the wall. The contours in Figure 2.8(a) are of wall-normal vorticity, and a stream-wise train of pairs of vortex legs, having opposite sign, are clearly visible along the center of the plot. The black outline encloses a region of reduced velocity momentum associated with this hairpin packet. Contours of Reynolds shear stress, $-uv^+$, are shown for the same measurement in Figure 2.8(b). Ganapathisubramani et al. (2003) failed to find such packet structures at $y^+ = 198\,(y/\delta = 0.2)$ and beyond, and they concluded that the legs of most hairpins did not extend this far from the wall.

Schröder et al. (2011) studied a zero pressure gradient flat plat boundary layer, with almost identical parameters to those initially proposed for the Newcastle rig, using time-resolved tomographic PIV. The experiments were carried out in a water tunnel, with free stream velocity and

turbulence intensity of $0.53\,\mathrm{ms}^{-1}$ and 0.5% respectively, giving a boundary layer of thickness $38.1\,\mathrm{mm}$ with $\mathrm{Re}_\tau = 800$ and $\mathrm{Re}_\theta = 2460$. The imaged volume of $63.2\,\mathrm{mm} \times 68\,\mathrm{mm} \times 15.1\,\mathrm{mm}$ in the streamwise, cross-stream and wall-normal directions, corresponded to $92 \times 99 \times 22$ vector locations. Measurement points were located every $0.687\,\mathrm{mm}$, that is every 15 wall units. A 1 kHz frame rate gave 500 vector fields per second, which is relatively fast compared to the estimated Kolmogorov time scale of $25 - 44\,\mathrm{ms}$. Six Photron CMOS cameras were used with 100 mm and 105 mm macro lenses so as to minimise the number of ghost particles generated by the MART processing software. Using a double head Nd:YLF laser with 25 mJ/pulse, together with $56\,\mu$m polyamide seeding particles gave sufficient illumination to stop the lenses down to f/11. Having verified the boundary layer velocity and normal stress profiles against DNS and planar PIV data, the authors went on to measure swirling strength representations of 3D structures, PDFs of the velocity components, and 3D space-time correlations of the velocity components. A 3D particle tracking algorithm was also used to generate Lagrangian fluid particle tracks and hence Lagrangian fluid particle accelerations, for which PDFs were presented, based on around 10^5 tracked particles.

Dennis and Nickels (2011*a*) high-speed stereo-PIV results show evidence of vortex packet type structures in a zero pressure-gradient boundary layer. They aligned their light-sheet perpendicular to the flow direction, allowing structures in the flow to pass through the measurement plane, enabling 3D reconstruction from a series of 2-D sectional snap-shots, to reveal the underlying structure. This technique was used by Doorne (2004) in a pipe flow, again with strereoscopic PIV, and also by Ganapathisubramani et al. (2008) in a turbulent jet flow to examine the small-scale features. Although the channel is wider and longer in comparison to the Newcastle open-channel rig, similar measurement could easily be carried out with the Newcastle rig. Our initial plan was to follow the same technique slicing through structures (hairpin vortices) and identify cross-stream signatures. This technique, would enable the recreation of a three-dimensional picture of the underlying vortices, similar to the work of Dennis and Nickels (2011*a*), but would be extended by simultaneously observing a second, particle phase, and its interaction with the vortex structures. In the event, due to rig manufacturing delays, this could not be achieved in the time available.

With similar setup to their earlier experiment, Dennis and Nickels (2011*b*) further investigations revealed that long structures are a common feature of turbulent boundary layers. They were found to be present in the lower half of the boundary layer with 80 % of the of the structures having a maximum height of being less than $y/\delta = 0.5$. Slices at $y/\delta = 0.15$ clearly show the presence of high and low-speed regions. Slicing at a greater height of $y/\delta = 0.32$ shows regions of strong positive and negative fluctuations, but these features do not show significant streamwise elongation.

2.5 Two-phase flow

Particle-turbulence interaction is a topic which has attracted continued attention for many years. Turbulent flows laden with particles occurs frequently in nature as well as in many engineering applications. In turbulent channel flows laden with particles, researchers have investigated the behaviour of particles and turbulence, either experimentally or numerically.

Although turbulence is associated with enhanced mixing, it has been known for some time now that the semi-organised structures present in turbulent flow, as described earlier in this chapter can, in two-phase flow, cause non-uniformity of the particle density field, even when the particles are initially uniformly distributed (e.g. Wang and Maxey, 1993; Aliseda et al., 2002; Yang and Shy, 2005). The presence of particles in turbulent flows can also increase or decrease the turbulence level of the flow compared to its natural level for particle free fluid, depending on turbulence and particle parameters (e.g. Tsuji and Morikawa, 1982; Kaftori et al., 1995*a*,*b*; Crowe, 2000). Particle/turbulence interactions are complex and depend on various parameters such as the ratio of particle diameter to flow length scale, The Reynolds and Stokes number of particles and particle loading density.

The Stokes number, St, (the ratio between the particle relaxation time and a characteristic time scale of fluid motion) is the main parameter that controls particle dynamics in the turbulent flow, as described in recent reviews by Toschi and Bodenschatz (2009) and Balachandar and Eaton (2010). Particles with Stokes numbers significantly less than 1 follow the fluid flow very closely, as in the seeding particles used in LDV and PIV, whilst particles with Stokes number

much greater than 1 tend to follow "ballistic" trajectories, with relatively weak influence from the surrounding flow. At intermediate Stokes numbers around unity, particles are influenced by turbulent eddies, but do not follow them exactly, as shown in Figure 2.9. In this regime "centrifuging" effects of the turbulent eddies may lead to particle segregation. A characteristic phenomenon of turbulent wall-bounded flow is the preferential accumulation of particles very near to the wall and a large number of experimental measurements and simulations have been carried out to study this phenomenon. Kallio and Reeks (1989) showed that this is a direct result of wall turbulence, and coined the name "turbophoresis", meaning "turbulent transport" to describe the effect.

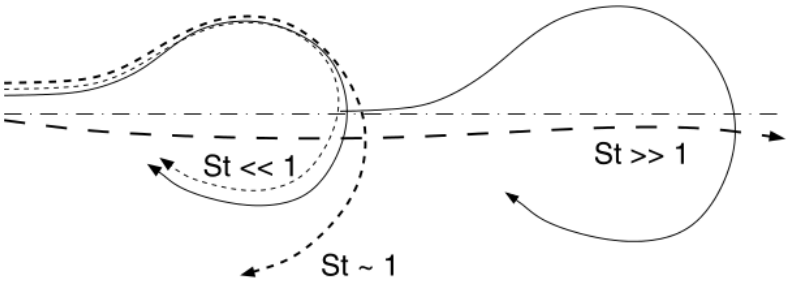

FIGURE 2.9: Influence of particle relaxation time on particle trajectory. Small inertia particles follow precisely the flow; large inertia particles filter the space changes of velocity; intermediate inertia particles respond to the flow structure (Soldati, 2005).

Rogers and Eaton (1991) in their vertical turbulent boundary layer experiments with Stokes number based on the eddy turnover time scale of order unity, found that the presence of particles tended to attenuate the fluid turbulence. Other studies (for example Kulick et al., 1994; Yamamoto et al., 2001; Li et al., 2001) found that turbulence fluctuations were less affected by particles with larger Stokes numbers. Rashidi et al. (1990) and Pan and Banerjee (1996) studied turbulence modification by near-neutral-density particles in horizontal open-channel flows, performing experiments and DNS, respectively. Particles were observed to accumulate in the low speed streaks. Small particles with small Stokes numbers ($St^+ < 1$) suppressed turbulence intensity and Reynolds stress, while larger particles enhanced these quantities.

Early investigations clearly show that particle entrainment in suspension (e.g. Niño and Garcia, 1996) is strongly influenced by the quasi-periodic coherent structures associated with wall flow turbulence. In terms of sediment transport, the so called bursting phenomenon, which

is a quasi-cyclic process of ejection and sweeps, is known to play an important role in particle entrainment (Nezu and Nakagawa, 1993). These events have been attributed to the well-known hairpins vortex and their packets. These structures (i.e. wall structure) have been shown to be the dominant factor affecting particle motion near a solid boundary in turbulent flow, as well as deposition and entrainment, and are often concentrated in regions of low velocity, see for example, Kaftori et al. (1995*a*,*b*).

Kaftori et al. (1995*a*,*b*) studied particle dynamics close to the wall in a water flume by utilizing both visualization technique and single point measurement (i.e. LDV) and focused on the role of coherent structures in particle motion and deposition. They concluded that coherent wall structures were the main influence on particle motion near the wall, but suggested "funnel vortices" as the major structure responsible for sweeps and ejections, rather than the classic hairpin structures. Righetti and Romano (2004) open channel flow experiment showed that the presence of particles does have an effect on the mean velocity and Reynolds stress. More recently, Geraschenko et al. (2008) investigated inertial particle acceleration in a turbulent wall boundary layer, using a sled-mounted high speed camera travelling with the flow in a wind tunnel. They observed that increasing the Stokes number of the particles produced an increase in the acceleration variance, contrasting with the opposite effect associated with homogeneous isotropic turbulence.

Fluid particles flows can be classified as being either dilute or dense (Crowe, 1982). In a dilute flow the particle motion is governed by the surrounding fluid via lift, drag forces, inertial and added mass force whilst in a dense flow, particle to particle interactions via collisions largely control the particle motion. Elghobashi (1994) classified particle / fluid interactions as one-way, two-way or four-way coupled. In one-way coupling the fluid flow influences the particle motion, but the fluid flow itself is not affected by the presence of the particles. In two-way coupling, significant momentum transfer occurs from the particles to the fluid, and the fluid flow, including turbulence quantities, is modified by this. In addition to these effects, particle-to-particle collisions become significant in four-way coupling.

For our experimental purpose, 20 grams of $200\,\mu$m neutral buoyant dispersed phase was used. For a cubic meter of water, this computes an approximate volumetric loading of 10^{-5}.

Kiger and Pan (2000) suggested that the volumetric loading should be lower than and not exceeding 10^{-4} for fluid flow. Rashidi et al. (1990) experimental work indicate that even average particle volume fraction ~ 10^{-4} lead to significant modulation of turbulence. Turbulence modulation by particle can occur due to three effects. One is the presence of particles at the wall, where their effect is somewhat similar to stationary roughness elements. Second is the presence and interaction of particles with the wall structures, such as quasi-streamwise vortices, sweeps, and ejections. This appears to be the cause for particle segregation and the modulation of wall structure characteristics. The third effect is the presence and interaction of particles in suspension, away from the walls (Kaftori et al., 1998).

Elghobashi (1994) states that for a particle volume fraction below 10^{-6}, two-way coupling may be neglected entirely. Even when particles are used for "seeding" in nominally single-phase fluid flow measurements by LDA or PIV, this density is often exceeded in practice. The experimental work of Rashidi et al. (1990) indicates that a particle volume fraction of 10^{-4}, with dense (non neutrally-buoyant) particles, can lead to significant modulation of turbulence. Increase in turbulence level as a result of mixing caused by particles moving from one eddy to another (Mei et al., 1991) or by vortex shedding (Hetsroni, 1998; Crowe, 2000) has also been proposed.

One and two-way couplings have been extensively studied using Direct Numerical Simulation (DNS) and Large Eddy Simulation (LES). The computational effort required limits the use of DNS to low Reynolds number flows at present (e.g. Marchioli and Soldati, 2002; Marchioli et al., 2008), but LES is possible at higher Reynolds numbers.

PIV is now a well-established tool for single phase flow measurements and has recently been applied to particle-laden flows by, for example, Kiger and Pan (2002), Borowsky and Wei (2006), Lelouvetel et al. (2009) and Van Hout (2011).

Kiger and Pan's original paper (Kiger and Pan, 2000) demonstrated the possibility of phase separation in PIV of 2-phase flow based on the particle size. The flow was seeded with small (15 μm) particles, acting as a fluid tracer, and also contained much larger particles (between 100 and 300 μm) particles as the secondary phase. PIV images were taken of both phases, then median filtered to remove images of the smaller tracer particles. Tracking algorithms

could then be applied to give the particle phase velocities. By constructing a mask from the filtered large particle images, the large particles could be removed from the original combined images, to isolate the tracer field. These tracer images could then be processed by standard PIV algorithms to yield the fluid velocity field. Because of particle image broadening by the optical systems used, a reasonably large difference in size is necessary between the two particle phases, but the problems of expensive multi-colour illumination systems, multiple camera setups and multiple image registration associated with alternative systems are avoided. Following this demonstration, Kiger and Pan (2002) applied the technique to measure two-phase flow in an open water channel with a Reynolds number $\mathrm{Re}_\tau = (u_\tau h/\mu) = 570$, based on channel half height, h. A conventional low-repetition digital PIV system was used, and so only instantaneous measurements could be made. Having verified that the channel floor boundary layer characteristics for clear water flow were in good agreement with the DNS data of Mosser et al. (1999), glass beads of mean diameter 195 μm and specific gravity 2.6 were added as inertial particles, with a bulk mass loading ratio of 6×10^{-4}. The results showed that even at this mass loading the presence of the relatively "heavy" inertial particles did modify the fluid mean velocity profile, and produced a 7% increase in the wall friction velocity u_τ. Normal and shear Reynolds stresses showed an increase of between 8 and 10% in the outer region of the boundary layer. Mean particle velocities were shown to lag the mean fluid velocity, whereas local instantaneous particle and fluid velocities were virtually identical, a phenomenon also noted by Kaftori et al. (1995*b*). Kiger and Pan (2002) conditionally sampled particles moving away from and towards the wall with the Willmarth perturbation quadrant, and confirmed Kaftori's suggestion that the apparent particle lag was associated with upward moving particles being preferentially found within Q2 or ejection events with reduced streamwise velocity. Wall-ward moving particles, however, showed little preference between Q3 and Q4 events, and hence had streamwise velocities similar to the mean fluid velocity.

Borowsky and Wei (2006) employed a two-color digital PIV system to record the velocity and acceleration fields of both the solid and liquid phases simultaneously in a vertical pipe flow facility, with a rather low Reynolds number of 4630. They used neutrally buoyant 60-80μm fluorescent particles as a tracer for the fluid phase (water), and silvered glass spheres of specific gravity 2.6 and mean diameter 89 μm as the inertial particle phase. The silvered particles scattered green light at the laser wavelength of 532 nm, whilst the tracer particles fluoresced

in the red wavelength band. The use of two cameras, fitted with interference filters, allowed absolute phase discrimination avoiding cross communication between the two phases. The volume fraction of the solid phase was high at 0.001, providing strong two-way coupling. In these experiments the authors were primarily concerned with turbulence modification and measurement of fluid and particle acceleration, rather than the interaction of dispersed particles with boundary layer structures. Although based on a low repetition rate dual pulse laser system, the use of two such systems allowed two velocity measurements to be made within a time interval of similar magnitude to the dual pulse interval, and hence fluid and particle accelerations could be measured. The presence of the particles led to turbulence reduction away from the walls. Histograms of fluid and particle axial accelerations were shown to be bell-shaped with a slight rise in the tails, the variance being approximately 1.5 times larger for the particles than for the fluid.

Lelouvetel et al. (2009) employed conventional planar PIV to measure turbulence characteristics and particle motion simultaneously in an open channel of length 9m and width 0.25 m. The depth of water was very small at between 20 and 40 mm, giving a high Froude number of just over unity, and the channel had a sandpaper floor to give a roughness of k_s = 0.15mm, these parameters being chosen to represent fluvial conditions.

The Froude number, Fr is a dimensionless value that describe different flow regimes of an open-channel flow. It is defined as the ratio of inertial to gravitational forces.

$$\mathrm{Fr} = \frac{U}{\sqrt{\mathrm{gD}}} \tag{2.16}$$

where U is the water velocity, D is the hydraulic depth (cross-sectional area of flow ÷ channel width), and g is the acceleration due to gravity.

The value of the Froude numbers indicates the types of flow, when Fr = 1, the flow is critical, when Fr > 1, the flow is super-critical (fast rapid flow), and if Fr < 1, the flow is subcritical (slow tranquil flow).

Reynolds numbers were varied between 1 and 3×10^4. Seeding was by 5 μm Merck iriodin particles having a Stokes number of 10^{-3}, whilst a range of ceramic and glass inertial particles

were used, with diameters between 164 and 208 μm and specific gravity between 2.5 and 3.8. The Stokes numbers for these inertial particles were all around 1.0 to ensure suspension of the particles. Phase separation was performed based on particulate size, following the technique of Kiger and Pan (2000). The work set out to determine the type and strength of turbulent structures responsible for particle suspension. Quadrant analysis was applied to the flow around each inertial particle and revealed a strong correlation between upward moving particles and the presence of Q2 events or ejections. Indeed it was found that all particles within an ejection that has an instantaneous momentum flux exceeding a critical value move away from the wall with a positive vertical velocity. However, the authors found no clear correlation between beads falling towards the wall and turbulent structures. Over 70% of the observed particles were within an ejection or sweep region, indicating the importance of turbulence structures in particle transport. Their quadrant analysis data is shown in Figures 2.10, 2.11 and 2.12 for clear water flow, particles with positive vertical velocity (away from the wall) and particles with negative vertical velocity (moving towards the wall).

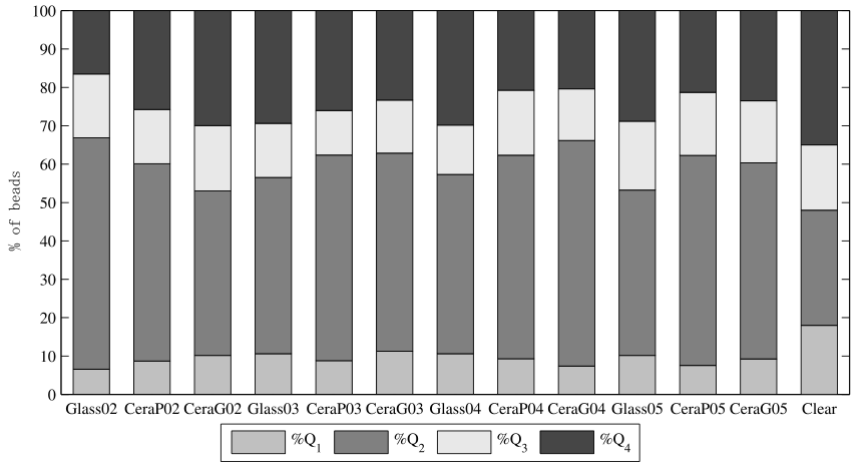

FIGURE 2.10: Quadrant analysis around all beads, with distribution of the turbulent events in clear water flow for Re = 24,000 (Lelouvetel et al., 2009).

Van Hout (2011) was the first to use Time Resolved PIV to investigate dilute, particle laden turbulent flow. His experimental rig consisted of a 50mm square section closed, horizontal channel through which water flowed with a bulk Reynolds number of 7353 and $Re_\tau = 435$. The flow was seeded with 10 μm hollow glass spheres and for the 2-phase experiments the particle phase was composed of near neutrally buoyant 580 μm polystyrene beads at a volumetric

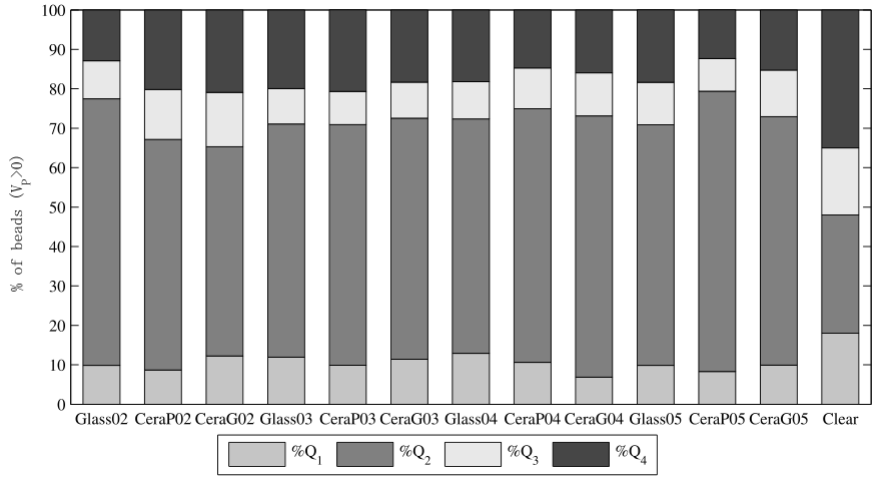

FIGURE 2.11: Quadrant analysis around beads with a positive vertical velocity ($V_p > 0$), with distribution of the turbulent events in clear water flow for Re $= 24,000$ (Clear) (Lelouvetel et al., 2009).

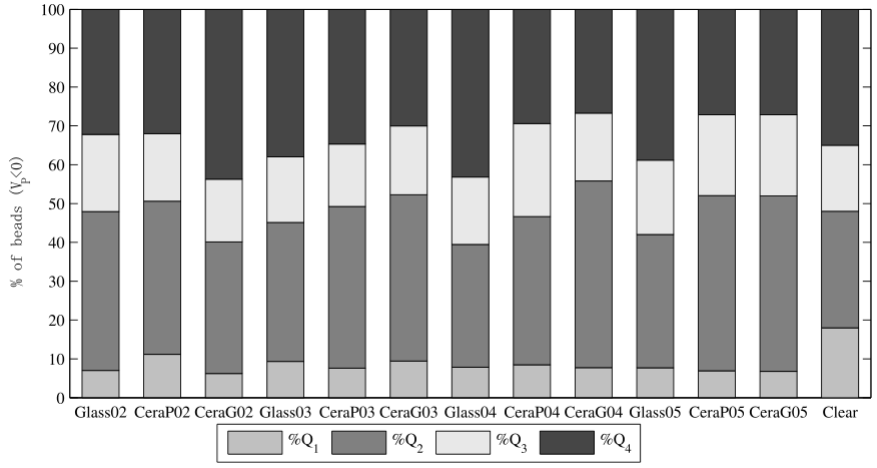

FIGURE 2.12: Quadrant analysis around beads with a negative vertical velocity ($V_p < 0$), with distribution of the turbulent events in clear water flow for Re $= 24,000$ (Lelouvetel et al., 2009).

loadings of 0.7 and 1.4×10^{-4}. Stokes number for the inertial particles was 1.65. Phase identification was again by size, as in (Kiger and Pan, 2000, 2002), but Van Hout (2011) masked a relatively large region around each inertial particle when analysing the carrier phase flow. Two series of experiments were carried out. The first set, at low frame rate, and using the lower volumetric loading, was to determine the effects of the particle phase on mean and turbulence flow quantities. In contrast to the findings of Kiger and Pan (2002) and (Righetti and Romano, 2004), using relatively "heavy" inertial particles, the addition of particles had no discernible

effect on the profiles of fluid mean velocity, or the fluid fluctuation rms in the streamwise and wall-normal directions. Slight differences were observed in the Reynolds shear stress profile with particle loading, particularly in the lower half of the channel, but why this asymmetry should exist with minimal sedimentation of near neutrally buoyant particles was not explained.

The second set of experiments was carried at a high frame rate, giving approximately 1000 vector maps per second, and so enabled tracking of flow features and individual particles. Most particles appeared to remain in the light sheet plane, and could be tracked across the full field of view, of width 500 wall units. Visualisation of such voluminous data is difficult, but van Hout presented sequential snapshots of representative particles crossing the field of view, against backgrounds of fluid velocity vectors, contours of fluid cross-stream vorticity and swirling strength, and contours of instantaneous uv and instantaneous u. Particle velocity statistics were also examined. Sorting the particles into ascending and descending beads, and comparing their conditional mean streamwise velocity to the fluid mean streamwise velocity, as in Figure 2.13, revealed that ascending particles tended to lag the fluid mean flow, whereas descending particles either led or corresponded to the fluid mean velocity. This was consistent with previous observations that ascending beads were strongly associated with Q2 ejection events and hence regions of reduced streamwise velocity. Particle velocity perturbation rms values were higher, and more scattered than the corresponding fluid values, as shown in Figure 2.14.

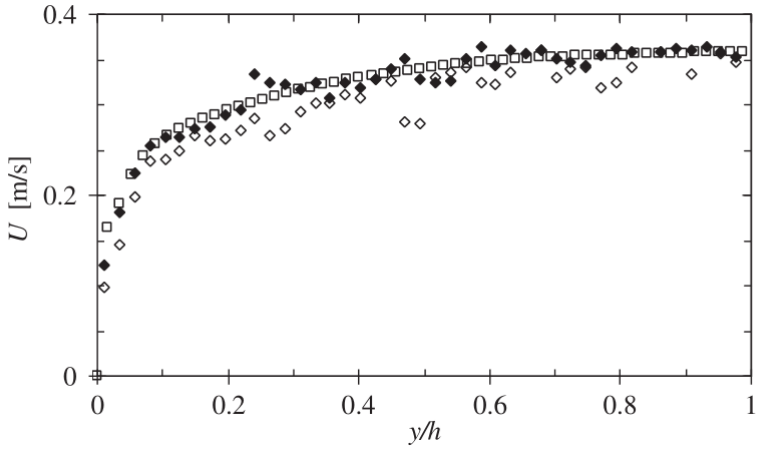

FIGURE 2.13: Comparison between the mean streamwise velocity of the fluid, ascending and descending bead (fluids □, PS beads masked: ◆ $V_p < 0$ m/s, ◇ $V_p > 0$ m/s) (Van Hout, 2011)

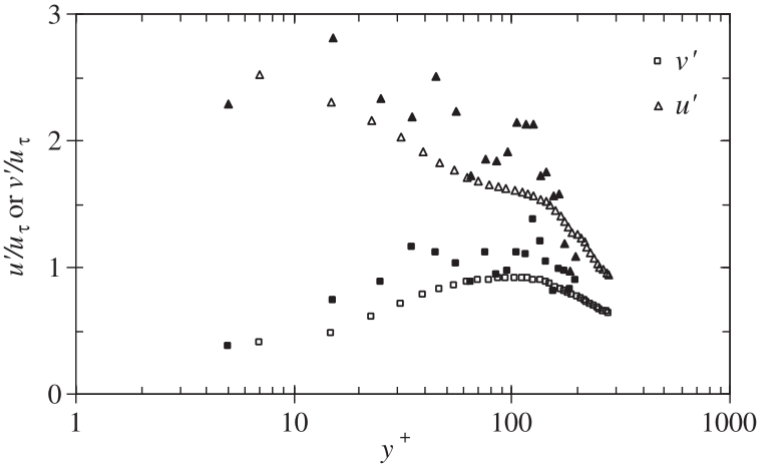

FIGURE 2.14: Comparison of the normalised rms values of the streamwise and wall-normal bead and fluid velocity fluctuations. Closed symbols: beads; Open symbols: fluid (Van Hout, 2011)

Finally, pdfs of fluid instantaneous velocity fluctuations, conditioned on the sign of the particle wall-normal velocity, confirmed that outward moving particles correlated strongly with Q2 ejection events, whilst inward moving particles did correlate, albeit less strongly, with Q4 or sweep events for $y^+ > 50$, these correlations weakening nearer the wall.

Although the detailed mechanisms of the interaction between inertial particle transport and coherent structures in turbulent boundary layers are still imperfectly understood, the evidence for the importance of structures in this process is so compelling that several attempts have been made to include their effects in CFD models for particle transport. Among these attempts are the early work of Cleaver and Yates (1975), and more recent models by Guingo and Minier (2008) and Jin et al. (2015). At least part of the motivation for the present work is to provide more physical data for the refinement of such models.

Chapter 3

Experimental Facilities and Instrumentation

3.1 Newcastle open-channel facility

At the time that Newcastle University was letting tenders for the Time Resolved PIV system, it was determined that a water flow facility would be necessary to increase the turbulence time scales to a level that could practically be resolved by TRPIV. Originally it was proposed to design and build a closed duct water tunnel in-house, but Dantec Dynamics, the successful instrumentation tenderer, offered to donate an open channel water flow facility to the School.

It appears that this channel was originally built by the National Gas Turbine Establishment at Pyestock, as a flow visualization facility. Since these facilities became part of Qinetic, the water channel was passed on to several Universities, none of which seem to have made any real use of it, before being acquired by Dantec. As a result of its history, the performance specification of the water channel was somewhat hazy, but what little documentation did exist suggested a working section velocity of 0.5 – 1.0ms^{-1}, which would satisfy the Newcastle 2-phase flow rig requirement of 0.5ms^{-1}. As supplied, the original water channel consisted of an open topped, rectangular, glass walled channel of internal width 332 mm, 210 mm deep, and 2000mm long, with a simple bell-mouth entry, connecting two stainless steel tanks, each of capacity approximately 0.5m^3. Water was recirculated between the two tanks by a centrifugal

pump with 76 mm bore connecting pipework. Two perforated baffle plates in the inlet tank were provided to reduce inlet flow disturbance. The pump was driven by a 1kW electric motor via a hydraulic variable speed coupling, the whole drive arrangement being mounted beneath the channel on a separate cradle, provided with vibration isolation mounts. The photograph, Figure 3.1, shows the original channel, as re-assembled at Newcastle.

FIGURE 3.1: The original water-channel, as supplied by Dantec and re-assembled at Newcastle.

Initial tests on the re-assembled water channel in its original condition showed the working section flow velocity to be an order of magnitude less than desired value, whilst the mechanical variable speed unit produced unacceptable levels of vibration. This limitation prompted immediate re-design of the drive mechanism as shown in Figure 3.2 and the repositioning of the drive mechanism to the outlet plenum tank as shown in Figure 3.4. The high head, low flow centrifugal pump was replaced with an axial flow pump with an electronic inverter variable speed drive and 134 mm bore connecting pipework.

This enabled a free-stream velocity of over 0.5ms^{-1}, and eliminated the mechanical vibration problems. However with only two perforated baffle plates in the plenum tank and a simple bell mouth inlet to the working section, free-stream turbulence level were of the order of 7%,

FIGURE 3.2: New axial flow propeller pump, drive shaft tube, seal and motor on vibration isolation cradle.

and the boundary layer profile, though looking like a typical turbulent layer up to and including the logarithmic region, lacked any form of wake region at the outer edge as shown in Figure 3.3. The overall thickness of 15mm was also less than desired, which was initially attributed to the relatively short working section.

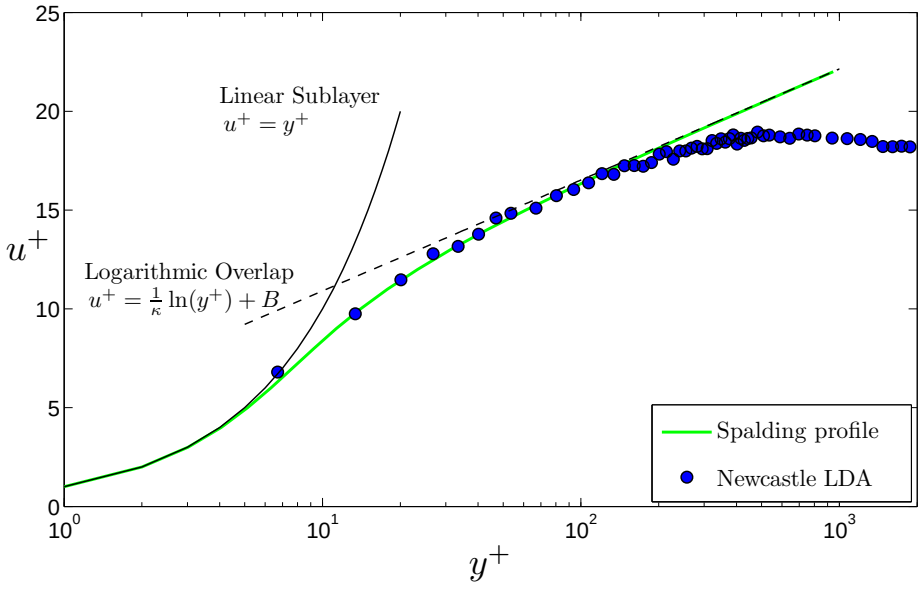

(a) Mean velocity profiles.

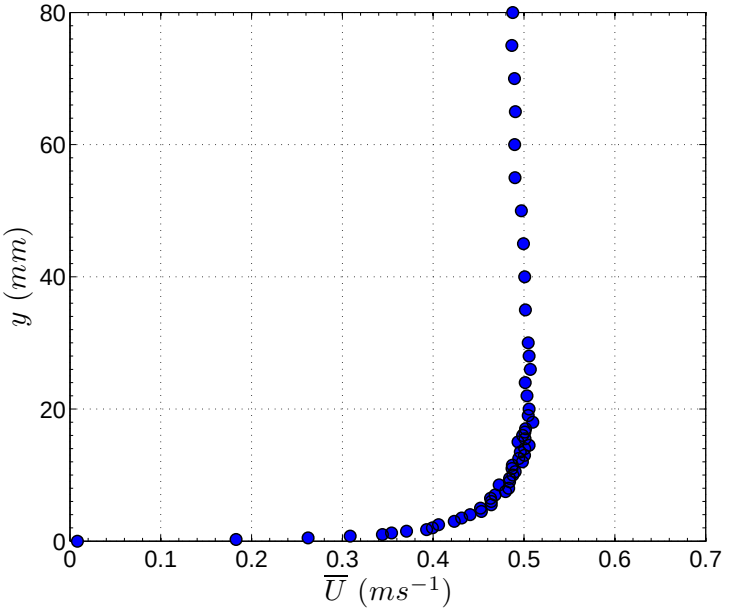

(b) Stream-wise mean velocity profile.

FIGURE 3.3: Floor boundary layer with original bellmouth inlet and 2m working section.

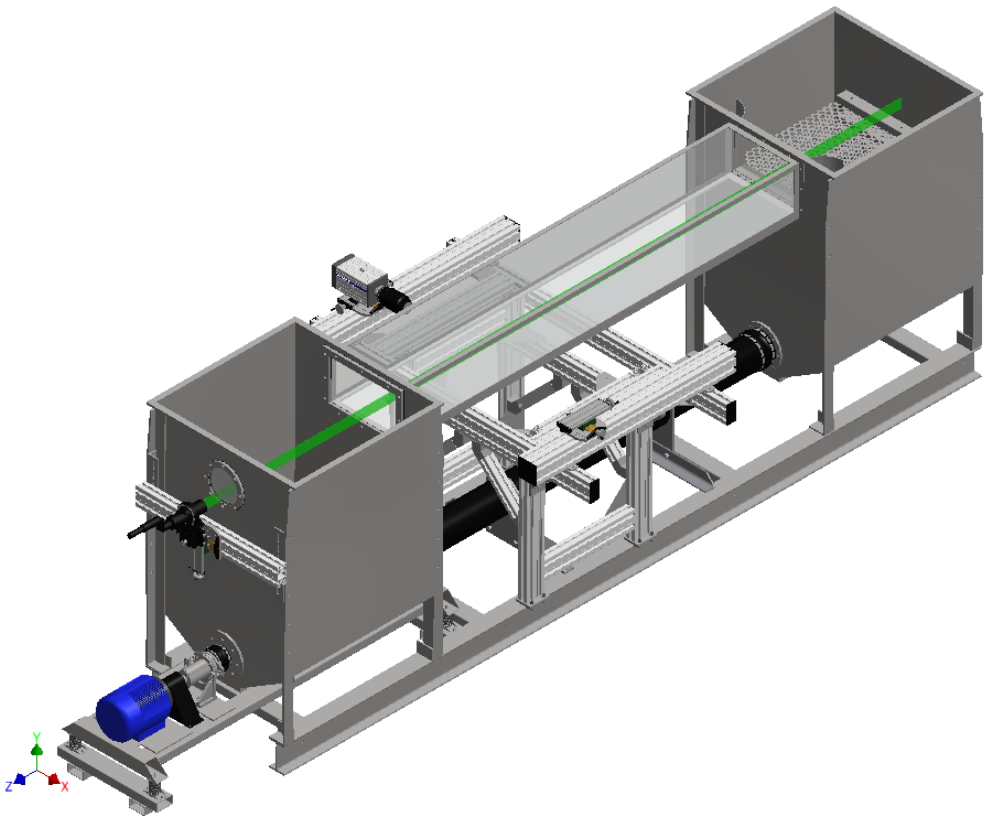

FIGURE 3.4: The original water-channel, with propeller drive system with proposed light-sheet setup.

3.1.1 New 3m Working Section

The immediate course of action was to extend the overall length of the open-channel from 2m to 3m, as this was the maximum channel length that Newcastle could fit in the new fluid dynamics research laboratory, G33 as shown in Figure 3.5. Backed up by theoretical estimates, the proposed length should be sufficient to develop the boundary layer to the desired thickness ($\delta \approx 50$mm), and therefore a longer channel was deemed unnecessary and could not be justified.

This extension has led to one major complication. The original plan had been to direct a parallel light sheet through a glass "port hole" in the outlet tank for PIV illumination, as shown in Fig. 3.4. With the extended channel the parallel light sheet had to travel a considerable extra distance through the seeded flow before reaching the intended measurement region, leading to significant reduction in illumination due to scattering. This approach had therefore to be abandoned, and a conventional, divergent light sheet was introduced from under the channel

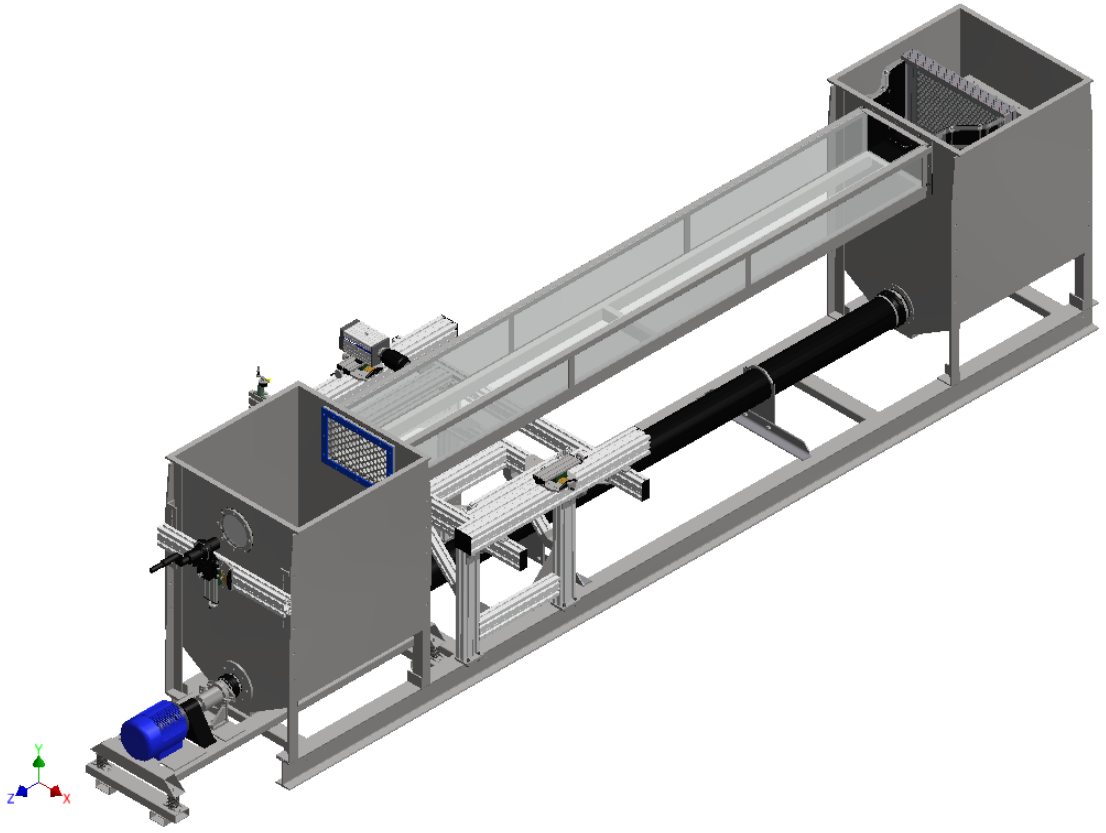

FIGURE 3.5: The Newcastle 3 m open-channel flow rig.

through the glass floor. To achieve this, the light-sheet optics were mounted to the side of the rig, and the light sheet reflected upwards using a surface silvered mirror, inclined at 45 degrees, beneath the channel as shown in Figure 3.6.

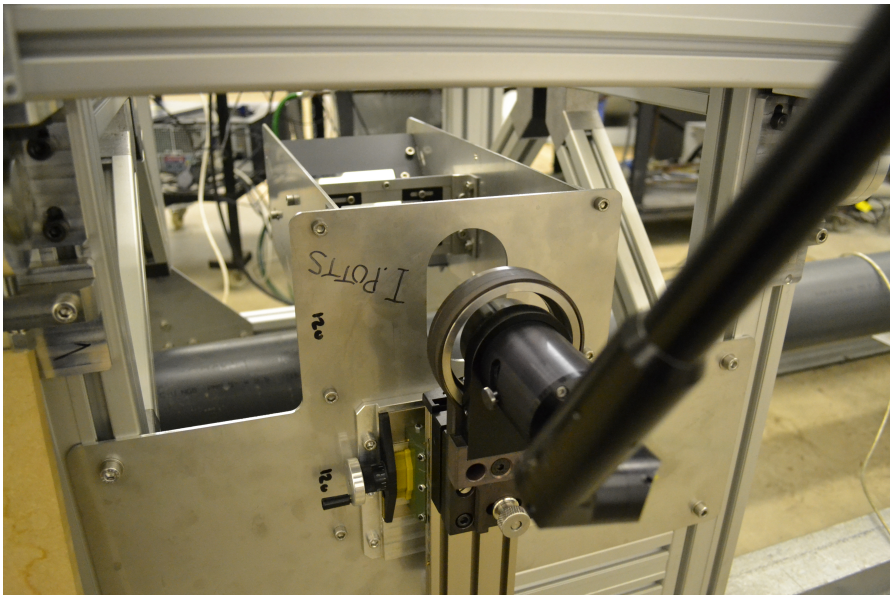

FIGURE 3.6: Laser setup at channel bottom.

3.1.2 New Profiled Inlet

In order to address the high free stream turbulence level, a new inlet section was added, featuring a hyperbolic tangent profile with approximately $3:1$ contraction ratio, replacing the original simple bell-mouth as shown in Figure 3.7. The structural frames of this were constructed from 6 mm clear acrylic sheets (i.e. Perspex), laser cut and glued using Tensol (an acrylic glue), whilst the curved wall surfaces were constructed from 1.0mm black plasticard. At the inlet to this was a single honeycomb of 20mm thickness, with 3.2mm (1/8in) cell size, giving the 6:1 aspect ratio recommended by Bradshaw. This was followed by a set of five gauzes; 3 coarse with porosity 60%, and 2 fine with a porosity of 45% as shown in Figure 3.8. Given the limited space, this was about all that could reasonably be squeezed in.

This new inlet has significantly decreased the free-stream turbulence, and improved the boundary layer profile. A recognizable wake region could now be observed, and the boundary layer thickness, for a given distance into the channel (2.1m downstream) was increased by a factor of 3. With this set-up, the turbulence intensity dropped to 1.7% in the free stream (i.e. at y $=$ 100mm). The increase in boundary layer thickness was puzzling, but it was believed that, rough edges around the new inlet section was the main culprit. To address this, any gaps and steps were smoothed over using car body filler and smoothed using emery to allow better

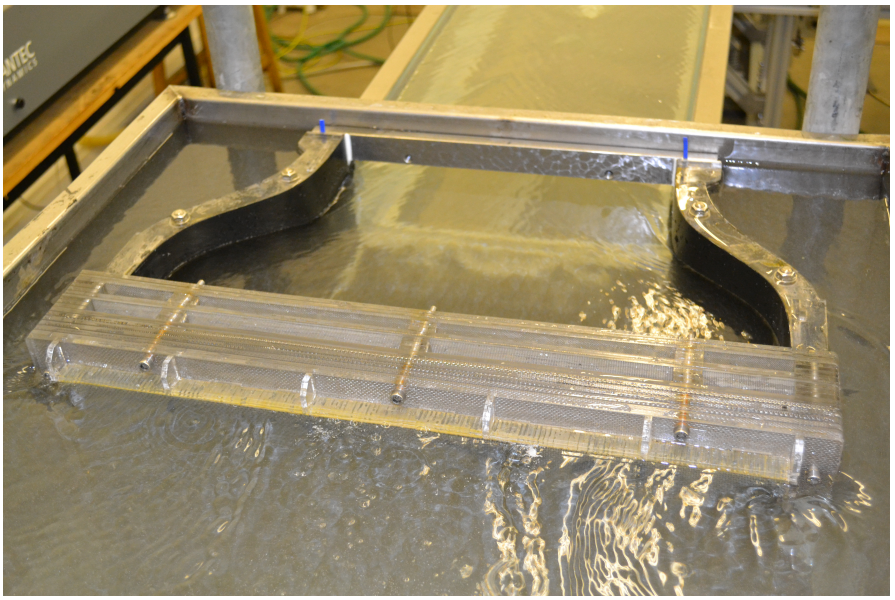

FIGURE 3.7: New hyperbolic tangent profile channel inlet design.

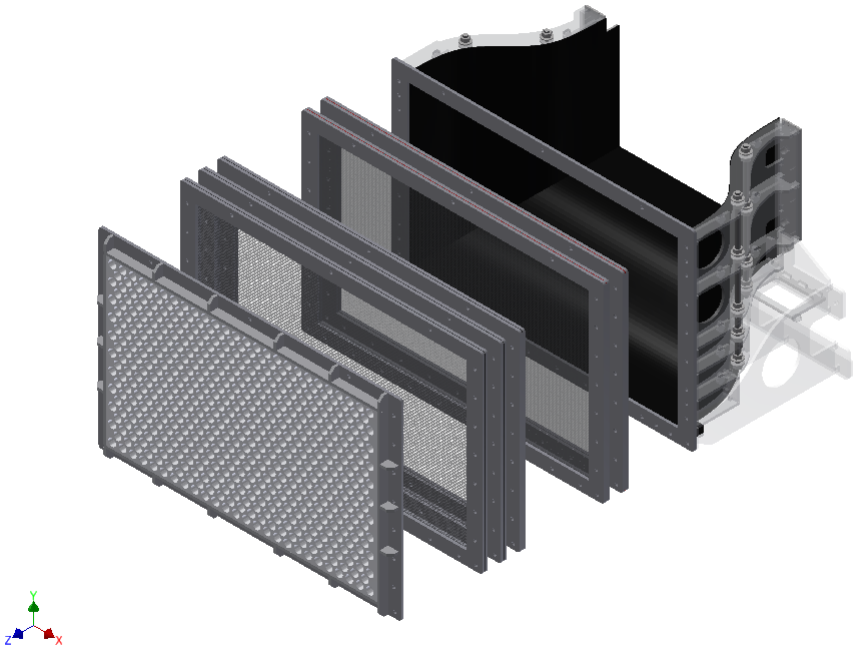

FIGURE 3.8: New hyperbolic tangent profile channel inlet design. From left, 1) Honeycomb, 2) 3 pc Coarse gauze, 3) 2 pc Fine gause, and 4) Channel inlet.

transition. This technique significantly reduced the boundary layer thickness from about 80mm down to around 40mm without tripping and to 50mm with a zig-zag strip placed at the start of the working section.

3.1.3 Design of inlet and outlet plenum tank

Initial investigation revealed that the original two perforated plates ($23\,\%$ porous) in the inlet plenum tank caused a significant reduction in the free-stream turbulent intensity. This was despite the dished side walls, used as a stiffening technique in the tank design, causing a considerable gap between the perforated plates and the side walls, allowing water to gush up at high velocity. In order to further reduce turbulence, an additional two perforated plates were later added, and the gaps on both sides were closed.

Whilst these measures did reduce free stream turbulence, examination of the free stream velocity data taken using laser Doppler velocimetry showed that much of the remaining unsteadiness was a low frequency sinusoidal pulsation, rather than random turbulence. This was attributed to a form of "U-tube oscillation" between the two large plenum tanks. The first attempt to suppress this involved fitting a cylindrical "diffuser" extension to the pump delivery pipe, rolled up from the same 23% porosity perforated plate as the baffle plates, and spanning the length of the inlet plenum tank. This addition was unsuccessful, actually raising the turbulence level, as the localised high velocities induced tank vibration, so the diffuser was removed.

The final solution to the low frequency oscillation proved to be fitting a pressure drop screen between the outlet of the working section and the outlet plenum tank. Various porosities were tested, using the same fine and coarse gauzes as at the inlet, and also the 23% porous perforated plate. The perforated plate gave the best results, and was the configuration adopted throughout the project. Figure 3.11 shows the schematic diagram for the water channel rig showing the measurement position and rig components.

An example of the velocity time trace plot showing the low frequency undulation is shown in Figure 3.12. A complete LDV velocity profile for various level of porosity were measured i.e. 1) without pressure drop screen, 2) 25% porous perforated plate, 3) 45% porous fine gauze,

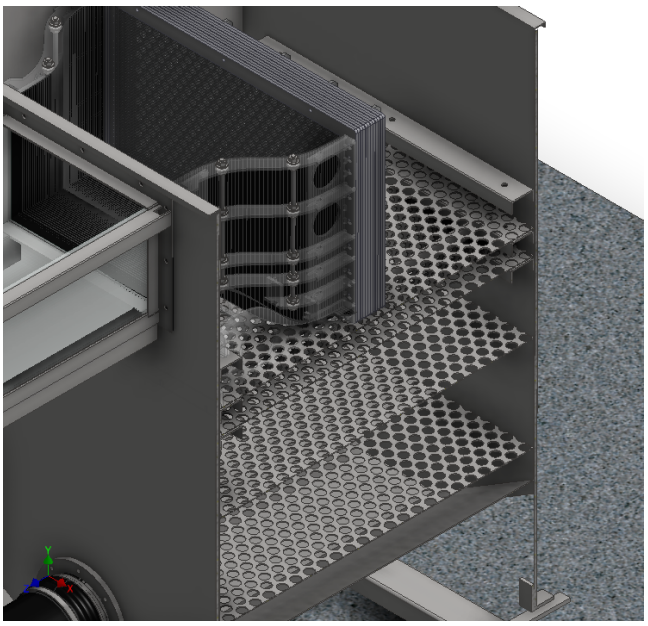

FIGURE 3.9: Inlet plenum tank design with 4 perforated plates at different height.

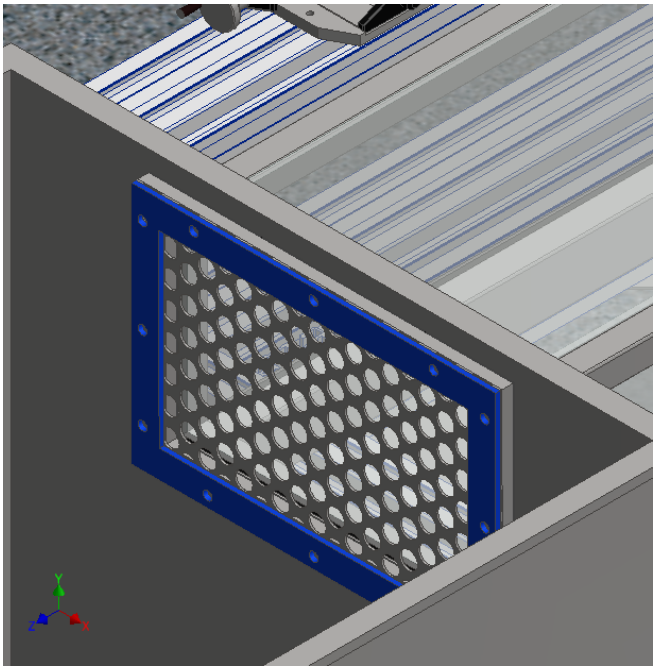

FIGURE 3.10: Exit plenum tank design with a perforated plate secured immediately after channel exit.

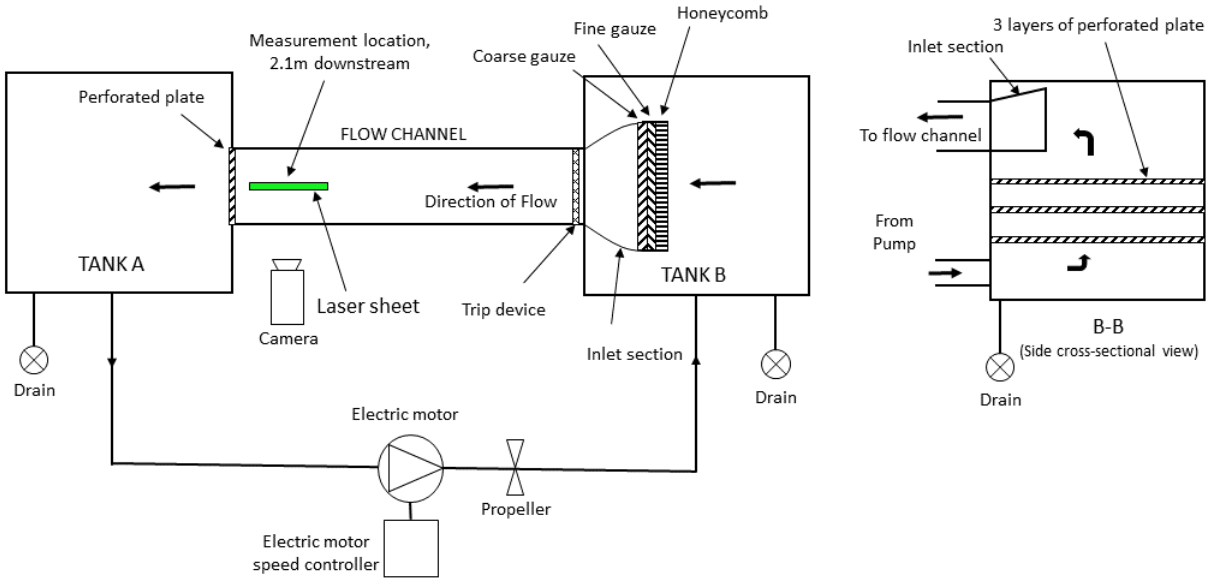

FIGURE 3.11: Schematic diagram showing all components of the water channel rig (Not to scale).

and 4) 60% porous coarse gauze. The free-stream turbulence intensity drops below 1% and the boundary layer profile collapse perfectly to the DNS data of Schlatter and Örlü (2010). Also, PIV investigations reveal that the introduction of the perforated plate does not introduce any back flow to the system at 2100mm or further down the channel.

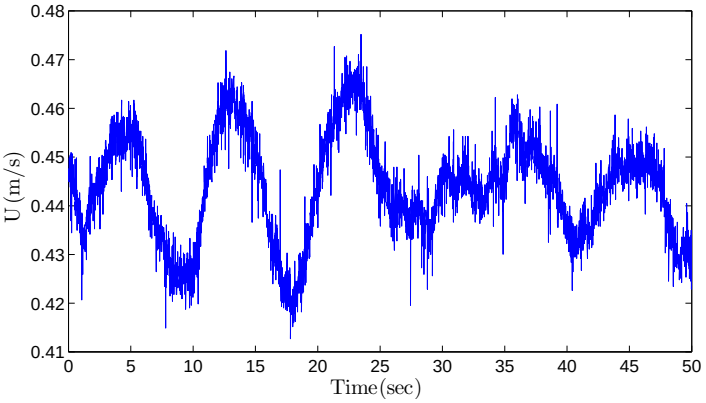

(a) Without back-plate.

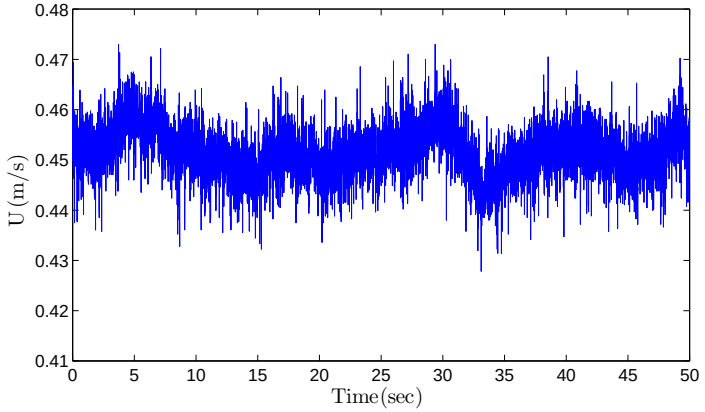

(b) With perforated plate.

FIGURE 3.12: LDV velocity time trace plot showing the reduction of the low frequency undulation with the use of a perforated plate at the channel exit.

3.1.4 Boundary layer tripping - via Zig-zag strip

Boundary layer tripping, i.e. forcing it from a laminar state into a turbulent state, is commonly used to fix the point of transition in fluid dynamics experimental rigs. Various tripping devices, such as surface mounted wires and roughness strips have been used, but recently it has been shown that zig-zag strips are particularly effective at producing a canonical boundary layer in a minimum development length. For the present water channel this forcing was performed by the use of a zig-zag strip (illustrated in Figure 3.13). Our channel flow experiments were tripped using a 2mm high zig-zag strip, similar to, but slightly higher than that used by (Elsinga and Westerweel, 2012). According to (Elsinga and Westerweel, 2012), the transition structures no longer affected the boundary layer at a distance of 500 δ_0 downstream of the trip, where δ_0 is

the thickness of the laminar layer upstream of the trip. Interpolating (Elsinga and Westerweel, 2012) to 0.45m/s gives the boundary layer thickness δ_0 to be approximately 3mm for the Newcastle channel, and so transition structures should have vanished by 1.5m downstream of the zig-zag strip. The primary intended measurement station for the channel is 2.1m downstream of the trip, 600mm further away from the estimated minimum distance of 1.5m.

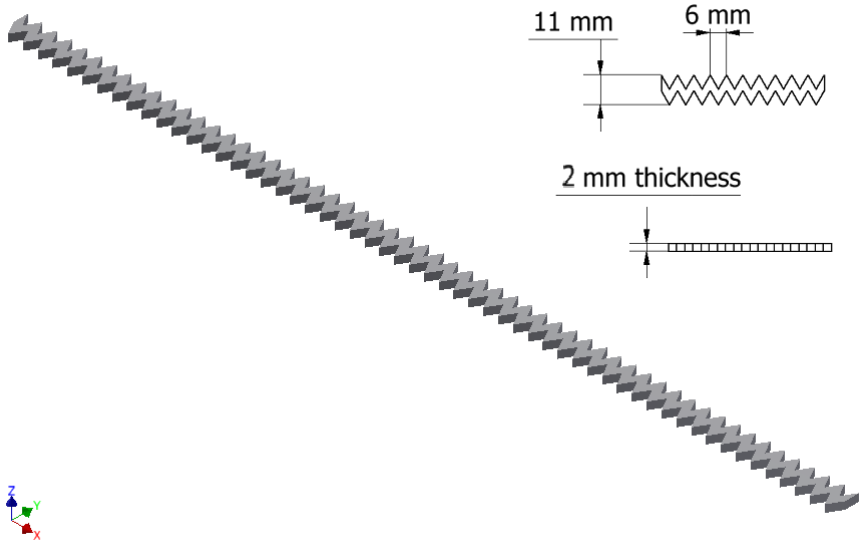

FIGURE 3.13: Zigzag strip (design following (Elsinga and Westerweel, 2012)).

3.1.5 Summary description of upgraded Newcastle flow channel

To summarize, the final open-channel working section is 3m long, 326mm wide and 200mm deep. Side and bottom walls are toughened flat glass, allowing full optical access. A substantial instrumentation support frame built from commercial aluminium profile sections provides adjustable but stable support for an LDA probe, PIV cameras and light sheet optics at any point along the channel. The channel inlet section features a hyperbolic tangent profile with approximately 3:1 contraction ratio, with a single honeycomb and a set of five gauzes (3 coarse and 2 fine) at inlet, replacing the original simple bell-mouth. The inlet plenum tank has four perforated plates (23% porosity) for flow calming, and immediately at the channel exit, a perforated plate of identical material was added to suppress low frequency "U-tube" oscillations between the two plenum tanks. Water is circulated via large bore pipework by a propeller type axial

flow pump with electronic variable speed control. The floor boundary layer is tripped at entry to the glass working section by a 2mm high zig-zag strip, and by the primary measurement station, 2.1m downstream of this, a canonical turbulent boundary layer of thickness approximately 50mm is achieved at a free stream velocity of 0.45m/s. This corresponds to Reynolds numbers of Re_θ = 3000 and Re_τ = 890. The turbulence intensity is less than 1% in the free-stream at y = 100mm. A full description of the commissioning test results for single phase water flow in this rig is given in Chapter 4.

3.2 Instrumentation

3.2.1 Time-resolved particle image velocimetry system

The Newcastle PIV time-resolved image acquisition system comprises of a high-repetition rate Nd:YAG laser with output wavelength 532nm, a parallel light-sheet optics system giving an approximately 37mm by 0.6mm parallel sheet, plus a conventional, divergent light sheet optics system, two IDT MotionPro X5PLUS high-speed CMOS (Complementary Metal-Oxide Semiconductor) cameras with 4-Gb on-board memory, and DynamicStudio v3.14 PIV software for data acquisitions, handling and processing (see Figure 3.14).

The Dantec Dynamics TR-laser is a cw-diode pumped, Q-switched and frequency doubled Nd:YAG laser, and suitable for generation of laser pulses at high repetition rates. This laser is a double head Lee Laser LDP-100MQG unit, designed for double-pulse operation, with a maximum power output of 50W/head at 10kHz repetition rate. Because the diodes need some time to pump the laser rod between pulses, the pulse energy reduces with increasing repetition rate, as shown in Figure 3.15.

For the sub kHz repetition rates used in the present project, pulse energies of over20 mJ are possible.

The twin beams from the laser head are routed to the light sheet optics via a Dantec 80X39 2m articulated light arm, allowing easy positioning of the light sheet without movement of the bulky laser head itself. Two alternative light sheet optics modules are available. The first

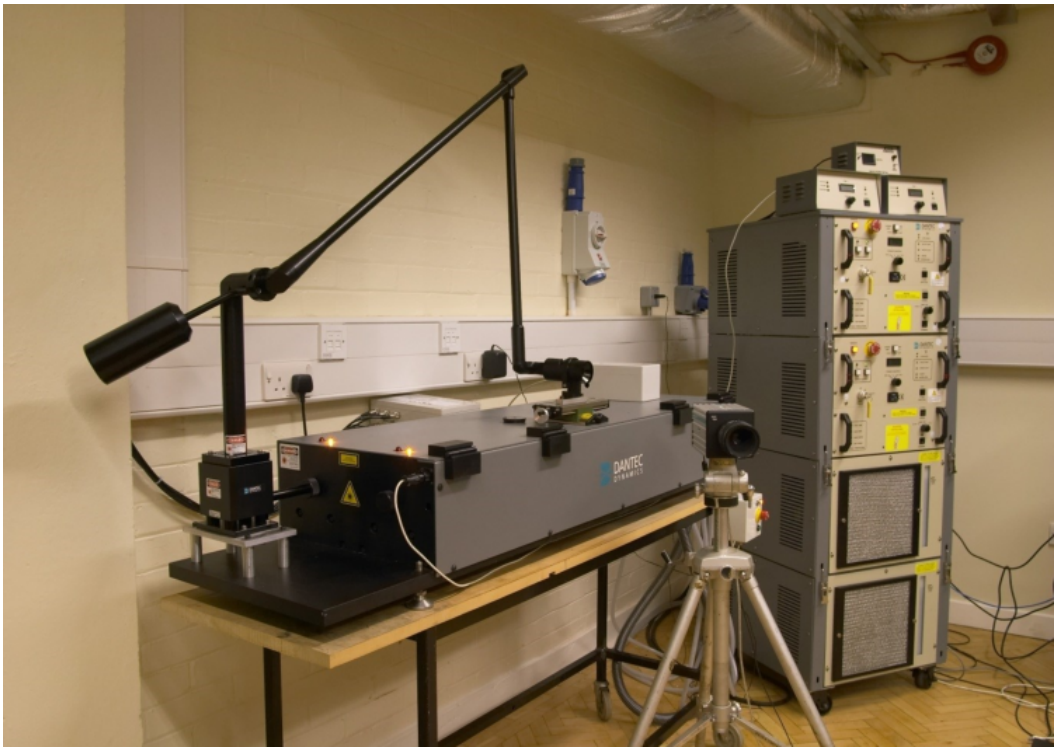

FIGURE 3.14: Newcastle University PIV System.

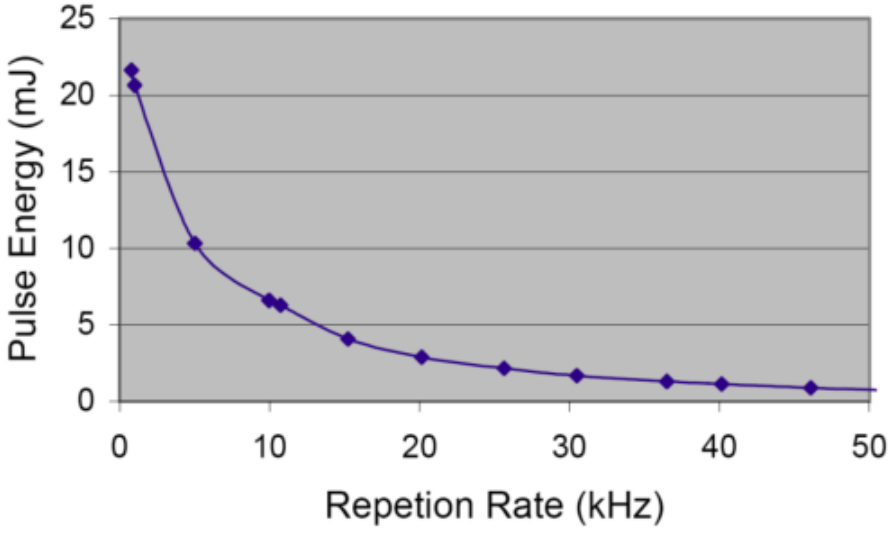

FIGURE 3.15: Pulse energy vs. repetition rate for LDP-100MQG laser.

produces a parallel light sheet of height approximately 37mm and thickness around 0.6mm. It was hoped that this would provide a concentrated strip illumination along a wall boundary layer. As described earlier, the length of light path using this option proved to be problematic, and so the second, conventional light sheet optics unit was used for the present project. This Dantec 80X74 module, including a Galilean telescope type thickness adjuster, was capable of generating a light sheet of 10° to over 30° divergence angle, with thickness between 0.6mm and 3.0mm at the focus position.

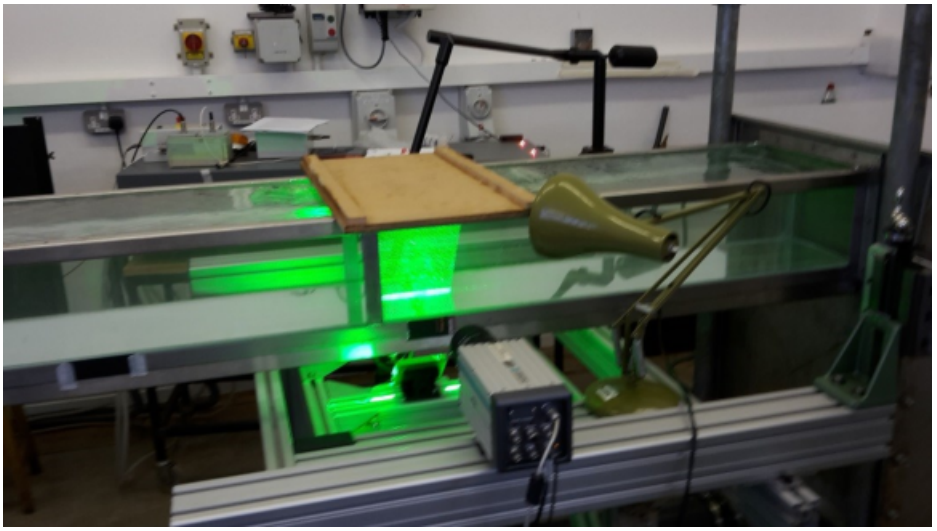

FIGURE 3.16: Vertical light-sheet, reflected from under floor of channel.

For the present work the minimum thickness and divergence values were used. The light sheet optics were located below and to the side of the channel producing a horizontal sheet which was reflected by a 45° inclined surface silvered mirror to give a vertical sheet entering the channel through the plate glass floor, illuminating the boundary layer measurement volume with minimum light path as shown in Figure 3.16. A beam stop was provided above the channel and although there was some slight back reflection from the free surface, this proved not to be a problem for PIV imaging. The light sheet optics module was itself mounted on a small X-Y traverse table fitted with a micrometer tip/tilt module, so that light sheet position and orientation could be finely adjusted.

The MotionPro® X5PLUS high-speed motion camera (see Figure 3.17) at full resolution (i.e. 2352 × 1728 pixels) has a maximum acquisition speed of 250 frames-per-second (fps) in the Standard-Mode and 500fps in the Plus-Mode. These acquisition speeds can effectively

be increased by reducing the vertical resolution or alternatively, operating in the Plus-Mode (see Table 3.1). For the latter, image data are scanned with every other horizontal line being skipped and later interpolated, but unfortunately the detailed operation of Plus-Mode was not made clear before the cameras were purchased. This interpolation is expected to degrade the image quality and subsequent flow statistics. In subsequent testing, direct comparison between standard and Plus-Mode PIV images revealed that the degradation was not as detrimental as feared. Although the percentage of overall bad vectors was slightly more with Plus-Mode, they are acceptable at well below 5%. The sensor is built with 7μm × 7μm pixels that are less sensitive than the typical 13 - 30μm pixels of other high speed cameras, but are ideal for PIV measurement as the small size helps to improve the ratio of acquired particle image size to the sensor pixel size d_e/d_τ. The MotionPro® X5PLUS is a true "frame straddling" camera, allowing independent control of the time interval Δt between the two images of a PIV pair, and the rate at which these image pairs are acquired. Further detail on the MotionPro® X5PLUS specification is tabulated in Table 3.2.

For single and two-phase applications, acquiring a wide field of view is advantageous for boundary layer structure visualization. Therefore operating at almost half the vertical resolution (i.e. 832 pixels) will effectively increase the aspect ratio of the imaged region by a factor of two, whilst also usefully doubling the acquisition speed. Standard mode gives 1000 double images with the maximum acquisition speed of 500Hz or 250 PIV vector fields per second. With the plus mode, the number of double images acquirable is 2000 with a maximum acquisition speed of 1000Hz or 500 PIV vector fields per second.

Vertical Resolution (pixels)	Standard-Mode (fps)	Plus-Mode (fps)
1728	250	500
864	500	1000
432	1000	2000
216	2000	4000
108	4000	8000
54	8000	16,000

TABLE 3.1: MotionPro X5PLUS sample frame rates (@ Max. Horizontal resolution of 2352)

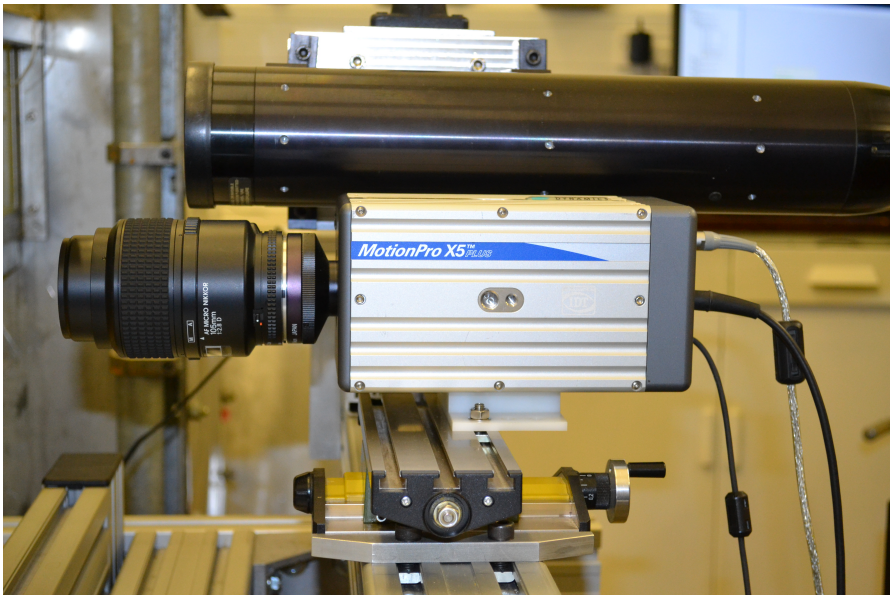

FIGURE 3.17: IDT Redlake's MotionPro X5PLUS high-speed camera.

Items	Description
Sensor Array	Area Array with 7μm × 7 μm pixels
Image Resolution	Up to 2352 pixels × 1728 pixels
On-board Storage	4Gb; with PLUS option, the memory is effectively doubled

TABLE 3.2: MotionPro X5PLUS Performance Specifications

3.2.2 Target plate and target traverse system

In order to position the light sheet correctly, and to calibrate the PIV camera field of view from pixels to physical units, a reference target plate is required. The PIV target plate used is the DantecDynamic standard target plate with a 2.5mm spacing between 36 1.0mm diameter circular dots giving a 100mm × 100mm field of view of the target plate. The target plate was then secured to an in-house built traverse system to allow movement in x- (streamwise) and z- (cross-stream) direction, allowing alignment with the laser light-sheet.

A short review of the measurement technique is detailed in the following subsections.

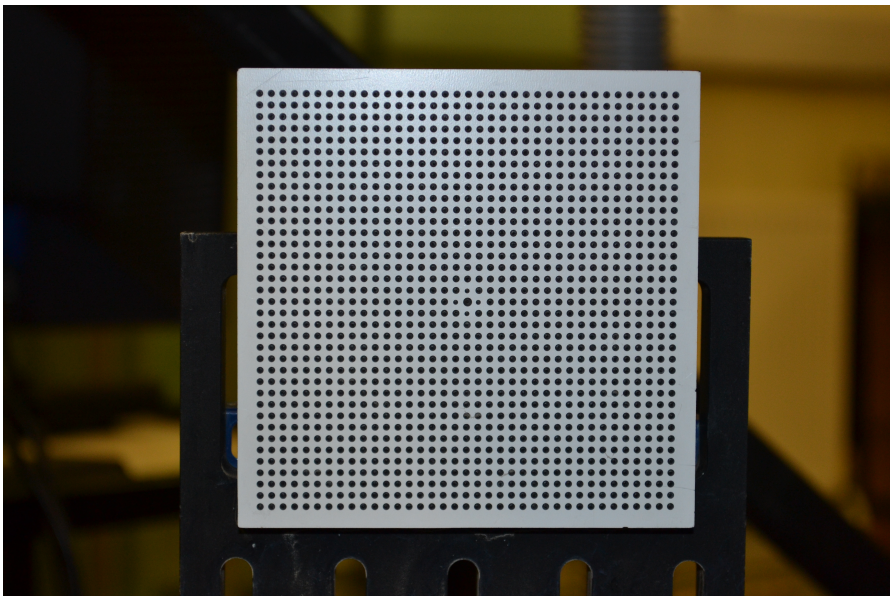

FIGURE 3.18: DantecDynamics target plate.

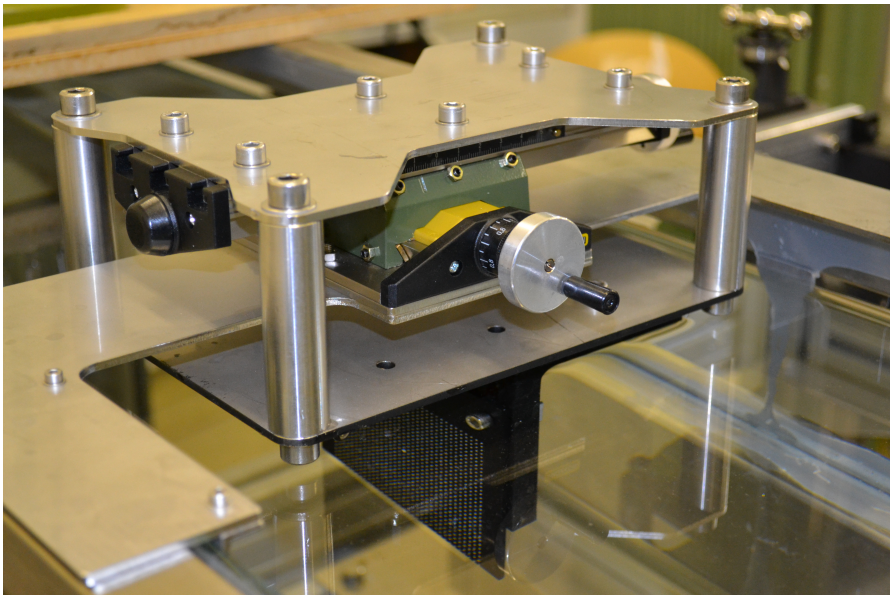

FIGURE 3.19: DantecDynamics target plate and custom traverse system.

3.2.2.1 Particle image velocimetry

Particle image velocimetry, or simply PIV, refers to a class of methods used in experimental fluid mechanics to determine instantaneous fields of the vector velocity by measuring the displacements of numerous fine particles that follow the motion of the fluid. The rate of particle movement is determined by recording images of the particles or patterns related to those images at two or more precisely defined times and inferring the displacements of individual particle or displacements of the images. This method has gone by many names, such as pulsed light velocimetry (Adrian, 1984), particle image displacement velocimetry (Lourenço and Krothapalli, 1986), and digital PIV (Willert and Gharib, 1991; Westerweel, 1993). Although these methods differ in some details, the term "PIV" emphasizes that all of them fundamentally deal with images of particles (Adrian, 1984).

Because of the long delays in modification of the flow channel, much time at the start of the project was spent in familiarisation with the new PIV instrumentation and optimising measurement parameters by benchmark testing for simple turbulent flows, such as the axisymmetric jet and some, then new, insight into the use of the technique was gained from this. Figure 3.20, shows the instantaneous velocity vectors (the field of view is 32mm by 100mm long and the jet velocity is 0.5m/s) for a typical jet flow experiment carried out during this phase.

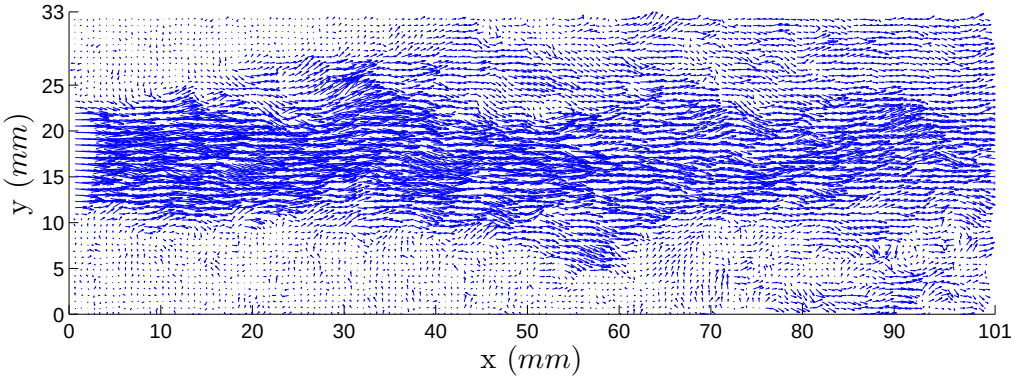

FIGURE 3.20: The velocity vector field of a jet flow measured by two-dimensional PIV.

3.2.2.2 Principle of PIV

The principles of PIV have been covered in many papers including Willert and Gharib (1991), Adrian (1991) and Lourenço et al. (1989) among many others. A more detail understanding of the full scope of the measurement technique and its development, can be found in the books of Raffel et al. (1998) and Adrian and Westerweel (2011), which are an excellent source of information on various aspects of PIV.

The fundamental layout of a PIV system is shown in Figure 3.21. The PIV measurement process includes illuminating a cross-section of the seeded flow field, typically by a pulsing light-sheet, recording multiple images of the seeding particles in the flow using a camera located perpendicular to the light-sheet, and analysing the images for displacement information. The recorded images are divided into small sub-regions called interrogation regions, the dimension of which determines the spatial resolution of the measurement. The interrogation regions can be adjacent to each other, or more commonly, have partial overlap (typically 50%) with their neighbours.

The preferred method in PIV is to capture two images on two separate camera frames, and perform cross-correlation analysis for each of the interrogation region. The displacement between the two interrogation region images which shows the best correlation then gives the mean particle movement for the region, and the local velocity vector may then be obtained by dividing this displacement by the known time interval between the images, Δt. Sufficient number of particles needs to exist in the interrogation regions, which are being correlated, otherwise only random correlation, or noise will exist. This will be discussed later in Section 3.2.2.4. The PIV measurement accuracy depends upon the time difference Δt between the laser pulses generating the image pair; too long and correlation will be lost, too short and the measurement uncertainty in the displacement will be large. A good rule of thumb is to obey the "one-quarter rule" by not allowing the particles to move more than a quarter of the interrogation area for in-plane motion, and for out-of-plane motion, not more than a quarter of the light-sheet thickness.

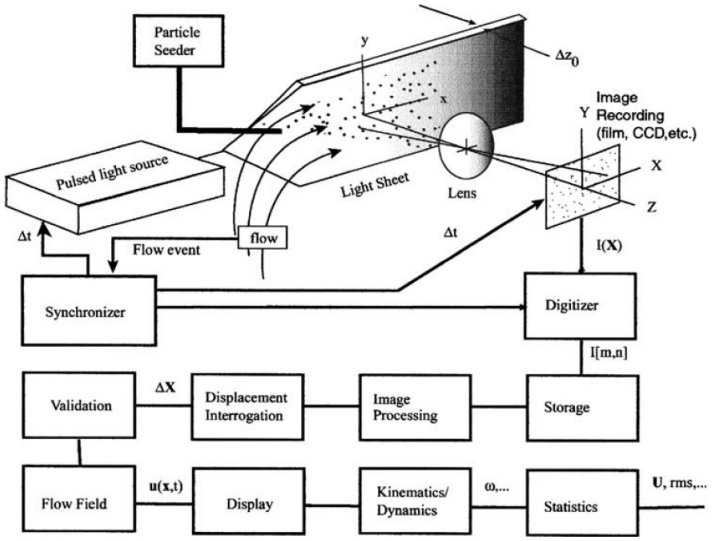

FIGURE 3.21: Elements and processes in a planar two-dimensional particle image velocimetry system (Adrian, 2005).

3.2.2.3 Imaging of small particles

At the time of the preliminary design of the channel PIV experiments the major source of information was the pioneering work of Adrian, Meinhart and Tomkins (2000), whose development of PIV was based on the use of medium format film cameras, rather than CCD or CMOS digital devices with 35mm camera lenses. From this work it was known that simple geometrical optics did not give the true image size when observing small particles. The geometric particle image size, d_{geom} assuming that the geometric optics are perfect can be estimated from

$$d_{geom} = \sqrt{M_0^2 \, d_p^2} \tag{3.1}$$

For Adrian's operating parameters the major effect was diffraction through the lens aperture. Assuming diffraction limited imaging, and a Gaussian intensity distribution of the geometric image of the particle, the diameter of the diffracted image of the particle is

$$d_e = \sqrt{d_s^2 + M_0^2 \, d_p^2} \tag{3.2}$$

where d_p is the particle diameter, and M_0 is the geometric magnification factor for the lens arrangement, and the diffraction limited spot size d_s is given by:

$$d_s = 2.44\,(1 + M_0)\,f^{\#}\,\lambda \tag{3.3}$$

where $f^{\#}$ is the f-number (or f-stop) of the lens, and λ is the wavelength of light.

For a typical boundary layer case in the present project, at x = 2.1m from the channel inlet with free stream velocity U_∞ = 0.45 m/s, the total boundary layer thickness is expected to be around 50mm, with a shear velocity u_τ = 0.0192m/s. Imaging a region of size Δx = 100mm × Δy = 75mm, corresponding approximately to $\Delta x^+ = 1900 \times \Delta y^+ = 1400$ would allow the entire thickness of the boundary layer and complete large-scale turbulent structures to be observed. For the X5PLUS camera, with sensor size 16.464mm × 12.096mm, this would require a geometric magnification factor of 0.164, achievable with a Nikon 60mm focal length macro lens at a stand-off distance of 400mm. Table 3.3 then shows the effect of lens stop number on the image size, d_e , of a 12μm seeding particle, allowing for diffraction effects.

f-number	d_p (μm)	d_{geom} (μm)	d_s (μm)	d_e (μm)
2.8	12	1.98	4.233	4.671
3.5	12	1.98	5.291	5.648
4	12	1.98	6.047	6.361
5.6	12	1.98	8.466	8.693
8	12	1.98	12.094	12.254
11	12	1.98	16.629	16.746

TABLE 3.3: Effect of diffraction on image size for 12 μm particle.

It is generally accepted from the work of Adrian and others that to locate the particle image position with sub-pixel accuracy the optimum image size must correspond to between two and four pixels or 14 - 28μm in the present case. The basic image size assuming perfect geometric optics d_{geom} is less than 2μm, and it would seem necessary to reduce the lens aperture to f/11 to achieve an image greater than 2 pixels in size. This would greatly reduce the amount of light reaching the sensor, and would probably not give acceptable images with the current hardware. Practical tests with this type of configuration in jet flows, however, revealed that optimal image sizes could be obtained with apertures as large as f/2.8, as shown by the peak widths reported

by Dantec DynamicStudio in Figure 3.22 and 3.23. Note that peak width values correspond approximately to twice the image size in pixels.

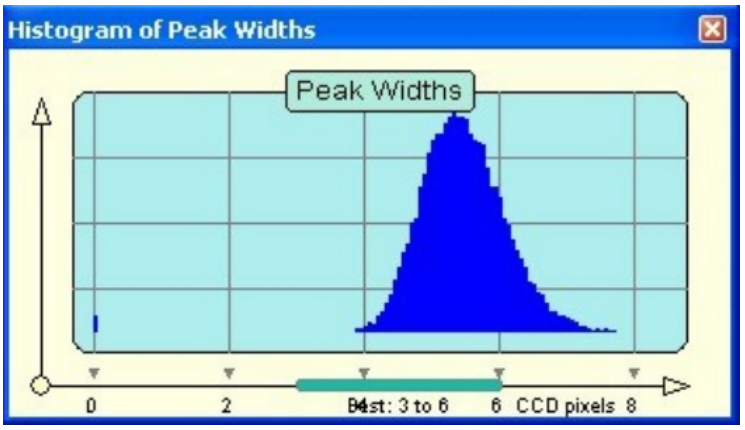

FIGURE 3.22: Peak widths for 12μm particles imaged with MicroNikkor 60mm lens at f/2.8

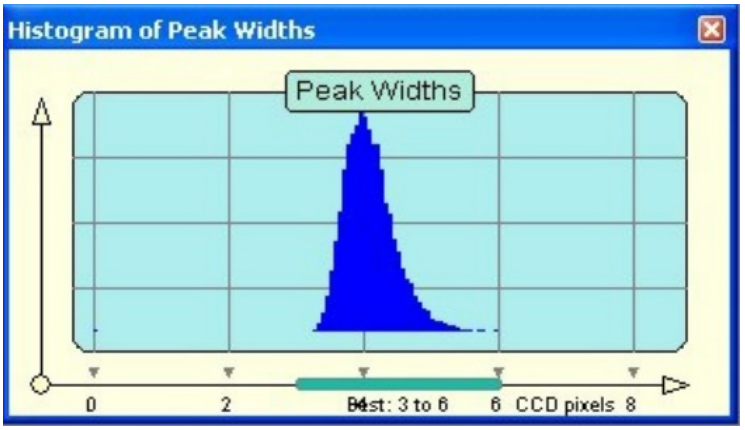

FIGURE 3.23: Peak widths for 12μm particles imaged with MicroNikkor 60mm lens at f/4.

This unexpected but fortuitous result was attributed at the time to the influence of aberrations with the standard, albeit high quality, 35mm camera lens, and this was later confirmed when the author came across the work of Chetelat and Kim (2002), who show that at large f-numbers it is diffraction which provides the increased magnification in image size, whilst at small f-numbers lens aberrations provide the dominant magnifying effect. Although this phenomenon does now seen to be more widely recognized, see e.g. Adrian and Westerweel (2011), it is not as clearly documented or acknowledged as the diffraction effect.

A common problem encountered in PIV analysis is the phenomenon known as "pixel-locking". This effect refers to the bias of detected particle displacements to integer pixel values.

The effect is always present when particle images are of the order of 1 pixel in size, but can occur even for optimal image sizes, as shown in Figure 3.24, which shows a velocity histogram for a jet flow experiment with PIV parameters similar to the boundary layer tests described above, analysed using the standard Dantec software. Such effects would clearly influence the accuracy of turbulence statistics taken from this data. Dantec provide a so-called "high accuracy" software module to reduce the pixel locking effect, but the basis of their method is not in the public domain. The module does virtually eliminate pixel locking for reasonable image sizes, and has been used for all present PIV measurements.

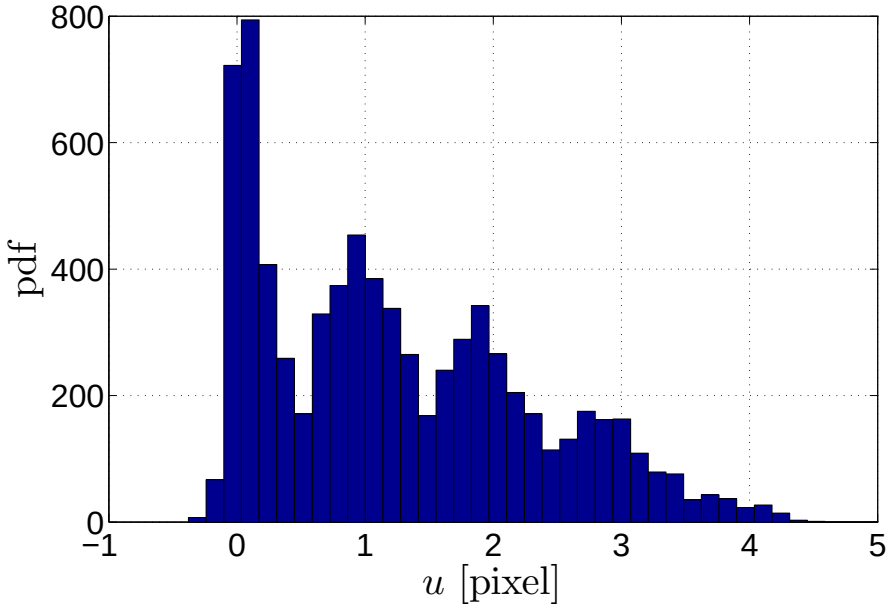

FIGURE 3.24: Velocity histogram plot for $10\mu m$ S-HGS (M = 0.17, $f_{\#}$ = 2.8, at $25\,W$) jet flow experiment clearly exhibiting pixel-locking behaviour.

3.2.2.4 Seeding

When it comes to the choosing tracers or inertial particles, the light scattering behaviour is important. This depends on various factors, such as the ratio of the refractive index of the particles to that of the surrounding medium and the particle size, shape and orientation. There is little control over the latter two properties, but average particle image size depends on particle actual size and properties. A trade-off is usually involved regarding the size of tracers, their ability to follow the flow accurately and to scatter sufficient light. Another aspect which is crucial in PIV

is the number of particle image per interrogation area. Keane and Adrian (1990) recommended that this value should be at least 15 per interrogation volume. This is not a problem when viewing the flow with lower magnification with large field of view, but for higher magnification and hence smaller field of view, the total number of seeding required is significantly more. With high seeding density, above 10^{-6} the flow properties may be affected by the tracer particles (two-way coupling). For a particle volume fraction below 10^{-6} two-way coupling may be completely neglected (Elghobashi, 1994), but the proposed concentration is for gas-solid flows. This may not be directly applied to water flow as the concentration is too small in gas-solid flow. Kiger and Pan (2000) suggested that the volumetric loading should be lower than and not exceeding 10^{-4} for fluid flow. Van Hout (2011) $583\,\mu$m PS bead volumetric loading was 10^{-4}. The work of Rashidi et al. (1990) indicates that even average particle volume fraction of around 10^{-4} may lead to significant modulation of turbulence. With our experimental setup, the volumetric loading is 10^{-4} for 18ppm by weight, which is much higher that suggested by Elghobashi (1994), but in line with many published PIV experiments. The tracer particles used in our study are the Silver-coated hollow glass spheres (S-HGS) with a mean diameter of $10\,\mu$m. These are borosilicate glass particles with a spherical shape, smooth surface and thin silver coating to increase reflectivity. They are specifically designed for liquid flows as they are close to neutrally buoyant in water, having a specific gravity of 1.4. The particle response time in water is 7.78ms and the Stokes number is 0.0028. The same seeding material was used for the LDV measurements, but with much smaller loading, 3ppm by weight.

3.2.3 Laser Doppler velocimetry System

The Newcastle LDV is a 2 channel TSI back-scatter system, using a fibre optic probe. Multi-wavelength laser light from a LEXEL Model 85, 1 Watt, Argon Ion laser is separated into three colours, green, cyan and blue, using a TSI 9201 Colorburst beam splitter. Each colour beam is further split into unshifted and frequency shifted beams by a Bragg cell within the Colorburst. The use of frequency shifting allows LDV to resolve reversing flows. For a two-channel system only the green and cyan beams are used, and these are launched via coupler units into fibre optic cables connected to a TSI model 9831 probe which has a focal distance of about 350mm. For the present work only one channel, using the green 514.5nm wavelength

beams, was used to measure the streamwise, x- component of velocity within the channel. The measurement volume with this probe configuration was 90μm in diameter, by 1.31mm in length. The probe was mounted on a Myford slide, adjacent to the side of the channel, so that the measurement volume could be traversed in the wall-normal direction up to 100mm from the channel floor, with a nominal positional accuracy of 0.02mm. Back- scatter light was collected by the probe and delivered by fibre optic link to a TSI PDM1000 Photo Detector Module, which produced an electronic signal for the TSI FSA3500 Signal Processor. This unit receives the signals and extracts information such as frequency, phase, burst transit time and burst arrival time from these signals and sends it to the computer. The data is analyzed using the FLOWSIZER™ (Version 2.0.1.0) software. A short review of the measurement technique is detailed in the following subsections.

3.3 Laser Doppler velocimetry

Laser Doppler velocimetry, LDV is a non-intrusive technique used to measure the velocity of particles suspended in a flow. If these particles are small, in the order of microns, they can be assumed to be good flow tracers following the flow and thus their velocity corresponds to the fluid velocity. As a well established single point measurement technique, it has been extensively used in the development of Newcastle University new open-channel experimental rig.

3.3.1 Data acquisition and analysis

Modern LDV signal processors are highly automated and, having set appropriate band pass filters for the velocity range to be measured, the major remaining control parameters on the FSA3500 are the Burst Threshold and the photo multiplier (PMT) voltage. The burst threshold sets the signal level at which the burst detection gate opens, with higher levels giving a better signal to noise ratio, but lower data rate. Appropriate settings may be selected based on the burst efficiency or ratio of valid bursts to burst detection triggers, reported by the processor. To minimise noise in the velocity data acquired, the burst efficiency needs to be set very high and ideally $90\,\%$ and above. Very close to the wall, data rate is very low, and this could be

increased slightly by increasing the PMT voltage or reducing the burst threshold or both if required. This will allow more noise to get through. A portion of this could be filtered off before exporting and processing the data. Another important consideration is the quantity of data acquired. Simple analysis of the mean and rms data reveals that the mean data converge to a stable mean value and the rms to a minimum with 10,000 data points suggesting that we need to acquire a minimum 10,000 velocity data per measurement point.

In LDV there are two major problems faced when making statistical analysis of the measurement data: velocity bias and the random arrival of seeding particles to the measuring volume. While velocity bias is the predominant problem for simple statistics, such as mean and rms values, the random sampling is the main problem for statistical quantities that depend on the timing events, such as spectrum and correlation functions. Since our use of LDV is primarily to extract the boundary layer profile and associated data such as shear velocity u_τ, boundary layer thickness δ, Reynolds number etc., the removal of velocity bias is important.

The mean and variance estimated from LDV data set through

$$\overline{U} = \frac{1}{N}\sum_{i=1}^{N} u_i \tag{3.4}$$

$$\sigma^2 = \frac{1}{N}\sum_{i=1}^{N} (u_i')^2 \tag{3.5}$$

where N is the total number of velocity samples, u_i is the instantaneous velocity u_i. When a significant variation in instantaneous velocity samples is present, the actual meal velocity cannot accurately be determined as a simple average of the sample values, since a larger number of samples will be recorded when the velocity is high; a velocity known as velocity biasing. With a weighting technique (Buchhave et al., 1979) with individual weights w_i for each measured velocity value u_i the result are much more reliable:

$$\overline{U} = \frac{\sum_{i=1}^{N} u_i w_i}{\sum_{i=1}^{N} w_i} \tag{3.6}$$

$$\sigma^2 = \frac{\sum_{i=1}^{N} (u_i')^2 w_i}{\sum_{i=1}^{N} w_i} \tag{3.7}$$

Several methods to derive the weights from the LDV data set has been developed, for example velocity weighting (Laughlin and Tiederman, 1973), arrival time weighting (Barnet and Bentley, 1974) and transit time weighting (Hösel and Rodi, 1977). The transit time weighting ($w_i = \tau_i$) uses the time the tracer particles need to pass through the measurement volume. With a good estimate of the transit time τ_i this weighting method is ideal for constant particle concentrations even for three-dimensional turbulence. This technique was used in processing our LDA measurements in the turbulent boundary layer for both single and two-phase flows.

3.4 Water channel boundary layer calculations

LDV allows very accurate measurement of the channel floor boundary layer velocity profile, but to express this in the conventional non-dimensional form, the shear velocity u_τ , and hence the wall shear stress τ_w is required. A common method for obtaining the non-dimensional profile is the Clauser plot method, where dimensionless velocity U^+ is plotted against dimensionless wall normal coordinate y^+ for various assumed values of τ_0 , and compared with the expected linear relationship in the "log-law" region $30 < y^+ < 200$, taking the value of τ_0 which gives best agreement as the true value. The weakness of this approach is that it assumes the log-law relationship. As a result, the use of this method to compute τ_0 can result in an artificial collapse of the data onto the universal log-law. A more fundamental approach, used wherever possible in the present work, is to plot the profile in the laminar sublayer region, $y^+ < 5$, on a linear basis, so that the gradient may be used to determine τ_0 directly from Newton's law of viscosity.

The feasibility of this approach can be demonstrated from early design calculations for the channel. Assuming the density of water, ρ as $1000\,\mathrm{kg\ m^{-3}}$, dynamic viscosity, $\mu = 0.001\,\mathrm{kg/ms}$, and a flow with a free-stream velocity U_∞ as approximately $0.45\,\mathrm{m/s}$, the boundary layer thickness can be estimated by (Munson et al., 2002)

$$\delta_{99} = 0.370\,x\,\mathrm{Re}_x^{-1/5} \tag{3.8}$$

where the Reynolds number based on the distance from the leading edge of the plate, $Re_x = \rho U_\infty x/\mu$. The wall shear stress and shear velocity can be estimated by

$$\tau_w = \frac{0.0288\,\rho\,U_\infty^2}{Re_x^{1/5}} \tag{3.9}$$

Table 3.4 shows the theoretical estimates of the boundary layer characteristics at various distances x from the channel inlet.

x (m)	Re_x	δ_{99} (mm)	τ_0 (N/m^2)	$u_\tau = \sqrt{\tau_0/\rho}$ (m/s)
1	4.50×10^5	27.39	0.4317	0.02078
1.4	6.30×10^5	35.85	0.4036	0.02009
2.1	9.45×10^5	49.58	0.3722	0.01921
2.5	1.13×10^5	57.00	0.3594	0.01896

TABLE 3.4: Theoretical estimates of boundary layer characteristics

At the intended measurement location x = 2.1m downstream of the channel inlet

$$y^+ = \frac{u_\tau\, y}{\nu} = 19210y \tag{3.10}$$

Assuming $y^+ = 5$, the laminar sublayer extends to 0.26mm from the wall, so with the available Myford traverse system with resolution 0.02mm per graduation, it should be theoretically possible to obtain over 10 measurement points within this region. This would enable us to fit the experimental data to the linear sublayer for the estimation of both the shear stress, $\tau_w = \mu(\partial u/\partial y)_{y=0}$ and shear velocity $u_\tau = \sqrt{\tau_w/\rho}$. In actual experiments, however, the number of measurement points achievable in the laminar sublayer region depended on the actual LDV data rate, and generally 5 points or less could be obtained for the higher speed flow of 0.45m/s, with more for low-speed flow.

Chapter 4

Commissioning and testing of Newcastle open-channel facility.

4.1 Introduction

Establishing the capability of the Newcastle open-channel experimental rig was vital prior to any detailed single/two-phase measurements. The rig itself had just been designed, commissioned and its operational characteristics and boundary layer profile were only vaguely known. This investigation was crucial to fine tuning the rig to meet measurement requirements. A brief descriptions of various stages of rig development has been outline earlier, in Chapter 3. In this Chapter, a detailed report of the experimental results is presented. The main purpose for testing the rig was firstly, to reduce the turbulence level in the free-stream down to acceptable level (i.e. lower than 1%), secondly, to achieve sufficient boundary layer thickness at the measurement position to enable accurate measurement with the instrumentation available, and thirdly, to investigate whether the flow channel exhibits comparable boundary layer and turbulence intensity profiles with available published data before any single and two-phase measurement can be carried out. Both particle image velocimetry and laser Doppler velocimetry techniques were employed for these purposes.

Initial investigations on the original 2m channel revealed that the boundary layer thickness was of the order of 15mm, 1.5m downstream of the inlet, and wake region was clearly absent in

the turbulent boundary layer profile. Turbulence intensity in the free-stream was of the order of 7%. Recognizing this situation, the rig has undergone five major modifications. These include:

1. increasing the channel length to 3 meters,
2. fitting a new inlet section featuring a hyperbolic tangent profile with approximately 3:1 contraction ratio, with a single honeycomb, three coarse and two fine gauzes,
3. addition of another two perforated plates to the original two in the inlet plenum tank, and
4. inserting a perforated plate immediately at channel exit to suppress low frequency unsteadiness.

Before going into more specific detail on the experimental test results, a brief summary on the rig development process is presented. Here, the reader is pointed to Chapter 3 for a more detailed description of the development process. After successfully commissioning of the new open-channel rig, it has undergone numerous testing and fine-tuning processes. The purpose of this Chapter is to characterize and document the new Newcastle open-channel rig. A detailed investigation was carried out and is broken down and presented below.

Firstly, the cause of the high turbulence level in the free-stream (e.g. at y=100mm) needed to be understood and this value had to be brought down to acceptable level (i.e. below 1%). Extensive experimental investigation was carried out to establish the best possible rig setup to deal with this problem.

Secondly it was necessary to determine the boundary layer thickness at the chosen measurement region, 2.1m downstream of the channel inlet. Initial LDV measurement reveal that the boundary layer thickness was of the order of 80mm, which was higher than our theoretical estimate. Investigation into the problem suggested that the possible cause of this high thickness was that the flow may have been tripped earlier in the flow prior to the zig-zag strip that was located 23mm downstream of the channel inlet. This was solved by smoothing all transition joints between perspex and plasticard, and between plasticard and glass surfaces with car body filler, which was then smoothed using emery. This technique successfully reduced the boundary layer thickness down to 50mm, in line with the theoretically expected value.

Thirdly, the effect of using the zig-zag strip as a boundary layer trip was investigated. A clear distinguishable difference can also be observed in the velocity profile with and without the use of zig-zag strip.

Next, the low frequency oscillation observed in the LDV signal was addressed. The undulation observed was attributed to a design flaw of the channel itself. The inlet and outlet plenum tank together with the open-channel behave like a u-tube, introducing a low-frequency signal into the free-stream region. This effect can be observed in the LDV velocity history data, as shown in Figure 3.12(a), and artificially increased the measured turbulence level. The cure for this was the fitting of a perforated plate at the exit plane of the channel. The effects of this on free stream turbulence can be seen in Table 4.1, whilst a detailed description is given in Section 4.6.

A shallow dip in the velocity profile at the outer edge of the wake region was observed. This was thought to be due to the relatively low aspect ratio (width/depth) of the channel, so experiments were carried out at various water depths. The observed results revealed that the velocity dip phenomenon disappeared at high aspect ratio, as reported in various published articles on open channel flow.

The bottom wall velocity profile was measured at a range of distances from the channel inlet, to verify the expected development of the floor boundary layer, and to observe the effect of varying Reynolds number Re_θ and Re_τ.

Finally, detailed measurements at the chosen standard measurement location, 2.1m downstream of the channel inlet are presented, and verified against comparable data from the literature.

4.2 Turbulence level in the free-stream of the open-channel experimental rig

Systematic testing was conducted to measure the turbulence level in the free stream at x= 2.1m, y = 100mm, using LDV, and the results are tabulated in Table 4.1. Setups 1 and 2 both used a simple inlet without screens or honeycomb. The presence of the two perforated plates as a

flow calming device in the inlet plenum tank had a significant effect in halving the free stream turbulence level from 12% to under 6%. Adding the honeycomb and 3 coarse screens upstream of the profiled inlet further reduced the turbulence level to just over 2%, whilst replacing the 3 coarse screens with two fine ones in setup 4 brought the level down to 1.89%. In setup 5 both the 3 coarse and two fine screens were combined, but the resulting drop in turbulence to 1.74% was relatively small. Since flow disturbances were still visible within the inlet plenum tank at this stage, and the existing perforated plate screens had a strong effect in reducing the turbulence, another two perforated plate screens were later added, together with a cylindrical "diffuser" constructed from a rolled up perforated plate, fitted to the inlet tank returned pipe. Whilst these combined measures reduced the free stream turbulence further, to 1.25%, more severe vibration could be observed originating from the inlet tank. This was attributed to the cylindrical diffuser, which was subsequently removed. Examination of the LDA time history plots showed that much of the remaining disturbance was due to a low frequency sinusoidal pulsation, rather than to random turbulence, and the low frequency suggested a form of "U-tube" oscillation between the two plenum tanks. The cure for this proved to be fitting a pressure drop screen at the outlet from the working section to the exit tank, with a 23% open perforated plate screen giving the best results. Setup 7 incorporated all the previous modifications, with the exception of the diffuser, plus the outlet screen. This final setup will be used for all future measurement purposes. The measured turbulence level is well below 1% and it is believed that the true level is even lower, as the LDV system used for these measurements operates in back-scatter mode, and is therefore expected to have a higher noise level compared to a forward scatter system. The far right three column data in Table 4.1 shows the effect of passing the velocity data through a low-pass filter to remove the high frequency noise from the back-scatter system. A 0.3Hz and 0.5Hz low-pass filter were used to show a significant reduction in the turbulence intensities.

Setup	Diffuser	Perf. Plate	HComb	Gauze		Turbulent intensity (%)		
				Coarse	Fine	Unfiltered	*0.3 Hz	*0.5 Hz
1	-	-	-	-	-	12.09	9.95	9.09
2	-	✓$_2$	-	-	-	5.71	4.71	4.34
3	-	✓$_2$	✓$_1$	✓$_3$	-	2.16	1.15	1.05
4	-	✓$_2$	✓$_1$	-	✓$_2$	1.89	0.99	0.92
5	-	✓$_2$	✓$_1$	✓$_3$	✓$_2$	1.74	0.73	0.67
6	✓$_1$	✓$_4$	✓$_1$	✓$_3$	✓$_2$	1.25	-	-
**7	-	✓$_4$	✓$_1$	✓$_3$	✓$_2$	0.86	-	-

TABLE 4.1: Plenum tank and channel inlet configuration. (** High-pass filtered data, ** With perforated plate at channel exit; subscript represents the number of items installed) Perf.Plate = Perforated plate in inlet plenum tank, HComb = Honeycomb

4.3 LDV measurement of velocity profiles and boundary layer thickness

Having addressed the issue of free stream turbulence level, the velocity profile at the target measurement region, 2.1m downstream of the inlet to the working section was studied. To do this the fibre optic LDV probe was mounted on a Myford vertical slide, and mounted on to the aluminium section instrumentation platform. This enabled the measurement volume to be manually traversed in the wall-normal y-direction with a resolution of 0.025mm. The total maximum traverse distance was 100mm.

For LDV measurement, it was theoretically possible to fit in at most 10 measurement points within the linear sublayer ($y^+ < 5$ corresponding to $y < 0.25$mm) with the available Myford traverse system. This enabled us to fit the experimental data to the linear sublayer for the estimation of both the wall shear stress, and the shear velocity. But first, the y- location of the bottom of the channel needed to be known, and this could easily be acquired by linear interpolating the assumed distance from the channel bottom to the exact zero position. For later particle image velocimetry measurements, the LDV data for the shear velocity, u_τ was used. This is done by taking LDV measurement for a few near wall points whenever particle image velocimetry measurement were carried out. Therefore, it is important to experimentally acquire enough data points within the linear sublayer for this purpose.

The Clauser chart (Clauser, 1956) method could alternatively be used to estimate u_τ by fitting the data to the log-layer profile. However, this technique assumes the existence of the universal logarithmic law. As a result, the use of this method to compute u_τ can result in an artificial collapse of the data onto the universal log-law.

The boundary layer thickness δ_{99}, was extracted from the mean velocity data. It is the value where the mean velocity is equal to 99% of the free-stream velocity. For a free-stream velocity of 0.45ms^{-1}, the boundary layer thickness was 50mm, slightly higher than our theoretical estimate of 47mm. Nevertheless, the boundary layer thickness was sufficient for our final purpose of two-phase flow investigation.

4.4 Effects of fine, coarse and perforated pressure drop screen (Back-plate)

To understand the effects of back-plate on the velocity profiles, LDV measurement were taken at for various porosities:

1. Without back-plate,
2. 25% porous perforated plate,
3. 45 % porous fine gauze, and
4. 60 % porous coarse gauze.

Experimental data revealed that the use of 25%perforated plate was most effective in reducing the low frequency undulation motion compared to using gauzes. It is interesting to note that although all the velocity profiles look very similar when plotted in Figure 4.1, the profile with no outlet obstruction deviates most significantly from the classical non-dimensional profile plotted in Figure 4.2, with the perforated plate giving the best agreement with the DNS data of Schlatter and Örlü (2010). The turbulence level in the free-stream is the lowest with perforated plate as can be clearly be seen in Figure 4.3. The free-stream turbulence intensity dropped

below 1 % and the boundary layer profile collapsed perfectly to the DNS data of (Schlatter and Örlü, 2010).

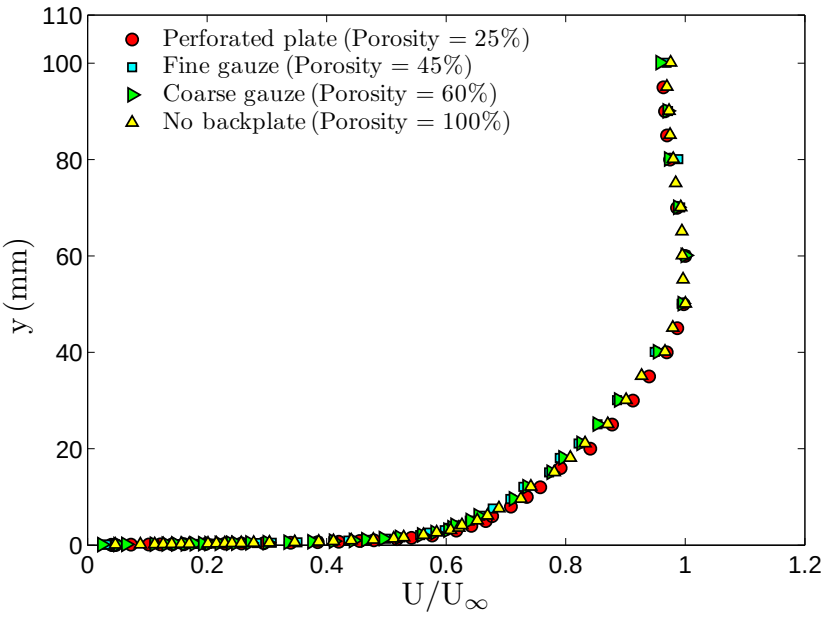

FIGURE 4.1: Mean velocity profile for various back-plate porosity level (perforated plate, 25%, fine gauze, 45 %, and coarse gauze, 60 % porous).

One concern was that the porous back-plate might introduce recirculation or other disturbances in the working section. However, PIV investigation revealed that the introduction of the perforated plate did not introduce any back flow to the system at 2100mm or further down the channel. A 60mm Nikon Micro-Nikkor lens was used to view a 100mm × 74mm region, that captured the whole boundary layer in the flow. 1000 double-frames view of the flow were captured and processed by adaptive correlation using a 32 × 32 pixel final interrogation window and 50 % overlap, giving approximately 15,000 vectors. The flow was seeded with 12ppm of 10 μm silver-coated hollow glass sphere (specific gravity = 1.4). The centre of the measurement region was located at 2115mm, 2215mm , 2315mm, 2415mm and 2515mm downstream of the boundary layer trip in a series of measurements, covering a total streamwise length of 500mm. Figure 4.5 shows the time averaged velocity profile along the channel at 2065mm up to 2565mm downstream of the channel inlet.

The time averaged velocity contours, based on an average over 1000 double frames show the expected gradual growth in boundary layer thickness, with no observable distortion due to

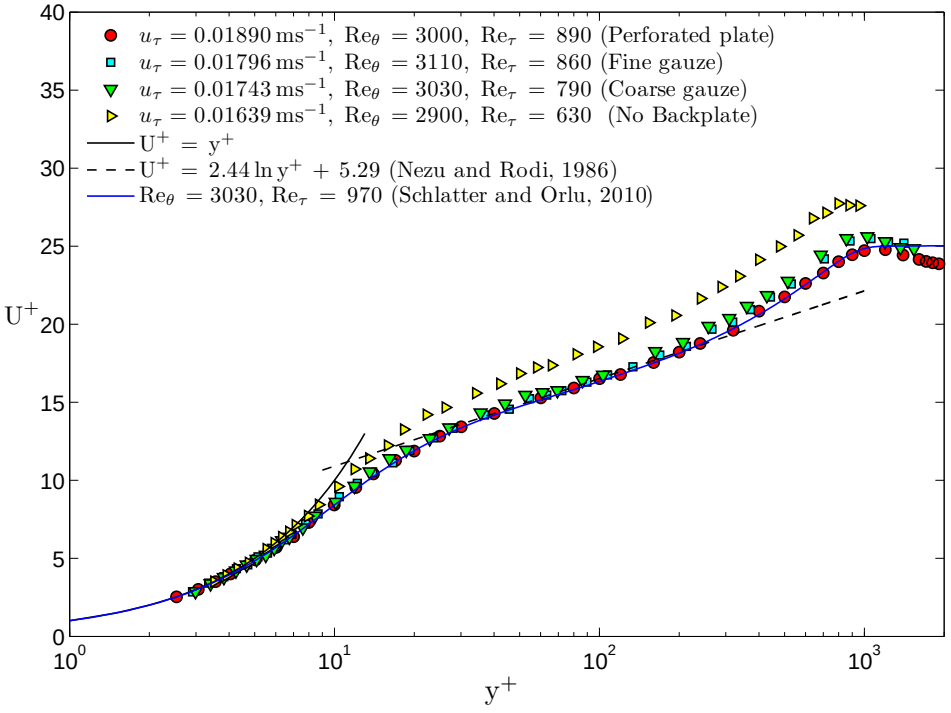

FIGURE 4.2: Dimensionless mean velocity in the Newcastle open-channel with various backplate porosity levels (Perforated plate, 25%, fine gauze, 45 %, and coarse gauze, 60 % porous).

the presence of the downstream porous plate.

Two-dimensional plot of the velocity profile along streamwise direction are presented in Figure 4.5 downstream of the measurement position. The figure shows that the velocity profile along the field of view behaves similarly but the boundary layer thickness increases, showing that the boundary layer is still developing along the channel up to the channel exit position.

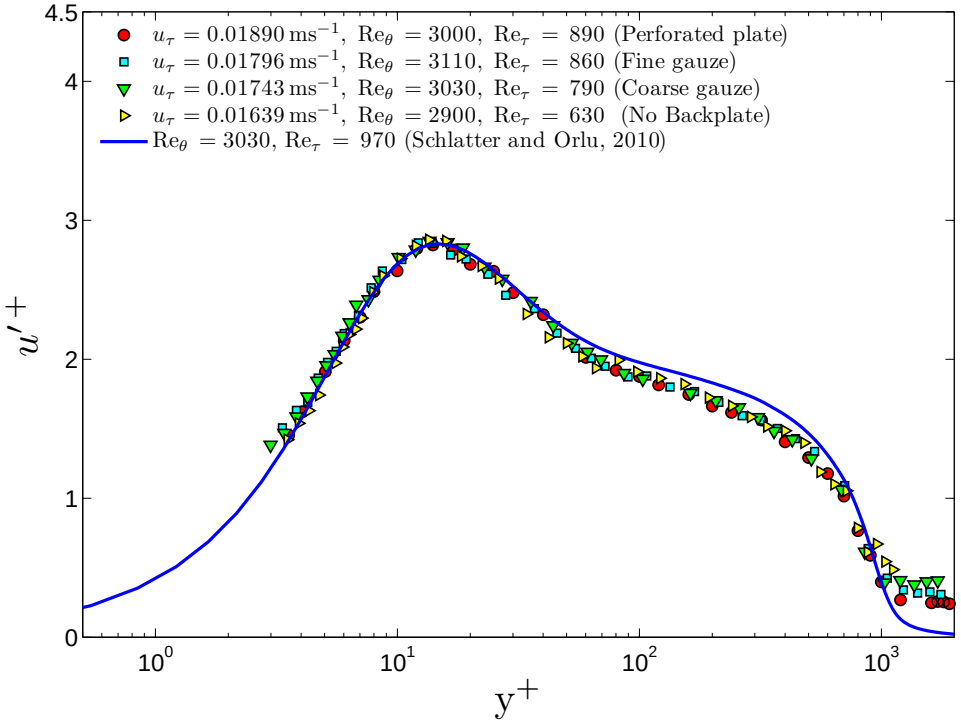

FIGURE 4.3: Turbulence intensity u'/u_τ for various level of back-plate porosity (Perforated plate, 25%, fine gauze, 45 %, and coarse gauze, 60 % porous).

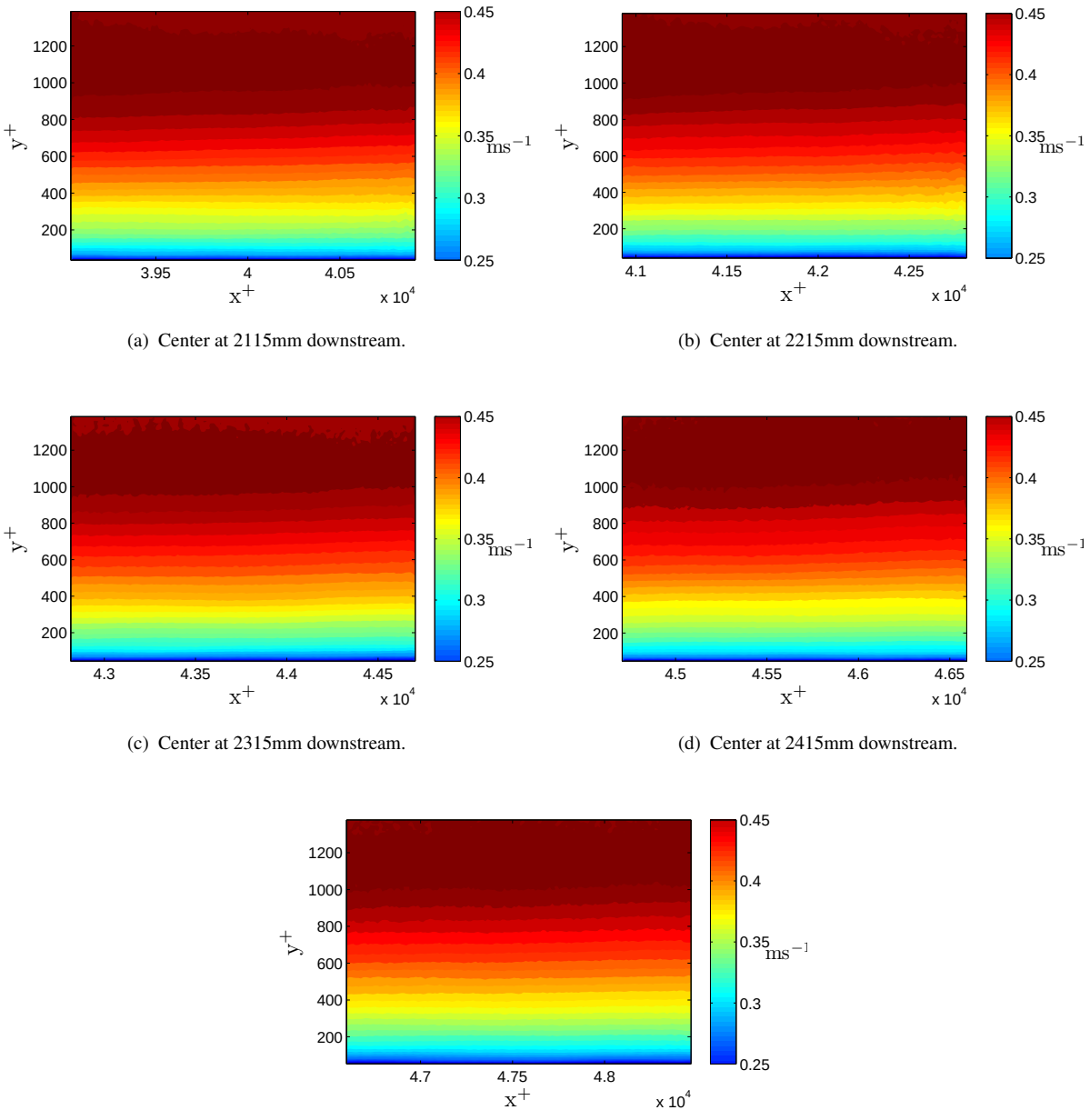

(a) Center at 2115mm downstream.

(b) Center at 2215mm downstream.

(c) Center at 2315mm downstream.

(d) Center at 2415mm downstream.

(e) Center at 2515mm downstream.

FIGURE 4.4: PIV time-averaged velocity contour plots along the channel from 2115mm up to 2515mm.

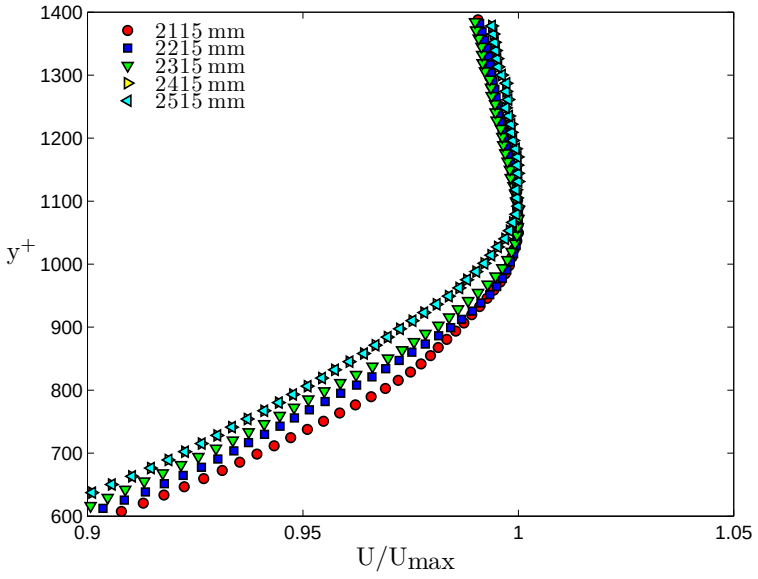

FIGURE 4.5: Time-averaged velocity profile plotted at central position of frames in Figure 4.4, i.e. 2115mm, 2215mm, 2315mm, 2415mm and at 2545mm.

4.5 Effects of zig-zag strip on the boundary layer profile and thickness

The zig-zag strip used in the present experiments is schematically shown in Figure 3.13 and has been explained in greater detail in Chapter 3, Section 3.1.4. The effect of the zig-zag strip was investigated using particle image velocimetry. Measurements were taken at 2100mm downstream of the channel inlet, and the 2mm zig-zag strip, when present, was placed with its centreline 23mm downstream of the channel inlet.

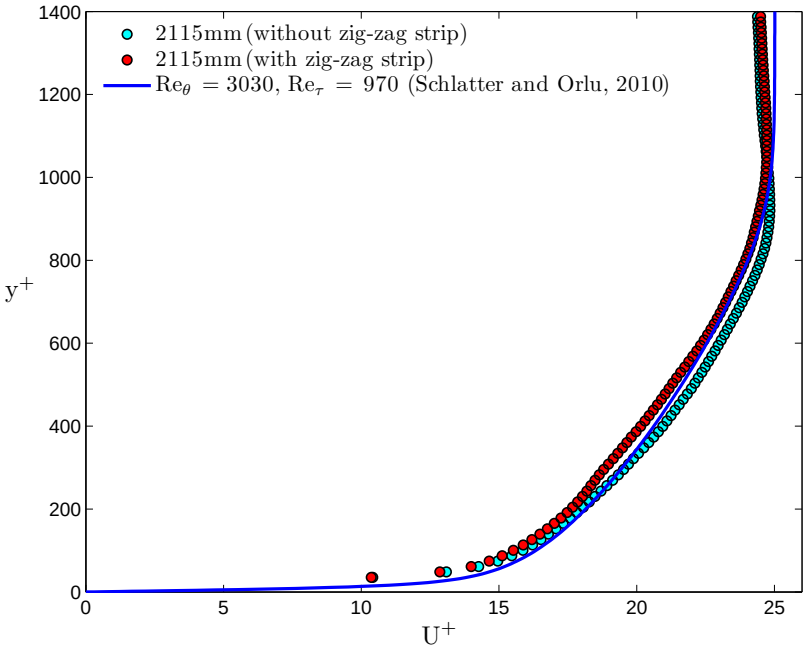

FIGURE 4.6: Time-averaged velocity profile at 2115mm with and without zig-zag tripping device.

Figure 4.6 and fig:BLP 2075mmv shows the velocity profile at 2115mm downstream of the leading edge. The data presented are plotted based on the average value at 2115mm only. The velocity profile with the zig-zag strip in place collapse well with the data of Schlatter and Örlü (2010) within y^+ = 600 and 1100. For all y^+ above 1000 a significant lag can be observed due to the velocity dip-phenomenon. Below $y^+ = 600$, a lag in the velocity profile can be observed. In the outer region of the boundary layer the effect of the zig-zag strip is to move the mean velocity profile closer to the DNS profile of Schlatter and Örlü (2010) at similar Re_τ.

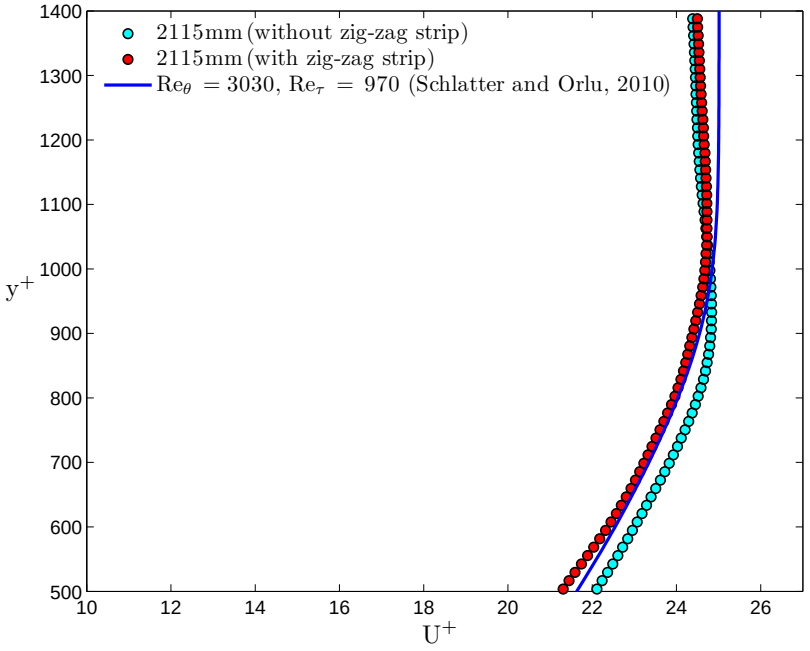

FIGURE 4.7: Time-averaged velocity profile at 2115mm with and without tripping device - magnified view.

From Figure 4.6 and 4.7 it can be clearly seen that the zig-zag strip does increases the boundary layer thickness and changes the velocity profile significantly.

4.6 Velocity dip phenomenon

One clearly distinguishable phenomenon in all the LDV profiles was the dip in the velocity profile after the wake region. The literature suggests that this behaviour occurs when the aspect ratio, AR, of the flow channel is less than 5 or when measuring near the side-wall.

The Newcastle open-channel maximum flow area is 325mm by 200mm. At full flow height, the aspect ratio is 1.63 and all measurement taken at this flow height would therefore be expected to exhibit this dip phenomenon. To investigate this, the flow height was reduced down to 60mm giving an aspect ratio of 5.42. This is still above the expected boundary layer thickness, δ estimated to be 50mm. Profiles were taken within the logarithmic region up to the free-stream to test the suggested theory in the literature. The LDV profiles, shown with a shifted origin in Figure 4.6 to highlight the wake region, showed clearly that the channel aspect ratio does play an important role and the velocity dip disappears at higher aspect ratio.

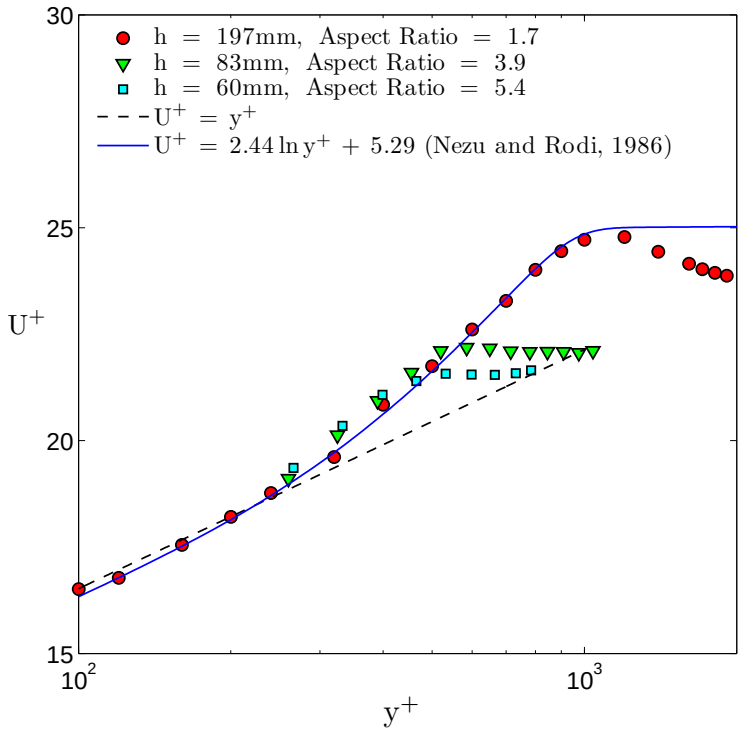

FIGURE 4.8: Effect of the channel aspect ratio on the wake region of the boundary layer profile plotted against the data of (Nezu and Rodi, 1986).

It is important to note that, although the slight dip in velocity in the free stream looks disconcerting, all other data taken within the boundary layer have been demonstrated to show canonical behaviour. It should also be noted that, because of limitations of the channel rig in varying depth and flow velocity independently, it was not possible to maintain a constant Reynolds number. The reduction in the maximum free stream U^+ value with reducing depth, evident in the figure, is a result of the falling Reynolds number, rather than an aspect ratio effect.

4.7 Effect of Reynolds number

LDV experiments were performed at three measurement positions along the channel. These were at 0.5m, 1.2m and 2.1m downstream of the inlet edge. The inlet section comprised a honeycomb, 3 coarse gauzes and 2 fine gauzes. Immediately after the channel inlet, a 2mm thick zig-zag strip was secured 23mm downstream. These experiments were carried out with a free-stream velocity of 0.45m/s and a Froude number of 0.32. From Figure 4.9 to 4.11, it can be seen that the agreement with Schlatter and Örlü (2010) for Re_θ values around 2000 and 3000 is very good. Single low Reynolds number test without tripping device shows agreement with theoretical laminar velocity profile.

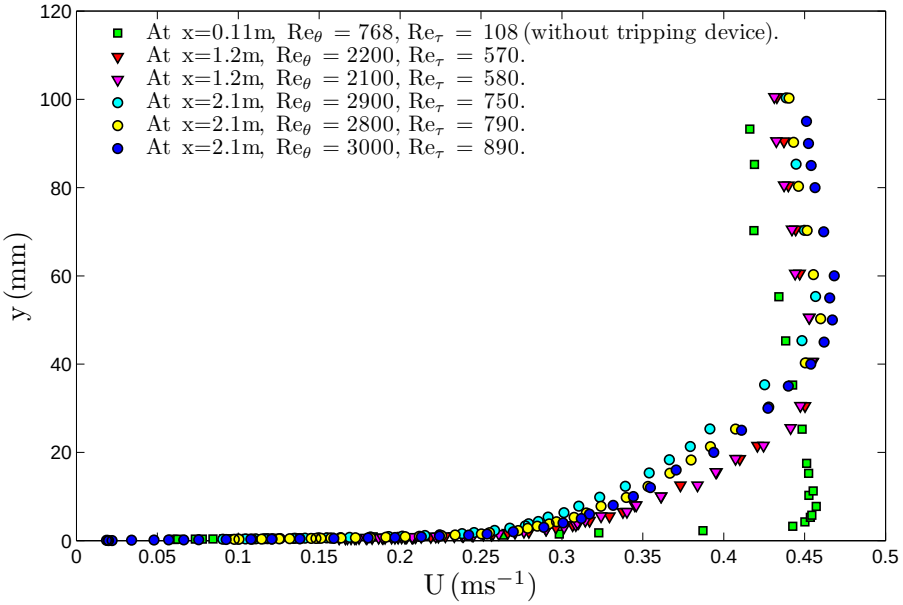

FIGURE 4.9: Velocity profile at 0.11m, 1.2m and 2.1m corresponding to x^+ = 9450, 22680 and 39690.

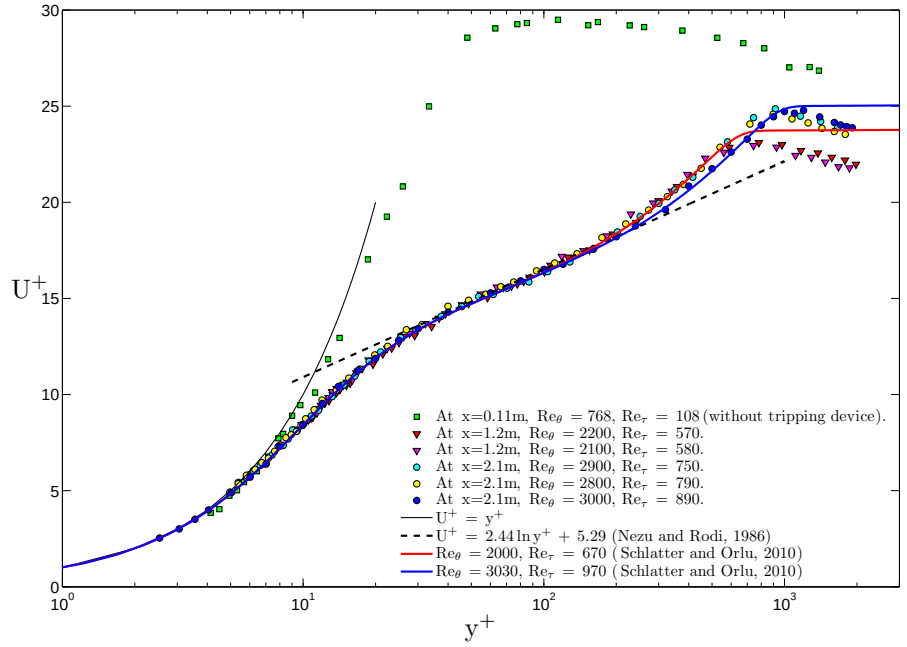

FIGURE 4.10: Boundary layer profile at 0.11m, 1.2m and 2.1m corresponding to x^+ = 9450, 22680 and 39690.

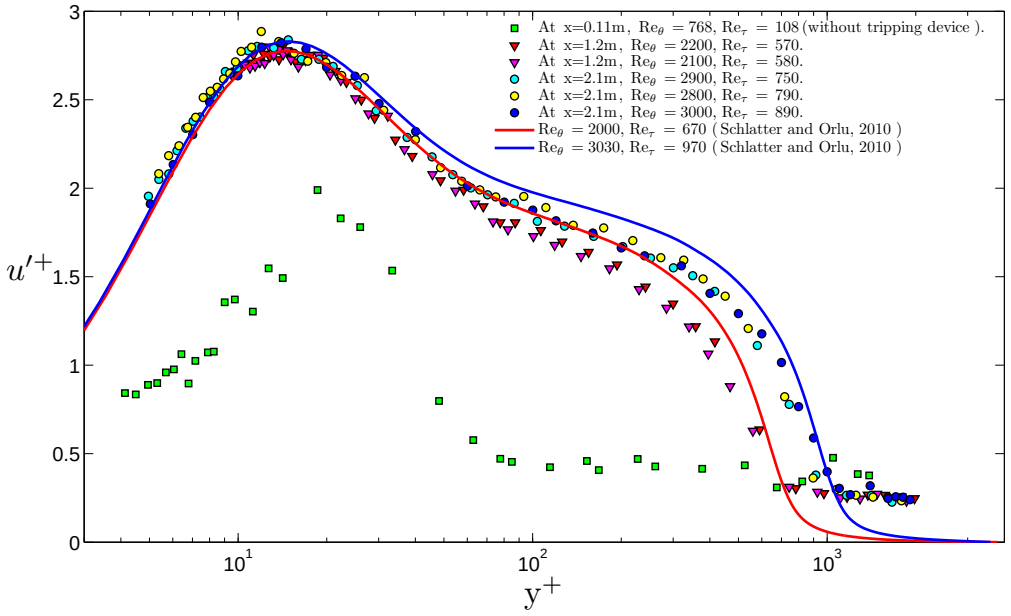

FIGURE 4.11: Turbulence profile at 0.11m, 1.2m and 2.1m corresponding to x^+ = 9450, 22680 and 39690.

4.8 Comparison of LDV and PIV measurements

Comparing the profiles between LDV and PIV gives a clear indication of the characteristics of the Newcastle channel. Direct comparisons of profiles were plotted and these are the plots of U^+ vs. y^+ and $u'^+ u'^+$ vs. y^+. The results indicate that the results are in good agreement between the two measurement techniques (i.e. PIV and LDV). These are also compared to DNS at similar Reynolds numbers.

Figure 4.12 and 4.13 are LDV profiles plotted for the Newcastle open-channel where a tripping device (zig-zag strip) was located 23mm downstream of the channel inlet. A clear agreement can be observed in comparison to DNS of Schlatter (2010) at similar Reynolds number. Nevertheless, between the region of $y^+ = 40$ up to 800, there is a slight reduction in u'^+. This slight deviation was observed in all of our LDV measurements. In the case of PIV, this disagreement was insignificant if compared to LDV which may point out to a possible LDV instrument's lack of accuracy given the age and the back-scatter system technique it employs.

The accuracy and resolution should be better with LDA, but this technique shows only point or profile data, whereas PIV provide 2D field data. Nevertheless, comparison of profile along channel between PIV and LDV will used as a benchmark for the accuracy of the PIV systems.

Next, the LDV data were compared directly with those of PIV and DNS to investigate if there are any significant deviations. Dimensionless semi-log velocity profile plots show excellent agreement between Newcastle LDV and DNS of Schlatter and Örlü (2010). Turbulence profile is also in very good agreement, the only significant deviation from Orlu and Schlatter's DNS data being the slightly lower values around $y^+ = 100$. Comparing the PIV and LDV measurements, velocity profiles of Figures 4.14, 4.15, and 4.16 agree to within plotting accuracy, though the PIV range is limited by the field of view at the outer region, and by achievable resolution close to the wall. Figure 4.16 reveals a more significant difference in the u' turbulence measurements, with LDV measurements being slightly lower than the DNS values in the $y^+ = 100$ region, as previously noted, whilst the PIV results were higher than DNS by a similar amount. The level of agreement between the PIV and LDV turbulence intensity profile can be considered to be acceptable. It can thus be concluded that, the general level of agreement gave good confidence in the rig and measurement techniques.

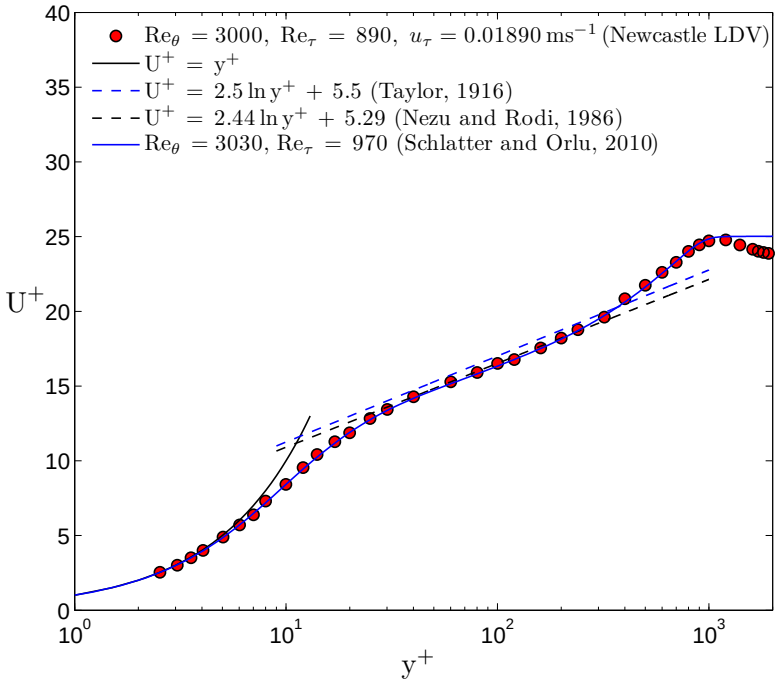

FIGURE 4.12: Boundary layer profile at 2075mm downstream of zig-zag strip (Newcastle LDV data).

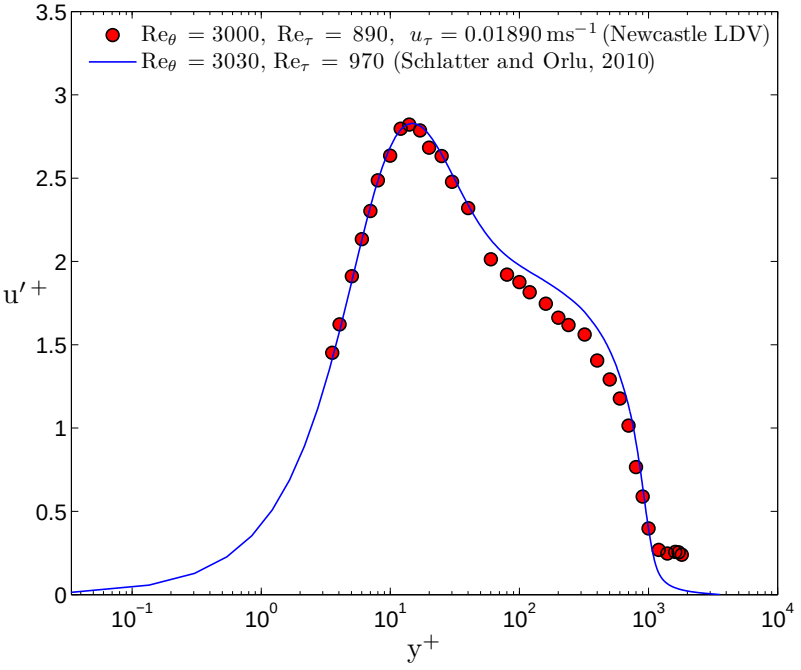

FIGURE 4.13: Turbulence intensity profile at 2075mm downstream of zig-zag strip (Newcastle LDV data).

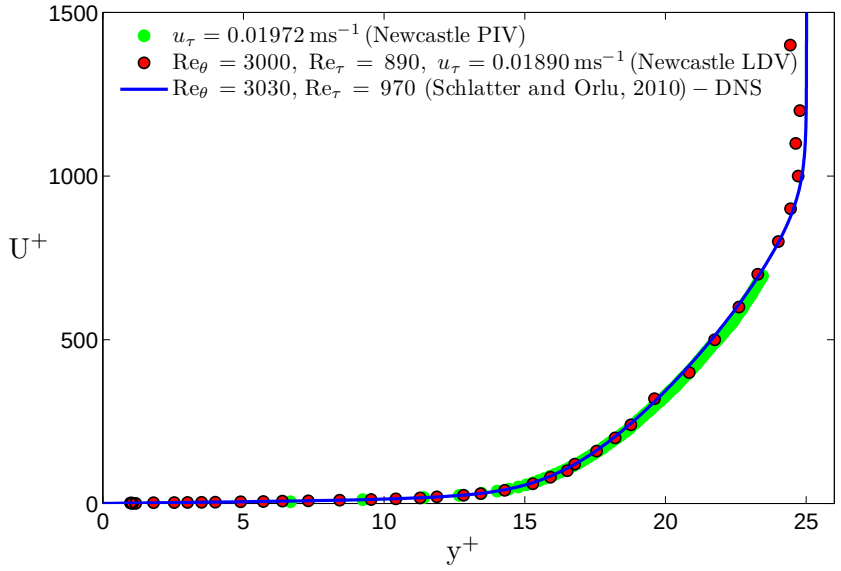

FIGURE 4.14: Velocity profile at 2075mm downstream of zig-zag strip (Newcastle LDV data).

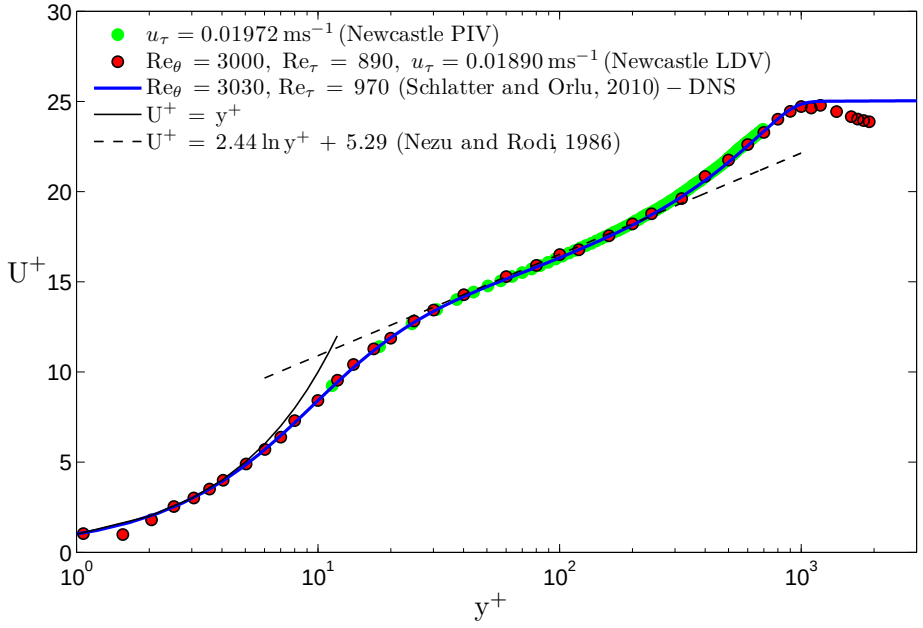

FIGURE 4.15: Turbulence profile at 2075mm downstream of zig-zag strip (Newcastle LDV data).

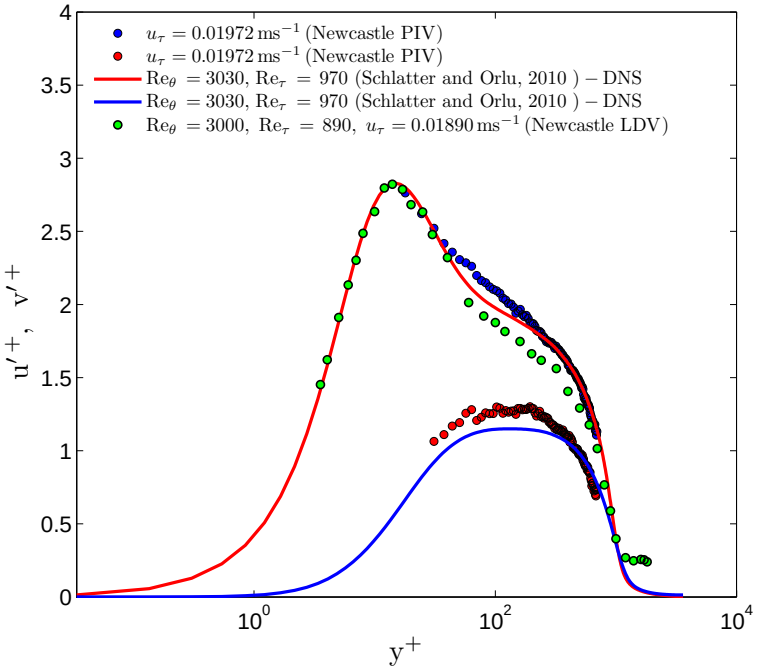

FIGURE 4.16: Turbulence profile at 2075mm downstream of zig-zag strip (Newcastle LDV data).

4.8.1 Spectra

The power spectrum plot indicates the required frame rate for PIV measurement to ensure the flow is captured at the correct frequency. The plot presented in this thesis were calculated using the Flow Sizer built-in power spectrum analysis algorithm.

Since LDV relies on seeding particles to obtain velocity data, samples can only be taken when particles passes the measurement volume. Assuming randomly distributed particles throughout the flow, the time between samples are non-uniform. This non-uniform time between samples prevent the use of standard spectral estimates. The standard methods rely on the fast Fourier transform (FFT) because the speed at which it can compute the spectral estimates. However, the FFT does not apply to randomly sampled data.

The Flow Sizer employs the slotted correlation method that provide an initial estimation of the auto-correlation function of the raw data, and secondly to use this data to generate an auto-correlation function having random values of the time delay. The auto-correlation values are then computed for equally spaced time delay. Fourier transform of this provides the power spectrum values. For more detail on the technique the reader is directed to the paper of Bell (1986).

To perform spectral analysis, the LDV provides a set of data that consist of a sequences of discrete velocity measurement $x(t_j)$ taken at times t_j. The estimate of the auto-correlation function is given by

$$R_{XX}(k) = \frac{1}{N(k)} \sum_{i=1}^{N_T} x(t_i) \sum_{j} x\left(t_i + \Delta\tau + t'_j\right) \tag{4.1}$$

where $N(k)$ is the number of lagged products in the k_{th} time slot, k is the time lag at the center of the slot with $\Delta\tau$, and t'_j is a random variable such that $-\Delta\tau/2 < t'_j < \Delta\tau/2$. The variable t'_j accounts for the random distribution of points over the lagged time slots.

The spectra shown in Figure 4.17 up to 4.20 are extracted from the LDV data at various height at the 2.1m downstream of the channel inlet. The log-log plots show expected roll-off. The maximum frequency at which the roll-off flattens out into general noise, reduces with

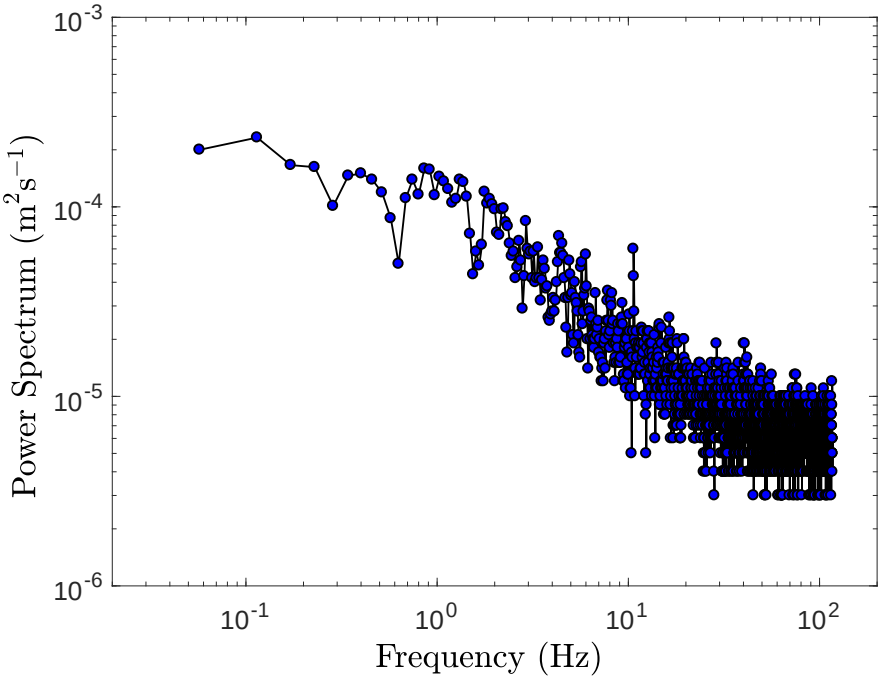

FIGURE 4.17: Spectra at y ≈ 10mm at x = 2.1m downstream of channel inlet.

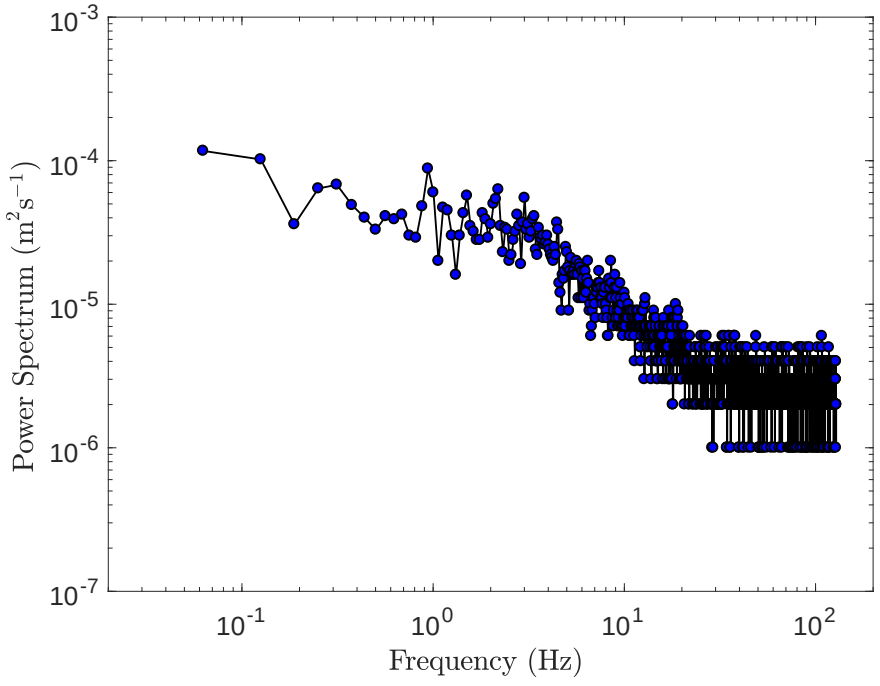

FIGURE 4.18: Spectra at y ≈ 30mm at x = 2.1m downstream of channel inlet.

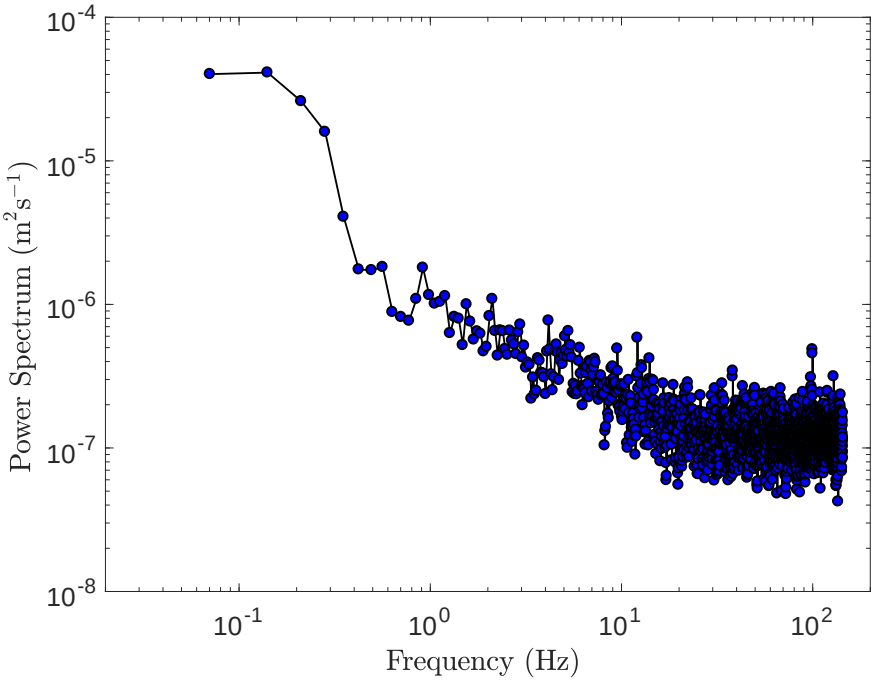

FIGURE 4.19: Spectra at y ≈ 60mm at x = 2.1m downstream of channel inlet.

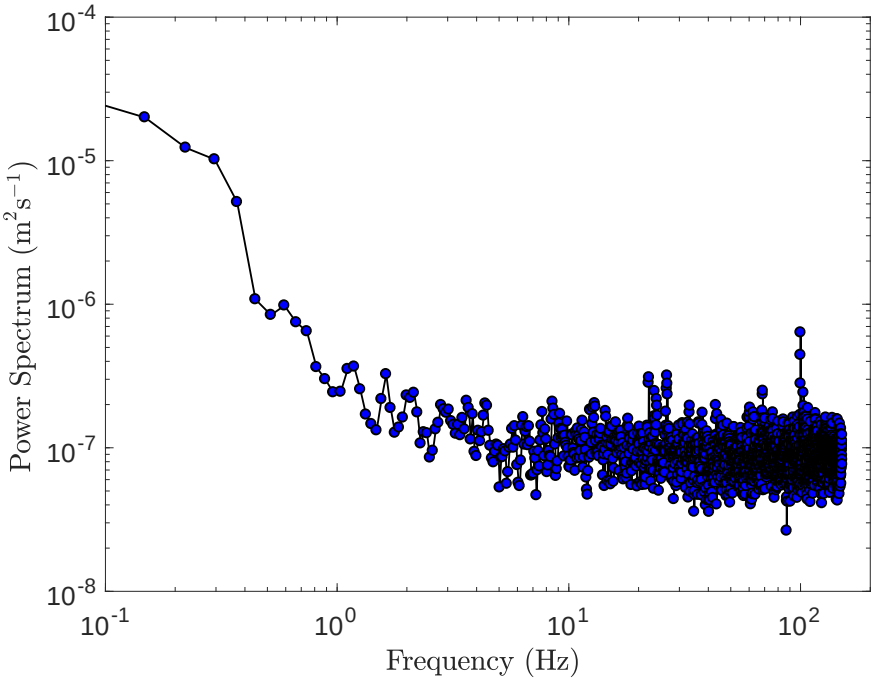

FIGURE 4.20: Spectra at y ≈ 95mm at x = 2.1m downstream of channel inlet.

distance from the wall, as expected with increasing eddy size. Even quite close to the wall (y = 10mm) the maximum frequency is around 100Hz. The proposed TRPIV sampling rate of 500Hz comfortably exceeds the Nyquist criterion for accurate time resolution of the turbulence fluctuations.

4.9 Mean and turbulence statistics of the flow in the channel

Prior to PIV measurements for the three Reynolds number; LDV measurements were carried out at 2.1m downstream of the channel inlet for the estimation of the shear velocity, u_τ. This shear velocity will be used as the first estimate. For PIV measurements, the Clauser method will be used to determine the shear velocity with reference to the LDV estimate. As the captured FOC includes the channel bottom; vectors within this area (i.e. the channel bottom) were masked and the wall distance interpolated to zero.

From Figure 4.21 to 4.23 it can be seen that at all three Reynolds numbers, both the mean and turbulence statistics profiles behave very well. At low Reynolds numbers (i.e. Re_θ = 730), the turbulence intensity in the free-stream is of the order of 1.7%. At all Reynolds numbers the LDV data collapsed well within the linear sublayer and logarithmic layer. Nevertheless, the velocity dip of the wake region is still evident and this has been attributed to the aspect ratio of the channel which is 1.7 (i.e. channel width / flow height).

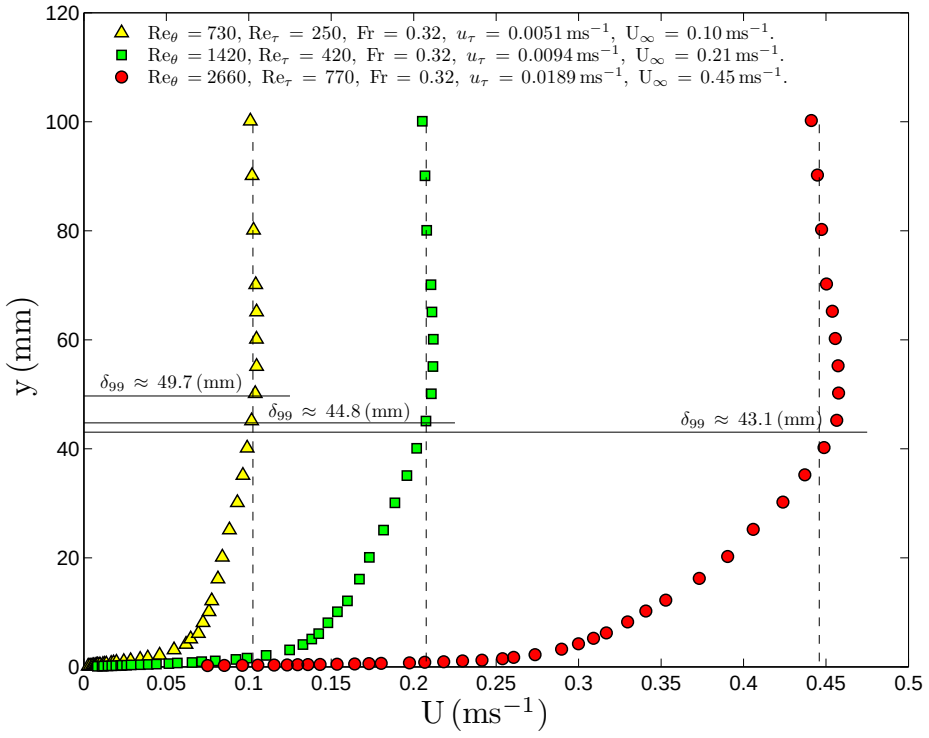

FIGURE 4.21: LDV Velocity profile at 2075mm downstream of zig-zag strip without inertial particles.

The rms velocity fluctuation profile also agrees well with the profile of Schlatter (2010) at Re_θ = 2000, but since our Reynolds number based on momentum thickness is slightly higher, a clear distinction can be observed in Figure 4.22, which indicates that the newly built channel turbulence profile can be considered as acceptable.

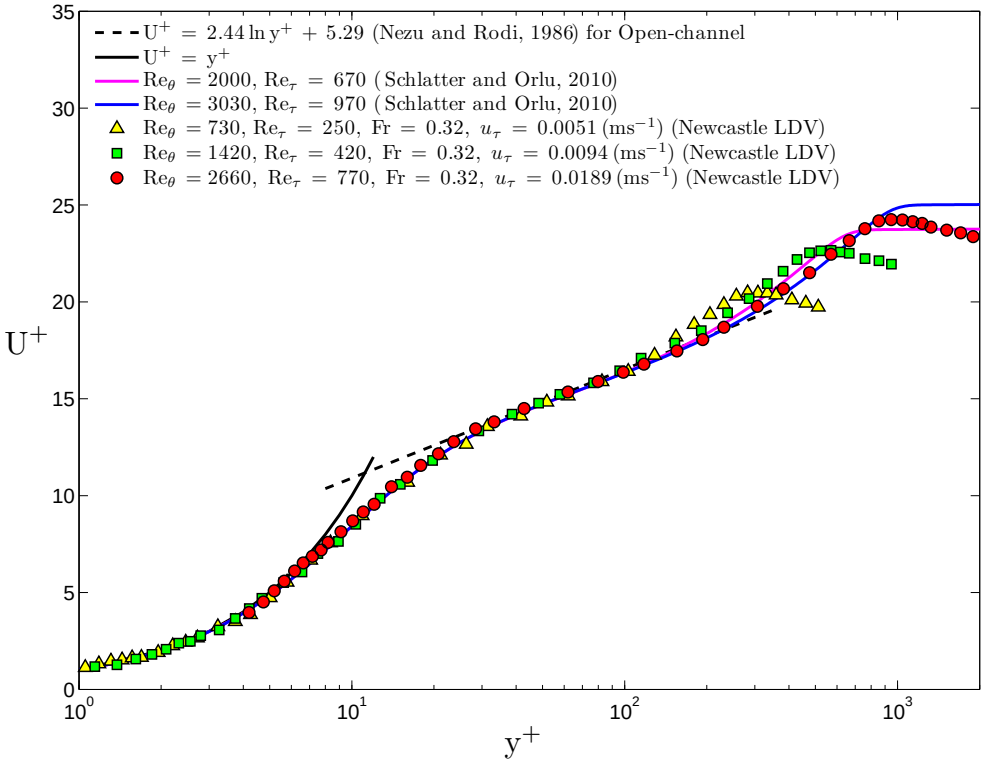

FIGURE 4.22: LDV Boundary layer profile at 2075mm downstream of zig-zag strip without inertial particles.

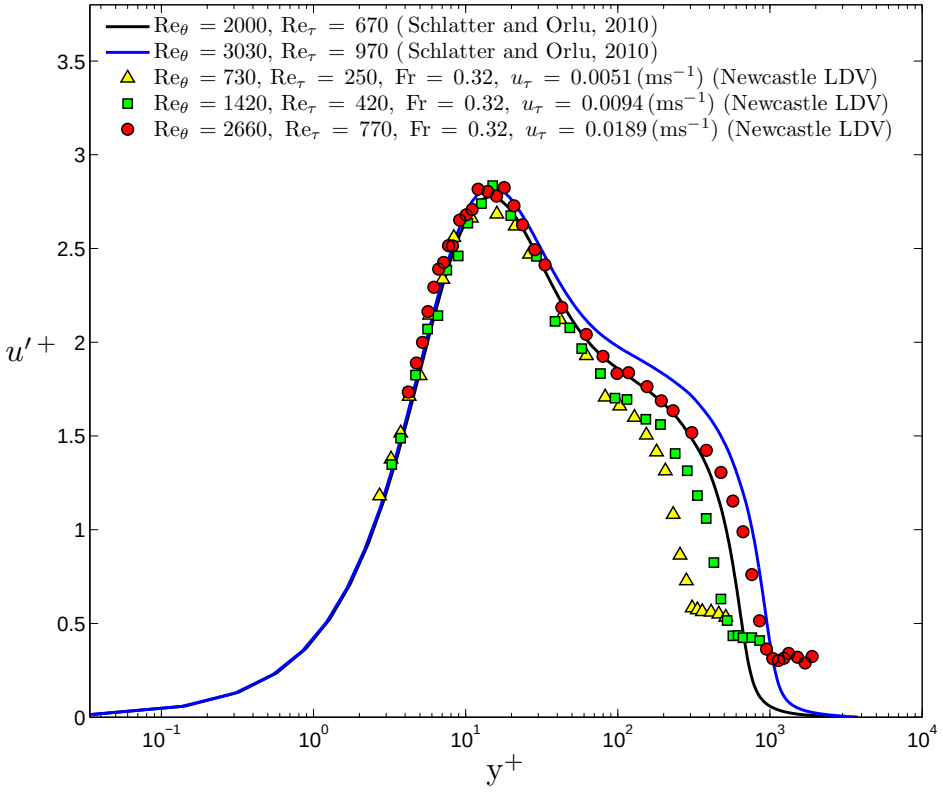

FIGURE 4.23: LDV turbulence intensity profile at 2075mm downstream of zig-zag strip without inertial particles.

Next, PIV measurements are compared to that of the LDV measurements at the same Reynolds numbers. boundary layer profiles as depicted in Figure 4.24, show similar behaviour. PIV data agree well with LDA data as expected, showing that the PIV measurments is sufficiently reliable for the measurement of flow properties.

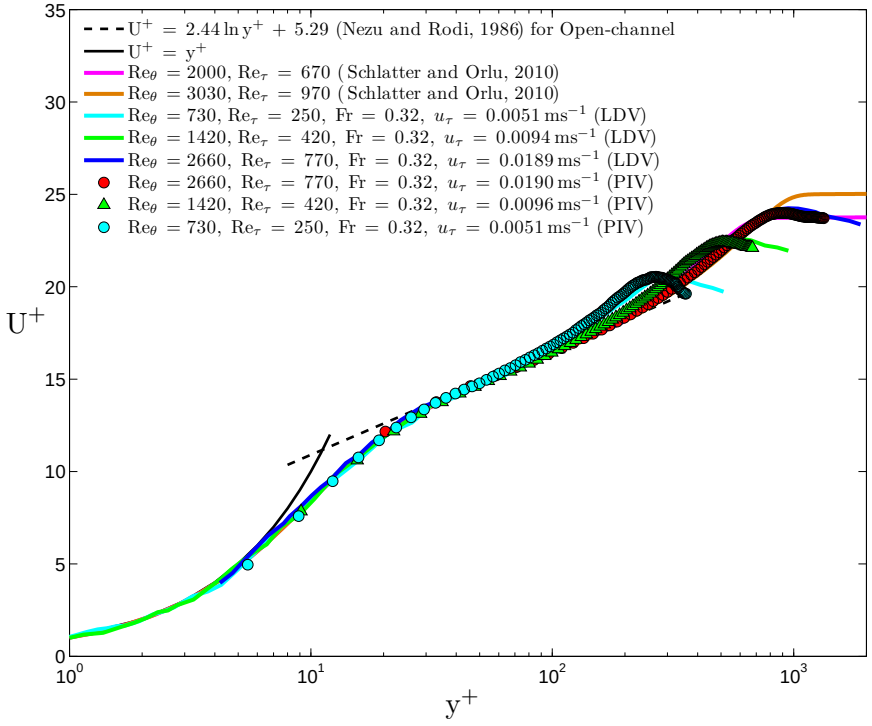

FIGURE 4.24: Velocity profiles at Re = 730, 1420, and 2660 for LDV and PIV.

The flow were seeded with 10μm silver-coated hollow glass spheres as flow tracers and measurements were taken at various Reynolds numbers (Re_θ = 730, 1420 and 2660).

Extended development of the rig has produced a facility which provides a canonical wall boundary layer of sufficient quality to proceed to meaningful 2-phase measurement. Extensive and thorough testing has confirmed both the quality of the flow and the capability of the TRPIV measurement equipment and technique. Further investigations were carried out and examples of various plots such as those for the Q-criterion, swirling strength, time averaged velocity profiles, velocity fluctuations and Galilean decomposition velocity following the work of Adrian are presented.

The time average velocity profile indicates normal behavior as shown in Figure 4.25. The data in the plot were time-averaged across 2000 instantaneous double-frames images. The particle images were subtracted from the original two-phase images and processed using Dantec Dynamic cross-correlation algorithm. The averaged number of bad vectors are on average less than 3.6%. The horizontal displacement of the seeding particles is shown in Figure 4.26. The maximum velocity is 0.45m/s which is approximately 6 to 7 pixels. This is just below the one-quarter rule with cell size of 32 pixels by 32 pixels. Pixel-locking characteristic, where pixel movement is biased towards integer value is clearly absent in Figure 4.26(b).

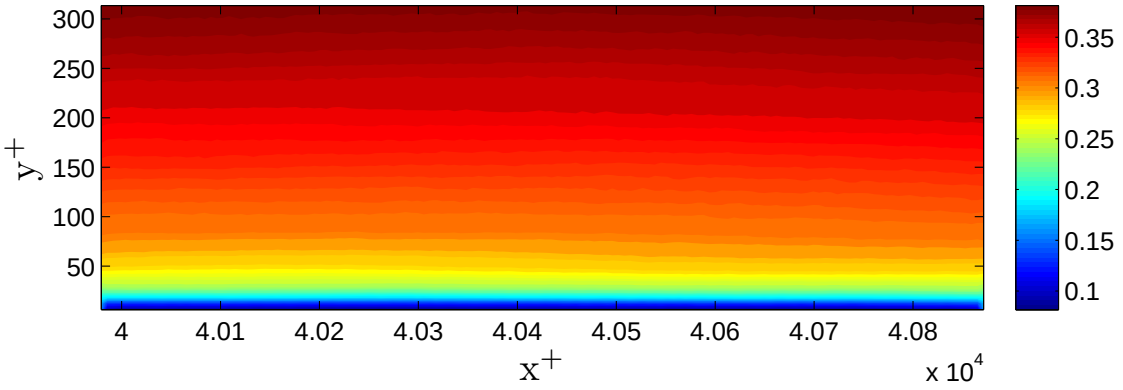

FIGURE 4.25: Time average velocity profile from the PIV measurements. Colorbar in m/s.

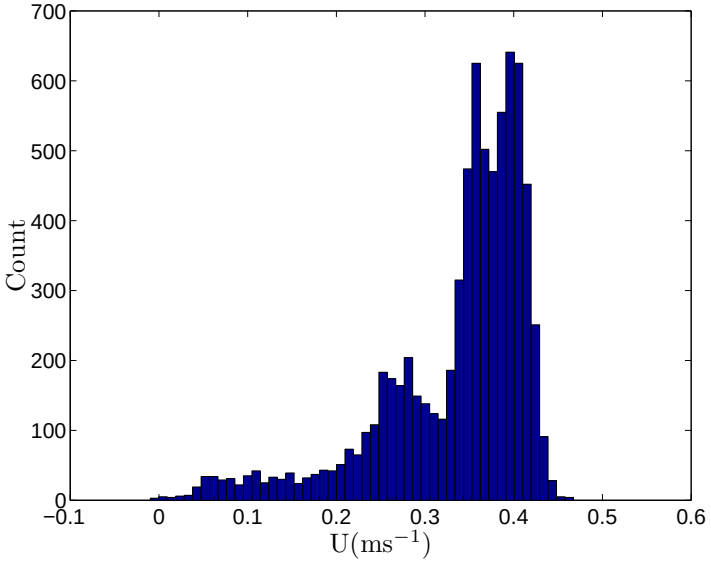

(a) Velocity histogram plot (in m/s)

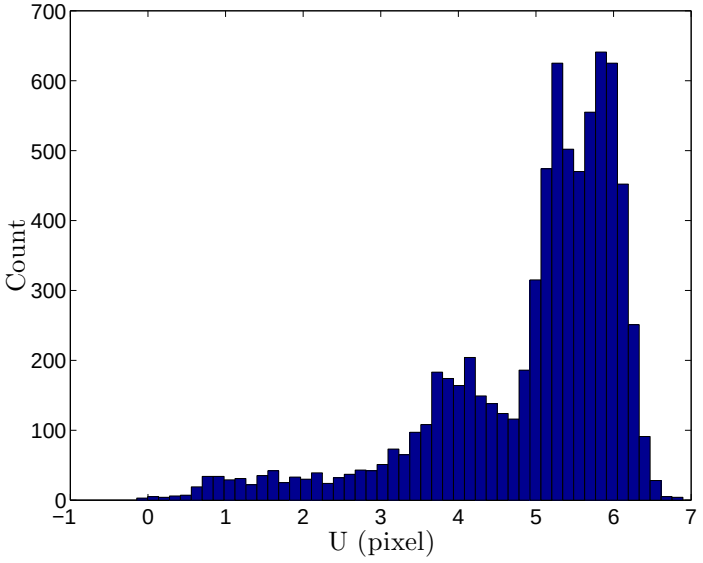

(b) Velocity histogram plot (in pixels)

FIGURE 4.26: Velocity histogram plot (in m/s and pixels).

4.9.1 Two-dimensional visualization of PIV data

Figure 4.27 shows the ramp-like structure as suggested by (Adrian, Meinhart and Tomkins, 2000) indicating the presence of hairpin packets.

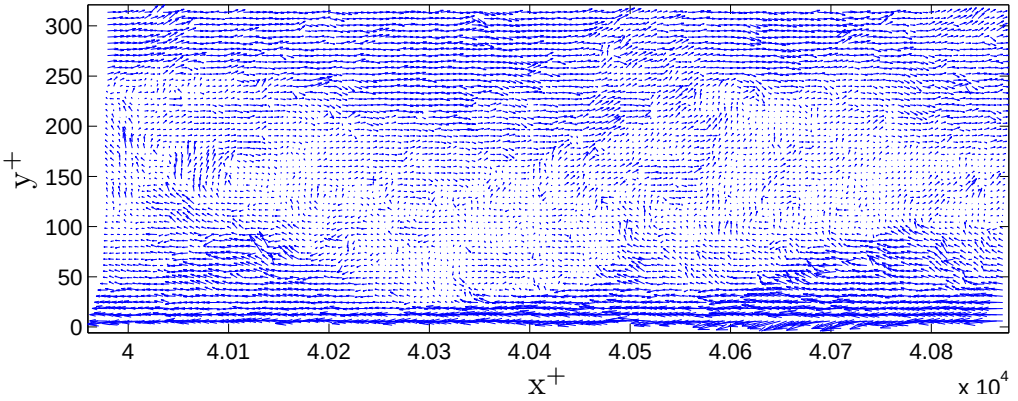

FIGURE 4.27: Galilean decomposed revealing ramp like structures close to the wall following Adrian, Meinhart and Tomkins (2000).

This clearly indicates that the flow within the newly built open-channel are generating hairpins which is important before proceeding to two-phase measurements. To further visualize the presence of structures within the boundary layer, further plots were made. Figure 4.27 and 4.28(b) show the velocity fluctuations profile that indicates the presence of ramp-like structure close to the wall. Swirling strength, Q-criterion and vorticity plot of the same data is presented in Figure 4.29(a) up to 4.29(c) showing presence vortices close to the channel floor. The two-dimensional visualization techniques (i.e. the calculation of vorticity, swirling strength and Q-criterion) were coded into MATLAB and a brief descriptions of its implementation is describe below and in Section 2.3.1.

The gradient of the velocity in the streamwise and wall-normal direction were calculated using Equation 2.9 and 2.10 which is a filtered second-order difference scheme (Westerweel, 1993) that are expected to attenuate the noise in the velocity data and to retain the velocity signals as an alternative to the unfiltered second-order difference scheme (Equation 2.8) that can amplify the noise in the measured velocity data. This technique was applied to all data positioned in the central region of the field-of-view, and for wall vectors, the backward and forward difference scheme were applied.

Once the velocity gradients in the wall-normal and streamwise directions has been determined, Equation 2.7 were used to compute the two-dimensional vorticity value, Equation 2.12 for the swirling strength, λ_{ci}, and Equation 2.15 for the two-dimensional Q-criterion. These data were then visualized using the iso-surface function available in MATLAB.

The swirling strength profile plot shown in Figure 4.29(a) and in the velocity plot in Figure 4.30(a) and 4.30(b) clearly shows vortices incline at approximately 20° which is attributed to hairpin vortices, comparable to the work of Van Hout (2011) with 17.5°. Figure 4.31(a) up to Figure 4.31(c) illustrate the vortical head of an hairpin centered approximately at x^+=4.042 × 10^4, y^+=100, at x^+=4.056 × 10^4, y^+=100, and at x^+=4.066 × 10^4, y^+=100. The Q-criterion profile plot as shown in Figure 4.29(b) shows rotational area along the 20° inclination that may be related to packets of hairpins and the vorticity plot shown in Figure 4.29(c) were only able to show vortical structure but without the presence of clear vortices. Regions having constant velocity momentum can be observed from the velocity profile plots from Figure 4.30(a) up to Figure 4.32(b), and also in Figure 4.33.

The experimental data indicate the presence of a hairpin vortex, a simple structure that explains many of the observed features of wall turbulence (e.g. Theodorsen, 1952; Head and Bandyopadhyay, 1981; Adrian, Meinhart and Tomkins, 2000). The induced ejection (Quadrant 2) and sweep events (Quadrant 4) by the hairpin vortex, will thus be expected to transport particle upwards or downward towards the wall.

Figures 4.30(a) up to 4.31(a), and 4.31(b) up to 4.32(b) illustrate the velocity profile showing the propagation of coherent structures at the proposed measurement position which is 2.1m downstream of the channel inlet. Located left of the FOV, propagating along the channel (dark blue region) as shown in Figure 4.30, ramp-like structure can be observed. The structures observed in the plots is believed to be hairpins vortices. In Figure 4.30 alone, three ramp-like structures are present indicating that it is a common feature in boundary layer as suggested in the literature such as Adrian and others. Regions of momentum zones can clearly be seen across the velocity profile plot in Figure 4.30 up to 4.32 and Figure 4.33.

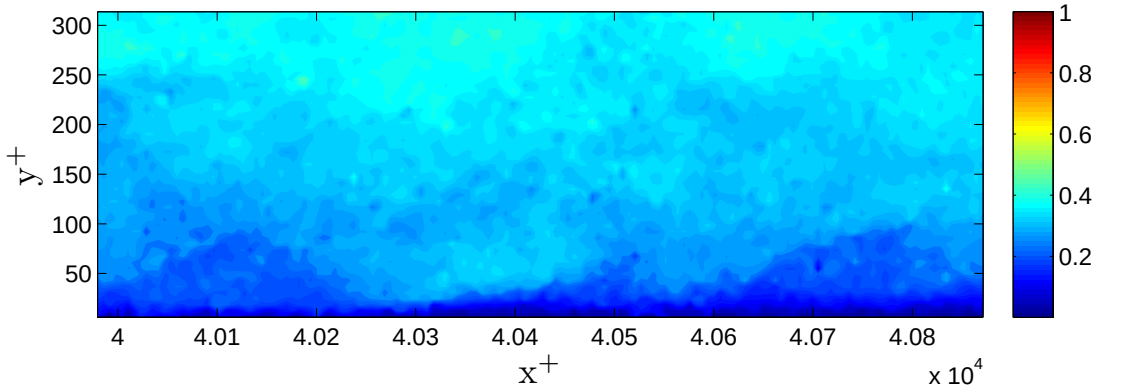

(a) Velocity profile plot. Colorbar in m/s.

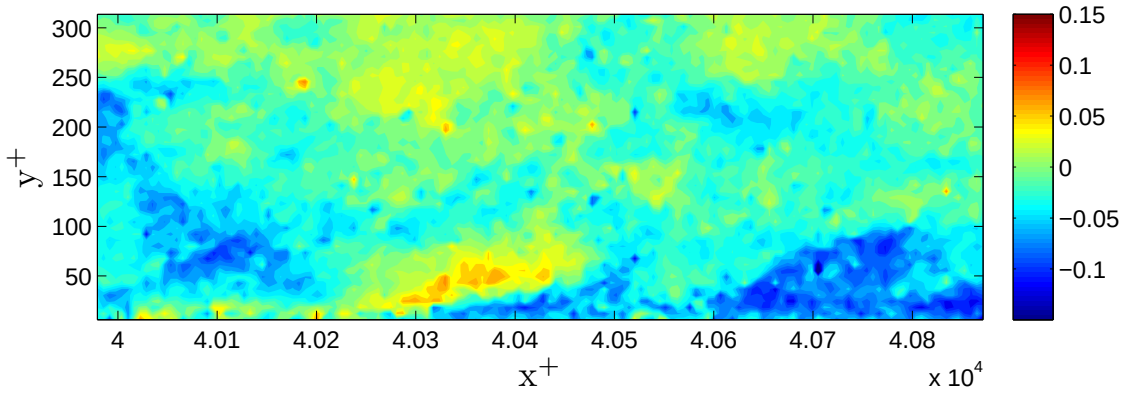

(b) Velocity fluctuation profile plot. Colorbar in m/s.

FIGURE 4.28: Velocity and velocity fluctuations profiles plot.

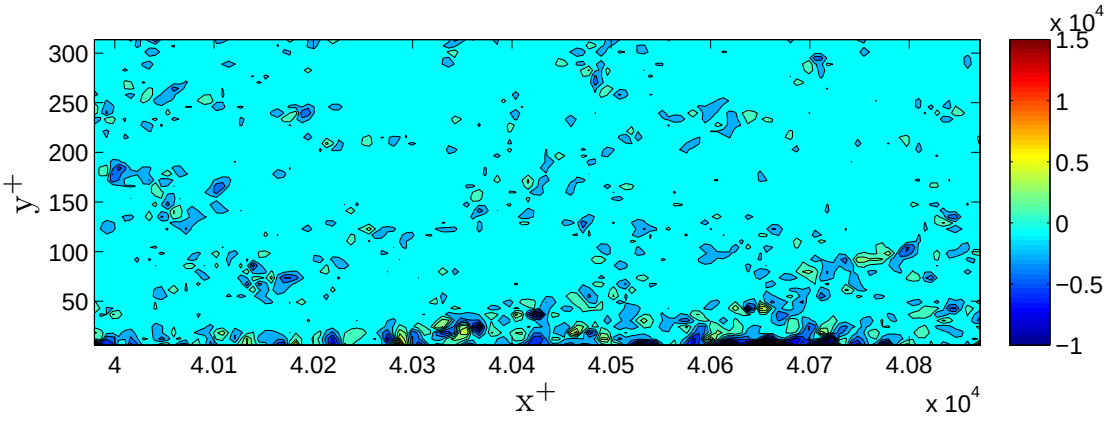

(a) Iso-surface of $|\lambda_{ci}|$ swirling strength. Colorbar in 1/s.

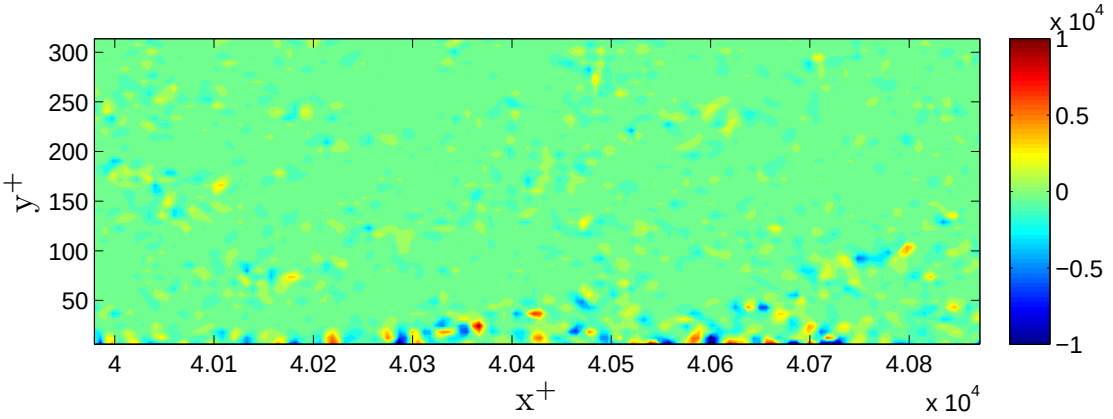

(b) Iso-surface of Q. Colorbar in 1/s

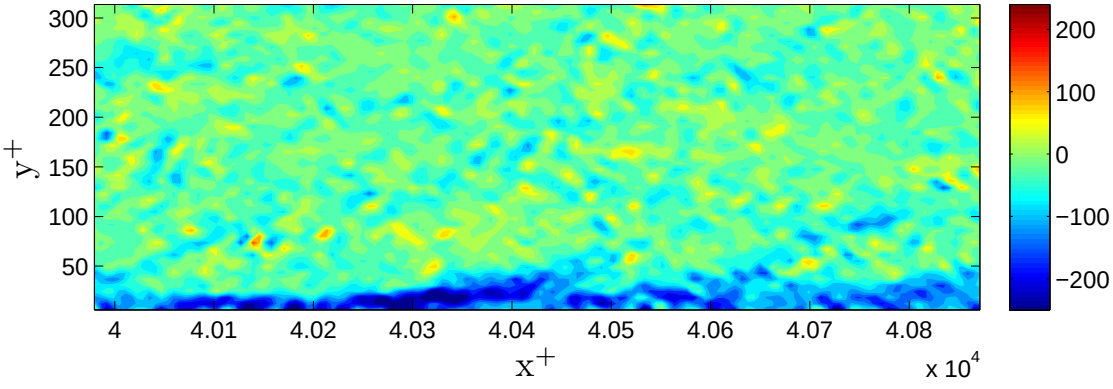

(c) Vorticity profile. Colorbar in 1/s.

FIGURE 4.29: Iso-surface of $|\lambda_{ci}|$ swirling strength and Q-criterion and vorticity profile plot.

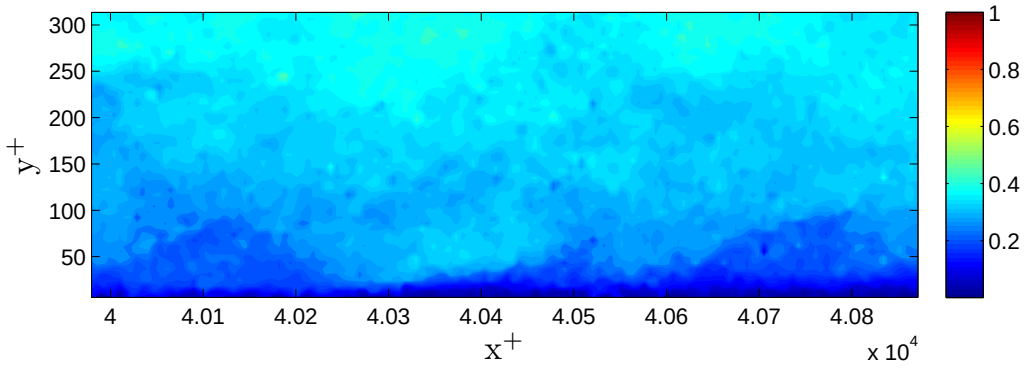

(a) Velocity profile plot for frame 200. Colorbar in m/s.

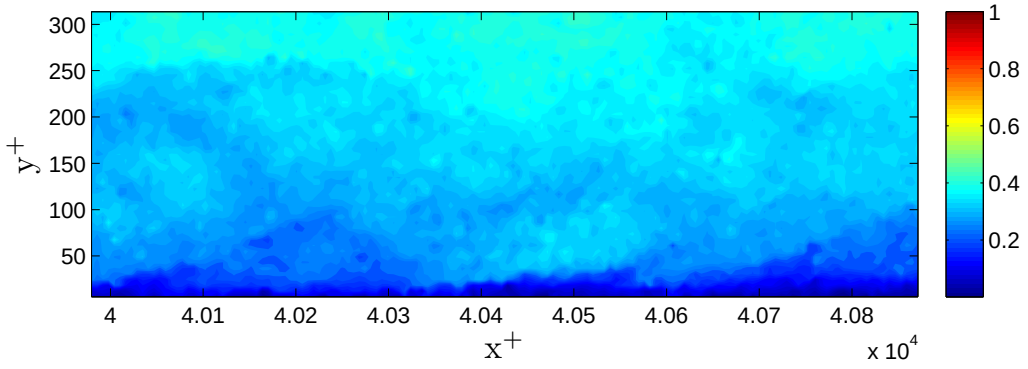

(b) Velocity profile plot for frame 210. Colorbar in m/s.

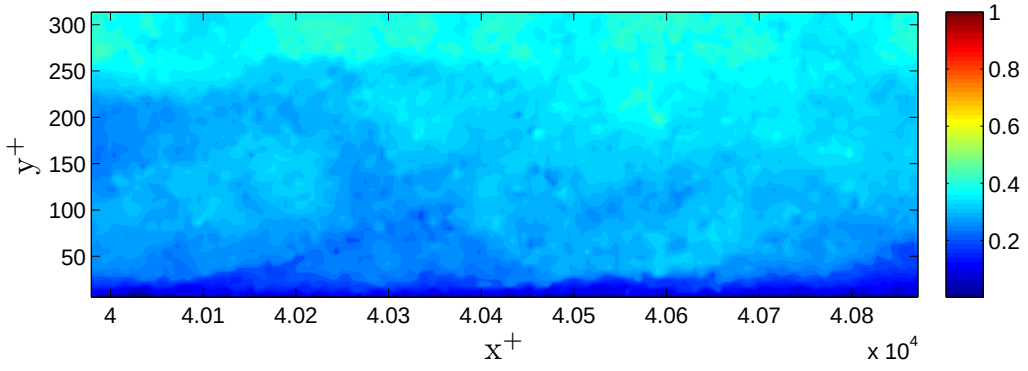

(c) Velocity profile plot for frame 220. Colorbar in m/s.

FIGURE 4.30: Examples of velocity profile for frame 200 up to 220 showing hairpin structure propagating across the FOV (Part 1). Colorbar in m/s.

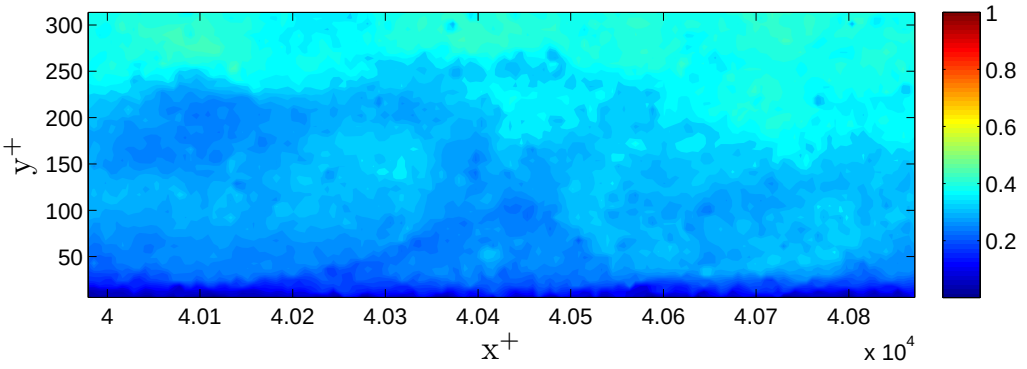

(a) Velocity profile plot for frame 230. Colorbar in m/s.

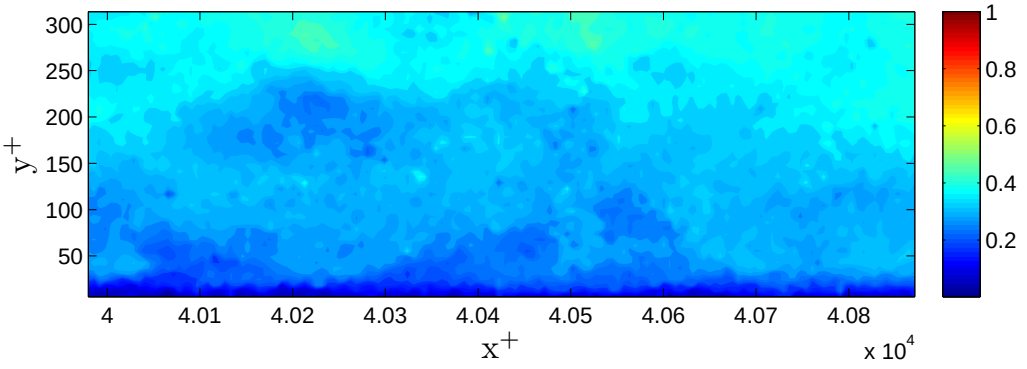

(b) Velocity profile plot for frame 240. Colorbar in m/s.

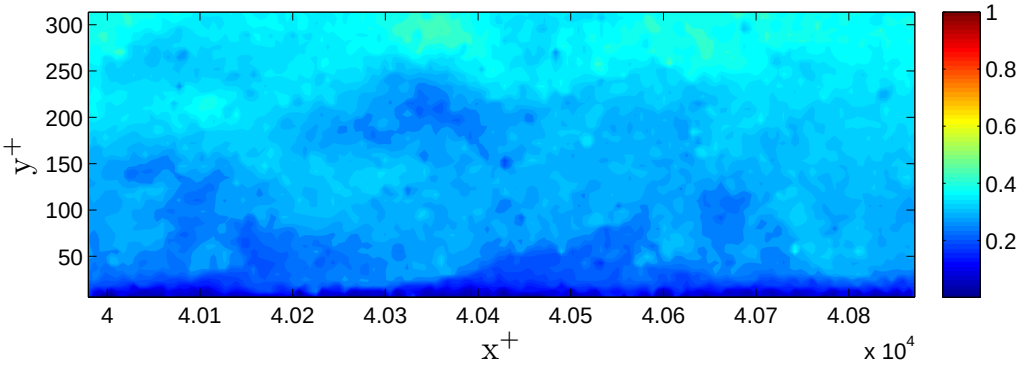

(c) Velocity profile plot for frame 250. Colorbar in m/s.

FIGURE 4.31: Examples of velocity profile for frame 230 up to 250 showing hairpin structure propagating across the FOV (Part 2). Colorbar in m/s.

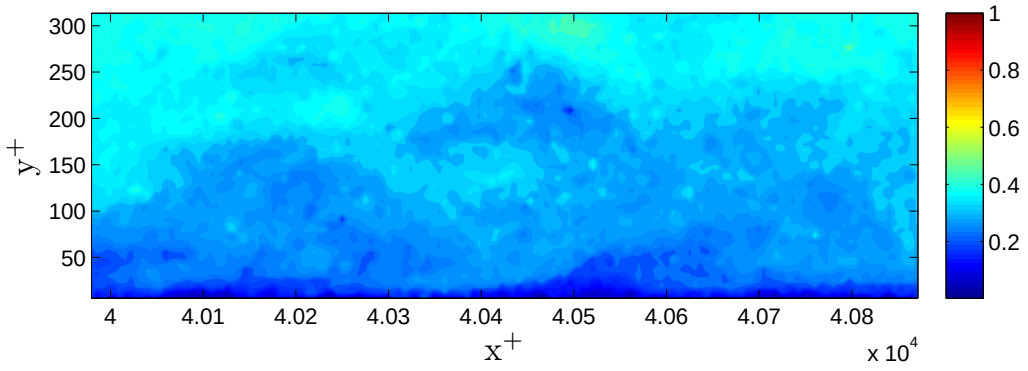

(a) Velocity profile plot for frame 260. Colorbar in m/s.

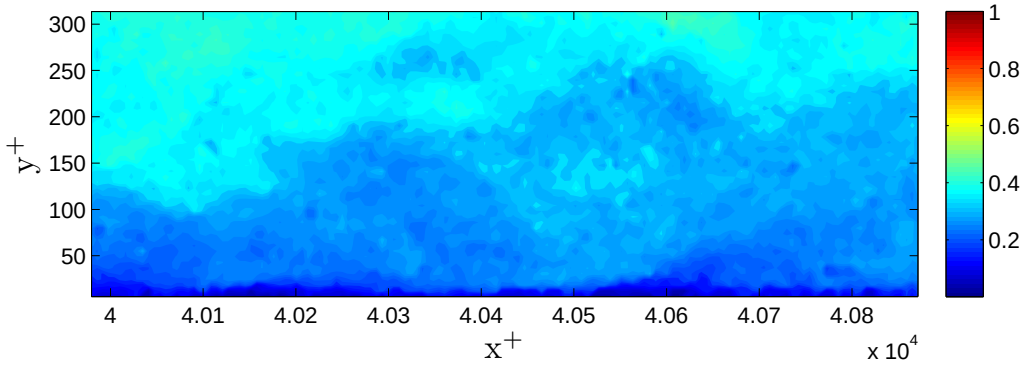

(b) Velocity profile plot for frame 270. Colorbar in m/s.

FIGURE 4.32: Examples of velocity profile for frame 260 up to 270 showing hairpin structure propagating across the FOV (Part 3). Colorbar in m/s.

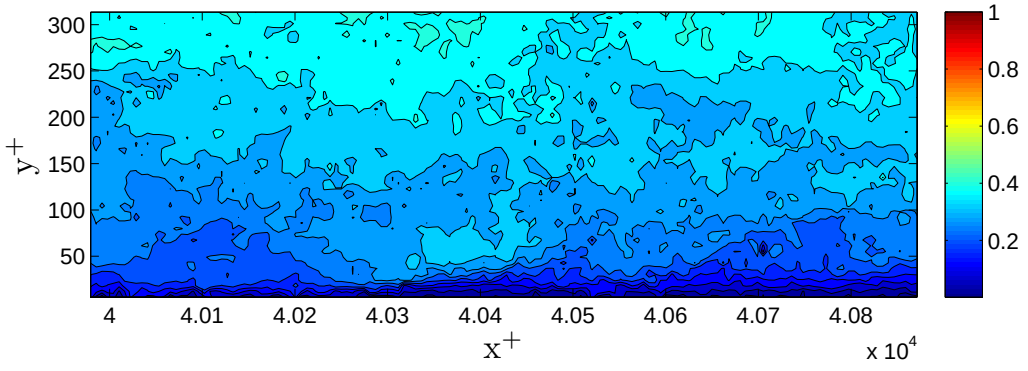

FIGURE 4.33: Velocity profile plot indicating the presence of regions of constant velocity momentum across the measurement region following the work of Adrian, Meinhart and Tomkins (2000).

Chapter 5

Two-phase flow in turbulent boundary layer

5.1 Introduction

Having established that the Newcastle open channel rig was capable of producing a canonical turbulent boundary layer of adequate thickness for reliable PIV measurements with mean and statistical properties in good agreement with accepted results from the literature for the range $730 < \mathrm{Re}_\theta < 3000$, and showing typical hairpin structures, two-phase flow measurement could begin.

For two-phase flow measurement, polyethylene microsphere with specific gravity of 0.997 g/cc and with diameter range between 180 - 212 μm were added to the flow as the dispersed phase. The viscous response time for the particles is estimated to be $\tau_p = \rho_p d_p^2/18\mu$ = 2.1ms. This value does not correct for the effects of Reynolds number nor added mass, where both alters the particle response time. To account for these two effects, the equation of motion for a stationary particle is integrated until the particles velocity reaches its terminal value.

The particle equation of motion (Kiger and Pan, 2002) neglects effect of Basset history force but retains the terms describing buoyancy, added mass and quasi-steady drag force respectively , and is given by

$$\frac{dv_p}{dt} = \frac{\rho_p - \rho_f}{\rho_p} \mathrm{g} - \frac{\rho_f}{2\rho_f} \frac{dv_p}{dt} - \frac{3}{4} \frac{C_d \rho_f v_p^2}{d} \tag{5.1}$$

where the drag coefficient developed by (Schiller and Newmann, 1933) is given by

$$C_d = \frac{24}{\mathrm{Re}_p} \left(1 + 0.15\,\mathrm{Re}_p^{0.687}\right) = \frac{24}{\mathrm{Re}_p} f\left(\mathrm{Re}_p\right) \tag{5.2}$$

The particle Reynolds number is given by

$$\mathrm{Re}_p = |u - v_p| \frac{d_p}{\nu} \tag{5.3}$$

The term in the right hand side of Equation 5.1 represent buoyancy, a force caused by the acceleration of the undisturbed fluid, the added mass force due to the inertia of fluid displaced by the particle movement, and the quasi-steady viscous drag force as a result of the relative velocity difference between the particle and the surrounding fluid, respectively.

The response time of a particle is defined as

$$\tau_p = \frac{\rho_p d_p^2}{18\,\mu} \tag{5.4}$$

where ρ_p is the density and d_p is the diameter of the particles respectively, and μ is the dynamic viscosity of the flow phase.

The response time, τ_p represent a characteristic time scale for velocity changes for the particles (τ_p = 2.2ms) and the characteristic time scale for a fully developed boundary layer is defined in Equation 5.5. The characteristic time scales for particle and fluid is calculated to be 2.1ms and 0.00739ms respectively.

$$\tau_f = \frac{v}{u_\tau^2} \tag{5.5}$$

where, u_τ is the wall friction velocity and is given by

$$u_\tau = \sqrt{\frac{\tau_w}{\rho}} \tag{5.6}$$

where τ_w is the wall shear stress.

The Stokes number is a dimensionless parameter defined as the ratio of the particle response time, τ_p to the characteristic time-scale of the continuous phase, τ_f and is given by

$$\mathrm{St} = \frac{\tau_p}{\tau_f} \tag{5.7}$$

For particles in a turbulent boundary layer, the Stokes number may be estimated by

$$\mathrm{St} = \frac{\rho_p}{\rho_f} \frac{d_p^2 \, u_\tau^2}{18 \, \nu^2} \tag{5.8}$$

Roughly spherical in size, the Stokes number for the inertial and fluid tracers particles were calculated to be 0.0028 and 0.95. The stokes number of the tracers particles and inertial particles suggests that they would not have any effects on the continuous phase flow, and thus it can be assumed that the particles will responds to flow fluctuations. Stokes number, St $\ll$1 indicates that the particle inertia is sufficiently high compared to the flow and its trajectory is unaffected by the flow field.

Conventionally, the time constant is presented non-dimensionally as the Stokes number. Particle with small Stokes number (<0.01) will follow the flow and will not affect the turbulence. Particle with large Stokes number ($\gg$1) will not respond significantly to turbulent velocity fluctuations. The particles in the present two-phase experiment has a Stokes number of <1, thus, it is expected to follow the turbulence.

The effect of gravity also affects particles from following the turbulence. Combined with inertial effect as described above, the two forces will pull the particles through a series of different fluid regions, making it difficult to predict the behaviour of the fluid surroundings. This effect is called the “crossing-trajectories effect” and was first reported by Yudine (1959). This crossing-trajectories effect reduces the fluctuation levels of the particles (Wells and Stocks,

1983). The density of the inertial particles is 0.997g/cc which is almost identical to that of the density of flow phase, ρ_f = 1000kg/m^3 with a fluid/particle density ratio of almost a unity. The buoyancy term in Equation 5.1 becomes zero as the density of the inertial particles is lower than that of the fluid, thus the effect of gravity can be assumed to be not important for the current experiments.

The particle mass loading, that is the ratio of the total mass of the particles to the mass of the fluid characterizes the influence of the particles to their surroundings. Low mass loadings imply that the total particle drag is small compared to other forces involved and therefore the fluid behaviour remains unaffected by the particle. Non-uniform particle loading will cause mean flow variations leading to changes in the turbulence. These velocity gradient would serve as a source of turbulence production, thus uniform particle loading is important and can be achieve by allowing the particles to mix well before taking measurements.

As described previously the 10μm seeding particles used as flow tracers had a Stokes number of around 0.0028, and so could be expected to accurately follow the fluid flow. The secondary phase was to be made up of particles with much higher Stokes number, behaving as inertial particles. Recent work has revealed that particles with Stokes number around unity show interesting interactions with turbulence, notably a "de-mixing" effect, leading to emergence of regions of preferential concentration outside of turbulent eddies, and so the primary tests were to concentrate on this Stokes number range. Increased Stokes number could be achieved either by increasing the density of the secondary phase particles, or by increasing their diameter. Since the flow channel is horizontal, increased particle density would lead to secondary effects of gravitational sedimentation, and so large diameter particles of near neutral buoyancy were chosen. With a fluid/particle density ratio very close to 1.0, added mass effects are significant. Taking all these factors into account, a suitable diameter for the inertial particles was around 200 μm, and with almost 20:1 diameter ratio between the inertial and seeding particles, separation based on image size as described by Kiger and Pan (2002) was a practical proposition.

For the 200 μm secondary phase particles two series of experiments were run, both with two particle loadings of $\phi = 1.4 \times 10^{-5}$ and 2.8×10^{-5}. These values were chosen as a compromise, to give as many particles as possible in the PIV imaged region whilst not significantly modifying

the fluid turbulence. The primary aim of the first series of experiments was to investigate the effect of inertial particle loading on the mean velocity, turbulence and stress profiles obtained from PIV, in comparison to clear water results from both PIV and LDV. These tests were carried out at a single Reynolds number of $\mathrm{Re}_\theta = 3000\,(\mathrm{Re}_\tau = 890)$.

The second series of experiments, carried out at the same two volumetric loadings and at three Reynolds numbers, Re_θ = 730, 1420 and 2660, concentrated on tracking the inertial particles in real time. Two experimental setups were used, one at a larger field of view of 100mm (x) × 75mm (y), allowing a longer tracking distance, and one at a reduced field of view of 48mm × 17mm with half sensor resolution, to look at the effects of turbulent structures on the inertial particle transport.

5.2 Experimental setup and methodology

The present experiments were performed in the newly upgraded open-channel experimental rig. The floor boundary layer flow was tripped via a zig-zag strip, 2mm high, located 23mm downstream of the inlet edge of the working section. Upstream of this, the inlet section comprised a 3mm cell honeycomb, 3 coarse gauzes with 60% porosity each and 2 fine gauzes with a porosity of 45% each. Access spaces were left between the fine gauzes to allow clearing of any lodged inertial particles. Following the gauzes a profiled transition section with approximately 3:1 contraction ratio lead to the parallel working section. At the outlet plane of the working section a 25% porous plate was located, to eliminate low frequency flow oscillations. Full details of the rig construction have been detailed earlier in Chapter 4.

A MotionPro X5, high-frame rate camera with a 105mm Nikon Micro-Nikkor lens was used to capture the flow in the reference region, 2100mm downstream of the boundary layer trip, with a resolution of 48.6mm by 35.6mm (x^+ = 1030 and y^+ = 750) using the full sensor size of 2352 by 1728 pixels. The flow was also captured using half the vertical resolution with the purpose of zooming in closer to better resolve the flow. In this case, the field-of-view was 48.6mm by 17.2mm (x^+ = 1030 and y^+ = 370). The lens was operated at an aperture of f4. Although this is a much larger aperture than suggested in the literature, experimental results

showed a high percentage of good vectors (i.e. less than 5% bad vectors) and pixel-locking could not be observed in the histogram plot of pixel movements. Good vectors are velocity vectors that can be accepted to represent the flow velocities, while bad vectors refer to those that deviate significantly from their surrounding vectors, thus require to be substituted. This behaviour was attributed to enlargement of the particle images by lens aberration, rather than the diffraction effect associated with small apertures. The laser power in all cases has been set to 25W and was determined to be adequate to illuminate both tracers and inertial particles.

The flow was seeded with 10μm silver-coated hollow glass spheres (ρ = 1.4 g/cc) that behave as a tracer, with a volumetric loading of 1.6×10^{-6}. The dispersed phase was added in two stages; first with $\phi = 1.4 \times 10^{-5}$ and, second with $\phi = 2.8 \times 10^{-5}$. These were 180 - 212$\mu$m diameter polyethylene microspheres, with density 0.997g/cc, and were mixed with the flow sufficiently long before the start of the experiment to obtain a well-mixed suspension. Firstly, the inertial particles were added into the exit plenum tank and allowed to circulate within the system for at least 2 minutes. This would allow sufficient time for the particle to mix uniformly.

The velocity in the free-stream, at y = 100mm, was set to 0.45m/s with a channel fluid full depth of 193mm (Fr = 0.32) for all experiments. This free-stream velocity was set using the LDV probe at a fixed height of y = 100mm for all measurements. The employed coordinate system is as shown in Figure 5.1(c) where the x, y and z are the the streamwise, wall-normal and transverse directions, respectively. The instantaneous streamwise and wall-normal velocities are denoted by U and V, respectively; corresponding fluctuating velocities (Reynolds decomposed) by u and v and their rms values by u' and v'.

Three sets of experiments were carried out, a full sensor FOV of the flow at zero-dispersed particle loading, and at two volumetric loadings (i.e. $\phi = 1.4 \times 10^{-5}$, and 2.8×10^{-5}), and corresponding sets at half-vertical sensor resolution allowing high-frame rate acquisitions at 1000Hz (500 vector maps/s) with the plus mode. The 4-Gb camera memory allowed the acquisition of 2000 double images giving 2000 vector maps for each measurement run at half vertical resolution. For every setup 5 such runs were made, giving a total of 10,000 double frame images. These data sets should be large enough to extract the mean statistics of the flow.

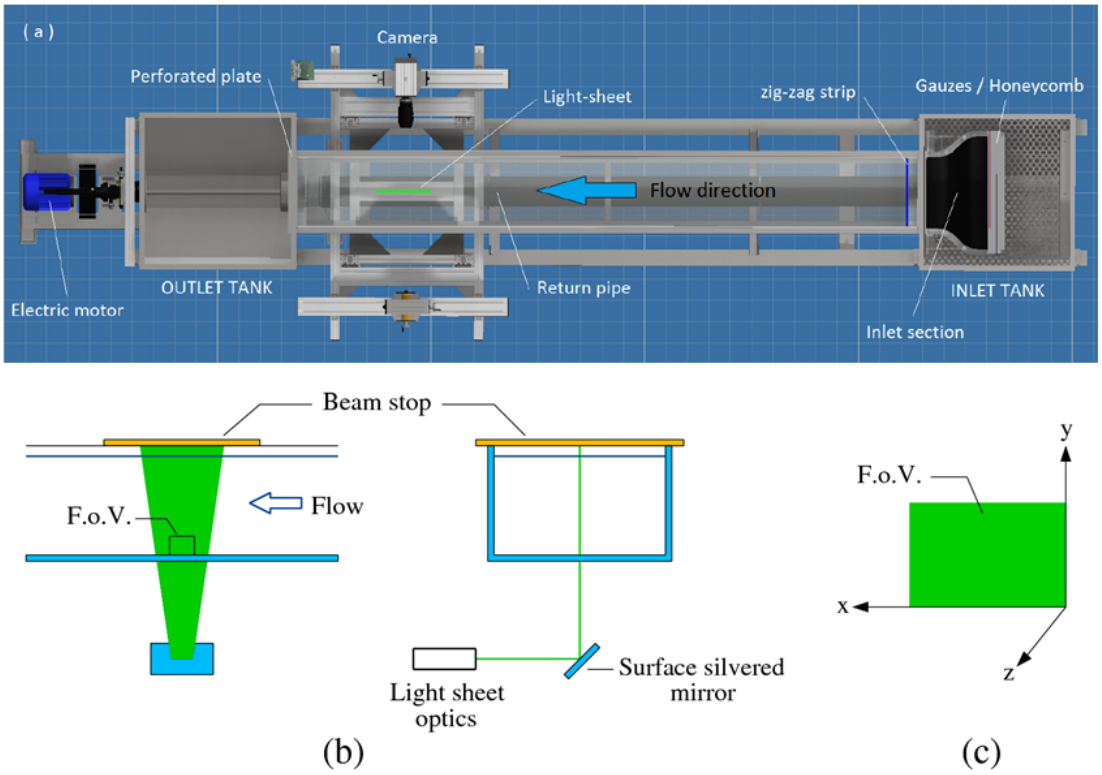

FIGURE 5.1: Schematic layout of experimental setups, (a) top view, (b) PIV setup (channel cross-section), (c) coordinate system and field-of-view (FOV).

In all cases, PIV images were processed for instantaneous fluid flow velocities according to the same basic procedure within Dantec's DynamicStudio software package. The single-phase images first undergo a background removal stage, where the image mean of the run batch of 2000 double-frame images are subtracted from each image. Secondly, the background-subtracted, double-frame images were processed using an adaptive correlation algorithm with 32 by 32 pixel interrogation regions and a 50% overlap, giving 7446 vectors when operating the camera at half of its vertical resolution. At full resolutions, this gives approximately 15,000 vectors. Velocity vectors were than validated using the moving average technique, and vectors outside the target area (i.e. below the channel bottom glass) were masked off. The total number of bad vectors were well below 5 % for all acquisitions.

For LDV measurements, the number of samples collected to determine the mean velocity is important. To determine the total number of data at a point can be extracted from the plot of the mean or fluctuation velocities against the number of data collected. This are shown in Plot 1, and 2, where the mean value converge to a single value with 10,000 data. Although

large number of data is preferable, the value obtain from these plot gives an indication to the minimum numbers of data required.

For PIV measurements, large data for a single position is a limitation. The numbers of two-phase images captured in a single run for a 10 run measurement is 1000 double-frame images for the 60mm lens. This gives us a total of 10,000 double image frames. For the close up view of the flow, a 105mm lens were used to capture 5 runs at 2000 double-image per run. Therefore, for each setup, 10,000 double-image frames were used to determine the mean velocity. For the particulate phase, the particles are binned based on their locations in the y^+ direction at an incremental height of $\Delta y^+ = 10$. The particle counts is given in Figure 5.7 where it can be observed that the average number of particles from $y^+ = 6$ up to $y^+ = 400$ on average is approximately 2500. Number of particles between $y^+ = 0$ up to $y^+ = 5$ is approximately 750. These are extracted from the 10,000 frames, which are significantly less than the mean velocity of the flow.

One of the major difficulty in applying LDV to near wall measurement is the difficulty in collecting large amount of data to deduce the mean velocity and subsequent velocity perturbation. Secondly, is to collect enough data point within the linear sublayer (i.e. $y^+ \leq 5$) for fitting purposes. With the Myford swivelling vertical slide (with accuracy ±0.001mm), LDV measurement as close as 0.13mm (y^+=2.5) from the wall were possible. Some LDV measurement goes even below the 0.13mm limit, at the expense of data quality, number of data collected and do significantly increased the measurement time at a particular measurement position. Theoretically, 10 measurement points can be fitted within the linear sublayer ($y^+ < 5$ corresponding to $y < 0.25$mm), but experimentally the numbers of data points that can be fitted were between 4 to 5. This would allow the fitting of the mean velocity data to the linear sublayer rather than to the logarithmic layer profile.

In the case for PIV, the main limitation is the size of the interrogation window used in the correlation process. Using Dantec's DynamicStudio adaptive correlation technique, and a 105mm Nikon Nikkor lens, for a close up view of the measurement area within the boundary layer (magnification $M_0 = 0.34$), the nearest velocity data acquired is 0.65mm from the wall (y^+) = 12. In this circumstances where available data is outside the linear sublayer, the boundary layer profile have to be fitted to the logarithmic region using the Clauser chart technique.

With the Clauser chart technique, there are several aspects that can introduce uncertainties in the estimation of the shear stress and subsequent friction velocity, u_τ. One aspect of concern is the selection of the von Kármán constant κ that is directly related in the estimation of the friction velocity. Different values of this constant are reported in the literature (e.g. Zanoun et al., 2003).

The logarithmic region is defined by

$$U^+ = 2.44 \ln y^+ = 5.29 \text{ (Nezu and Rodi, 1986)} \tag{5.9}$$

For LDV measurements, the data within the linear sublayer allows for fitting of the mean velocity data to the linear sublayer. This is important, as the friction velocity, u_τ can be determined without using the Clauser technique where the data are fitted to the logarithmic layer profile where a selection of the von Kármán constant κ is available that directly effect the estimation of the friction velocity. Fitting the data to the linear sublayer is preferable and accurate, but in the case of PIV measurements where the data points are constrained by the size of the interrogation window, the Clauser technique is unavoidable. As a result the estimation of the shear velocity is somewhat questionable. In our LDV measurement, the shear velocity is found to be 0.0198m/s, and for PIV measurements, this value is 0.0212m/s, this gives a percentage difference of 6.8%. This would effect not only the non-dimensionalising process of parameters such as y^+ and u^+ but also effects the Reynolds numbers and Stokes number values, that are directly related to the evaluation of flow behaviour.

5.2.1 Two-phase flow image processing and phase-separation

The separation of tracers particles and inertial particle images from the single two-phase images were achieved following the technique of Kiger and Pan (2000, 2002). For more detailed information's on the phase-separation technique used, please refer to Appendix A. Both inertial and tracer particles images were captured on a single frame, as shown in Figure 5.2(a), using a single camera, hence avoiding image registration problems. In general, a 3×3 two-dimensional median filter is convolve over the whole image area, and by assuming that the tracer particles

images are noises, their images were removed and dilated inertial particles images are left, as shown in Figure 5.2(b). This was then subtracted from the original combined image, leaving only the tracer particles, as shown in Figure 5.2(c). MATLAB scripts for extracting both flow and inertial particles images can be referred to in Appendix A.

After the separation process, the flow and particles double-images was processed separately. The flow phase images undergo Adaptive correlations using 32 × 32 interrogation area size, 50% overlap 3 refinement steps with sub-pixel accuracy, and 3 × 3 moving average validation to substitute spurious vectors. The moving average validation technique compare each vector with the average of its surrounding vectors within the 3 × 3 area and replaced all vectors that deviate too much by an average of the neighbour. Mean velocity profiles were then calculated using the available 2000 double-image frames and subtracted from the instantaneous velocity vectors to generate the fluctuation velocities for each frames. This size separation algorithm was implemented using a MATLAB script called from within Dantec's DynamicStudio software via the built-in MATLAB Link. Tracer particle image pairs could then be processed using the standard PIV technique, described in Section 5.2, to give the instantaneous fluid velocity field, whilst the corresponding inertial particle image pairs were processed using in-house MATLAB particle tracking algorithm, to give the position and instantaneous velocity of each inertial particle. MATLAB's scripts were developed to track fluid velocity perturbations, particle trajectories, particle velocity perturbations and quadrant number along particle tracks.

5.3 Fluid mean velocity and turbulence profiles

For clear water tests, LDV gave u_τ = 0.0189 m/s, using Newton's law of viscosity and a linear fit in the sub-layer region, whereas PIV gave u_τ= 0.0197 m/s, using the Clauser method since data was unavailable very close to the wall. This amounts to a 4% difference in friction velocity.

For the two-phase tests, only PIV data was available, and the value of u_τ obtained by the Clauser fit was 0.0212 for both inertial particle loadings, $\phi = 1.4 \times 10^{-5}$ and $\phi = 2.8 \times 10^{-5}$. This represents a 7.6% increase in friction velocity over the clear water result, based on PIV in all cases.

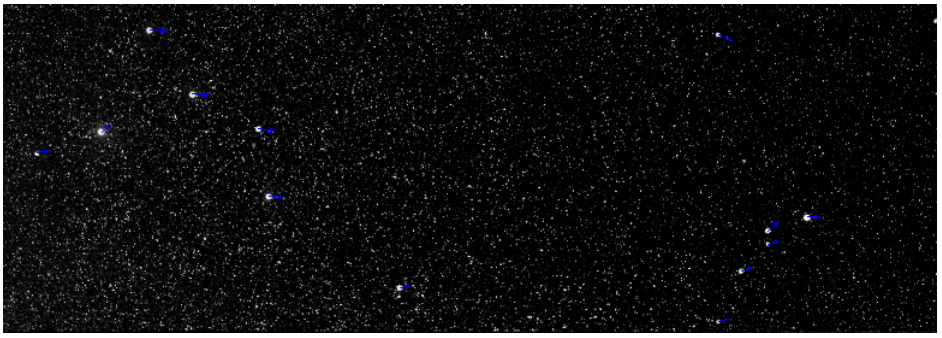

(a) Original, combined image.

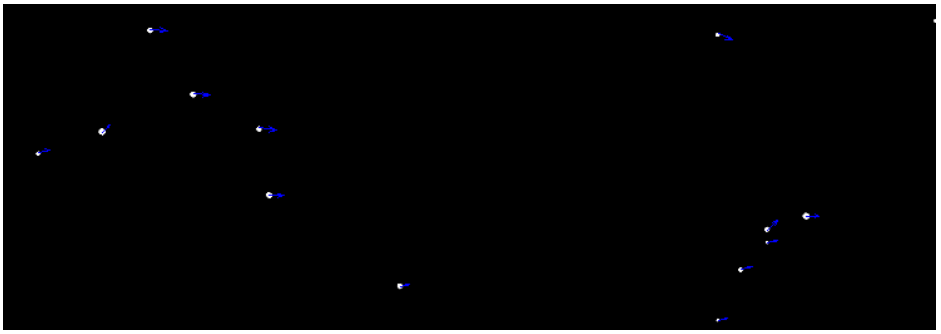

(b) Median filtered images, removing tracer particles to give inertial particles only.

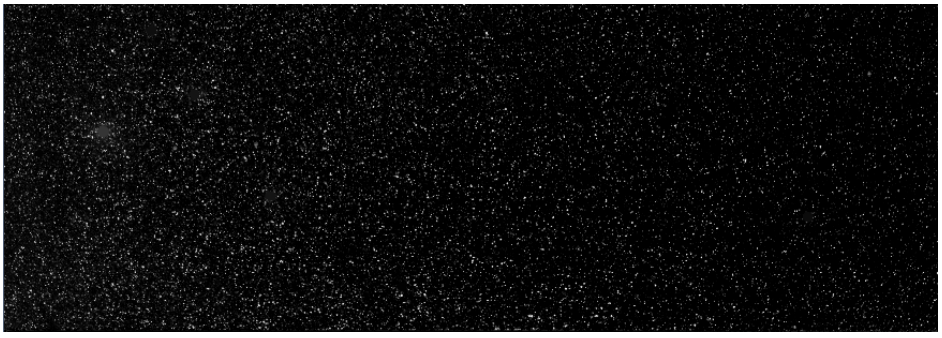

(c) Tracer particle only image, produced by subtracting dilated inertial particles from original combined image.

FIGURE 5.2: Separation of particle images for two-phase flow (FOV x=100mm × y = 71 mm)

Considering the dimensionless velocity profiles, shown in Figure 5.3, the first observation is the excellent collapse of the clear water PIV profile onto the LDV results up to the limit of the PIV field of view at $y^+ = 800$. Neither of the two inertial particle loadings showed any discernible deviation from the clear water PIV profile in the region between the wall and $y^+ = 400$. In the region $400 < y^+ < 800$ loading causes the mean velocity to fall progressively below the clear water value, with the higher loading increasing this deviation, approximately proportionally.

This contrasts with the results of Van Hout (2011), who found no variation in the velocity

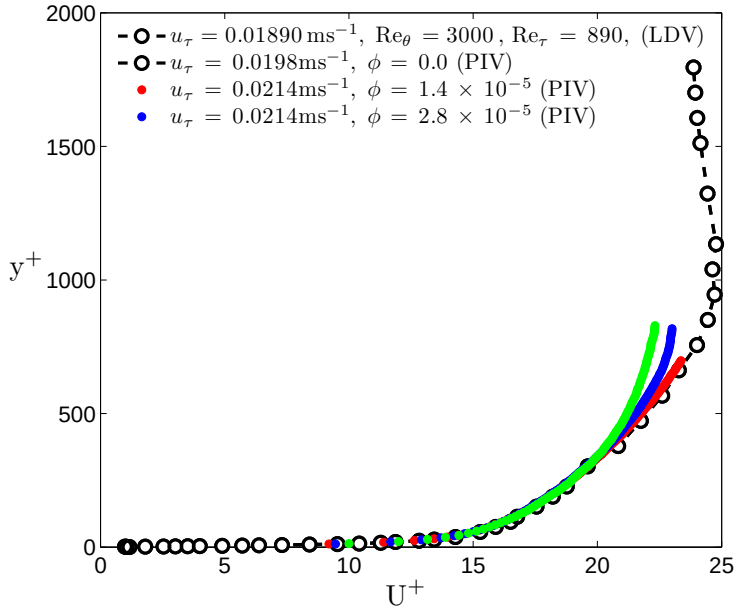

FIGURE 5.3: Fluid mean velocity profile for boundary layer with particle volumetric loading of $\phi = 0$, 1.4×10^{-5} and 2.8×10^{-5}

profile with loading for a fully developed closed channel flow. Kiger and Pan (2002) did find, again for fully developed closed channel flow, that the presence of inertial particles gave rise to a decrease in the mean velocity over the mid-region of the profile, but in their case the effect extended much closer to the wall. It should be noted also that their inertial particles were not neutrally buoyant, having a density ratio of approximately 2.6.

Re-plotting the profile with a logarithmic scale for y^+ to give the classic "law of the wall" plot in Figure 5.4 confirms both the quality of the measurements and insensitivity to particle loading in the sub-layer and logarithmic regions, with the deviation due to inertial particles being confined to the wake region.

Normalised rms values of streamwise and wall-normal velocity fluctuations for the fluid are depicted in Figure 5.5. The PIV u'^+ profiles for zero loading and for the maximum inertial particle loading of 2.8×10^{-5} are virtually indistinguishable; in fact the variations are significantly less than the small deviation from the LDV values. This is in agreement with previous work for neutrally buoyant inertial particles, but differs from Kiger and Pan (2002) increase in u'^+ for "heavy particle" laden flow.

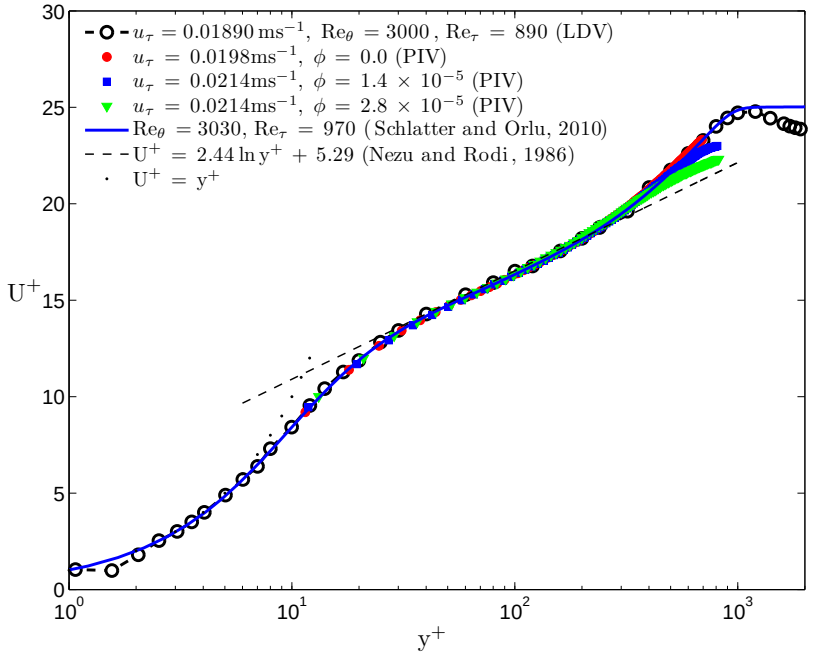

FIGURE 5.4: Fluid mean velocity profile for boundary layer with particle volumetric loading of $\phi = 0$, 1.4×10^{-5} and 2.8×10^{-5} in wall law form.

For the wall-normal v'^+ profile only PIV data are available. In this case, the inertial particle loading results in a drop ofof v'^+, on average by around 7.8%, in the region $5 < \mathrm{y}^+ < 400$, with the lower values being in good agreement with the clear water DNS results of Schlatter and Örlü (2010).

Figure 5.6 shows the effect of these variations in rms fluctuations on the normalised Reynolds stresses. All the stress profiles shown indicate a reduction in stress associated with inertial particle loading, with the effect being more significant for the normal stresses.

The closest comparable two-phase measurements are those of Kaftori et al. (1995*b*, 1998) and Van Hout (2011) as shown in Table 5.1. Both used near neutral buoyancy secondary phase particles, but at higher volumetric loading. Kaftori et al.'s results were for the floor boundary layer of an open channel and were obtained by LDA, whilst van Hout's PIV results were for fully developed flow in a closed channel.

Van Hout (2011) observed no change in friction velocity u_τ with loading, whilst the extensive data of Kaftori et al. consistently showed an increase, which was attributed to particles

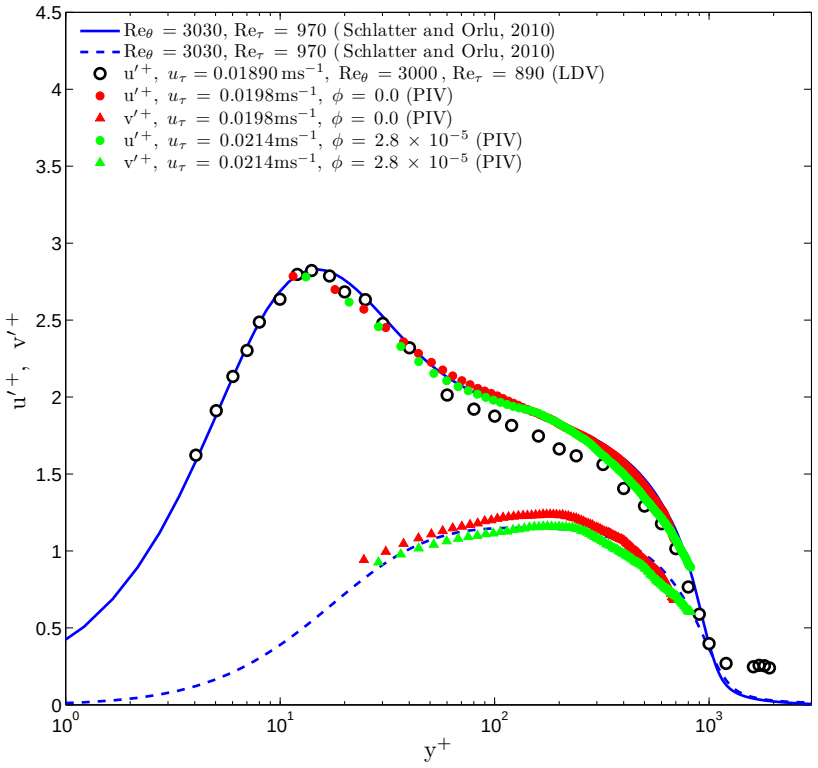

FIGURE 5.5: Normalised rms of streamwise and wall-normal velocity fluctuations for boundary layer with particle volumetric loading of $\phi = 0$, and 2.8×10^{-5} in wall law form.

	u_τ (m/s) (clear water)	Re$_\tau$	Particle dia. d_p	Volumetric loading ϕ	Change in u_τ with loading
Present work	0.0189	770*	180 - 212	2.8×10^{-5}	+7.6 %
Kaftori et al.	0.0150	679+	275	0.87×10^{-4}	+6.7 %
van Hout	0.0174	435++	583	1.4×10^{-4}	0 %

TABLE 5.1: Comparable 2-phase experimental data. (* Based on δ_{99}; + Based on depth = 35.36mm; ++ Based on half-height = 25mm).

deposited on the floor acting as wall roughness. Despite having the highest volumetric loadings of the group of experiments, van Hout observed no effect of loading on the mean or rms fluid velocity profiles. In contrast to the present results, Kaftori et al. (1998) observed a slight increase in mean velocity in the outer region, for the Re$_\theta$ = 679 flow with 100 μm and 275μm particles. However, at lower Reynolds numbers, or with larger 900μm particles, where a significant number of particles were settled on the channel floor, they observed a reduction in mean fluid velocity in the outer region, similar to the present results. This may tie in with the

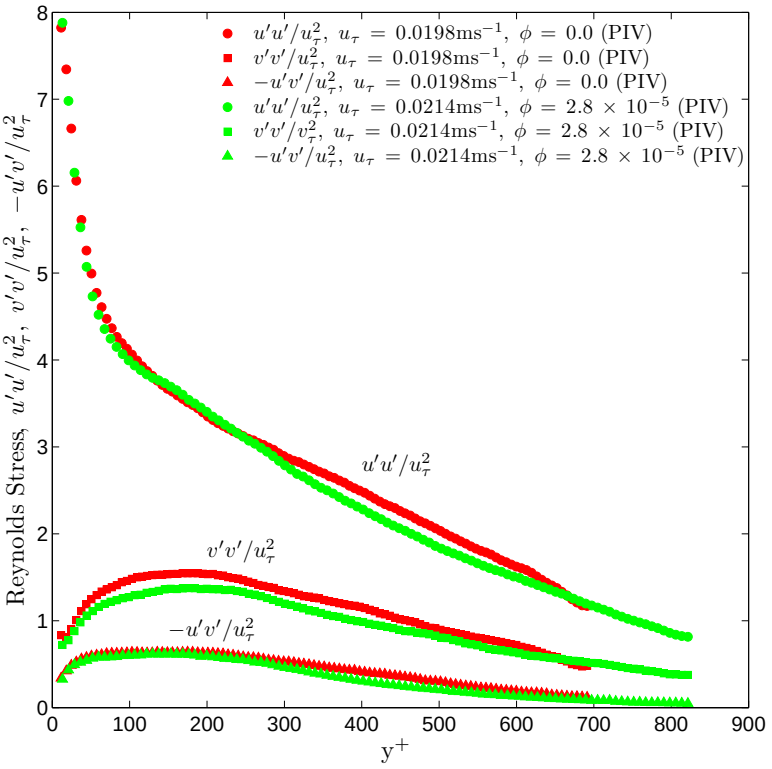

FIGURE 5.6: Normalized Reynolds stresses profile at particle volumetric loading of $\phi = 0,$ and 2.8×10^{-5}.

proportionately larger increase in shear velocity seen in the present results. Apart from very close to the wall, beyond the resolution of the PIV methods, the fluid turbulence fluctuations measured by Kaftori et al. (1998) were virtually unaffected by particle loading, whereas the present results did suggest a slight reduction, particularly in the u'^+ rms. All three sets of data suggested some influence of particle loading on the $\overline{u'v'}$ stresses. Van Hout suggested that for particle laden flow the Reynolds shear stress was more peaked close to the walls, whilst being reduced in the region $0.3 < \text{y}/h < 0.8$, with h being the channel half-height. However, both the clear water and particle loaded results differed from the linear variation expected across the central region of a fully developed closed channel flow. Kaftori et al. (1998) showed that the Reynolds shear stresses were increased in the outer flow region for a range of particle sizes at the lower Reynolds numbers tested, whilst for the higher Reynolds number, closer to that of the present work, these stresses were reduced compared to the clear water values. The present results, shown in Figure 5.6, indicate a slight reduction in both direct and shear Reynolds stresses

in this outer region with particle loading. In summary it is apparent that the effects of particle loading on the fluid flow are small throughout in the loadings associated with these series of experiments, that can be approximated to one-way coupled two-phase flows.

5.4 Inertial particle mean and RMS velocity profiles

In this section, the high-speed result are presented, where double-frame images are acquired at 500Hz. With half vertical resolution, this doubled the number of double-frames which could be acquired (i.e. 2000 double-images per acquisition), increasing the total number of double-frame two-phase images for five runs to 10,000 vectormaps. This amount which is significantly higher than that of Van Hout (2011) two-phase experiment should be adequate to obtain reliable statistics for the inertial particles. Dantec's particle tracking add-on to the DynamicStudio software uses double frame images of sparse particle data to determine individual particle velocities via localised image correlation for displacement detection. Particle data points for all the recorded inertial particles were binned according to wall-normal position, with a bin size: $\Delta y^+ = 10$, and average values were allocated to the bin centre positions. A total of 99,600 particle positions were tracked using the DynamicStudio particle tracking algorithm, with a total of approximately 2,000 particle positions per acquisition. A total of 40 bins were located along the wall-normal direction with each bins accumulating on average 2500 data points for bin number 2 up to 40, with the exception of bin number 1, where the total number of particles detected within $0 < y^+ < 10$ was 768 particles only. Bin number 1 is located next to the bottom wall, and the low particle count is acceptable. Fig. 5.7 shows a histogram representation of the number of particles detected within each bin over the 10,000 vector maps. Within the limitations of the sample size, this indicates a reasonably uniform distribution of particles across the thickness of the boundary layer up to $y^+ = 400$, with a significantly reduced particle count in the bin adjacent to the wall.

In Figure 5.8 the mean fluid streamwise velocity (particle masked) is compared to the average particle streamwise velocity according to wall-normal positions, with particle average values presented at bin center positions. A clear lag in particle streamwise velocity can be observed throughout the measurement height. Nevertheless, the particle streamwise velocity

almost coincides with the water velocity (particle masked) and there is no significant modification of streamwise velocity profile throughout the measurement volume. Apart from this slight lag, which is also seen in the corresponding mean velocity profiles of Kaftori et al. (1995*b*), the local differences between the inertial particle mean velocity and the fluid mean velocity are small.

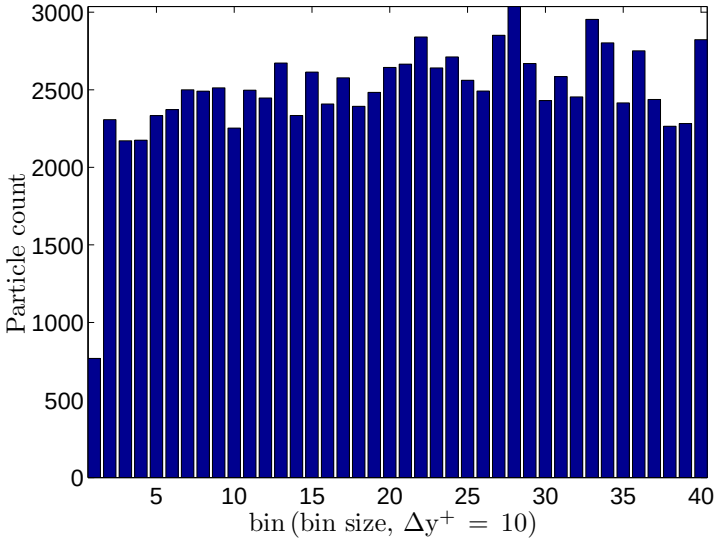

FIGURE 5.7: Histogram of particle count for all runs vs. distance from wall ($\Delta y^+ = 10$).

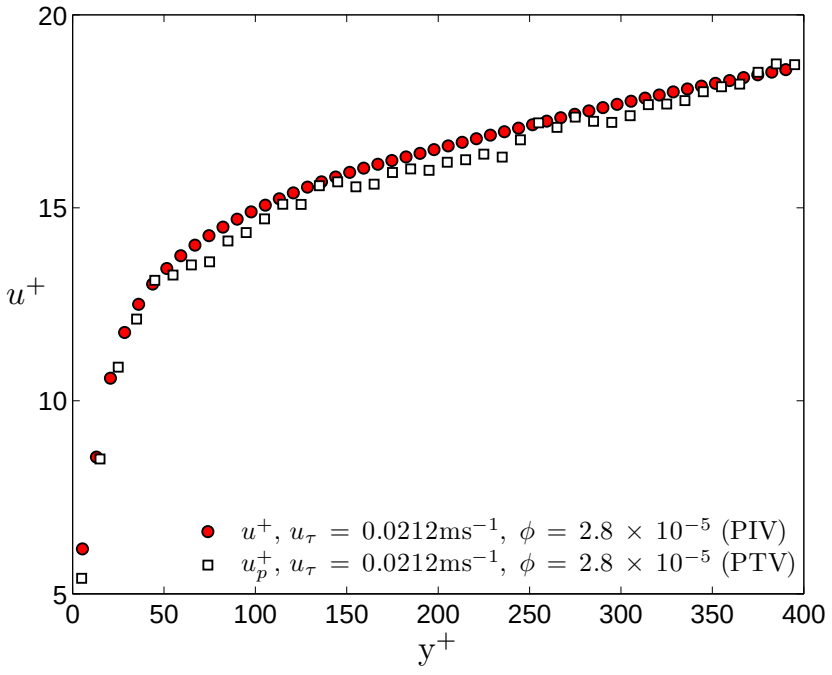

FIGURE 5.8: Comparison between the mean streamwise velocity of the fluid (particle image masked), and inertial particle streamwise velocity (bin size: $\Delta y^+ = 10$ for volumetric loading $\phi = 2.8 \times 10^{-5}$)

Kaftori et al. (1995*b*) comment that the reason for the streamwise velocity deficit of the inertial particles is not obvious. Their investigations led to the conclusion that effect was due to particles clustering in regions of low velocity fluid. Both previous publications, Kaftori et al. (1995*a*) and Kaftori et al. (1995*b*) showed that the slow moving inertial particles were primarily ascending particles (moving away from the wall), which could be associated with the slower moving fluid in turbulence ejections, whilst descending inertial particles did not exhibit this velocity lag.

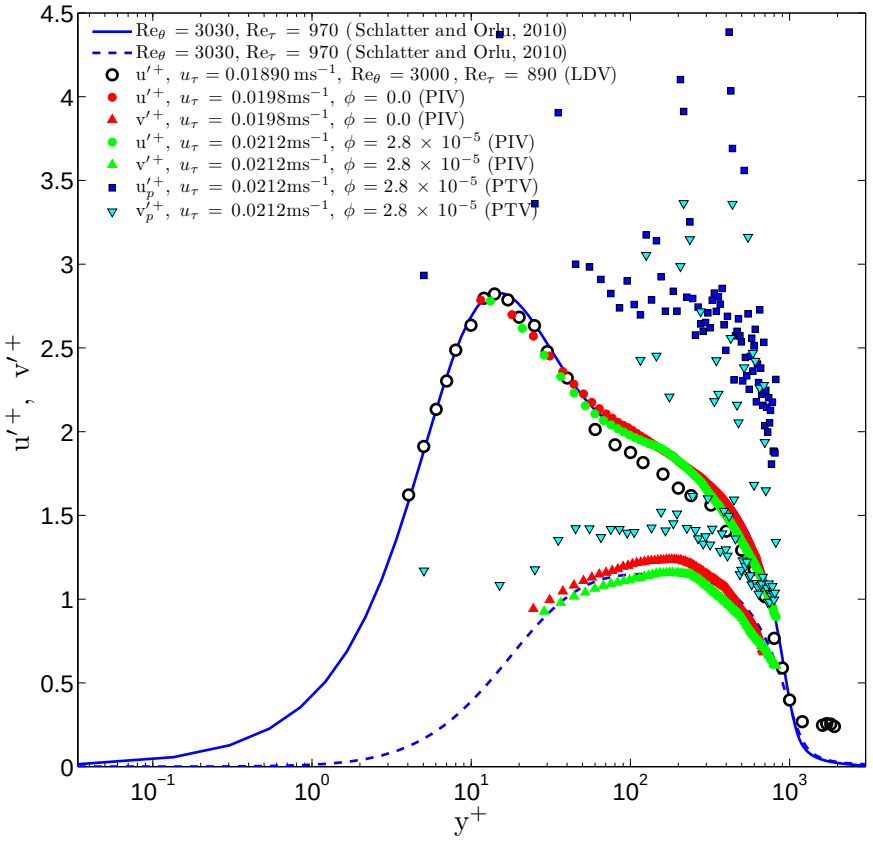

FIGURE 5.9: Rms of fluctuating velocity components of open-channel at two particle volumetric loading ($\phi = 0,$ and 2.8×10^{-5}), particle rms plot for u_p'/u_τ, and v_p'/u_τ.

Rms values of the fluid velocity fluctuations, plotted in inner wall coordinates, are compared to the rms of the binned inertial particle velocity fluctuations, and the results are depicted in Figure 5.9. Particle rms values are plotted for the whole field-of-view (i.e. up to $y^+ = 370$). Over most of the measurement range, particle rms values exceed those of the fluid, consistent with Kaftori et al. (1995*b*) and Van Hout (2011) for near neutrally buoyant polystyrene beads ($d_p > 275\mu m$). The large scatter in the particle rms results is also typical of the previous measurements of Kaftori et al. (1995*b*) and Van Hout (2011). This is despite the fact that the statistics were based on an average of 2500 particle samples per point, as opposed to a minimum of 50 samples for Kaftori et al. (1995*b*), and 100 samples per point for Van Hout (2011). The particle velocity rms exhibits a generally similar pattern of anisotropy to the fluid rms, but with higher values and much higher scatter. The ratio of u_p'/v_p' is approximately 2, compared to the fluid $u_f'/v_f' = 1.4$.

5.5 Inertial Particle Tracking

One of the main advantages of using time resolved PIV to investigate 2-phase particle laden flow is the facility to track inertial particles in real time. Dantec's DynamicStudio particle tracking add-on provides identification of sparse particle images and "tracking" between the two images of a classic double image pair, to give instantaneous position and velocity data. For the present work, a custom MATLAB script was written to read this data for each double image pair and hence track particles over multiple frames. The algorithm used is based on the "nearest neighbour" technique. Tracks extend as long as nearest neighbour positions can be validated, many extending over the whole width of the field of view. This tracking process was applied to each PIV data acquisition run of 1000 or 2000 double frames of each acquisition run. The analysis was repeated for 10 acquisition runs. Statistics could then be processed for the tracks from all of these acquisitions, totaling 10,000 or 20,000 frames of data. In all, 7 PTV data acquisitions were run, covering 3 Reynolds numbers, 2 particle loadings and 2 field of view setups. The first set of data acquisitions used the full camera resolution of 2352 × 1728 pixels to capture a field of view of 100mm × 75mm at a magnification of $M_0 = 0.16$. One acquisition, each of 10,000 double frames, was obtained at a particle loading of $\phi = 1.4 \times 10^{-5}$ for Reynolds numbers of $Re_\theta = 730$, 1420 and 2660 for this configuration. Acquisitions were next made at the same 3 Reynolds numbers for a smaller field of view of 47mm × 17.6mm, corresponding to 2352 × 832 pixels at a magnification of 0.34, but with a higher loading of $\phi = 2.8 \times 10^{-5}$. The reduced vertical resolution here allowed the frame rate to be doubled. Finally, returning to the original large field of view, the $Re_\theta = 2660$ test only was repeated for the higher loading of $\phi = 2.8 \times 10^{-5}$. Some typical particle trajectories from these tests are shown in Figure 5.10 and 5.11.

From Figure 5.10(a) an inertial particle initially at position $x^+ = 0$ and $y^+ \approx 55$, can be observed traveling stream-wise and then rapidly moving upwards from $x^+ = 200$ and $y^+ \approx 60$ to $x^+ = 300$ and $y^+ \approx 100$. Similarly from Figure 5.11(b), a particle initially at position $x^+ = 450$ and $y^+ \approx 25$, can be observed moving upwards and downwards while travelling in the stream-wise direction until it moves out of the field-of-view. This upwards and downward motions. Across the field-of-view (Figure 5.11(a), in general inertial particles close to the channel floor

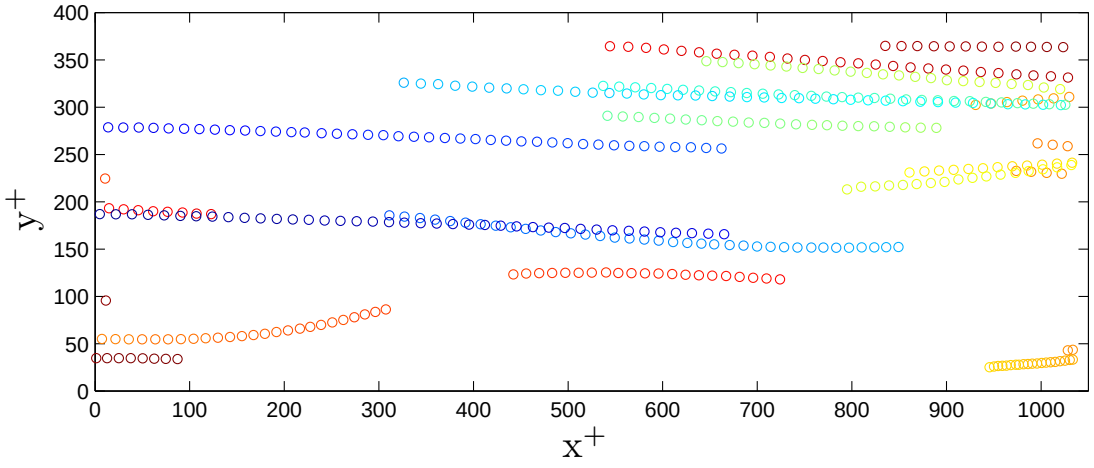

(a)

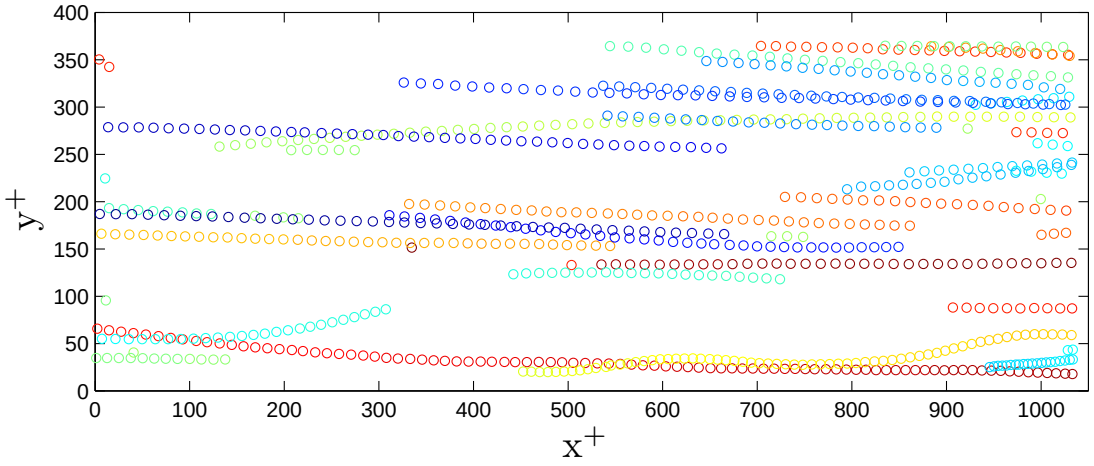

(b) .

FIGURE 5.10: Example of particle trajectories (Part 1)

can be seen to move either upwards away from the wall or towards the wall, indicating the presence of near wall flow structures and perhaps the hairpin vortex or its packets.

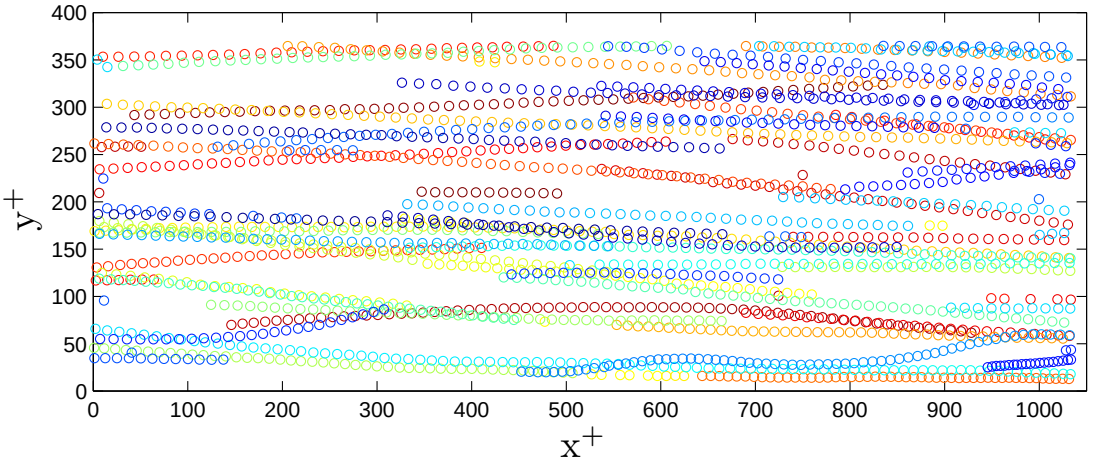

(a)

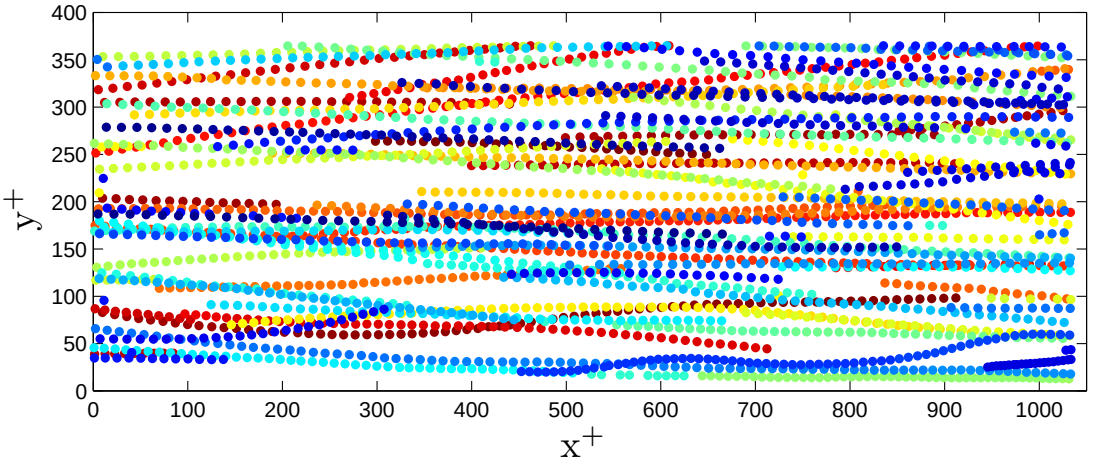

(b)

FIGURE 5.11: Example of particle trajectories (Part 2)

5.5.1 Particle track lengths

With the 2-D PIV, the ability to track a particle is limited by the time for which the particle remains within the light sheet thickness, as turbulence driven motion will occur normal to the light sheet plane. Use of a thicker light sheet would extend the recordable track lengths, but would "smear" the 2-D resolution of the fluid phase velocity field, obtained by conventional PIV, and so a compromise must be struck in order to simultaneously record both phases. At the outset, the only previous data for the 2-phase, time-resolved PIV were due to Van Hout (2011) who, at Re_θ= 435, recorded tracks for 583μm particles of length between 250 and 500 wall

units, where the full width of the field of view was just over 500 wall units. Maximum t^+ values for the tracks were up to 40. In view of the maximum track length corresponding to the width of the field of view, it is unclear whether this corresponds to a true maximum or not. One of the first objectives in tracking therefore was to investigate achievable track lengths.

Particle track length data in terms of non-dimensional time t^+ (= $t.u_\tau^2/\nu$) and non-dimensional streamwise displacement x^+ (= $dx.u_\tau/\nu$), using inner wall scaling were determined by analysing the PTV data for the three Reynolds numbers, two different magnifications and two particle loadings detailed at the beginning of Section 5.5, and the data are presented in Tables 5.2 to 5.4. Figure 5.12 shows examples of Pdf of particle tracks fro Re_θ = 730, 1420 and 2660 at volumetric loading, ϕ = 1.4 × $10^{-}5$ (Figure 5.12(a), 5.12(b), 5.12(c)), and 2.8 × $10^{-}5$ (Figure 5.12(d), 5.12(e), 5.12(f)) .

Parameters	Re_θ=730	Re_θ=1420	Re_θ=2660
Shear velocity, u_τ (m/s)	0.0051	0.0094	0.0189
Kinematic viscosity, ν (m^2/s)	9.7937×10^{-7}	9.6188×10^{-7}	9.7819×10^{-7}
Time between double frames, Δt (s)	0.004	0.004	0.004
Total no. particles images	25,6090	27,7402	25,8519
Total no. of particle tracks	13,357	17,431	23,142
Average track length (frames)	19.27	15.93	11.18
Average track length, t^+	2.05	5.86	16.33
Average track length, x^+	35.20	114.87	338.89
FOV width (wall units)	520	977	1932
Total no. of double-frames (taken over 10 acquisitions)	10,000	10,000	10,000

TABLE 5.2: Average track lengths in t^+ and x^+ for large FOV (M=0.16) at $\phi = 1.4 \times 10^{-5}$.

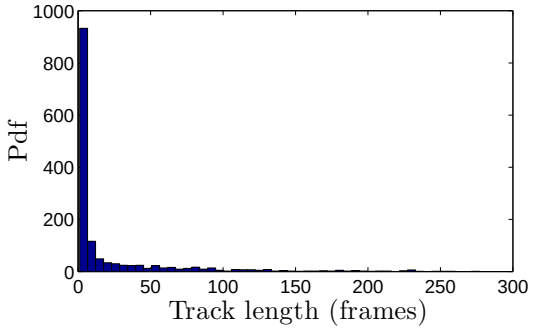

(a) Example of PDF of particle tracks (frames) for Re_θ = 730, FOV = 100mm × 75mm, $\phi = 1.4 \times 10^{-}5$.

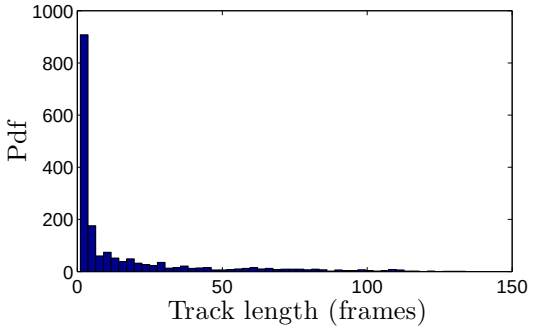

(b) Example of PDF of particle tracks (frames) for Re_θ = 1420, FOV = 100mm × 75mm, $\phi = 1.4 \times 10^{-}5$.

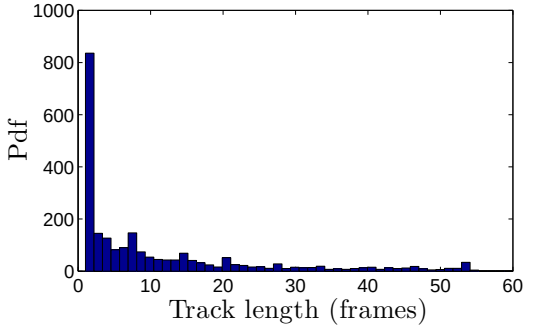

(c) Example of PDF of particle tracks (frames) for Re_θ = 2660, FOV = 100mm × 75mm, $\phi = 1.4 \times 10^{-}5$.

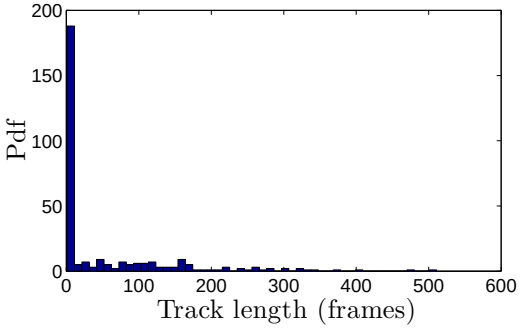

(d) Example of PDF of particle tracks (frames) for Re_θ = 730, FOV = 48mm × 17mm, $\phi = 2.8 \times 10^{-}5$.

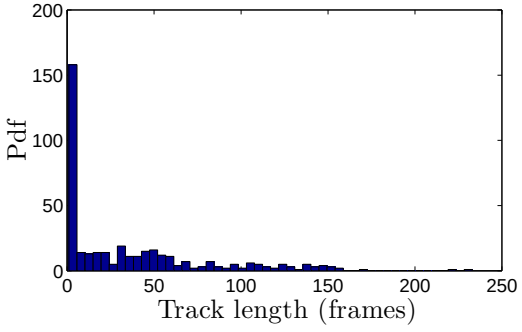

(e) Example of PDF of particle tracks (frames) for Re_θ = 1420, FOV = 48mm × 17mm, $\phi = 2.8 \times 10^{-}5$.

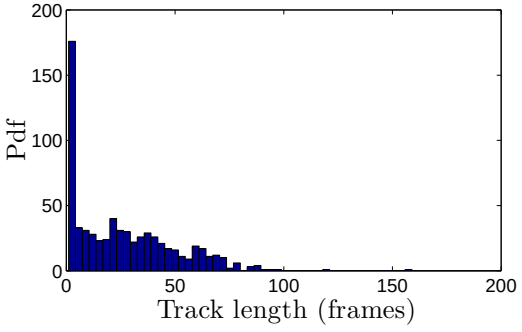

(f) Example of PDF of particle tracks (frames) for Re_θ = 2660, FOV = 48mm × 17mm, $\phi = 2.8 \times 10^{-}5$.

FIGURE 5.12: Pdf of particle tracks for Re_θ = 730, 1420 and 2660 at volumetric loading, $\phi = 1.4 \times 10^{-}5$ (Figure 5.12(a), 5.12(b), 5.12(c)), and $2.8 \times 10^{-}5$ (Figure 5.12(d), 5.12(e), 5.12(f))

.

Parameters	Re_θ=730	Re_θ=1420	Re_θ=2660
Shear velocity, u_τ (m/s)	0.0051	0.0094	0.0189
Kinematic viscosity, ν (m^2/s)	9.3931×10^{-7}	9.7189×10^{-7}	9.7937×10^{-7}
Time between double frames, Δt (s)	0.002	0.002	0.002
Total no. particles images	221,297	174,747	165,788
Total no. of particle tracks	8,052	5,034	6,703
Average track length (frames)	33.17	35.19	24.74
Average track length, t^+	1.84	6.40	18.04
Average track length, x^+	31.08	171.98	621.76
FOV width (wall units)	520	977	1932
Total number of double-frames	18,000	20,000	20,000

TABLE 5.3: Average track lengths in t^+ and x^+ for small FOV (M=0.34) at $\phi = 2.8 \times 10^{-5}$.

Parameters	Re_θ=2660
Shear velocity, u_τ (m/s)	0.0189
Kinematic viscosity, ν (m^2/s)	9.34487×10^{-7}
Time between double frames, Δt (s)	0.004
Total no. particles images	506,444
Total no. of particle tracks	43,227
Average track length (frames)	11.72
Average track length, t^+	17.72
Average track length, x^+	353.55
FOV width (wall units)	1932
Total number of double-frames	20,000

TABLE 5.4: Average track lengths in t^+ and x^+ for large FOV (M=0.16) at $\phi = 2.8 \times 10^{-5}$.

5.6 Conditional statistics for inertial particles

Figure 5.13 shows all the inertial particle samples sorted according to the quadrant of the local velocity perturbation, as first suggested by Willmarth and Lu (1972). As described by Willmarth and Lu (1972), the quadrants may be associated with turbulence structures, with fluid ejections having positive v' and negative u' perturbations, hence lying in the second quadrant, whilst sweep features have perturbations of opposite signs, and so lie in the fourth quadrant. First and third quadrant events have no such clear interpretations. Even from this figure it is clear that most of the particle samples are associated with second or fourth quadrant events. However, as observed by Willmarth and Lu (1972), whilst ejection events are always associated with the second quadrant, not all second quadrant events are ejections. The other conditional

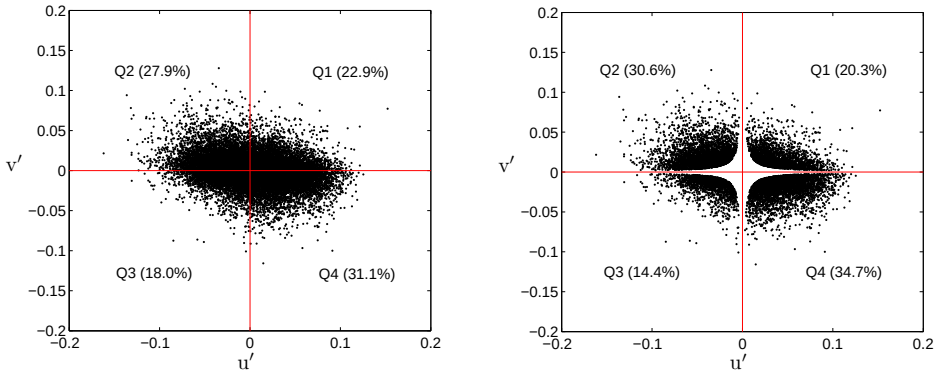

(a) H=0

(b) H=0.1

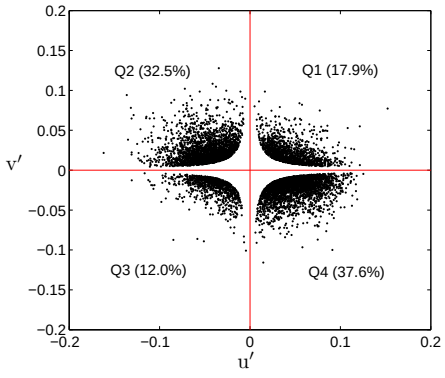

(c) H=0.2

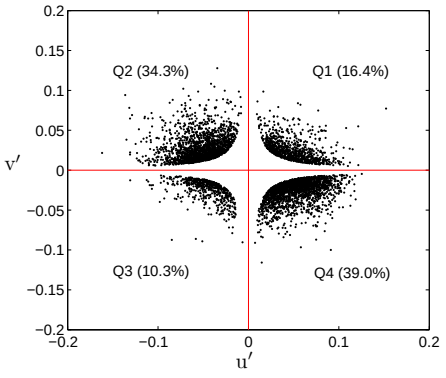

(d) H=0.3

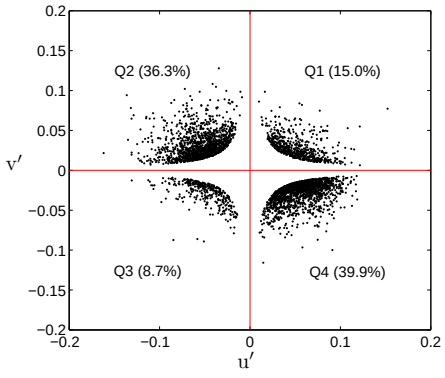

(e) H=0.4

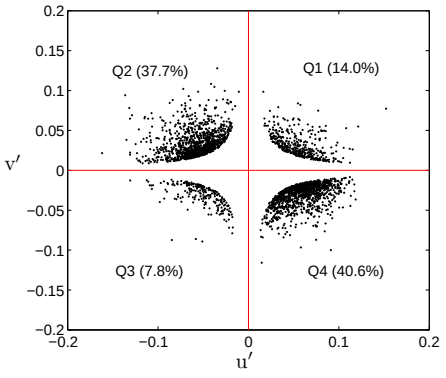

(f) H=0.5

FIGURE 5.13: Particle samples sorted by quadrant of local fluid velocity perturbation (after Willmarth and Lu (1972)). Figure 5.13(a) Raw data, Thresholded data: 5.13(b) H=0.1, 5.13(c) H=0.2, Figure 5.13(d) H=0.3, 5.13(e) H=0.4, and 5.13(f) H=0.5 .

factor is the magnitude of the perturbations. To filter off weak perturbations, Willmarth and Lu (1972) used a perturbation threshold to produce a central hyperbolically bounded "hole" in the quadrant diagram, and the present inertial particle samples are plotted with this convention in Figure 5.13(b), 5.13(c), 5.13(d), 5.13(e), and 5.13(f). The actual threshold value used is clearly somewhat subjective. After sorting, a hyperbolic bounded hole with value that is still subjective, the preference to the second and fourth quadrant event is clearer.

On this basis, the preference for second and fourth quadrant event is even clearer. Particle counts for each quadrant are given in Table 5.5. Lumping the indeterminate quadrant 1 and 3 events with the weak events in the central "hole", this suggests that typically a particle will spend 100*(N Q2)/(total) $\%$ of its time interacting with an ejection event, 100*(N Q4)/(total) $\%$ of its time interacting with a sweep event, and 100*(remainder)/(total) $\%$ of its time in random "quiescent" turbulence. From table 5.5, a clear preference of particle can be observe to reside in both ejections and sweeps, 37.7$\%$ and 40.6$\%$, a difference of approximately 2$\%$. For Q1 and Q3, percentage of particle residing in each quadrant are significantly less. With H set to 0.5, the percentage particle residing in Q1 and Q3 are 14$\%$ and 7.8$\%$ respectively. Raw data also indicate similar behaviour where preferential are to Q2 and Q4 events.

The quadrant data indicate that, when the threshold, H is set to 0.5, the percentage of the particle residing within quadrant 2 and quadrant 4 are almost similar in percentage value, with only a 2$\%$ difference. Theoretically, in the presence of a hairpin vortices or its packets, both ejection and sweeps are also present. The inclined leg and head of the hairpin induce low speed fluid through the inclined loop of the structure, resulting in the Q2 ejection event, where fluid together with the inertial particles to move upward and a countering Q4 sweep event which resulted in the particle moving downwards towards the channel floor. It is does expected that, since the Q2 and A4 event occurs in pairs, then their effects on particle trajectory would be almost similar in percentage and this is clearly indicated in the quadrant analysis data. Thus it can be said that, based on the reported data, the presence of hairpin vortex is supported.

The hairpin structures can be identified by their velocity signatures as described in Section 2.2.2, and as shown in Figure 2.4 and Figure 2.5. Although contour profiles plot of velocity fluctuations or velocity profiles, swirling strength and Q-criterion profile do indicate the presence of ramp-like structures thus indicating the presence of hairpins vortex or hairpin packets,

as shown in Figure 4.28(b), Figure 4.28(a), Figure 4.29(a), and Figure 4.29(b) respectively, the presence of ejections (Q2) and sweeps (Q4) events causing particles to move upwards and downwards relatively close to the wall also indicate the presence of hairpin vortices and its packets at play as discussed in Section 2.2.1. The high percentage of Q2 ($+v'$, $-u'$) and Q4 event ($-v'$, $+u'$), each having 38% and 40% compared to Q1 and Q3 events do indicate the major role played by hairpin vortices and its packets in particle traveling upwards and downwards within the turbulent boundary layer.

	Total count	Quadrant 1 (%)	Quadrant 2 (%)	Quadrant 3 (%)	Quadrant 4 (%)
Raw Data	22671	22.9	27.9	18.0	31.1
Thresholded H=0.1	11764	20.3	30.6	14.4	34.7
H=0.2	7691	17.9	32.5	12.0	37.6
H=0.3	5353	16.4	34.3	10.3	39.0
H=0.4	3855	15.0	36.3	8.7	39.9
H=0.5	2783	14.0	37.7	7.8	40.6

TABLE 5.5: No. of particles recorded in each fluid velocity perturbation quadrant.

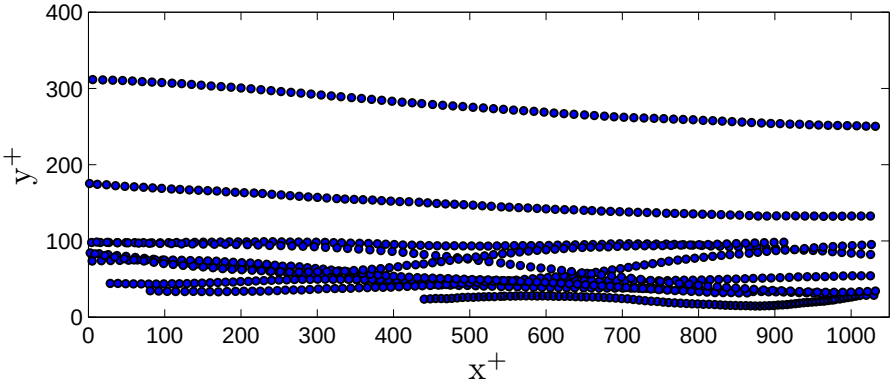

FIGURE 5.14: Plot of particle trajectories for the 10 longest tracks.

Both figure 5.16 (a) and 5.17 shows the same particle trajectory near to the channel wall at approximately y^+ = 21 that is affected by Q4 sweep event along its trajectory between approximately X(pix) = 0 up to 900, then Q1 upward motion between X(px) = 900 to 1500, and later by a Q4 sweep event between X(px) = 1500 to the end of the field-of-view. The particle track shown Figure 5.17, indicates the influence of velocity perturbation on the particle trajectory, and the quadrant events responsible for the particle motion within the available field-of-view.

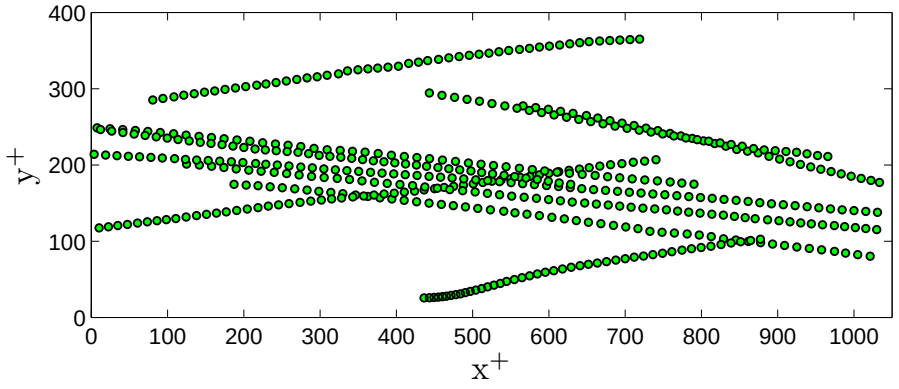

FIGURE 5.15: Plot of particle trajectories for the 10 greatest y^+ movement.

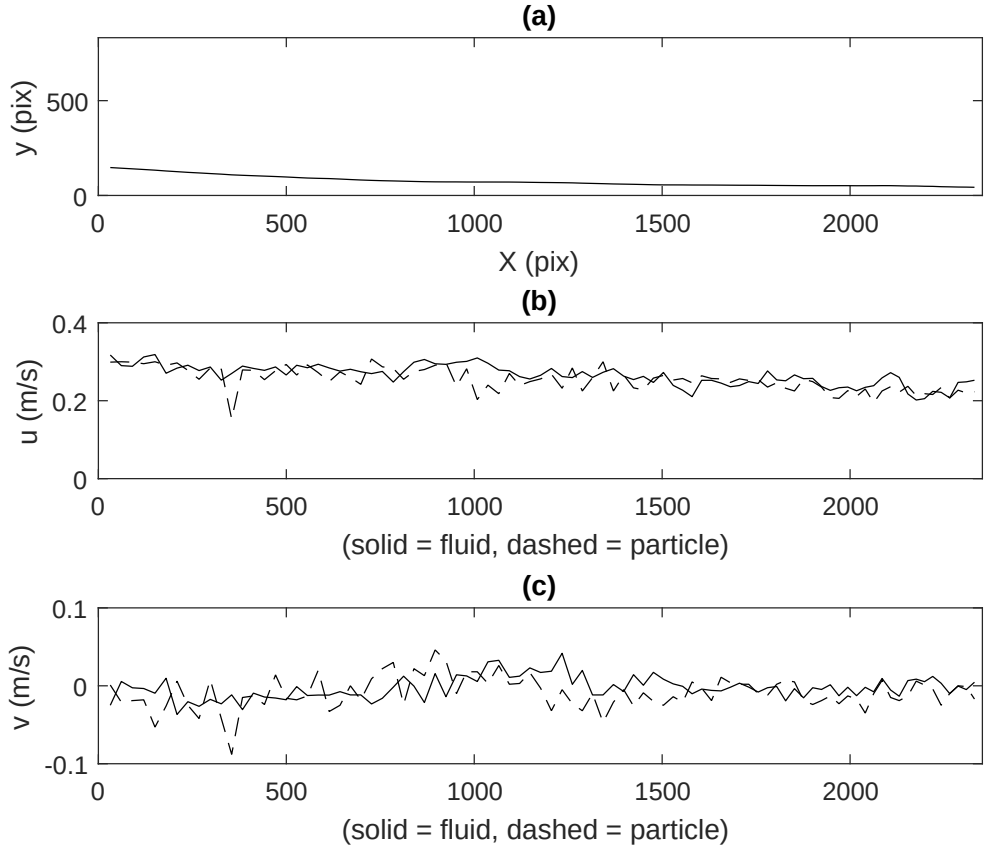

FIGURE 5.16: Plot of a) Particle trajectory near the channel wall, $y^+ \approx 21$ down to $y^+ \approx 7$ at the end of the FOV. b) Plot of stream-wise fluid and particle velocity along particle track, and c) plot of wall-normal fluid and particle velocity along particle track.

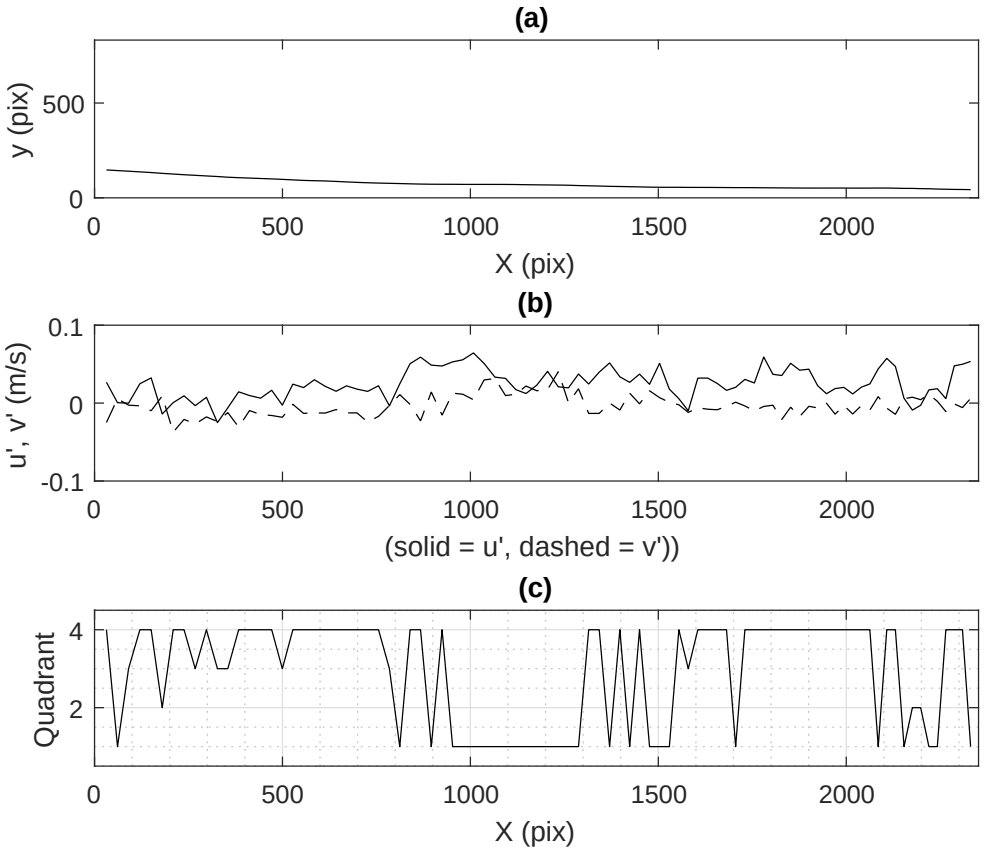

FIGURE 5.17: Plot of a) Particle trajectory near the channel wall, $y^+ \approx 21$ down to $y^+ \approx 7$ at the end of the FOV, b) Plot of fluid velocity perturbation along particle track, and 3) Quadrant number along the particle track with Q4 sweeps event along the particle trajectory.

Figure 5.18, Figure 5.19 and Figure 5.20 shows particle trajectory dominated by the Q2 ejection event along its trajectory. Figures 5.21 and 5.21 shows particle trajectory at approximately $y^+ \approx= 36$ (mid FOV) traveling up to $y^+ \approx= 72$ showing Q2 ejection and Q4 sweeps event at $y^+ \approx 65$ traveling down to $y^+ \approx= 14$, respectively affecting the particle trajectories. Figure 5.19a shows an interesting behaviour where the particle started off moving horizontally, and suddenly moving upwards. The velocity fluctuation plot in Figure 5.19b shows a high vertical velocity perturbation in the fluid flow starting at X (px) at 1500, and it can be seen from Figure 5.19c showing the quadrant event plot, that the particle within the region X(px) approximately 1400 to 1800 is subjected to an ejection event.

For particle further up the FOV at approximately $y^+ = 65$ up to 130, similar Q2 and Q4

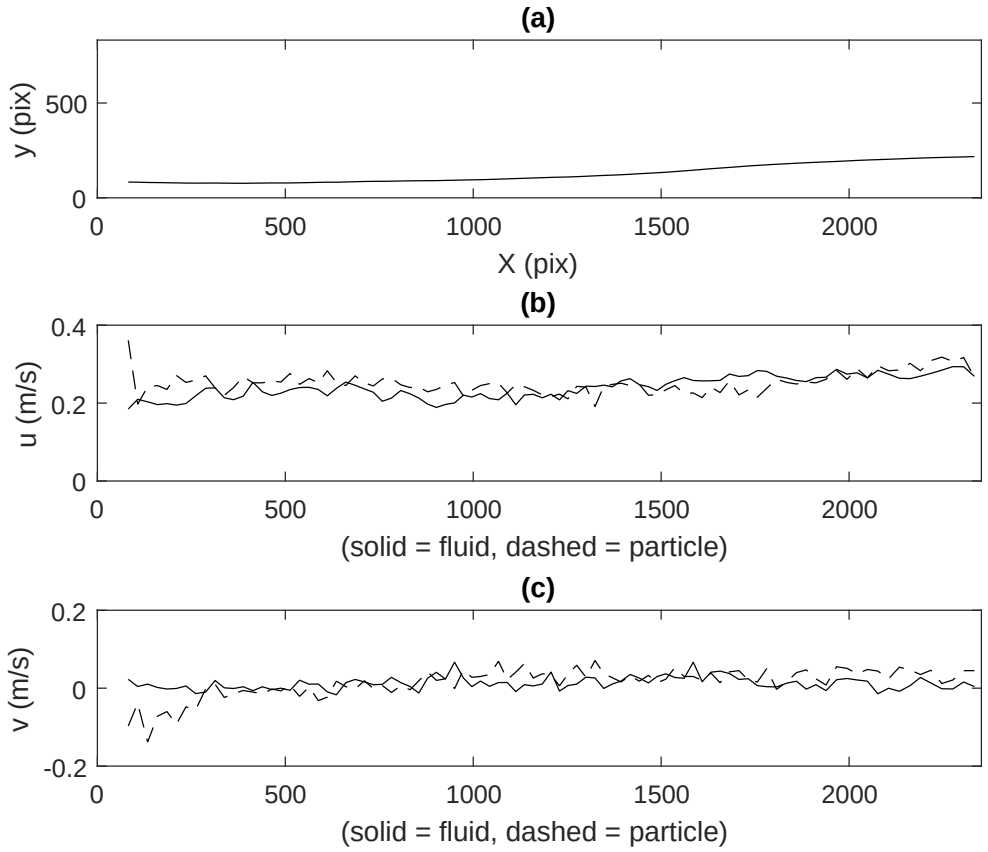

FIGURE 5.18: Plot of a) Particle trajectory near the channel wall, $y^+ \approx 7$ up to $y^+ \approx 36$ at the end of the FOV, b) Plot of stream-wise fluid and particle velocity along particle track, and c) plot of wall-normal fluid and particle velocity along particle track.

events are also found to affect particles trajectories as shown in Figure 5.23 and Figure 5.24, where Q2 and Q4 events affecting the particle trajectories respectively. Figure 5.23 shows a particle trajectory cleanly affected by only the Q2 ejection event. Figure 5.25 shows particle trajectory moving along $y^+ \approx 58$ affected by Q1, Q2, Q3 and Q4 event.

From the particle trajectory plots, it can be seen that particles trajectory are affected by the Q2 ejection and Q4 sweep event resulting in particle moving upwards or downwards towards the wall. This can be linked to the presence of hairpin vortices or their packets within the turbulent boundary layer affecting particle movement along the channel. Although some plots are not as clear compared to some (e.g. Figure 5.23), but in general the indication to the presence of boundary layer structure namely, haipin vortices is does supported.

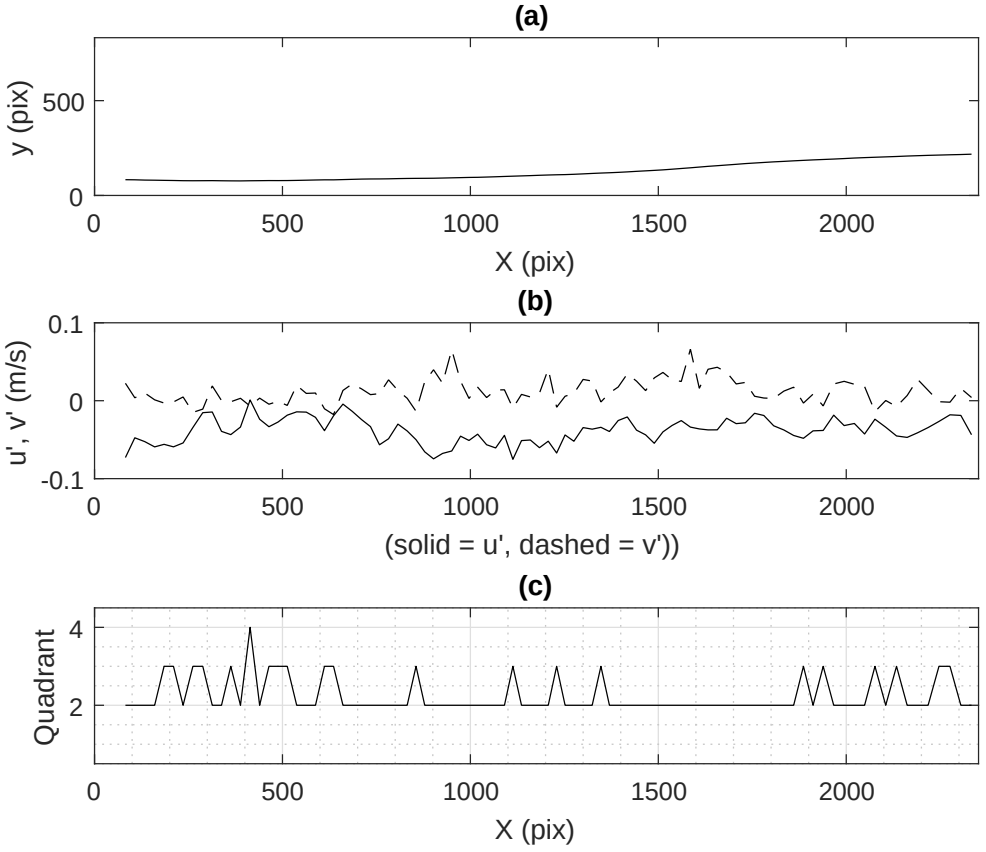

FIGURE 5.19: Plot of a) Particle trajectory near the channel wall, $y^+ \approx 7$ up to $y^+ \approx 36$ at the end of the FOV, b) Plot of fluid velocity perturbation along particle track, and 3) Quadrant number along the particle track with Q2 ejection event along the particle trajectory.

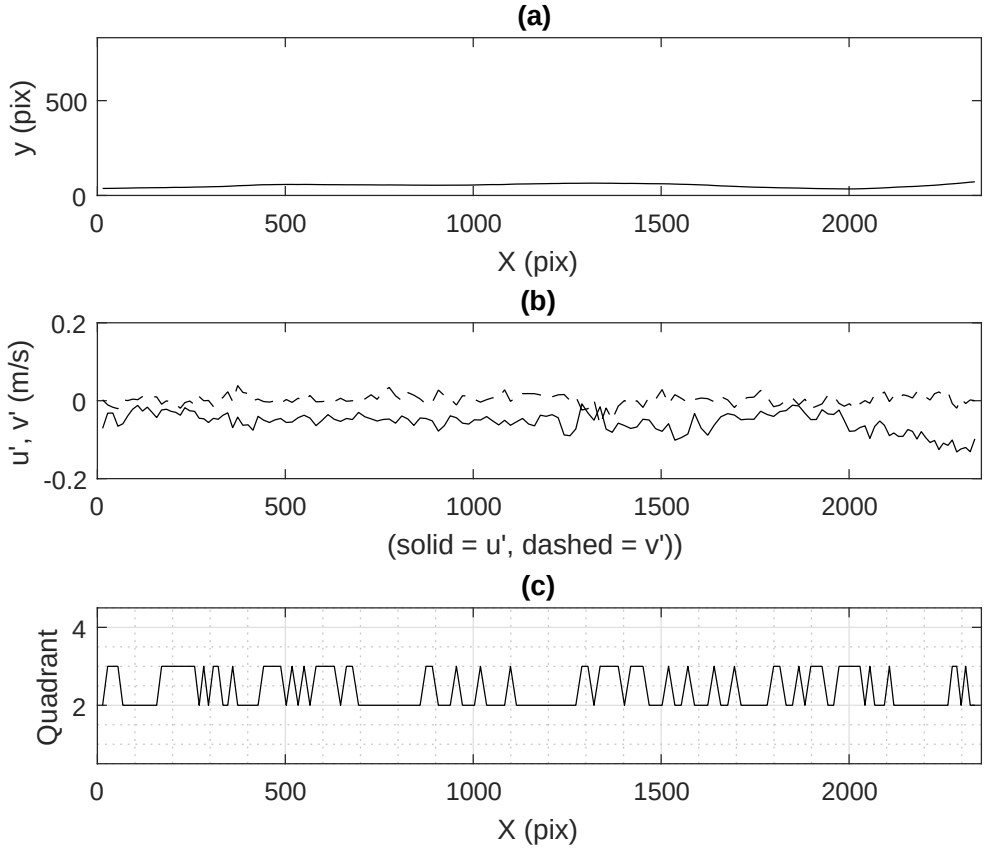

FIGURE 5.20: Plot of a) Particle trajectory near the channel wall, $y^+ \approx 7$ along the trajectory, b) Plot of fluid velocity perturbation along particle track, and 3) Quadrant number along the particle track with Q2 ejection event along the particle trajectory.

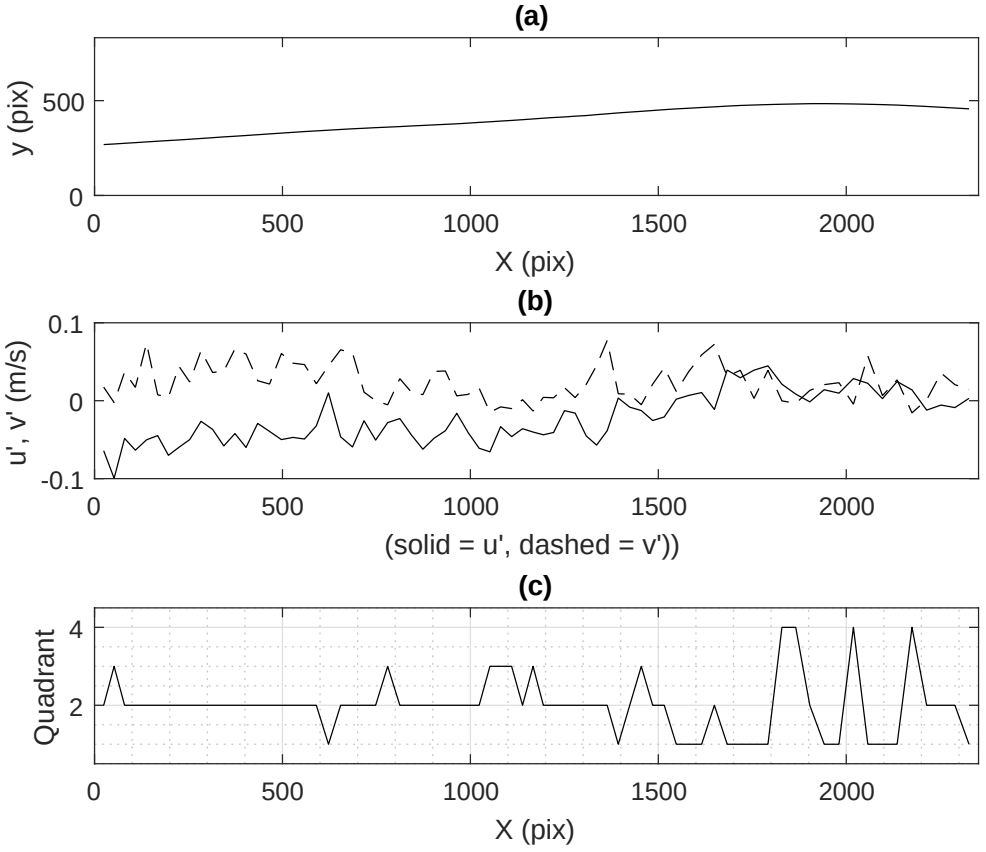

FIGURE 5.21: Plot of a) Particle trajectory near the channel wall, $y^+ \approx 36$ up to 72, b) Plot of fluid velocity perturbation along particle track, and 3) Quadrant number along the particle track with Q2 ejection event dominating the particle trajectory.

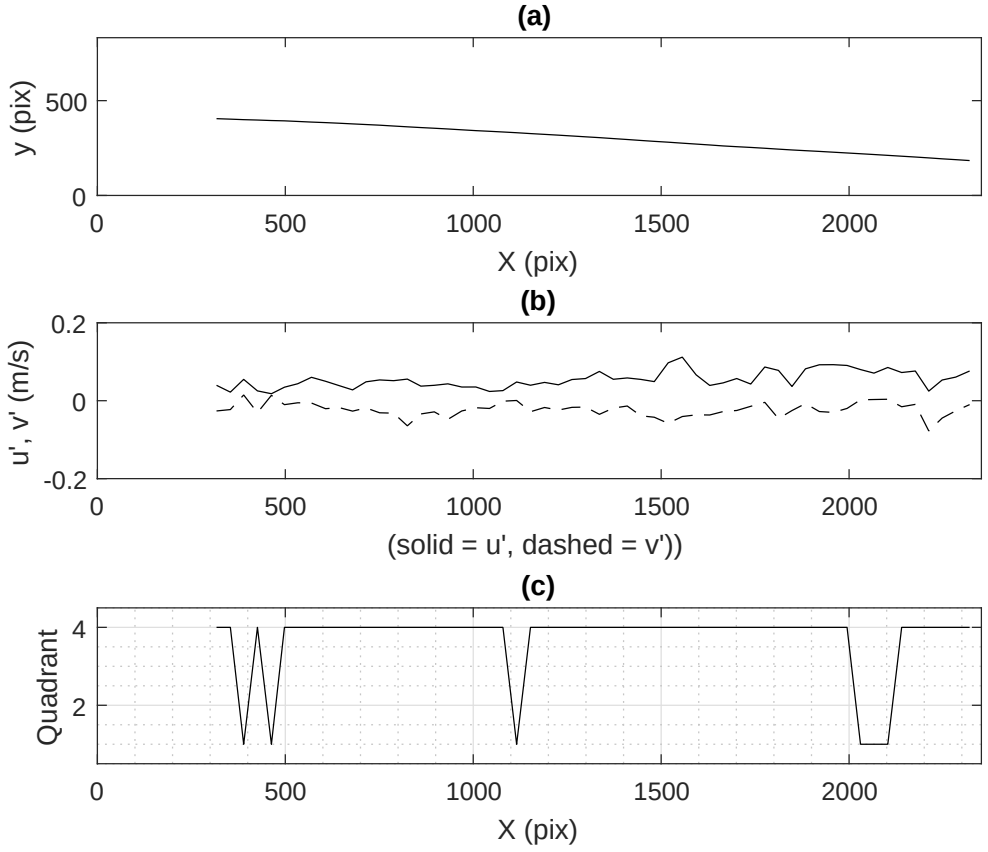

FIGURE 5.22: Plot of a) Particle trajectory near the channel wall, $y^+ \approx 72$ down to 28, b) Plot of fluid velocity perturbation along particle track, and 3) Quadrant number along the particle track with Q4 sweep event dominating the particle trajectory.

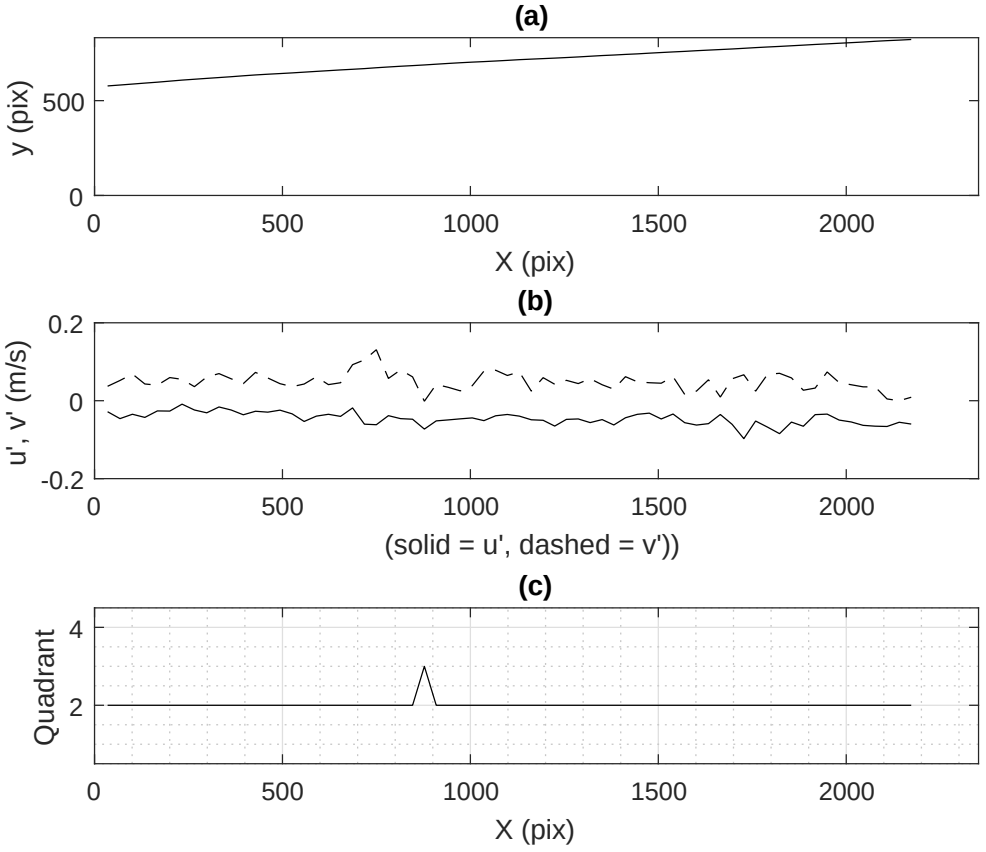

FIGURE 5.23: Plot of a) Particle trajectory near the channel wall, $y^+ \approx 86$ up to 130, b) Plot of fluid velocity perturbation along particle track, and 3) Quadrant number along the particle track with Q2 ejection event dominating the particle trajectory.

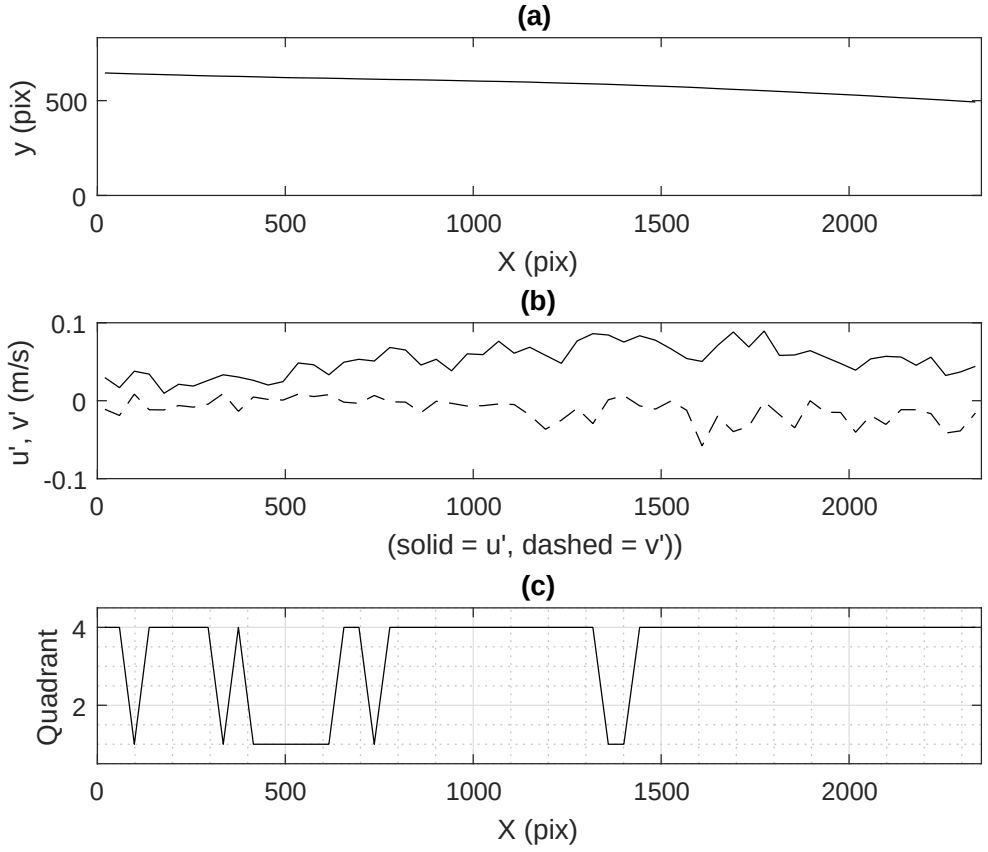

FIGURE 5.24: Plot of a) Particle trajectory near the channel wall, $y^+ \approx 86$ down to 65, b) Plot of fluid velocity perturbation along particle track, and 3) Quadrant number along the particle track with Q4 sweep event dominating the particle trajectory.

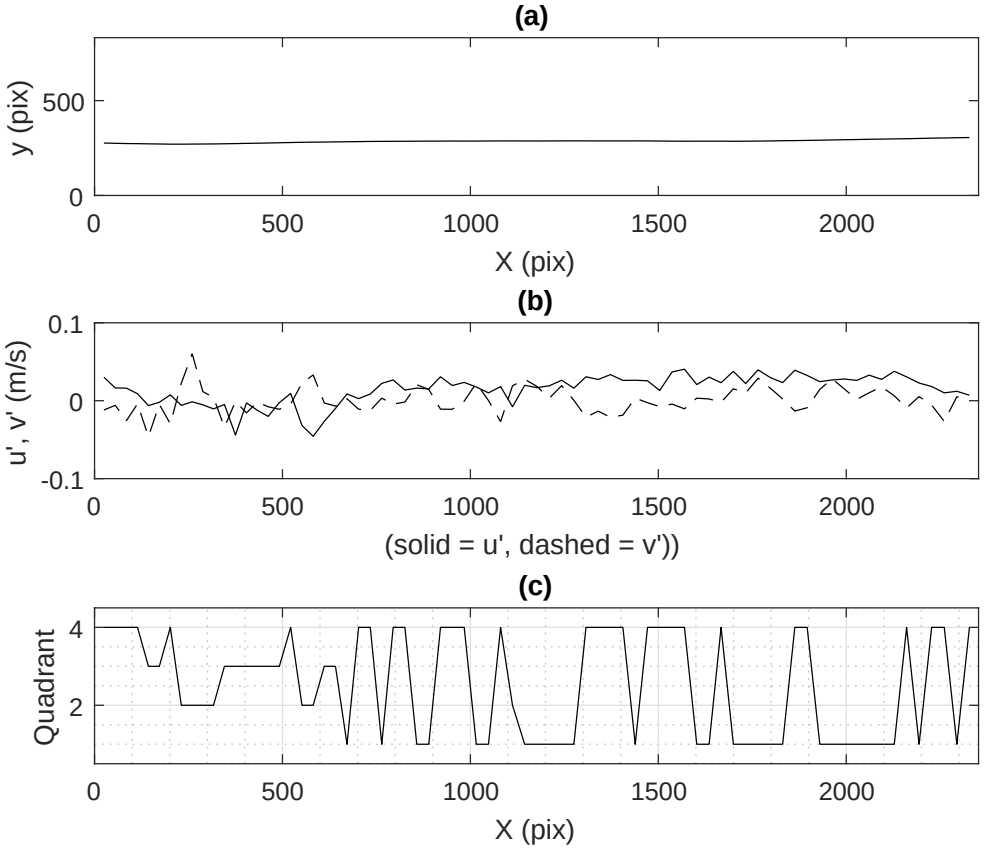

FIGURE 5.25: Plot of a) Particle trajectory near the channel wall, $y^+ \approx 58$, b) Plot of fluid velocity perturbation along particle track, and 3) Quadrant number along the particle track affected byQ1, Q2, Q3 and Q4 event along the particle trajectory.

5.6.1 Particle-fluid velocity correlation

The fluid-particle velocity correlation, r_{pf} for each trajectory were calculated using the instantaneous velocity data from both the particle and flow phase. In the case where we are following actual velocity values along a trajectory, rather than a time series, the relevant correlation coefficient formula is:

$$r_{pf} = \frac{s_{pf}}{s_p . s_f} = \frac{\sum (u_p - \overline{u}_p) . (u_f - \overline{u}_f)}{\sqrt{\sum (u_p - \overline{u}_p)^2 . (u_f - \overline{u}_f)^2}} \tag{5.10}$$

where $\overline{u}_p$ and $\overline{u}_f$ are the average values for u_p and u_f for all samples along the trajectory. The fluid-particle velocity correlation along the measured particle trajectories, averaged over all the available trajectories is R, given by:

$$R = \frac{1}{N} \sum r_{pf} \tag{5.11}$$

where N is the number of trajectories.

The result should be a single number between -1 and 1, with 1 indicating perfect correlation, 0 indicating no correlation, and -1 indicating perfect negative correlation. Thus, each trajectory will yield only one number. This correlation values could be averaged over all trajectories to give an "average" correlation coefficient.

Figure 5.26 is an example of a single particle track near to the channel floor where it can be observed that the streamwise and wall-normal velocities correlates very well from X (pix) approximately 600 to 2500. The correlation value for this particular trajectory is $r_{pf} = 0.7740$ for the streamwise velocities and 0.2118 for the wall-normal velocities, which indicates a higher degree of correlation between the the particle and fluid velocities.

Figure 5.27 is an example of another particle track near to the channel floor where it can be observed that the streamwise and wall-normal velocities do not correlate at X (pix) approximately from 0 to 1100. The correlation value for this particular trajectory turns out to be r_{pf}

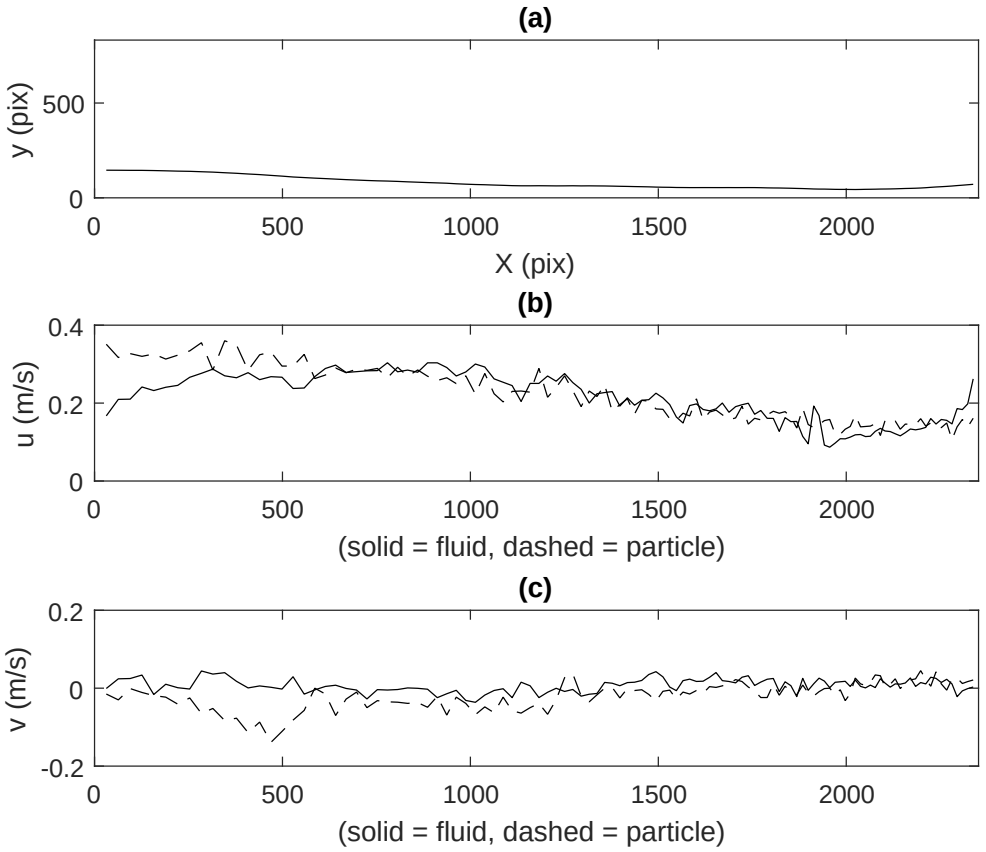

FIGURE 5.26: Plot of a) Particle trajectory near the channel wall, b) Plot of stream-wise fluid and particle velocity along particle track, and c) plot of wall-normal fluid and particle velocity along particle track.

= 0.3758 for the streamwise velocities and −0.0744 for the wall-normal velocities, which indicates a weaker correlation between the particle and fluid velocity streamwise velocity, and a negative correlation between the wall-normal velocity, which could be visually observed from the Figure 5.27.

So the picture seems to be that the mean particle velocity does seem to follow the mean fluid velocity fairly closely, with intervals where the two velocities do show evidence of correlation, as shown in the combined velocity plots, but looking at the statistical correlation between the short time-period velocity variations overall, the correlation is much weaker. Perhaps this is not so surprising, given the significant inertia of the large particles.

Figure 5.26 and Figure 5.27 are two examples of particle trajectories and their streamwise

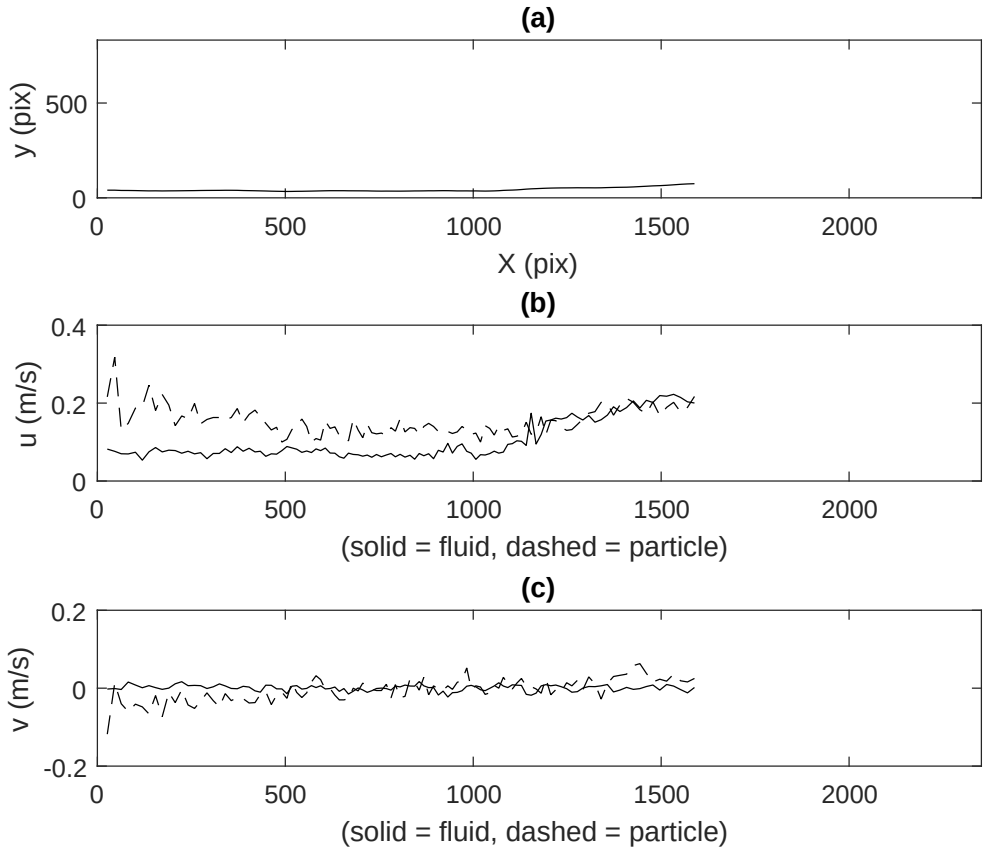

FIGURE 5.27: Plot of a) Particle trajectory near the channel wall, b) Plot of stream-wise fluid and particle velocity along particle track, and c) plot of wall-normal fluid and particle velocity along particle track.

and wall-normal particle-fluid velocity correlation would not represent the whole available data from the two phase measurements. The correlation from the two figures (Figure 5.26 and 5.27 indicate that the streamwise correlation between the particle and fluid is higher than that of the wall-normal.

The histogram plot of the particle-velocity correlation shown in Figure 5.28 and Figure 5.29, indicate that correlation between the particle and fluid velocities both in the streamwise and wall-normal, follows almost a normal distribution that peak around zero values indicating no correlation. It can be concluded that the correlation between the particle and fluid velocities are weak, except for the present of "spikes" at the two extremes, i.e. -1 and 1, but these two extremes do not represent the whole available data. Figure 5.28 and Figure 5.29 represent

each single measurement run only, and to determine the average correlation coefficient for the available seven run with 8,225 particle trajectories altogether, the average correlation coefficient for all tracks are calculated based on the data in Figure 5.28, Figure 5.29 and other available data from the measurement. Table 5.6 gives the particle-fluid velocity correlation for each experimental run and their average correlation coefficient values.

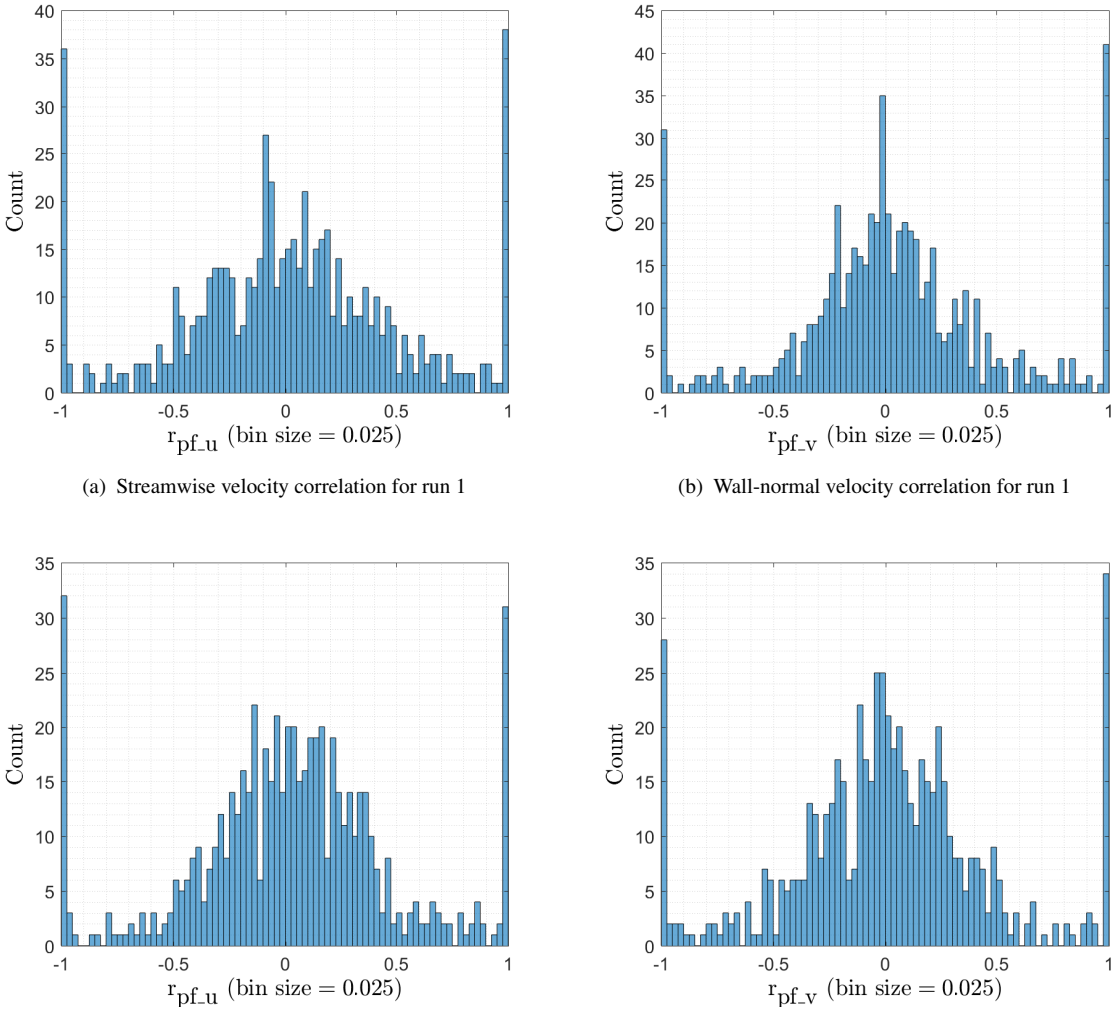

(a) Streamwise velocity correlation for run 1

(b) Wall-normal velocity correlation for run 1

(c) Streamwise velocity correlation for run 2

(d) Wall-normal velocity correlation for run 2

FIGURE 5.28: Histogram plot of particle-fluid velocity correlation for run 1, and 2.

Table 5.6 gives the correlation coefficient for each run of the 2000 double-frame images acquired as Ru and Rv, where Ru are the averaged particle-fluid streamwise velocity correlation coefficient, and Rv is the particle-fluid wall-normal velocity correlation coefficient for each individual run. The total number of particle tracks used to calculate the average correlation coefficient, R for the streamwise and wall-normal velocity is 8225, and this gives a correlation

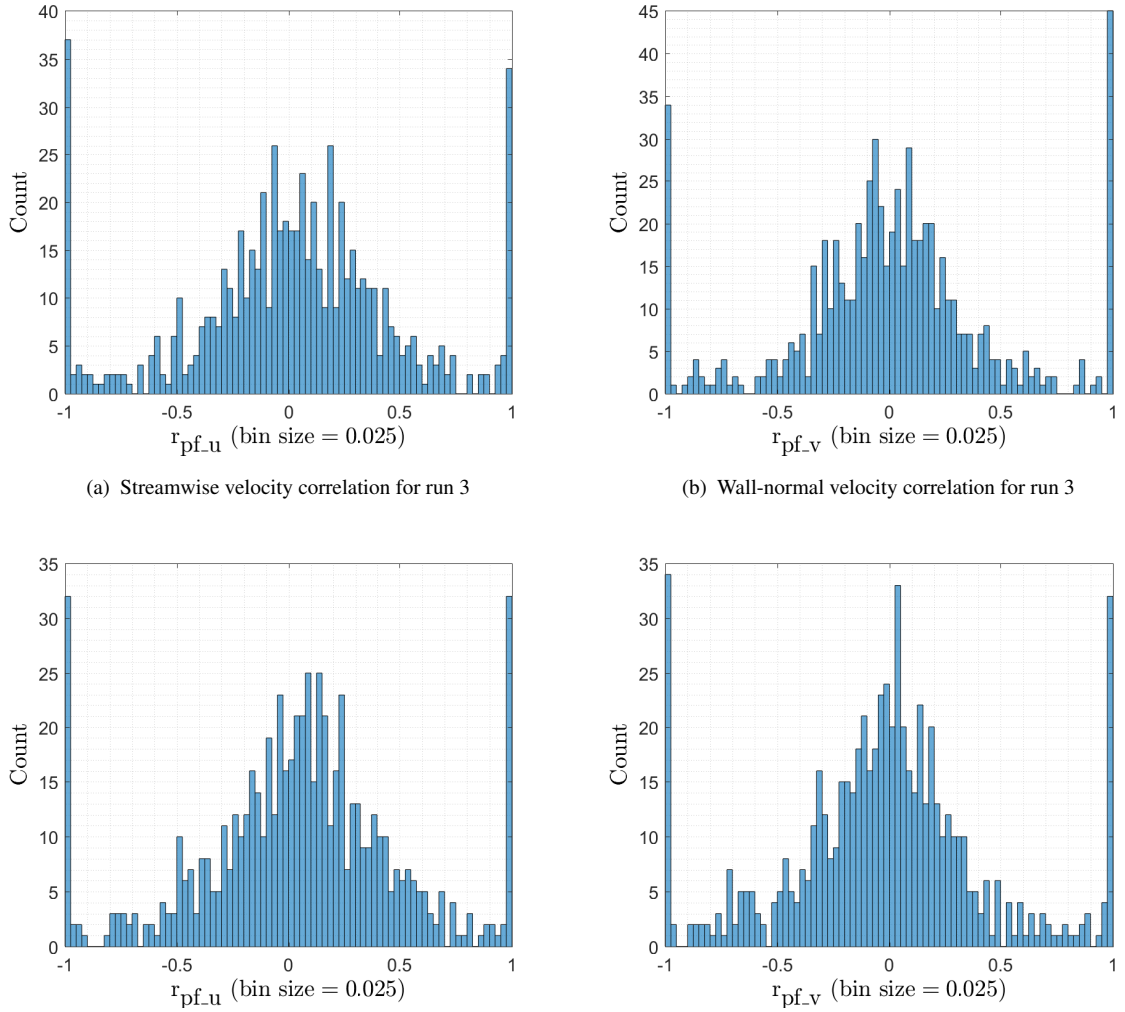

(a) Streamwise velocity correlation for run 3

(b) Wall-normal velocity correlation for run 3

(c) Streamwise velocity correlation for measurement run 4

(d) Wall-normal velocity correlation for measurement run 4

FIGURE 5.29: Histogram plot of particle-fluid velocity correlation for run 3 and 4.

coefficient, R for streamwise and wall-normal as 0.0261 and 0.000643, respectively. This value shows much weaker correlation as opposed to individual particle tracks, where the the wall-normal value indicates almost no correlation. These two values indicate that the mean particle velocity does seem to follow the mean fluid velocity, but on average, the correlation is much weaker for both streamwise and wall-normal velocity components.

Experimental run no.	Ru	Rv	No. of particle tracks
1	0.0053	0.0221	1114
2	0.0260	0.0088	966
3	0.0207	0.0118	1222
4	0.0433	-0.0206	1149
5	0.0018	-0.0178	1164
6	0.0608	-0.0188	1403
7	0.0248	0.0190	1207
Total no. of particle tracks	-	-	8225
Correlation Coefficient, R	0.0261	0.000643	-

TABLE 5.6: Streamwise particle-velocity correlation coefficient, Ru, and wall-normal particle-velocity correlation coefficient, Rv, and the average particle-fluid velocity correlation, R, for streamwise and wall-normal velocities.

5.7 Conclusions

Two-phase experiments have been carried out using the newly built 3m open-channel experimental rig. Initial experimental testing of the channel using both LDV and PIV has proven that the characteristic behaviour of the flow was sufficient and meets the two-phase experiments requirement.

For the two-phase measurements, 200μm secondary phase particles that are neutrally buoyant were used and two series of experiments were run with two particle loadings of $\phi = 1.4 \times 10^{-5}$ and 2.8×10^{-5}. These tests were carried out at a single Reynolds number of $\mathrm{Re}_\theta = 3000\,(\mathrm{Re}_\tau = 890)$. The second series of experiments, carried out at the same two volumetric loadings and at three Reynolds numbers, Re_θ = 730, 1420 and 2660, concentrated on tracking the inertial particles in real time. Two experimental setups were used, one at a larger field of view of 100mm (x) × 75mm (y), allowing a longer tracking distance, and one at a reduced field of view of 48mm × 17mm with half sensor resolution, to look at the effects of turbulent structures on inertial particle transport.

For clear water tests, LDV gave u_τ = 0.0189m/s, using the Newton's law of viscosity and a linear fit in the sub-layer region, whereas PIV gave u_τ= 0.0197m/s, using the Clauser method since data were unavailable very close to the wall. This amounts to a 4% difference in friction velocity. For the two-phase tests, only PIV data were available, and the value of u_τ obtained by

the Clauser fit was 0.0214m/s for both inertial particle loadings, ϕ = 1.4 × 10^{-5} and ϕ = 2.8 × 10^{-5}. This represents a 7.6% increase in friction velocity over the clear water result, based on PIV in all cases.

The LDV profile agrees well with the PIV and neither of the two PIV inertial particle loadings showed no discernible deviation from the clear water PIV profile. In the region 400 < y^+ < 800 loading causes the mean velocity to fall progressively below the clear water value, with the higher loading increasing this deviation, approximately proportionally. This contrasts with the results of Van Hout (2011), who found no variation in the velocity profile with loading for a fully developed closed channel flow. Kiger and Pan (2002) did find, again for fully developed closed channel flow, that the presence of inertial particles gave rise to a decrease in the mean velocity over the mid-region of the profile, but in their case the effect extended much closer to the wall. It should be noted also that their inertial particles were not neutrally buoyant, having a density ratio of approximately 2.6.

Re-plotting the profile with a logarithmic scale for y^+ to give the classic "law of the wall" plot confirms both the quality of the measurements and insensitivity to particle loading in the sub-layer and logarithmic regions, with the deviation due to inertial particles being confined to the wake region.

The PIV u'^+ profiles for zero loading and for the maximum inertial particle loading of 2.8 × 10^{-5} are virtually indistinguishable; in fact the variations are significantly less than the small deviation from the LDV values. This is in agreement with previous work for neutrally buoyant inertial particles, but differs from Kiger and Pan (2002) increase in u'^+ for "heavy particle" laden flow. The stress profiles indicate a reduction in stress associated with inertial particle loading, with the effect being more significant for the normal stresses.

The velocity profile of the flow and particle agrees well for both low and high magnifications with a slight increase and decrease in the friction velocity. The difference equates to 2.3 % and 2.5% respectively. The slight increase and decrease in the friction velocity of both the fluid and the particle phase indicates that the particles used for the experiments have negligible effect on the fluid phase. The only discernible effect can be seen from the rms plot where particle rms of fluctuating velocities are significantly higher compared to fluid ones.

Conditional statistics for the inertial particles based on the quadrant method following the work of Willmarth and Lu (1972) show a clear preference for the particles to reside in both ejections and sweeps with both accumulating to 37.7% and 40.6% respectively, a difference of approximately 2%. A low preference can be observed to Quadrant 3 compared to Quadrant 1.

Analysis on the trajectory of a particle were carried out and various plots were created on 1) particle trajectory near the wall and moves upwards from the channel floor, 2) particle trajectory near the wall and moves inwards towards the wall, 3) particle trajectory almost horizontal to the channel floor, 4) particle trajectory in the mid section moving away from the wall 5) particle trajectory in the mid section moving towards the wall, 6) particle trajectory in upper section of the FOV moving upwards, 7) particle trajectory in upper section moving downwards, and 8) particle moving almost horizontally in the mid-section of the FOV.

These figures indicate that when particle movement are influence by both the fluctuation in the streamwise velocities, and also the wall-normal velocity, where the latter plays a much influential role in the upwards and downwards movement. The upward motion is generally as a result of the Q2 or ejection event, and downward motion is influence by Q4 or sweep event. Particle trajectory that are horizontal with slight upward and downward fluctuations, the quadrant event as shown in Figure 5.25, fluctuates form Q1, Q2, Q3 and Q4. This fluctuations in the quadrant event shows the complex motion of particles along the FOV, but it can clear be observed that upward motion correlates to Q2 event and downward motion to Q4 sweep event.

Particle-fluid velocity correlation results indicate that, the average correlation between the particle and fluid streamwise and wall-normal is fairly week. The average particle-fluid velocity correlation coefficient is determined to be 0.0261 and 0.000643 for streamwise and wall-normal velocities, respectively. This results is surprising because visual observation indicate otherwise, but given the significant inertia of the large particles, this results seem to be realistic. For a single particle trajectory, the particle-fluid velocity correlation is rather weak for both especially for the wall-normal velocities, where it is found to be nearly uncorrelated.

Chapter 6

Discussion and Conclusions

6.1 Discussion and Conclusion

A major task prior to the research work were to develop and improve an existing open-channel experimental rig donated by Dantec Dynamics to meet the requirement of a two-phase flow investigations. As received, the experimental rig was a two meter long open-channel and the documentation that existed suggested a working section velocity of 0.5 - 1.0 m/s that would satisfy Newcastle two-phase flow rig requirement of 0.5m/s. The original water channel consisted of an open top, rectangular, glass walled channel with width 332mm and depth 210mm and length 2000mm. The inlet consisted of a simple bell-mouth entry and two perforated plate were fitted in the inlet tank to reduce inlet flow disturbances. The pump was driven by a 1kW electric motor via a hydraulic variable speed coupling and mounted beneath the channel on a separate cradle with vibration isolation mounts

Initial test in the rig's original conditions showed that the working flow section flow velocity was an order of magnitude less than the desired value, whilst mechanical variable speed unit produced unacceptable levels of vibration. This limitation prompted immediate redesign of the drive mechanism. The high head, low flow centrifugal pump was replaced with an axial flow pump with an electronic inverter variable speed drive. This enabled a free stream velocity of around 0.5m/s and reduced the mechanical vibration. However with only two perforated plates present in the plenum tank and a simple bell-mouth inlet, the free-stream turbulence level was

of order of 7% and the boundary layer profile, though looking like a typical turbulent layer up to an including the logarithmic region, lacked any form of wake region at the outer edge. The boundary layer thickness at this point in time was approximately 15mm which was significantly less than desired. This was initially attributed to the relatively short working section.

With this problem in mind, the immediate course of action was to extend the overall length of the open-channel to 3m as this is the maximum length that Newcastle could fit in the new fluid dynamics research laboratory. Backed up by theoretical estimates, the proposed length should be sufficient to develop the boundary layer thickness desired and therefore a longer channel was deemed unnecessary.

This extension led to one major complication. The original plan to direct the parallel light sheet through the glass "port hole" had to be abandoned as the extended distance the light sheet needed to travel to illuminate the FOV has led to significant loss of illumination. A conventional divergent light sheet introduced from under the channel and reflected upwards through the glass flow was adopted. To achieve this, a new mounting mechanism was built, where the light-sheet optics were mounted to the side of the rig, and the light sheet reflected upwards using a surface silvered mirror, inclined at 45 degrees. The newly built mounting mechanism enabled a three dimensional movement of the light-sheet head to allow accurate alignment of the light-sheet to the FOV.

To address the high free stream turbulence level, a new inlet section was added, featuring a hyperbolic tangent profile with approximately 3:1 contraction ratio, replacing the original bell-mouth, and fitted with a single honeycomb and a set of five gauzes, 3 coarse with 60% porosity and 2 fine with 45% porosity. This arrangement has significantly decreased the free-stream turbulence down to 1.7% and improved the boundary layer profile but the boundary layer thickness was increased by a factor of five. To address this, gaps and steps were smoothed within the inlet itself and the transition between the inlet and channel inlet. This significantly reduced the boundary layer thickness down to 40mm without the zig-zag strip and 50mm with the strip. This agrees well with initial theoretical estimates of 38mm.

To further reduce the turbulence level, additional two perforated plates were fitted in the inlet plenum tank as earlier tests shows a significant reduction in the turbulent intensity is

achievable with the two existing perforated plates. To avoid water gushing up from the side, all gaps were closed by proper fitting of the additional perforated plates. The additional two perforated plates were found to be sufficient to reduce the turbulence level down to 1% . The LDV system used for the investigations was of a back-scatter type which was known to be noisy compared to a forward scatter system. The turbulence level became much lower than 1% and the LDV investigation revealed that the actual value is 0.86% and since the LDV is a back-scatter system, the true value must be even lower.

Whist these measures did reduce the free stream turbulence, examination of the LDV velocity data showed that much of the remaining unsteadiness was a low frequency sinusoidal pulsation, rather than random turbulence. A cylindrical diffuser tube was located immediately after the return pipe with the hope that the diffuser would further dampen the high velocity flow exiting from the return pipe and reduce the low frequency sinusoidal pulsation; however, high frequency vibrations were generated instead so that the technique was abandoned. Instead a back-plate cut from the same material (perforated plate) was secured immediately at the channel exit. This was found to cause a significant drop in the low frequency sinusoidal pulsations where the screen acted as a pressure drop device. Various levels of porosity were tested but the 23% porous perforated plate gave the best result. With this device in place, possible back-flow may be present that may affect the canonical flow behaviour. PIV was used to assess the problem where initial test and time averaged velocity profile show a bowing of velocity profile. Further test were later carried out with particular attention to aligning the camera precisely to the measurement FOV. The bowing features disappeared and further PIV measurement were taken further downstream. The test revealed that the concerns related to the presence of back-flow can be laid to rest as time averaged profile plot confirms its absence.

In order to position the light-sheet precisely and to calibrate the PIV camera FOV, a new transverse mechanism was manufactured and fitted with the Dantec Dynamic target plate. This new transverse system allowed movement of the target plate in the x- (streamwise) and z- (cross-stream) directions, allowing alignment with the laser light-sheet. A new target plate was manufactured in-house for 3-dimensional calibrations for stereo-PIV application. Due to the shortage of time and unavailability of processing software, 3 dimensional study of two-phase flow was abandoned and only two-dimensional two-phase flow was adopted for this research.

Investigation of the newly built 3 meter open-channel was carried out using both LDV and PIV. The two techniques were employed to ensure that the channel flow characteristics agree well with those of published results. For LDV, the flow was seeded with 10 micron silver-coated hollow glass sphere at a ratio of 3ppm. To ensure reliability of the acquired velocity data, and to minimise noise in the velocity data acquired, the burst efficiency was set as high as possible especially further away from the wall where the number of particles is sufficiently high. Near the wall, the burst efficiency was slightly reduced down to about 70% to allow faster accumulation of point velocity. For a stable mean and rms of the velocity fluctuation, at least 20,000 data points need to be acquired. To avoid velocity bias of the LDV measurements, a transit time weighting of the mean velocity was adopted.

Systematic investigations of the newly built open-channel experimental rig were carried out and the full results are presented in Chapter 4. A summary of the main results is presented here. The initial part of the work was to verify the existence of a canonical turbulent boundary layer at the intended working section for later 2-phase measurements, approximately 2.2m downstream of the inlet to the channel. Wherever possible; comparisons were made to published data; notably the DNS simulations of Schlatter and Örlü (2010). In order to have a well-defined boundary layer transition a tripping device in the form of a zig-zag strip similar to that used by Elsinga and Westerweel (2012) was placed 23mm downstream of the channel inlet. The effects of this trip were investigated, and it was shown that at 2.115m downstream, the boundary layer was slightly thicker, at 60mm, than with no trip, whilst the profile in the outer region was in a better agreement with the data of Schlatter and Örlü (2010) for a similar Reynolds number of $Re_\tau = 970$. The zig-zag trip was used for all subsequent measurements.

One phenomenon that was observed in all measurements was a tendency for the mean velocity at the outer edge of the boundary layer to slightly "overshoot" the free stream value further from the wall. Researching the literature suggested that this "velocity dip" phenomenon is associated with the aspect ratios of open-channel if the value is below 5. Accordingly the aspect ratio was increased by reducing the water depth in the channel, and the "velocity dip" was shown to disappear. Apart from this slightly disconcerting discrepancy in the velocity profiles at the outer edge of the boundary layer, all other characteristics measured were consistent with a canonical turbulent boundary layer, and so it was felt that this phenomenon did not constitute

a significant problem. The effect of Reynolds number was investigated, both by measurement of profiles at different x-locations and by fixing the x-location and varying the free stream velocity. Good agreement was obtained with Schlatter and Örlü (2010) DNS data for the range of Reynolds number 670 < Re_τ <970 (2000 < Re_θ < 3030), both for mean velocity and rms of streamwise perturbations. Using LDV, values were taken between free stream and well into the laminar sublayer, allowing direct determination of friction velocity u_τ from the laminar stress data.

Since subsequent 2-phase measurements were to be made using Particle Image Velocimetry, PIV measurements were then compared with both the present LDV data and the DNS of Schlatter and Örlü (2010). Excellent agreement was obtained for the mean velocity profiles, though clearly the PIV data were limited by the field of view at large wall distance and by a resolution close to the wall. Slight differences were evident in the u' rms data. 2D mean velocity contour plots and velocity profiles from PIV over the range 40,000 < x^+ < 47,500 were studied, and showed the expected boundary layer thickness growth, with no evidence of flow interference from the downstream flow restrictor plate.

For two-phase measurements, 200 micron secondary phase particles that are neutrally buoyant were used and two series of experiments were run, with particle loading of 1.4×10^{-5} and 2.8×10^{-5} It was found that there is a 7.6% increase in the friction velocity over the clear water results. For clear water, there is a 4%difference in friction velocity between LDV and PIV measurement.

The LDV fluid velocity profile agrees well with the PIV results and neither of the two PIV inertial particle loadings showed very significant deviation from the clear water PIV profile. In the region 400 < y^+ < 800 loading caused the mean velocity to fall progressively below the clear water value, with the higher loading increasing this deviation, approximately proportionally. This contrasts with the results of Van Hout (2011), who found no variation in the velocity profile with loading for a fully developed closed channel flow. Kiger and Pan (2002) did find, again for fully developed closed channel flow, that the presence of inertial particles gave rise to a decrease in the mean velocity over the mid-region of the profile, but in their case the effect extended much closer to the wall. It should be noted also that their inertial particles were not neutrally buoyant, having a density ratio of approximately 2.6.

Re-plotting the boundary layer profile with a logarithmic scale for y^+ to generate the classic "law of the wall" plot confirms both the quality of the measurements and insensitivity to particle loading in the sub-layer and logarithmic regions, with the deviation due to inertial particles being confined to the wake region.

The PIV u'^+ profiles for zero loading and for the maximum inertial particle loading of 2.8 $\times$ 10^{-5} are virtually indistinguishable; in fact the variations are significantly less than the small deviation from the LDV values. This is in agreement with previous work for neutrally buoyant inertial particles, but differs from Kiger and Pan's increase in u'^+ for "heavy particle" laden flow. The Reynolds stress profiles indicate a reduction in stress associated with inertial particle loading, with the effect being more significant for the normal stresses.

The overall conclusion is that, for the particle loadings studied in the present work, the effect of loading on the fluid flow is very slight, and the flow may therefore be considered to be a good approximation to the "one way coupled".

Inertial particle behaviour was based on samples binned at y^+ intervals of 10, and histograms of particle count show a reasonably uniform particle distribution, except for a drop-off very close to the wall. Based on this data, the average particle streamwise velocity follows the fluid mean velocity profile very closely, but with a slight reduction, similar to that reported by Kaftori et al. (1995*a*) and by Van Hout (2011). Kaftori et al. (1995*a*) suggested that this velocity deficit phenomenon may be associated with particles preferentially segregating into regions of reduced fluid streamwise velocity, that is the regions of negative u'. Particle velocity fluctuation rms values, however, are significantly higher than the corresponding fluid rms fluctuation velocity for both x and y components, as observed by Van Hout (2011). Despite the number of samples used being much larger than that for van Hout's study, the particle rms values still show a very large scatter.

Conditional statistics for the inertial particles based on the quadrant method following the work of Willmarth and Lu (1972) show clear preference for the particles to reside in both ejections and sweeps accumulating to 37.7% and 40.6%, of particles, respectively, a difference of approximately 2% when the threshold is set to 0.5. A low preference can be observed to Quadrant 3 compared to Quadrant 1.

Observation of particle trajectories affect of Q1, Q2, Q3 and Q4 were carried out and it clearly shows that particle trajectory close to the wall and moving towards the wall are affected by the Q4 sweep events, and those that are moving away from the wall are affected by Q2 ejections events. The same principals can be applied to particle that are further away from the wall (within the turbulent boundary layer), both Q2 and Q4 events affects particle trajectories indicating the presence of hairpin vortices and their packets.

Correlation analysis on available particle track show that the particle-fluid velocity correlation is significantly low for both streamwise and wall-normal velocity, where the later was found to be nearly uncorrelated. The particle-fluid velocity correlation for streamwise and wall-normal velocity are estimated to be 0.0261 and 0.000643, respectively. This clearly, on an average sense, indicate that the wall-normal particle-fluid velocity correlation is almost uncorrelated. The streamwise particle-fluid velocity correlation, on the other hand is surprising quite weak. This result is despite of the almost neutrally buoyant 200μm polystyrene bead having a density of 997g/cc. The particle-fluid velocity correlation coefficient were determined from 8225 particle trajectories as a result of over 14,000 PIV double-frame two-phase images for a particular Reynolds number, Re = 1000.

6.2 Recommendation for Further Work

With the availability of proper time history particle data for various Reynolds number, further analysis can be carried out to determine the effect of Reynolds number on the particle-fluid velocity correlation. Further average displacement, velocity and acceleration of particles can be investigated for different y^+ band region. Areas around each particle for conditional averages can also be studied to identify the turbulent structures responsible for particle transport. This type of detailed experimental information will be useful for validation, or modification, of the speculative theoretical models of particle transport and deposition in the presence of turbulence structures, such as that suggested by Guingo and Minier (2008).

Appendix A

Phase-separation of two-phase image

The separation of both tracer particles images and inertial particles images from a single frame two-phase images were achieved following the technique of Kiger and Pan (2000, 2002). This was achieved by employing a two-dimensional median filter to separate the larger inertial particle images from the two-phase images. A median filter is a non-linear signal processing technique that is effective in reducing random noises without degrading the original signals (Huang, 1981). In this technique, the smaller tracer particles images can be considered as noise scattered over a uniform background. To remove the small tracers particles, a median filter is performed by convolving a two-dimensional filter stencil A of width $N_f \times M_f$ pixels over the two-phase images. After filtering, the small tracer particles are removed, leaving only the larger inertial particles. The filter width is a critical parameter to determine whether the two-phases are separated properly and this value need to be thoroughly investigated before performing the phase-separation processes. In our case the optimal filter size for our two-phase images is 9 $\times$ 9 pixels (p in the MATLAB script). A mask was then formed by dilating the inertial particle images (k in the MATLAB script) and this was then subtracted from the original combined images, leaving only tracer particles images.

The phase-separation algorithm was implemented using a MATLAB script called from within Dantec's DynamicStudio software via the built-in MATLAB link. The tracer particles images were then processed using Adaptive Correlation as described in Section 5.2 to give the instantaneous fluid velocity field, whilst the corresponding inertial particle image pairs were

processed using the DynamicStudio particle tracking add-on, to give the position and instantaneous velocity of each inertial particle.

A.1 MATLAB script for tracer particles image separation

```
%% Median Filter for phase separation of tracers particles.
%------  Settings for Median filter, Threshold and Image dilation   ------%
% IMPORTANT : Settings must be identical to Inertial_phase_split.m  %
% Median filter setting [medfilt2(frame1/2, [n,m],'symmetric')]
n=9;
m=9;

% Threshold setting [im2bw(filt_image1/2, threshold), for k = 1 (white), 0
% black) and 0.5 (mid-range).
threshold=0.6;

% Image dilation setting [imdilate(thresh_image1/2, k)], Note: larger k
% values gives larger particles image diameter.
k=5;

%% Input images from Dyanmic Studio into MATLAB's workspace.
rawimage1 = Input{1}.dataset.frame1;      % get first frame.
rawimage2 = Input{1}.dataset.frame2;      % get second frame.
[x,y] = size(rawimage1);
carrier1 = rawimage1;
carrier2 = rawimage2;

% PROCESSING FIRST FRAME
filt_image = medfilt2(rawimage1,[n,m],'symmetric');  % median filter
thresh_image = im2bw(filt_image,threshold);  % threshold
se = strel('disk',k);                % structuring element
dil_image = imdilate(thresh_image, se);
particles1 = im2uint8(dil_image);   % dilated particle image
[L,num] = bwlabel(particles1,4);   % label particles

for p=1:num                % repeat for each particle...
    [r,c] = find(L==p);     % pix. coords. of particle
    rbar = round(mean(r));  % find centroid of particle...
    cbar = round(mean(c));  % then ccords. of local patch...
    rmin = rbar-10;         % minimum row
    if rmin < 1             % check within image...
        rmin = 1;
    end
    rmax = rmin+20;         % maximum row
```

```
    if rmax > x             % check within image...
        rmax = x;  rmin = x - 20;
    end
    cmin = cbar-10;         % minimum column
    if cmin < 1             % check within image...
        cmin = 1;
    end
    cmax = cmin+20;         % maximum column
    if cmax > y             % check within image...
        cmax = y;  cmin = y - 20;
    end
    sample = rawimage1(rmin:rmax, cmin:cmax);  % extract patch
    min_cols = min(sample);   % min intensity of patch columns
    mean_int = round(mean(min_cols));  % mean intensity of patch
    carrier1(L==p) = mean_int;  % "blank out" particle
end
% end for first frame.

% PROCESSING SECOND FRAME
if ~isempty(rawimage2)  % if frame 2 exists (double-frame)
   filt_image = medfilt2(rawimage2,[n,m],'symmetric');  % median filter
   thresh_image = im2bw(filt_image,threshold);  % threshold
   se = strel('disk',k);                % structuring element
   dil_image = imdilate(thresh_image, se);
   particles2 = im2uint8(dil_image);   % dilated particle image
   [L,num] = bwlabel(particles2,4);   % label particles

   for p=1:num                % repeat for each particle...
       [r,c] = find(L==p);     % pix. coords. of particle
       rbar = round(mean(r));  % find centroid of particle...
       cbar = round(mean(c));  % then ccords. of local patch...
       rmin = rbar-10;         % minimum row
       if rmin < 1             % check within image...
           rmin = 1;
       end
       rmax = rmin+20;         % maximum row
       if rmax > x             % check within image...
           rmax = x;  rmin = x - 20;
       end
       cmin = cbar-10;         % minimum column
       if cmin < 1             % check within image...
           cmin = 1;
       end
       cmax = cmin+20;         % maximum column
       if cmax > y             % check within image...
           cmax = y;  cmin = y - 20;
       end
```

```
87        sample = rawimage2(rmin:rmax, cmin:cmax);  % extract patch
88        min_cols = min(sample);   % min intensity of patch columns
89        %min_cols=0;
90        mean_int = round(mean(min_cols));  % mean intensity of patch
91         %mean_cols=255;
92        carrier2(L==p) = mean_int;  % "blank out" particle
93
94     end
95 end
96 % end for second frame.
97 % Transfer images back to Dyanmic Studio
98 OutputImage(carrier1, carrier2);
```

A.2 MATLAB script for inertial particle image separation

```
1  %% 2D Median filter for inertial particles
2  %------  Settings for Median filter, Threshold and Image dilation   ------%
3  % IMPORTANT : Settings must be identical to Tracer_phase_split.m  %
4  % Median filter setting [medfilt2(frame1/2, [n,m],'symmetric')]
5  n=3;
6  m=3;
7
8  % Threshold setting [im2bw(filt_image1/2, threshold), for k = 1 (white), 0
9  % black) and 0.5 (mid-range).
10 threshold=1;
11
12 % Image dilation setting [imdilate(thresh_image1/2, k)], Note: larger k
13 % values gives larger particles image diameter.
14 k=10;
15
16 %% Input images from Dyanmic Studio into MATLAB's workspace.
17 frame1 =Input{1}.dataset.frame1;      % get first frame.
18 frame2 =Input{1}.dataset.frame2;      % get second frame.
19
20 %% Processing first frame...
21 filt_image1 = medfilt2(frame1,[n,m],'symmetric'); % median filter
22 thresh_image1 = im2bw(filt_image1,threshold); % threshold
23 se = strel('square',k); % structuring element
24 dilated_image1 = imdilate(thresh_image1, se);
25 frame1 = im2uint8(dilated_image1); % dilated particle image
26 % end for first frame.
27
28 %% Processing second frame...
29 filt_image2 = medfilt2(frame2,[n,m],'symmetric'); % median filter
```

```
30 thresh_image2 = im2bw(filt_image2,threshold); % threshold
31 % parts1 = im2uint8(thresh_image);
32 se = strel('square',k); % structuring element
33 dilated_image2 = imdilate(thresh_image2, se);
34 frame2 = im2uint8(dilated_image2); % dilated particle image
35 % end for second frame.
36
37 %% Transfer back to Dyanmic Studio
38 OutputImage(frame1, frame2);
```

Appendix B

MotionPro X5PLUS Standoff Distance for 60mm, 105mm and 200mm AF Micro Nikkor lens

The purpose of investigating the stand-off distances for different AF Micro Nikkor lens was to generate data of the field-of-view (FOV) for different lenses against their distances from the measurement plane. These data would be useful in the design and setting up of PIV measurements. Figure B.1, B.2 and B.3 are the plots for each the AF Micro Nikkor 60mm, 105mm and 200mm lens stand-off position, respectively and Table B.1, B.2 and B.3 are the quantitative experimental data for the standoff measurements.

FOV Height (mm)	**Target-to-Lens** (mm)	**Target-to-Camera** (mm)
6	71	199
10	104	220
15	149	261
20	196	306
25	245	353
30	285	396
35	345	453
40	395	502
45	444	551

TABLE B.1: AF Micro Nikkor 60mm standoff data at f/2.8)

FOV Height (mm)	**Target-to-Lens** (mm)	**Target-to-Camera** (mm)
6	134	294
10	188	339
15	265	409
20	349	491
25	434	574
30	520	661
35	606	745
37	640	778

TABLE B.2: AF Micro Nikkor 105mm standoff data at f/2.8

FOVHeight (mm)	**Target-to-Lens** (mm)	**Target-to-Camera** (mm)
6	254	476
8	330	552
10	399	621
12	469	691
14	539	760

TABLE B.3: AF Micro Nikkor 200mm standoff data at f/2.8)

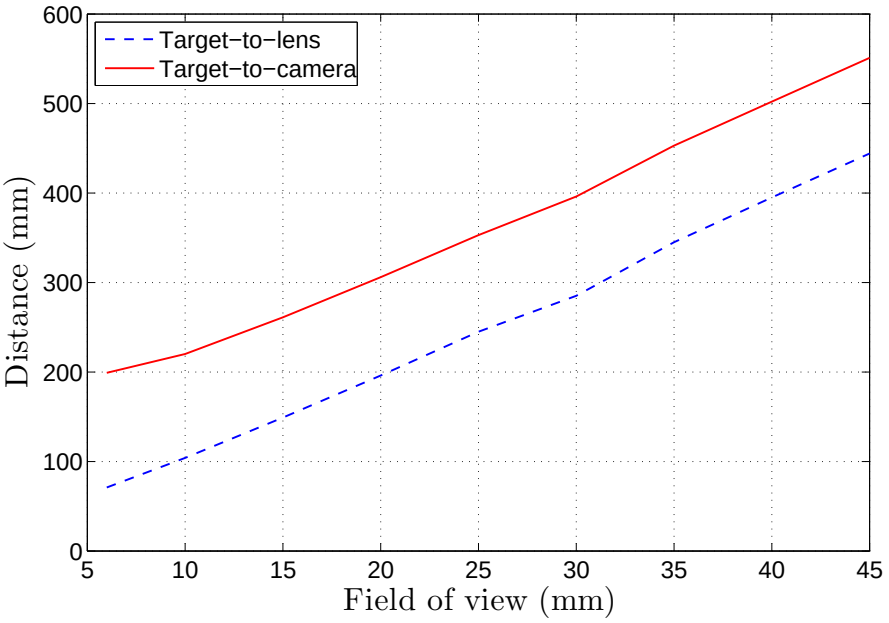

FIGURE B.1: AF Micro Nikkor 60mm standoff distance.

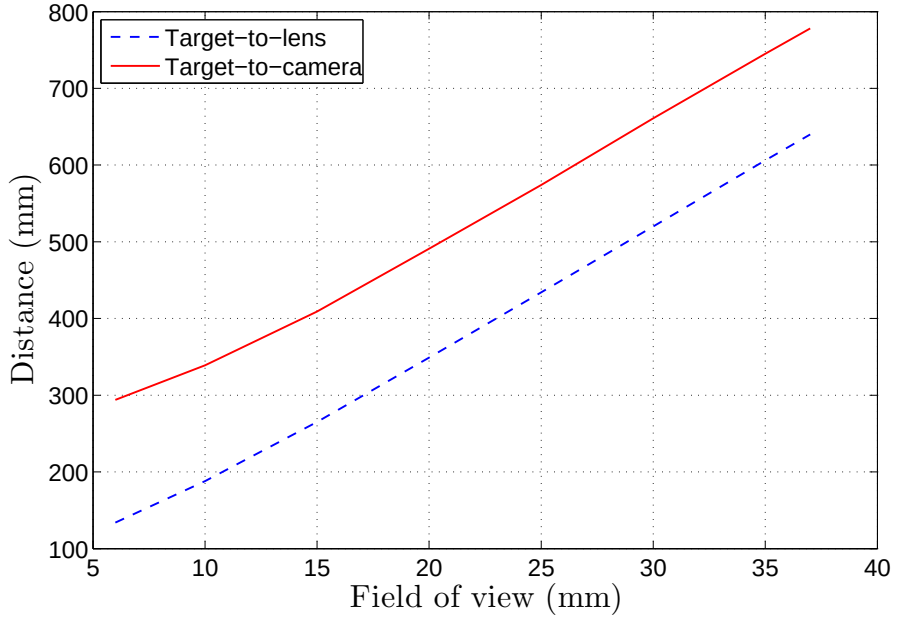

FIGURE B.2: AF Micro Nikkor 105mm standoff distance.

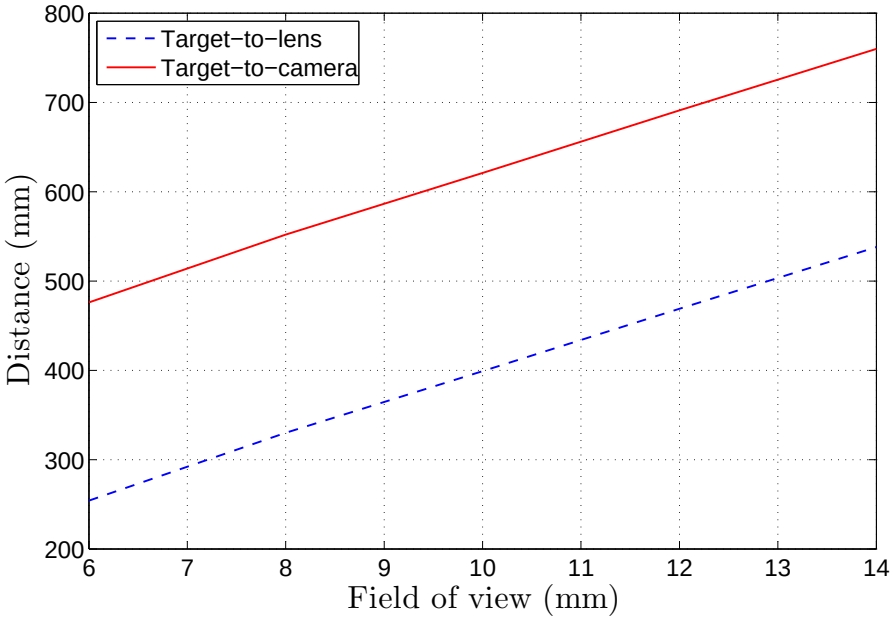

FIGURE B.3: AF Micro Nikkor 200mm standoff distance.

Appendix C

Depth-of-Field for 60mm, 105mm and 200mm AF Micro Nikkor lens

The theoretical depth-of-field, δz is given by

$$\delta_z = 4\,(1 + M_0^{-1})^2\, f^{\#2}\, \lambda \tag{C.1}$$

All particles lying within $\pm\delta z/2$ of the nominal object plane produces in-focus particle images. Outside of this range, the image is blurred by an amount exceeding 20% of the in-focus diameter (Adrian, 1991). Ideally, it must encompass the whole measurement volume (i.e. $l_x \times l_y \times \Delta z_0$). The depth-of-field is affected by the choice of f-number and the magnification M_0. Increasing the f-number increases the depth-of-field while increasing the magnification factor reduces the depth-of-field. In any practical application, a compromise between the two is needed, together with the laser power settings, which is a major constraint for selection of the f-number.

For planar or two-dimensional PIV application, the depth-of-field required is approximately 1.0 mm or less for light-sheet approximate thickness, $\Delta z_0 = 0.6$ mm. With stereo-PIV set-up, two camera's are positioned at $45°$ to the light-sheet, and this require a deeper range of depth-of-field which is theoretically achievable using large f-number. The f-number (sometimes called focal ratio, f-ratio, f-stop, or relative aperture) of an optical system is the ratio of the len's focal length to the diameter of the entrance pupil. The aperture settings is adjusted in discrete steps,

known as f-stops. Each "stop" is marked with its corresponding f-number, and represents a halving of the light intensity from the previous stop. Therefore, stopping down from $f/2.8$ to $f/4$ effectively reduces the entrance pupil by a factor of 2. As a consequence, the laser power has to be increased by a factor of 2 to achieve similar image quality. This prompted the need to experimentally determine the depth-of-field for various lenses type (i.e. AF Micro Nikkor 60, 106 and 200 mm lens) by varying the f-stops (i.e. $f/2.8$, $f/4$, $f/5.6$, $f/8$, etc.) to establish the Newcastle-PIV imaging system capability.

A depth-of-field target (DOF 5-15 by Edmund Optics) consisting of two scales, each when viewed at $45°$, consists of horizontal and vertical lines at a frequency of 5 and 15 line pairs per millimeter. A simple MATLAB line scanning script was written to extract the depth-of-field. To remove any effect of illumination intensity on the depth-of-field value, a percentage (for example 90%, 95% and 98%) of the maximum peak value was taken and, its peak width measured and compared with theoretical values with identical magnification, M_0 values. The magnification was determined from the known depth-of-field target physical dimensions and available sensor pixel size, d_r.

Theoretical DOF are determined using Equation C.1 with the magnification, M_0 set at 0.20. Experimental values are calculated based on the percentage of peak height to eliminate influences of illumination intensity on the experimental depth-of-field. The experimental results are as tabulated in Table C.1 for 60mm lens, Table C.2 for 105mm lens and Table C.3 for 200mm lens. The experimental depth-of-field (δ_z) was found to be slightly thicker than theoretical value even for values taken at higher percentage of the maximum peak value for $f/2.8$ for example. We are mainly interested at the experimental depth-of-field at $f/2.8$ as recent experimental investigations yields good results at $f/2.8$ for planar-PIV and this would be expected to give similar results for stereo-PIV applications that require a much thicker depth-of-field.

f-number	Theoretical δ_z (mm)	Experimental depth-of-field, δ_z (mm)		
		90%	95%	98%
2.8	0.59	2.8	2.0	1.2
4	1.21	3.1	2.2	1.4
5.6	2.37	4.7	3.3	1.7
8	4.83	7.6	4.3	1.9

TABLE C.1: Theoretical and experimental depth-of-field for AF Micro Nikkor 60 mm lens (M_0 = 0.20).

f-number	Theoretical δ_z (mm)	Experimental depth-of-field, δ_z (mm)		
		90%	95%	98%
2.8	0.51	3.0	2.0	1.2
4	1.05	3.1	2.2	1.4
5.6	2.05	3.7	2.7	1.8
8	4.19	5.5	3.9	2.4

TABLE C.2: Theoretical and experimental depth-of-field for AF Micro Nikkor 105 mm lens (M_0 = 0.22).

f-number	Theoretical δ_z (mm)	Experimental depth-of-field, δ_z (mm)		
		90%	95%	98%
4	0.24	0.42	0.29	0.18
5.6	0.47	0.54	0.36	0.22
8	0.97	0.84	0.56	0.34
11	1.83	1.39	0.95	0.22

TABLE C.3: Theoretical and experimental depth-of-field for AF Micro Nikkor 200 mm lens (M_0 = 0.60).

Appendix D

PIV laser power requirements

To establish optimal laser power for $10\,\mu$m silver-coated hollow glass spheres (S-HGS) as seeding particles for the flow phase, 100 double-frame images were acquired at various laser power settings and processed. Experimental data shows that laser power between $20\,$W up to $25\,$W is sufficient to generate approximately 99% valid velocity vectors. Local median and moving validation works well but latter becomes less effective at higher laser power setting. Figure D.1 shows the percentage of valid velocity vectors as a function of laser power for $10\,\mu$m S-HGS.

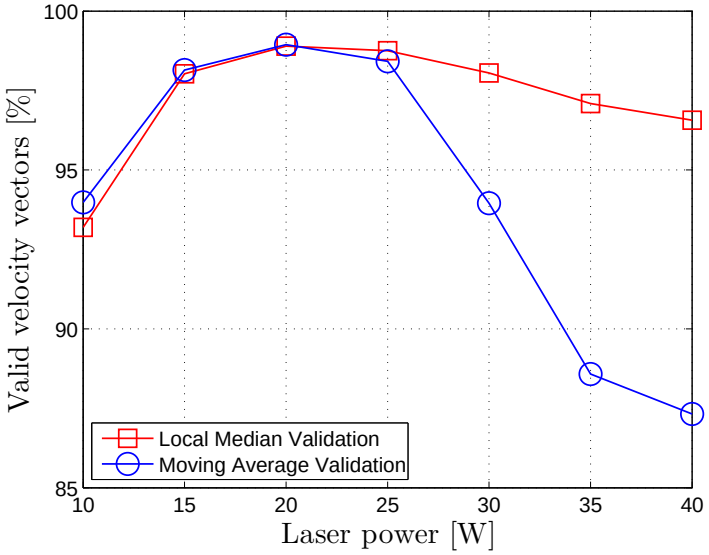

FIGURE D.1: The percentage of valid velocity vectors as a function of laser power for 10−μm S-HGS, Interrogation: Adaptive correlation using 32 by 32 pixels IW, 50% overlap and local-median abd moving-average validation based on 100 single-exposure double-frame images without image pre-processing.

Appendix E

Investigation into DynamicStudio tracking anomalies

Analysis of the particle tracking results from DynamicStudio showed apparently non-physical "spikes" in the particle x- velocity data, at approximately regular time intervals. This is illustrated by comparing the fluid and particle velocity data conditionally sampled along, for example, track 176:

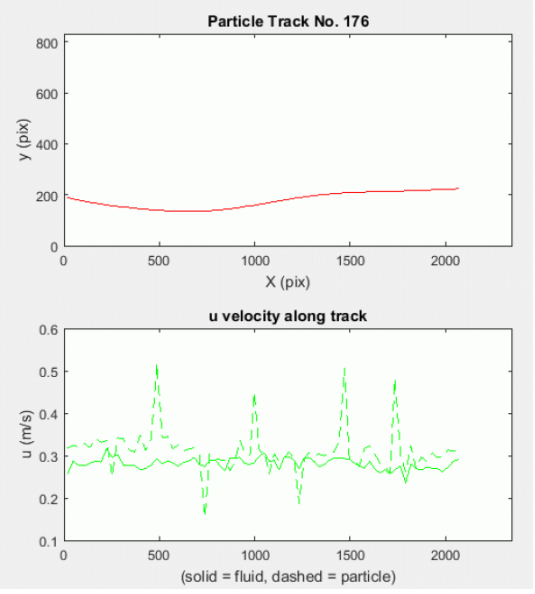

FIGURE E.1: Particle track and corresponding streamwise velocity for fluid and particle showing spikes at x = 500, 750, 1000, 1250, 1500 and 1750 pixels

The Matlab script written for conditional sampling analysis (TrackerCS.m) was modified to print out data along a given track (TrackerCS2.m), and was applied to track 176:

Track no. 176

Frame	Time (s)	xp (pix)	yp (pix)	up	vp	uf	vf
235	0.4680	19.85	188.72	0.3187	-0.0709	0.2579	-0.0267
236	0.4700	49.06	183.74	0.3238	-0.0651	0.2872	-0.0221
237	0.4720	78.13	178.88	0.3207	-0.0669	0.2763	-0.0071
238	0.4740	106.73	174.42	0.3285	-0.0573	0.2760	-0.0418
239	0.4760	135.74	170.72	0.3190	-0.0384	0.2817	-0.0144
240	0.4780	165.13	167.21	0.3405	-0.0335	0.2865	-0.0097
241	0.4800	194.89	163.51	0.3310	-0.0293	0.2852	-0.0086
242	0.4820	224.24	159.93	0.3353	-0.0557	0.3157	-0.0011
243	0.4840	252.44	157.01	0.2512	-0.0273	0.2963	-0.0073
244	0.4860	282.28	154.34	0.3419	-0.0361	0.3021	0.0360
245	0.4880	311.89	152.00	0.3397	-0.0155	0.2771	0.0134
246	0.4900	341.80	149.98	0.3132	-0.0251	0.2766	-0.0175
247	0.4920	371.17	147.32	0.3090	-0.0390	0.2765	-0.0444
248	0.4940	399.99	144.51	0.3488	-0.0178	0.2665	-0.0366
249	0.4960	428.19	142.79	0.3126	-0.0391	0.2696	-0.0199
250	0.4980	457.12	141.23	0.3385	-0.0303	0.2775	0.0023
251	0.5000	487.72	139.86	0.5159	-0.0468	0.2926	0.0176
252	0.5020	515.43	138.60	0.3414	-0.0714	0.2805	-0.0023
253	0.5040	543.96	136.86	0.3444	-0.0487	0.2879	0.0048
254	0.5060	571.78	135.63	0.3152	-0.0383	0.2823	-0.0088
255	0.5080	599.45	134.67	0.3265	-0.0452	0.2745	-0.0281
256	0.5100	627.47	134.64	0.3111	-0.0251	0.2844	-0.0048
257	0.5120	655.61	135.00	0.3153	-0.0181	0.2873	0.0042
258	0.5140	683.35	135.19	0.3179	-0.0197	0.2955	-0.0158
259	0.5160	710.25	135.71	0.3051	-0.0281	0.2787	-0.0115
260	0.5180	739.03	136.29	0.1542	-0.0314	0.2745	-0.0159
261	0.5200	764.05	137.12	0.3039	-0.0204	0.2882	-0.0065
262	0.5220	790.95	138.99	0.2933	-0.0274	0.2902	0.0034
263	0.5240	817.90	140.85	0.2903	-0.0017	0.2765	-0.0028
264	0.5260	844.31	142.62	0.2896	-0.0258	0.2642	-0.0030
265	0.5280	870.41	144.79	0.2651	-0.0098	0.2938	-0.0082
266	0.5300	896.24	147.33	0.2844	-0.0011	0.2941	0.0268
267	0.5320	922.17	150.25	0.3357	-0.0356	0.2956	0.0188
268	0.5340	948.20	154.44	0.3067	-0.0578	0.2809	-0.0040
269	0.5360	974.95	156.11	0.3001	-0.0242	0.2795	-0.0169
270	0.5380	998.29	158.56	0.4485	0.0151	0.2834	-0.0243
271	0.5400	1025.07	162.38	0.3105	0.0086	0.2991	-0.0159
272	0.5420	1050.92	165.63	0.3069	-0.0020	0.3061	-0.0051
273	0.5440	1076.72	169.18	0.2574	0.0139	0.2870	-0.0078
274	0.5460	1102.73	172.77	0.3041	-0.0135	0.2883	-0.0306
275	0.5480	1128.24	176.07	0.2866	0.0335	0.2664	-0.0214
276	0.5500	1154.07	179.22	0.2930	0.0089	0.2950	-0.0286
277	0.5520	1179.96	182.74	0.3086	-0.0023	0.2966	-0.0145
278	0.5540	1206.43	186.22	0.2933	0.0107	0.2898	-0.0122
279	0.5560	1233.28	189.21	0.1874	0.0198	0.2686	-0.0137
280	0.5580	1258.50	191.47	0.2911	-0.0065	0.2943	-0.0130
281	0.5600	1284.27	194.47	0.3071	-0.0036	0.2953	0.0172
282	0.5620	1310.72	196.99	0.3004	-0.0257	0.2872	-0.0173
283	0.5640	1336.93	199.16	0.3040	-0.0090	0.2739	-0.0421

FIGURE E.2: DynamicStudio particle tracking data output.

284	0.5660	1363.35	200.62	0.2992	-0.0315	0.2783	-0.0107
285	0.5680	1389.70	202.60	0.3072	-0.0136	0.2884	-0.0027
286	0.5700	1416.25	204.35	0.3083	-0.0423	0.2950	-0.0009
287	0.5720	1442.85	206.21	0.3328	0.0015	0.2939	0.0095
288	0.5740	1471.38	207.57	0.5058	-0.0133	0.2927	-0.0165
289	0.5760	1496.50	208.54	0.2943	-0.0200	0.2919	-0.0301
290	0.5780	1522.71	209.00	0.2857	-0.0065	0.2823	-0.0097
291	0.5800	1548.87	209.69	0.2763	-0.0056	0.2751	0.0246
292	0.5820	1575.50	210.76	0.3169	0.0114	0.2705	0.0299
293	0.5840	1602.55	212.02	0.3229	0.0070	0.2862	0.0110
294	0.5860	1629.97	212.66	0.3043	0.0035	0.2689	0.0146
295	0.5880	1656.95	212.80	0.2813	-0.0141	0.2587	0.0006
296	0.5900	1683.23	212.59	0.2741	0.0148	0.2666	-0.0116
297	0.5920	1709.96	213.16	0.2587	-0.0172	0.2565	-0.0061
298	0.5940	1735.53	213.64	0.4799	-0.0047	0.2665	-0.0062
299	0.5960	1764.55	214.73	0.3019	-0.0292	0.2751	-0.0038
300	0.5980	1791.95	215.29	0.2608	-0.0390	0.2356	-0.0146
301	0.6000	1819.14	215.88	0.3240	-0.0216	0.2803	-0.0012
302	0.6020	1846.08	216.48	0.2696	-0.0288	0.2690	0.0062
303	0.6040	1873.45	217.36	0.2960	-0.0591	0.2659	-0.0080
304	0.6060	1901.43	218.35	0.2868	-0.0321	0.2726	0.0204
305	0.6080	1929.66	219.49	0.3061	-0.0382	0.2704	-0.0049
306	0.6100	1957.47	220.32	0.2954	-0.0278	0.2688	0.0072
307	0.6120	1985.13	221.07	0.2953	-0.0472	0.2624	0.0010
308	0.6140	2013.30	222.03	0.3130	-0.0160	0.2721	-0.0027
309	0.6160	2042.37	222.83	0.3108	-0.0031	0.2866	0.0055
310	0.6180	2071.52	223.67	0.3118	-0.0073	0.2917	0.0311

FIGURE E.3: DynamicStudio particle tracking data output (Continue from Figure E.2).

This confirms the regularity of the “spikes”, and identifies the frames in which they occur. Note that the frame numbers start from 1, whilst the corresponding double image numbers start from 0, so the strong “spike” at frame 251 is associated with image 250.

Viewing the DynamicStudio tracking output file for frame 251, the particle associated with track 176 can be identified, and the velocity and displacement anomalies are evident:

```
>>*HEADER*<<
FileID:DSExport.TAB
Version:2
GridSize:{Width=2352, Height=832}
Originator:Rel1000.Project 2015-09-18 18:05:10.Run 8:04:15.Particle Tracking
CameraInfo:NanoSense.1
TimeStamp:0.5
>>*DATA*<<
Frame X[pix]            Y[pix]            Z[pix]   U[m/s]             V[m/s]             W[m/s]
0     366.761383056641  173.129333496094  0        0.298048812718218  -0.0503026805297702  0
0     483.914337158203  140.209930419922  0        0.51591331144699   -0.0467722867677281  0
0     847.518981933594  599.40771484375   0        0.331064666247915  -0.0323848719314424  0
0     1115.91931152344  335.926635742188  0        0.31231313442304   -0.0695362409198699  0
0     1126.90734863281  714.741149902344  0        0.351793963344699  -0.00311146335664299 0
0     1344.40173339844  428.711303710938  0        0.289606072054348  -0.0220140170066743  0
0     1356.2021484375   408.595703125     0        0.294852528884432  -0.00317352712040582 0
0     1288.16235351563  820.664794921875  0        0.359762950611846   0.0530686556014668  0
0     2129.28564453125  303.771179199219  0        0.331354297145475  -0.00454927388381512 0
1     371.158020019531  172.387298583984  0        0.298048812718218  -0.0503026805297702  0
1     491.524780273438  139.519973754883  0        0.51591331144699   -0.0467722867677281  0
1     852.402648925781  598.929992675781  0        0.331064666247915  -0.0323848719314424  0
1     1120.5263671875   334.90087890625   0        0.31231313442304   -0.0695362409198699  0
1     1132.09680175781  714.695251464844  0        0.351793963344699  -0.00311146335664299 0
1     1348.673828125    428.386566162109  0        0.289606072054348  -0.0220140170066743  0
1     1360.55163574219  408.548889160156  0        0.294852528884432  -0.00317352712040582 0
1     1293.46936035156  821.447631835938  0        0.359762950611846   0.0530686556014668  0
1     2134.17358398438  303.704071044922  0        0.331354297145475  -0.00454927388381512 0
```

FIGURE E.4: DynamicStudio particle tracking data output for frame 251.

The corresponding double image, PTracking.4bem6zt0.000250.tif , was split into two single tif images using the package Irfanview (Options -> Multipage images -> Extract all pages) for detailed examination. (Note: this splitting could have been done when extracting the images in DynamicStudio). These are raw images, containing both tracer and inertial particles, and reflection from the glass wall. Using Microsoft Paint, with a zoomed-in view, the particle reflection images were used to identify the wall position as 818 pixels from the top of the image, ie. (832 - 818) = 14 pixels from the bottom of the 2352 × 832 pixel image:

Next, again using Paint, the region to be masked off was measured to be 813 pixels from the top or 19 pixels from the bottom of the image:

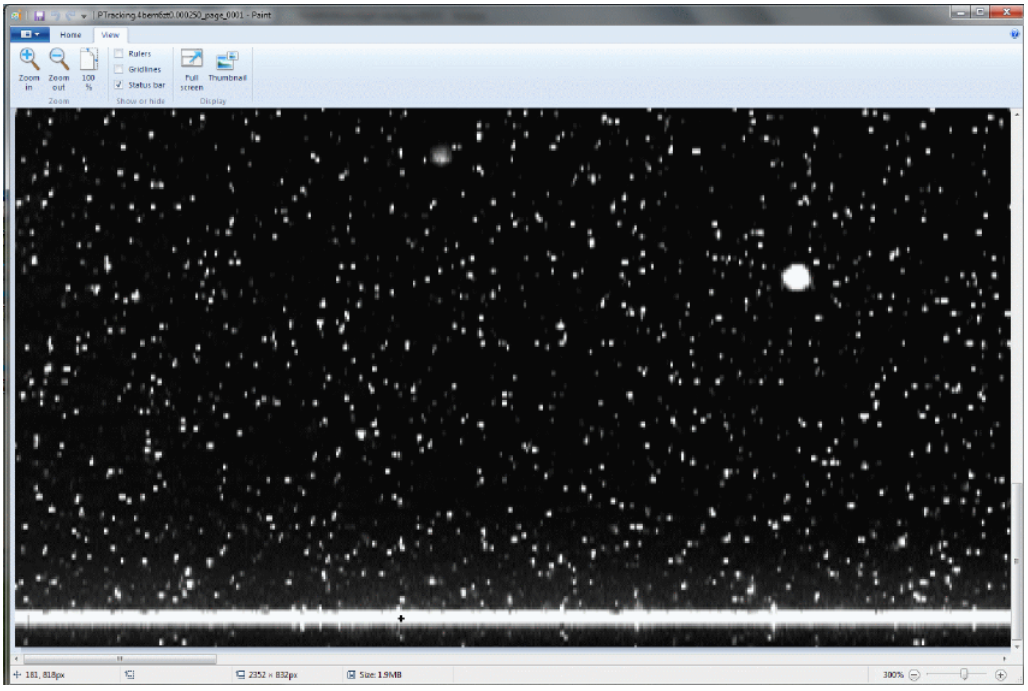

FIGURE E.5: Two-phase image showing inertial particles (Frame 1)

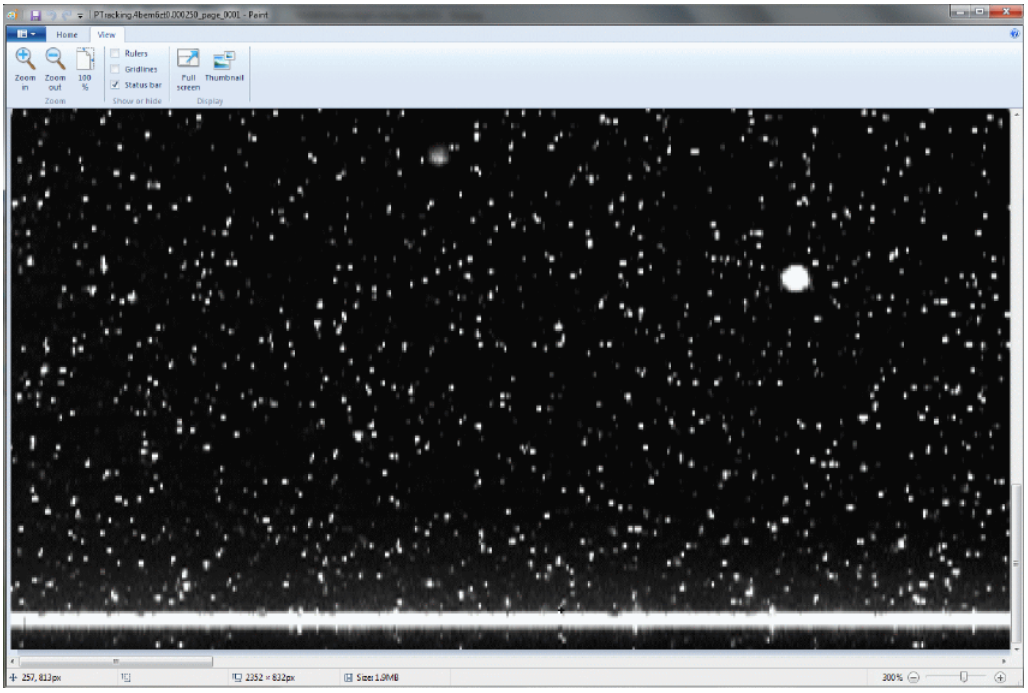

FIGURE E.6: Two-phase image showing inertial particles (Frame 2)

Consider frame 251, which exhibits a strong spike in velocity for track/particle number 176. DynamicStudio gives the x- coordinates for this particle as:

1. Frame 0 x = 483.9
2. Frame 1 x = 491.5

giving an x translation of approximately 7.6 pixels. However, direct measurement of the corresponding particle positions from a zoomed-in view in Paint gives the coordiates as approximately:

1. Frame 0 x = 484
2. Frame 1 x = 488.5

giving an approximate x translation of just 4.5 pixels. This error in the second frame x - coordinate will clearly lead to a significant over-prediction of the x - velocity by DynamicStudio.

An alternative tracking algorithm was coded in MatLab, operating on the raw tif images. This code was written to produce an output file of almost identical format to the DynamicStudio output, to simplify the re-use of downstream analysis code. Output for the double frame studied is:

The lines highlighted refer to the track/particle number 176, and the x- displacement is 489.31 – 484.96 = 4.35 pixels, in much better agreement with the approximate 4.5 pixels obtained by "visual" measurement in Paint. The code also tracked 10 particles in this frame, as opposed to the 9 detected by DynamicStudio. (The apparent difference in absolute pixel location of approximately 1 pixel is due to positions being numbered from 0 at the LHS of the image in Paint, and from 1 in MatLab).

Applying this to the full track for particle 176 removes the more serious "spikes" given by DynamicStudio tracking: (blue = MatLab, red = DynamicStudio, green = fluid)

```
>>*HEADER<<*
FileID:IPExport.TAB
Version:1
GridSize:{Width=2352, Height=832}
Originator:
CameraInfo:NanoSense
TimeStamp:0.50

>>*DATA*<<
```

Frame	X[pix]	Y[pix]	Z[pix]	U[m/s]	V[m/s]	W[m/s]
0	367.81	174.21	0	0.267	-0.017	0
0	484.96	140.70	0	0.296	0.021	0
0	848.47	600.44	0	0.296	0.001	0
0	1116.72	336.54	0	0.293	-0.005	0
0	1128.00	715.72	0	0.314	0.047	0
0	1289.16	821.84	0	0.326	0.058	0
0	1345.19	429.80	0	0.282	-0.009	0
0	1357.27	409.23	0	0.255	0.056	0
0	1463.76	667.62	0	0.401	-0.018	0
0	2130.37	304.89	0	0.307	0.026	0
1	371.73	173.97	0	0.267	-0.017	0
1	489.31	141.00	0	0.296	0.021	0
1	852.83	600.44	0	0.296	0.001	0
1	1121.02	336.46	0	0.293	-0.005	0
1	1132.62	716.41	0	0.314	0.047	0
1	1293.96	822.69	0	0.326	0.058	0
1	1349.33	429.67	0	0.282	-0.009	0
1	1361.02	410.05	0	0.255	0.056	0
1	1469.65	667.35	0	0.401	-0.018	0
1	2134.88	305.27	0	0.307	0.026	0

FIGURE E.7: New particle tracking algorithm output for particle velocities.

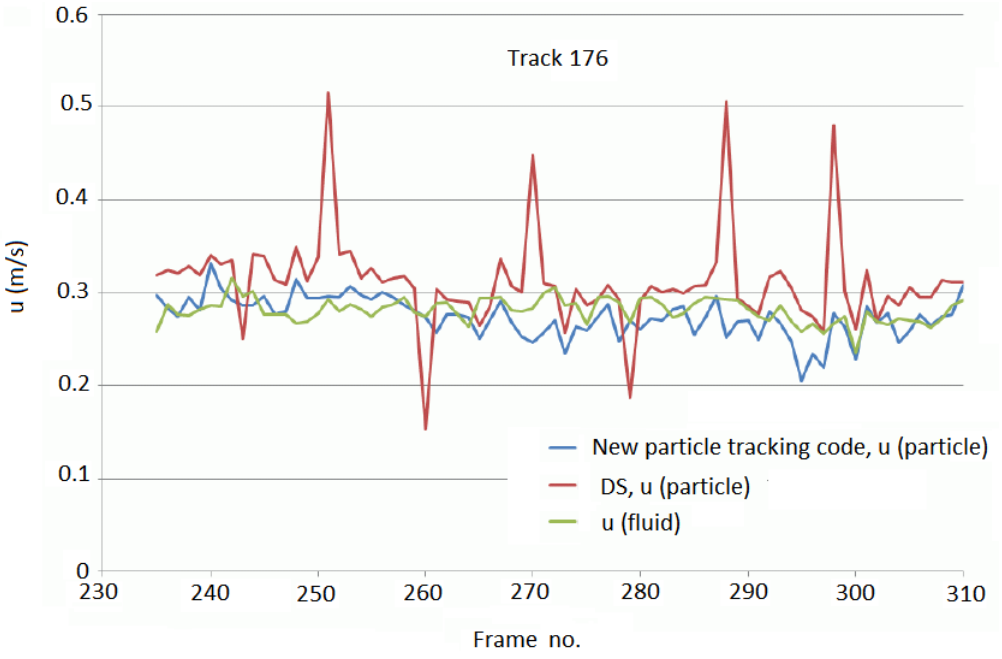

FIGURE E.8: Fluid and inertial particle velocities using DynamicStudio particle tracking algorithm showing velocity spikes.

Whilst this is a clear improvement, there are still some larger than expected velocity excursions (down to up = 0.2 m/s at frame number 295). Examining Frame 295 in detail revealed that the process of filtering and binarization had distorted the particle image in this case:

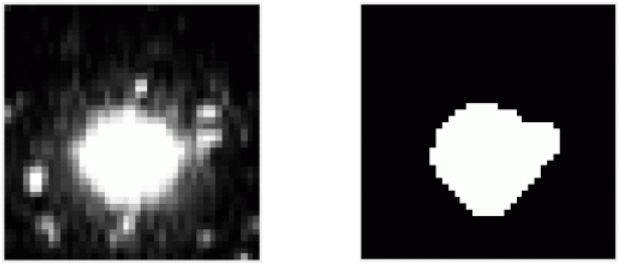

FIGURE E.9: Distorted particle image after filtering and binarization process.

Either this, or the details of the filtering process used (or both) may be responsible for the poor performance of DynamicStudio's correlation algorithm for particle tracking. Our simple method for large particle detection works fine for locating the particles approximately, but may not give good enough location accuracy for reliable velocity measurement. To address this the MatLab code was modified to use the original method for preliminary particle location, then go back to the raw image to refine the position data: (blue = fluid velocity, red = new method particle velocity, green = "filtered" particle velocity, determine by applying central differences to particle positions in consecutive frames) The RMS of the particle velocity is again reduced, and there does now seem to be some degree of correlation between the fluid and particle velocities. These results suggest that the large scatter in Suhaimi's particle velocity RMS could be significantly reduced.

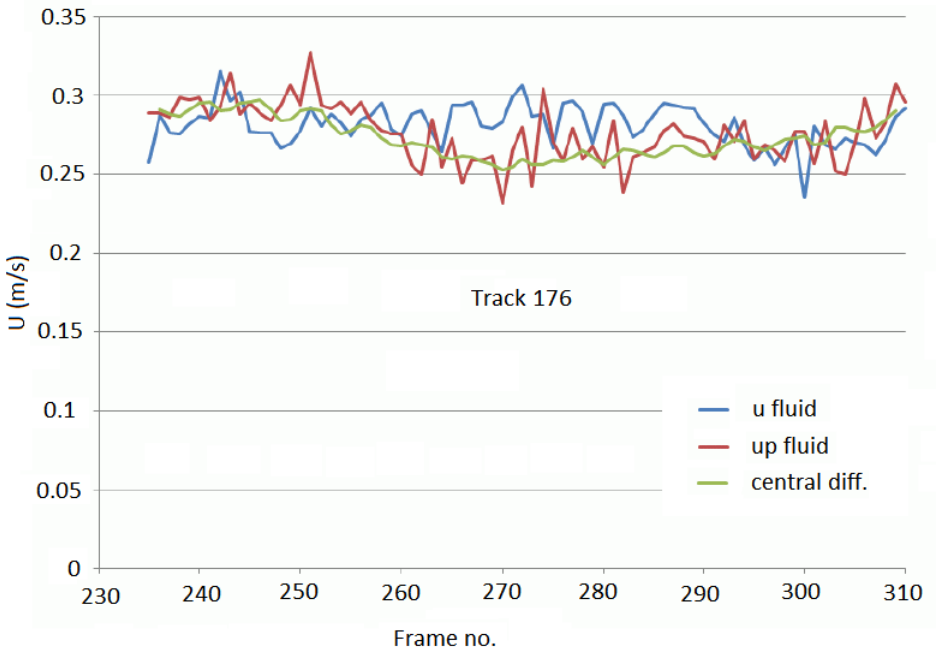

FIGURE E.10: Fluid and inertial particle velocities using in-house particle tracking algorithm showing the absence of velocity spikes.

The absolute error in particle location remains an open question, requiring more investigation. Since the particle movement is only of the order of 4 or 5 pixels, an error of 0.1 pixels in each particle position could lead to a maximum velocity error of (0.2/4) × 100% = 5% or around 0.015 m/s, so some of the scatter in the particle velocity data may be "noise" rather than physical. It is suspect that 0.1 pixels might be optimistic! However, It can't be believe that Kiger and Pan or van Hout can have done any better with "noisy" filtered 2-phase data and either of these authors have declared the accuracy of their particle location methods. If we did not have to filter (ie. using fluorescence to give clean inertial particle images), then correlation methods such as DynamicStudio's may give better resolution.

E.1 How does the code works?

- The images need to be supplied as individual tif images, rather than double frame images, with the naming convention: Image0001_1.tif and Image0001_2.tif
- Any number of image pairs from 1 to 9999 may be processed, at about 1 second / pair.

- Parameters for image size, time step size, intensity threshold intensity are "hard coded", and may need to be checked/updated.
- The wall boundary is masked off in the read image pair.
- Each image is then filtered using a 7×7 median filter to remove as much as possible of the PIV tracer particle images, and the resulting images are binarized.
- The MatLab graphics toolbox function "bwlabel" is then used to identify and number pixel structures corresponding to inertial particles.
- The centroid of each pixel cluster then gives the first estimate of particle position.
- Particle images below a threshold size, or straddling the frame boundaries are then removed.
- This is the basic algorithm of the original code, but artifacts in the binarized images may lead to some error in the particle location coordinates.
- In the modified code, these particle positions are used as a starting point for refined analysis based on the original raw grayscale images.
- Starting from the "seed" position of the original particle centroid, the raw image is scanned both horizontally and vertically until the brightness intensity gradient reaches a threshold value, taken to be the edge of the particle image, marking all pixels within this boundary.
- The centroid of these new pixel clusters are then computed to give the updated particle position.
- Finally, the pixel locations from image1 and image2 are compared, using a minimum separation algorithm to identify particle image pairs.
- Particle pairs exhibiting a movement greater than a specified threshold are discounted, as are leftover, unpaired particles.
- The particle displacements and image separation time are used to compute the particle velocity components, and the results for location and velocity are printed to file in the same format as the DynamicStudio tracking output.

E.2 MATLAB script for image frame separation and renaming

```
% Code for splitting PIV double-image into single frames and
% renaming the figures for subsequent particle tracking code.
%
tic
numfiles=1999; %Reading image 2 to 1999
for i=1:numfiles
    myfilename=sprintf('PTracking.4beovkbw.%06d.tif',i);
    A{:,i+1}=imread(myfilename,1);
    B{:,i+1}=imread(myfilename,2);
end

C=imread('PTracking.4beovkbw.000000.tif',1); %Reading first image (Frame 1)
D=imread('PTracking.4beovkbw.000000.tif',2); %Reading first image (Frame 2)
A{1,1}=C;
B{1,1}=D;

% Renaming the split images as Image001_1.tif and Image001_2.tif
numfiles=2000;
for i=1:numfiles
   imwrite(A{i},sprintf('Image%04d_1.tif',i));
   imwrite(B{i},sprintf('Image%04d_2.tif',i));
end
toc
```

E.3 MATLAB script for particle tracking

```
% script to process combined PIV images for inertial particle detection
% requires MatLab's Image Processing Toolkit.
clear all,clc
disp('====================== NOTE ========================');
disp('This script was written specifically to process     ');
disp('the 2-phase PIV data for the channel flow experiment');
disp('of Suhaimi Wahab, and contains embedded constants / ');
disp('parameters specific to that experiment.             ');
disp('This data will need to be reviewed / modified if the');
disp('code is to be used for other applications.          ');
disp(' ');

% Data...
```

```
MinArea = 15;     % min pixel area of image to be considered a particle
deltat = 0.0003;  % time interval between 2 exposures of an image pair (s)
Dt = 0.002;        % time between succesive image pairs (s)
width_mm = 48;    % frame width in mm
width_pix = 2352; % frame width in pixels
height_pix = 832; % for NanoSense IV at reduced frame height
% hence constant for converting displacement in pixels to vel in m/s...
vel_const = width_mm/(width_pix*1000*deltat);

% Input details of image files to process...
name = input('Enter generic name of image tif files (eg. image) :  ','s');
start = input('Enter number of first image pair to process       :  ');
finish = input('Enter number of final image pair to process       :  ');
disp(' ');

% Now loop for each image pair...
tic;
for image_no=start:finish

    message = sprintf('Processing %s%04d ...', name, image_no);
    disp(message);
    imfname1 = sprintf('%s%04d_1.tif', name, image_no);
    imfname2 = sprintf('%s%04d_2.tif', name, image_no);

image1 = imread(imfname1);
image2 = imread(imfname2);
% mask out wall region (above 813 pixels) using intensity 20...
image1(813:832, :) = 30;
image2(813:832, :) = 30;
% filter image 1 to reduce visibility of tracer particles
% using a median filter with a 7 x 7 mask...
filt = medfilt2(image1,[7,7],'symmetric');
% now binarise by thresholding...
bw1 = imbinarize(filt,0.5);
% imshow(bw1);    commented out.
[L1,num1] = bwlabel(bw1,4);

% check for "partial" particle images along frame boundaries...
cullmark = zeros(num1,1);
for j=1:width_pix
    if L1(1,j) ~= 0
        partID = L1(1,j);
        cullmark(partID) = partID;
    end
    if L1(height_pix,j) ~= 0
        partID = L1(height_pix,j);
        cullmark(partID) = partID;
```

```
    end
end
 for i=1:height_pix
    if L1(i,1) ~= 0
        partID = L1(i,1);
        cullmark(partID) = partID;
    end
    if L1(i,width_pix) ~= 0
        partID = L1(i,width_pix);
        cullmark(partID) = partID;
    end
 end
% "partial" particles now marked for culling.

% label located particles, and find centroid and size on image...
k1 = 0;
for k=1:num1
    [r,c] = find(L1 == k);
    npixels = size(r,1);
    % cull any detected "particles" smaller than specified area...
    if (npixels>MinArea) && (cullmark(k) == 0)
        k1 = k1+1;
        npix1(k1) = npixels;
        yp1(k1) = mean(r);
        xp1(k1) = mean(c);
    end
    clear r;
end
num1 = k1

% filter image 2 to reduce visibility of tracer particles
% using a median filter with a 7 x 7 mask...
filt = medfilt2(image2,[7,7],'symmetric');
% now binarise by thresholding...
bw2 = imbinarize(filt,0.5);
% imshow(bw2);    commented out
[L2,num2] = bwlabel(bw2,4);

% check for "partial" particle images along frame boundaries...
clear cullmark;
cullmark = zeros(num2,1);
for j=1:width_pix
    if L2(1,j) ~= 0
        partID = L2(1,j);
        cullmark(partID) = partID;
    end
    if L2(height_pix,j) ~= 0
```

```
        partID = L2(height_pix,j);
        cullmark(partID) = partID;
    end
end
 for i=1:height_pix
    if L2(i,1) ~= 0
        partID = L2(i,1);
        cullmark(partID) = partID;
    end
    if L2(i,width_pix) ~= 0
        partID = L2(i,width_pix);
        cullmark(partID) = partID;
    end
 end
% "partial" particles now marked for culling.

% label located particles, and find centroid and size on image...
k2 = 0;
for k=1:num2
    [r,c] = find(L2 == k);
    npixels = size(r,1);
    % cull any detected "particles" smaller than specified area...
    if (npixels>MinArea) && (cullmark(k) == 0)
        k2 = k2+1;
        npix2(k2) = npixels;
        yp2(k2) = mean(r);
        xp2(k2) = mean(c);
    end
    clear r;
end
num2 = k2


% Now improve estimate of particle positions, using original images...
% Image 1...
L1(:,:) = 0;   % clear L1
thresh = 18; %Original 18
for partID = 1:num1
xcen = round(xp1(partID));
ycen = round(yp1(partID));
i=ycen; j=xcen;  % estimated centre position
L1(i,j) = partID;
% First pass, scan by horizontal lines...
while (image1(i,j)-image1(i,j+1))<thresh  % scan x line for intensity cliff...
    j = j+1;
    L1(i,j) = partID;
end
```

```
xhi = j;
j=xcen;
while (image1(i,j)-image1(i,j-1))<thresh  % scan for intensity cliff...
    j = j-1;
    L1(i,j) = partID;
end
xlo = j;
xcen = round((xhi + xlo)/2);  % new estimate for x- centre
j = xcen;

% now check "up" one line at a time...
while (image1(i,j)-image1(i+1,j))<thresh
    i=i+1;
    L1(i,j) = partID;
    while (image1(i,j)-image1(i,j+1))<thresh % scan for intensity cliff...
        j = j+1;
        L1(i,j) = partID;
    end
    xhi = j;
    j=xcen;
    while (image1(i,j)-image1(i,j-1))<thresh  % scan for intensity cliff...
        j = j-1;
        L1(i,j) = partID;
    end
    xlo = j;
    xcen = round((xhi + xlo)/2);  % new estimate for x- centre
    j = xcen;
end

i=ycen;  j=xcen;
% now check "down" one line at a time...
while (image1(i,j)-image1(i-1,j))<thresh
    i=i-1;
    L1(i,j) = partID;
    while (image1(i,j)-image1(i,j+1))<thresh % scan for intensity cliff...
        j = j+1;
        L1(i,j) = partID;
    end
    xhi = j;
    j=xcen;
    while (image1(i,j)-image1(i,j-1))<thresh  % scan for intensity cliff...
        j = j-1;
        L1(i,j) = partID;
    end
    xlo = j;
    xcen = round((xhi + xlo)/2);  % new estimate for x- centre
    j = xcen;
```

```
202 end
203
204 % Now repeat, scanning by vertical lines...
205 xcen = round(xp1(partID));
206 ycen = round(yp1(partID));
207 i=ycen; j=xcen;  % estimated centre position
208 L1(i,j) = partID;
209 while (image1(i,j)-image1(i+1,j))<thresh % scan y line for intensity cliff...
210     i = i+1;
211     L1(i,j) = partID;
212 end
213 yhi = i;
214 i=ycen;
215 while (image1(i,j)-image1(i-1,j))<thresh  % scan for intensity cliff...
216     i = i-1;
217     L1(i,j) = partID;
218 end
219 ylo = i;
220 ycen = round((yhi + ylo)/2);  % new estimate for y- centre
221 i = ycen;
222
223 % now check "right" one line at a time...
224 while (image1(i,j)-image1(i,j+1))<thresh
225     j=j+1;
226     L1(i,j) = partID;
227     while (image1(i,j)-image1(i+1,j))<thresh % scan for intensity cliff...
228         i = i+1;
229         L1(i,j) = partID;
230     end
231     yhi = i;
232     i=ycen;
233     while (image1(i,j)-image1(i-1,j))<thresh  % scan for intensity cliff...
234         i = i-1;
235         L1(i,j) = partID;
236     end
237     ylo = i;
238     ycen = round((yhi + ylo)/2);  % new estimate for y- centre
239     i = ycen;
240 end
241
242 i=ycen;  j=xcen;
243 % now check "left" one line at a time...
244 while (image1(i,j)-image1(i,j-1))<thresh
245     j=j-1;
246     L1(i,j) = partID;
247     while (image1(i,j)-image1(i+1,j))<thresh % scan for intensity cliff...
248         i = i+1;
```

```
249         L1(i,j) = partID;
250     end
251     yhi = i;
252     i=ycen;
253     while (image1(i,j)-image1(i-1,j))<thresh  % scan for intensity cliff...
254         i = i-1;
255         L1(i,j) = partID;
256     end
257     ylo = i;
258     ycen = round((yhi + ylo)/2);  % new estimate for y- centre
259     i = ycen;
260 end
261 [r,c] = find(L1 == partID);
262 npixels = size(r,1);
263 npix1(partID) = npixels;
264 yp1(partID) = mean(r);
265 xp1(partID) = mean(c);
266 clear r;
267 end
268 % end of code to update particle positions from image1
269
270 % now repeat for image2...
271 L2(:,:) = 0;   % clear L2
272 for partID = 1:num2
273 xcen = round(xp2(partID));
274 ycen = round(yp2(partID));
275 i=ycen; j=xcen;  % estimated centre position
276 L2(i,j) = partID;
277 % First pass, scan by horizontal lines...
278 while (image2(i,j)-image2(i,j+1))<thresh  % scan x line for intensity cliff...
279     j = j+1;
280     L2(i,j) = partID;
281 end
282 xhi = j;
283 j=xcen;
284 while (image2(i,j)-image2(i,j-1))<thresh  % scan for intensity cliff...
285     j = j-1;
286     L2(i,j) = partID;
287 end
288 xlo = j;
289 xcen = round((xhi + xlo)/2);  % new estimate for x- centre
290 j = xcen;
291
292 % now check "up" one line at a time...
293 while (image2(i,j)-image2(i+1,j))<thresh
294     i=i+1;
295     L2(i,j) = partID;
```

```
296     while (image2(i,j)-image2(i,j+1))<thresh % scan for intensity cliff...
297         j = j+1;
298         L2(i,j) = partID;
299     end
300     xhi = j;
301     j=xcen;
302     while (image2(i,j)-image2(i,j-1))<thresh  % scan for intensity cliff...
303         j = j-1;
304         L2(i,j) = partID;
305     end
306     xlo = j;
307     xcen = round((xhi + xlo)/2);  % new estimate for x- centre
308     j = xcen;
309 end
310
311 i=ycen;  j=xcen;
312 % now check "down" one line at a time...
313 while (image2(i,j)-image2(i-1,j))<thresh
314     i=i-1;
315     L2(i,j) = partID;
316     while (image2(i,j)-image2(i,j+1))<thresh % scan for intensity cliff...
317         j = j+1;
318         L2(i,j) = partID;
319     end
320     xhi = j;
321     j=xcen;
322     while (image2(i,j)-image2(i,j-1))<thresh  % scan for intensity cliff...
323         j = j-1;
324         L2(i,j) = partID;
325     end
326     xlo = j;
327     xcen = round((xhi + xlo)/2);  % new estimate for x- centre
328     j = xcen;
329 end
330
331 % Now repeat, scanning by vertical lines...
332 xcen = round(xp2(partID));
333 ycen = round(yp2(partID));
334 i=ycen; j=xcen;  % estimated centre position
335 L2(i,j) = partID;
336 while (image2(i,j)-image2(i+1,j))<thresh % scan y line for intensity cliff...
337     i = i+1;
338     L2(i,j) = partID;
339 end
340 yhi = i;
341 i=ycen;
342 while (image2(i,j)-image2(i-1,j))<thresh  % scan for intensity cliff...
```

```
343     i = i-1;
344     L2(i,j) = partID;
345 end
346 ylo = i;
347 ycen = round((yhi + ylo)/2);  % new estimate for y- centre
348 i = ycen;
349
350 % now check "right" one line at a time...
351 while (image2(i,j)-image2(i,j+1))<thresh
352     j=j+1;
353     L2(i,j) = partID;
354     while (image2(i,j)-image2(i+1,j))<thresh % scan for intensity cliff...
355         i = i+1;
356         L2(i,j) = partID;
357     end
358     yhi = i;
359     i=ycen;
360     while (image2(i,j)-image2(i-1,j))<thresh  % scan for intensity cliff...
361         i = i-1;
362         L2(i,j) = partID;
363     end
364     ylo = i;
365     ycen = round((yhi + ylo)/2);  % new estimate for y- centre
366     i = ycen;
367 end
368
369 i=ycen;  j=xcen;
370 % now check "left" one line at a time...
371 while (image2(i,j)-image2(i,j-1))<thresh
372     j=j-1;
373     L2(i,j) = partID;
374     while (image2(i,j)-image2(i+1,j))<thresh % scan for intensity cliff...
375         i = i+1;
376         L2(i,j) = partID;
377     end
378     yhi = i;
379     i=ycen;
380     while (image2(i,j)-image2(i-1,j))<thresh  % scan for intensity cliff...
381         i = i-1;
382         L2(i,j) = partID;
383     end
384     ylo = i;
385     ycen = round((yhi + ylo)/2);  % new estimate for y- centre
386     i = ycen;
387 end
388 [r,c] = find(L2 == partID);
389 npixels = size(r,1);
```

```
npix2(partID) = npixels;
yp2(partID) = mean(r);
xp2(partID) = mean(c);
clear r;
end
% end of code to update particle positions from image2


% now use "nearest neighbour to pair particle images between exposures...
if (num2 <= num1)
    for k2 = 1:num2
        % for every particle in image 2...
        mindispsq = 1e6;
        x2 = xp2(k2);
        y2 = yp2(k2);
        for k1 = 1:num1
            % scan every particle in image 1 for possible displacement...
            x1 = xp1(k1);
            y1 = yp1(k1);
            dx = x2-x1;
            dy = y2-y1;
            dispsq = dx*dx + dy*dy;
            if (dispsq < mindispsq)
                mindispsq = dispsq;
                xpix1(k2) = x1;
                ypix1(k2) = y1;
                dssq(k2) = dispsq;
            end
        end
    end
    % cull particle pairs with unphysically large displacements...
    limit = 2.0*median(dssq);
    nparts = 0;
    for k2 = 1:num2
        if (dssq(k2) <= limit)
            nparts = nparts+1;
            xp1(nparts) = xpix1(k2);
            yp1(nparts) = height_pix-ypix1(k2)+1;
            % ie. change y-coord measured upwards
            xp2(nparts) = xp2(k2);
            yp2(nparts) = height_pix-yp2(k2)+1;
            % ie. change y-coord measured upwards
            up(nparts) = (xp2(nparts) - xp1(nparts))*vel_const;
            vp(nparts) = (yp2(nparts) - yp1(nparts))*vel_const;
        end
    end
else
```

```
437     % loop for num1 < num2...
438     for k1 = 1:num1
439         % for every particle in image 2...
440         mindispsq = 1e6;
441         x1 = xp1(k1);
442         y1 = yp1(k1);
443         for k2 = 1:num2
444             % scan every particle in image 2 for possible displacement...
445             x2 = xp2(k2);
446             y2 = yp2(k2);
447             dx = x2-x1;
448             dy = y2-y1;
449             dispsq = dx*dx + dy*dy;
450             if (dispsq < mindispsq)
451                 mindispsq = dispsq;
452                 xpix2(k1) = x2;
453                 ypix2(k1) = y2;
454                 dssq(k1) = dispsq;
455             end
456         end
457     end
458     % cull particle pairs with unphysically large displacements...
459     limit = 2.0*median(dssq);
460     nparts = 0;
461     for k1 = 1:num1
462         if (dssq(k1) <= limit)
463             nparts = nparts+1;
464             xp2(nparts) = xpix2(k1);
465             yp2(nparts) = height_pix-ypix2(k1)+1;
466             % ie. change y-coord measured upwards
467             xp1(nparts) = xp1(k1);
468             yp1(nparts) = height_pix-yp1(k1)+1;
469             % ie. change y-coord measured upwards
470             up(nparts) = (xp2(nparts) - xp1(nparts))*vel_const;
471             vp(nparts) = (yp2(nparts) - yp1(nparts))*vel_const;
472         end
473     end
474 end
475
476 % Finally, write results to file, in similar format to DynamicStudio...
477 time = (image_no-1.0)*Dt;
478 outfilename = sprintf('ImageTrack.%06d.txt', image_no);
479 % open file for writing...
480 fid = fopen(outfilename, 'w');
481 fprintf(fid, '>>*HEADER<<*\n');
482 fprintf(fid, 'FileID:IPExport.TAB\n');
483 fprintf(fid, 'Version:1\n');
```

```
484 fprintf(fid, 'GridSize:{Width=%4d, Height=%3d}\n', width_pix, height_pix);
485 fprintf(fid, 'Originator: %s%04d\n', name, image_no);
486 fprintf(fid, 'CameraInfo:NanoSense\n');
487 fprintf(fid, 'TimeStamp:%5.3f\n', time);
488 fprintf(fid, '>>*DATA*<<\n');
489 fprintf(fid, 'Frame   X[pix]  Y[pix]  Z[pix]  U[m/s]  V[m/s]  W[m/s]\n');
490 for f=1:nparts
491     fprintf(fid, '0   %8.2f %8.2f     0    ', xp1(f), yp1(f));
492     fprintf(fid, '%8.3f %8.3f    0\n', up(f), vp(f));
493 end
494 for f=1:nparts
495     fprintf(fid, '1   %8.2f %8.2f     0    ', xp2(f), yp2(f));
496     fprintf(fid, '%8.3f %8.3f    0\n', up(f), vp(f));
497 end
498 fclose(fid);
499
500 % may need to clear array variables between iterations.
501
502 end
503 elapsed_time = toc;
504 n_pairs = finish - start +1;
505 message = [num2str(n_pairs), ' image pairs processed in ', ...
506            num2str(elapsed_time), ' seconds'];
507 disp(message);
508 ''
```

Appendix F

Particle tracking

The tracking algorithm consist of three scripts: 1) to load DynamicStudio PIV data (PIVDataLoading.m), 2) to re-format fluid data exported from DynamicStudio cross-correlation algorithm for conditional sampling (reform.m), 3) a function (ReadDST.m) that reads the particle tracking output from in-house particle tracking algorithm, and 4) the main tracking script - matrix version (TrackerCS.m).

F.1 MATLAB script for processing DynamicStudio PIV cross-correlation data output

```
clear all clc
disp('2-D Newcastle-PIV Data Processing by Suhaimi.Wahab v29.12.2015')

ListOfTextFiles = dir('*.txt');
numfiles= numel(ListOfTextFiles); % Number of exported frames

%% DATA INPUT REQUIRED

Nx=146; % FOV interrogation grid size, Nx (streamwise) and Ny (wall-normal)
Ny=51;


%% DATA LOADING AND ALLOCATIONS
tic
disp('Extracting 2-D data: ');
```

```
for i=1:numfiles
    myfilename=sprintf('Re1000105mm30gR10.4fclpan5.%06d.txt',i); % Need to change this
    accordingly. IMPORTANT !!!!!   'XXXX.%06d.txt'
    main_data{i}=importdata(myfilename);

    % Data Allocations
    U_px{i}=main_data{1,i}.data(:,7); % Stream-wise velocity
    U_ms{i}=main_data{1,i}.data(:,9);
    V_px{i}=main_data{1,i}.data(:,8); % Cross-stream velocity
    V_ms{i}=main_data{1,i}.data(:,10);
    Status{i}=sum(main_data{1,i}.data(:,12)==16); % For calculating % good/bad vectors
    Status_2{i}=sum(main_data{1,i}.data(:,12)==17); % For calculating % vector masking
    BadVectors(:,i)=Status{1,i};
    U_ms_max(1,i)=max(U_ms{1,i});
    U_ms_min(1,i)=min(U_ms{1,i});
    U_px_max(1,i)=max(U_px{1,i});
    U_px_min(1,i)=min(U_px{1,i});

        fprintf('.');
    if (rem(i,50) == 0)
        fprintf('\n');
    end
end

    X_grid=main_data{1,1}.data(:,1); % X-coords.
    X_pixel=main_data{1,1}.data(:,3);
    X_mm=main_data{1,1}.data(:,5);
    Y_grid=main_data{1,1}.data(:,2); % Y-Coords.
    Y_pixel=main_data{1,1}.data(:,4);
    Y_mm=main_data{1,1}.data(:,6);

    [m n]=size(X_mm); % m=7446 and n=1
for i=1:m
    X_m(i,1)=X_mm(i,1)/1000; % Convert X_mm and Y_mm to metres.
    Y_m(i,1)=Y_mm(i,1)/1000;
end

clear myfilename ListOfTextFiles i m n main_data

%% Calculate Mean and fluctuation velocities

Uall=cat(2,U_ms{:}); % Collate all U velocity for calculation of mean and fluctuating velocity
    .
Uall_pixel=cat(2,U_px{:}); % Collate all U velocity in pixels value for calculation of mean
    and fluctuating velocity.
Vall=cat(2,V_ms{:}); % Collate all V velocity for calculation of mean and fluctuating velocity
    .
```

```
U_mean=(mean(Uall.'))'; % Calculate U mean velocity
U_mean_pixels=(mean(Uall_pixel.'))'; % Calculate U mean velocity in pixels
V_mean=(mean(Vall.'))'; % Calculate V mean velocity
% clear Uall Vall
% Plotting script for mean velocity
% e.g. R=reshape(U_mean(:,1),Ny,Nx); contourf(R,20); daspect([1 1 1])

for i=1:numfiles
    U_fluc{i}=U_ms{1,i}(:,1)-U_mean(:,1);
    V_fluc{i}=V_ms{1,i}(:,1)-V_mean(:,1);
end
%disp('>>> Mean and fluctuation velocity data calculation completed.')

% %% Reshaping data for calculation of gradients, derivatives and correlations
% Nx=146; % FOV interrogation grid size, Nx (streamwise) and Ny (wall-normal)
% Ny=51;
% for i=1:numfiles
%     Ur_ms{i}=reshape(U_ms{1,i}(:,1),Ny,Nx); %%%%%%
%     Vr_ms{i}=reshape(V_ms{1,i}(:,1),Ny,Nx);
%     Ur_fluc{i}=reshape(U_fluc{1,i}(:,1),Ny,Nx);
%     Vr_fluc{i}=reshape(V_fluc{1,i}(:,1),Ny,Nx);
%     Xr_m=reshape(X_m(:,1),Ny,Nx); %%%%%%%
%     Yr_m=reshape(Y_m(:,1),Ny,Nx); %%%%%%%
% end
%disp('>>> Data Reshaping completed.')
%% Organising data for export and tracking.
U=Uall;
V=Vall;
UPrime=cat(2,U_fluc{:});
VPrime=cat(2,V_fluc{:});
X_px=X_pixel;
Y_px=Y_pixel;
X_plus=(X_m.*0.0212)./0.0000010272;
Y_plus=(Y_m.*0.0212)./0.0000010272;

save PIVData U V UPrime VPrime X_px Y_px X_plus Y_plus X_mm Y_mm
save PIVData105mm30gR10 U V UPrime VPrime X_px Y_px X_plus Y_plus X_mm Y_mm
toc
```

F.2 MATLAB script for loading PIV data for conditional sampling

```
% Script to re-format fluid data for conditional sampling
```

```
2
3 load PIVData105mm30gR8;   % load data as supplied by Suhaimi.
4 % pre-allocate arrays for re-formatted data...
5 % x along columns, y along rows.
6 U_f = zeros(51,146,2000);
7 udash_f = zeros(51,146,2000);
8 V_f = zeros(51,146,2000);
9 vdash_f = zeros(51,146,2000);
10 X = zeros(146,1);
11 Y = zeros(51,1);
12 for frame = 1:2000
13     copy = U(:,frame);          % first U...
14     mat = reshape(copy,[146,51]);
15     U_f(:,:,frame) = mat';
16     copy = UPrime(:,frame);     % then udash...
17     mat = reshape(copy,[146,51]);
18     udash_f(:,:,frame) = mat';
19     copy = V(:,frame);          % then V...
20     mat = reshape(copy,[146,51]);
21     V_f(:,:,frame) = mat';
22     copy = VPrime(:,frame);     % then vdash...
23     mat = reshape(copy,[146,51]);
24     vdash_f(:,:,frame) = mat';
25 end
26 % interrogation cell centre coords. for fluid phase...
27 for n = 1:146
28     X(n) = X_px(n);
29 end
30 n2 = 1;
31 for n = 1:51
32     Y(n) = Y_px(n2);
33     n2 = n2 + 146;
34 end
35 % now output file in new format...
36 save PIVDataR U_f udash_f V_f vdash_f X Y;
```

F.3 MATLAB script for particle tracking

```
1 function[nparts, time, xpix, ypix, up, vp] = ReadDST(frameno)
2 % Read DynamicStudio particle tracking output...
3 % Given frameno, ReadDST returns number of particle images, nparts,
4 % TimeStamp, time, and vectors for x,y position (in pixels), and
5 % particle velicity components up and vp (in m/s) for each particle.
6
```

```
trackfilename = sprintf('Re1000105mm30gR1.4dzi0agx.%06d.txt',frameno);
% open first file...
fid = fopen(trackfilename);
for n=1:6
   line = fgets(fid);
end;
time = fscanf(fid, 'TimeStamp:%f\n', 1);
line = fgets(fid);  line = fgets(fid);
datavec = fscanf(fid, '%f');
fclose(fid);
% data is read as a vector.  Find no. of elements...
dimn = size(datavec);
% With 7 columns, find no. of rows...
rows = dimn(1)/7;
% Convert to a 2d array...
datat = reshape(datavec, [7,rows,]);
% ...and transpose to get correct ordering.
data = datat';
nparts = rows/2;
for i=1:nparts
    xpix(i) = (data(i,2) + data(i+nparts,2))/2;
    ypix(i) = (data(i,3) + data(i+nparts,3))/2;
    up(i) = data(i,5);
    vp(i) = data(i,6);
end;
```

```
% main tracking script - matrix version.

% Set verbose to 1 for debug output, else 0.

% editabe data for estimation of displacement from velocity...
Dt = 0.002;   % time between successive double frames.
width_mm = 48;      % frame width in mm
width_pix = 2352;   % frame width in pixels
% hence constant to calculate pixel displacement from velocity in m/s...
dispConst = Dt*1000*width_pix/width_mm;

% pre-allocate arrays for track storage...
% format = xp(track, frame)
maxtracks = 2000;
maxframes = 100;
xp = zeros(maxtracks, maxframes);
yp = zeros(maxtracks, maxframes);
up = zeros(maxtracks, maxframes);
vp = zeros(maxtracks, maxframes);
time = zeros(maxtracks, maxframes);
globalframeno = zeros(maxtracks, maxframes);
```

```
time = zeros(maxtracks, maxframes);
globalframeno = zeros(maxtracks, maxframes);
active = zeros(maxtracks,1);
nframes = zeros(maxtracks,1);

n = 1;
[np, timestamp, xpix, ypix, upart, vpart] = ReadDST(n);

% initialise first set of tracks for global frame 1...
for track=1:np
    xp(track, 1) = xpix(track);
    yp(track, 1) = ypix(track);
    up(track, 1) = upart(track);
    vp(track, 1) = vpart(track);
    time(track, 1) = timestamp;
    globalframeno(track, 1) = n;
    active(track) = 1;
    nframes(track) = 1;
end
currtracks = np;  %current total number of tracks

for n=2:2000
    % for each subsequent file (frame) build tracks...
    [np, timestamp, xpix, ypix, upart, vpart] = ReadDST(n);
    for j=1:np
        matched(j) = 0;
        % record if particles in frame 2 have been matched.
    end

    for track=1:currtracks
        if active(track)
            index = nframes(track);
            x1 = xp(track, index);
            y1 = yp(track, index);
            minsq = 1e10;
            for j=1:np
                dx = xpix(j) - x1;  dy = ypix(j) - y1;
                distsq = dx^2 + dy^2;
                if distsq < minsq
                    minsq = distsq;
                    dx12 = dx;  dy12 = dy;
                    jmatch = j;
                end
            end
            % need to verify match is valid!
            trackdisp = sqrt(minsq);  % displacement based on end pts.
            dx = dispConst*(up(track, index) + upart(jmatch))/2;
```

```
69            dy = dispConst*(vp(track, index) + vpart(jmatch))/2;
70            estdisp = sqrt(dx^2 + dy^2);  % displacement based on vel*dt
71            % dimensionless displacement error..
72            disperr = abs(trackdisp - estdisp)/estdisp;
73            % direction error (rads)..
74            dirnerr = abs(atan2(dy12, dx12) - atan2(dy, dx));
75            if disperr < 0.5 && dirnerr < 0.4
76                % now add matched point to track...
77                matched(jmatch) = track;
78                index = index+1;
79                xp(track, index) = xpix(jmatch);
80                yp(track, index) = ypix(jmatch);
81                up(track, index) = upart(jmatch);
82                vp(track, index) = vpart(jmatch);
83                time(track, index) = timestamp;
84                globalframeno(track, index) = n;
85                nframes(track) = nframes(track) + 1;
86            else
87                active(track) = 0;  % end of this track, so disable.
88                disp( ['Track ', num2str(track), ' killed'] );
89                disp( ['disperr = ', num2str(disperr)] );
90                disp( ['dirnerr = ', num2str(dirnerr)] );
91            end
92        end  % not active ... skip to next track
93    end
94
95    % check for new tracks starting...track(currtracks).
96    matched   % temporary
97    for j=1:np
98        if matched(j) == 0
99            % unmatched particle, so set up a new track...
100           currtracks = currtracks + 1;
101           xp(currtracks, 1) = xpix(j);
102           yp(currtracks, 1) = ypix(j);
103           up(currtracks, 1) = upart(j);
104           vp(currtracks, 1) = vpart(j);
105           time(currtracks, 1) = timestamp;
106           globalframeno(currtracks, 1) = n;
107           active(currtracks) = 1;
108           nframes(currtracks) = 1;
109           disp( ['New track no. ', num2str(currtracks)] );
110       end
111   end
112   clear matched;
113
114 end  % end for file loop.
115
```

```
% calculate some track statistics...
% sort tracks by length...
for track=1:currtracks
    nf(track) = nframes(track);
    for f=1:nf(track)
        ycoord(f) = yp(track,f);
    end
    ymin = min(ycoord);
    ymax = max(ycoord);
    % mean value of y for each track...
    ymean(track) = mean(ycoord);
    % maximum y excursion for each track...
    dymax(track) = ymax - ymin;
    clear ycoord;
end



% Test visualisation...
figure(1);
% show all tracks...
axis( [0, 2352, 0, 832], 'equal' );
for track=1:currtracks
    for f=1:nframes(track)
        xplot(f) = xp(track,f);
        yplot(f) = yp(track,f);
    end
    plot(xplot, yplot, 'r');
    clear xplot yplot;
    if track == 1
        hold on;
    end
end
hold off;

% show 10 longest tracks...
figure;
axis( [0, 2352, 0, 832], 'equal' );
% sort tracks on no. of frames...
[val, ind] = sort(nf);
% print 10 longest tracks...
disp('10 longest tracks...');
index = currtracks;
for k=1:10
    disp( ['Track no. ', num2str(ind(index)), '  =  ', ...
           num2str(val(index)), 'frames'] );
       track = ind(index);
```

```
    for f=1:nframes(track)
        xplot(f) = xp(track,f);
        yplot(f) = yp(track,f);
    end
    plot(xplot, yplot, 'r');
    if k == 1
        hold on;
    end
    plot(xplot, yplot, 'or');
    clear xplot yplot;
    index = index - 1;
end
hold off;

% show 10 tracks with greatest y excusions...
figure;
axis( [0, 2352, 0, 832], 'equal' );
% sort tracks on y excusion...
[val, ind] = sort(dymax);
% print 10 longest tracks...
disp(' ');
disp('10 tracks with greatest y movement...');
index = currtracks;
for k=1:10
    disp( ['Track no. ', num2str(ind(index)), '  dy max =  ', ...
           num2str(val(index))] );
       track = ind(index);
    for f=1:nframes(track)
        xplot(f) = xp(track,f);
        yplot(f) = yp(track,f);
    end
    plot(xplot, yplot, 'g');
    if k == 1
        hold on;
    end
    plot(xplot, yplot, 'og');
    clear xplot yplot;
    index = index - 1;
end
hold off;

% Now do conditional sampling of fluid data alng tracks...
% First load fluid data..
% U_f, udash_f, V_f, vdash_f as (51, 146, 2000) arrays,
% X as (146) vector and Y as (51) vector.
disp(' ');  disp('Loading fluid data...');
load PIVDataR;
```

```
disp('Done.');
uf = zeros(maxtracks, maxframes);
vf = zeros(maxtracks, maxframes);
udashf = zeros(maxtracks, maxframes);
vdashf = zeros(maxtracks, maxframes);
quadrant = zeros(maxtracks, maxframes);

for track = 1:currtracks
    for index = 1:nframes(track)
        f = globalframeno(track, index);
        xpart = xp(track, index);   % particle position
        ypart = yp(track, index);
        uf(track, index) = interp2(X,Y,U_f(:,:,f),xpart,ypart,'spline');
        vf(track, index) = interp2(X,Y,V_f(:,:,f),xpart,ypart,'spline');
        udashf(track, index) =...
            interp2(X,Y,udash_f(:,:,f),xpart,ypart,'spline');
        vdashf(track, index) =...
            interp2(X,Y,vdash_f(:,:,f),xpart,ypart,'spline');
        % calculate Willmarth quadrant...
        if udashf(track, index) > 0
            if vdashf(track, index) > 0
                quadrant(track, index) = 1;
            else
                quadrant(track, index) = 4;
            end
        else
            if vdashf(track, index) > 0
                quadrant(track, index) = 2;
            else
                quadrant(track, index) = 3;
            end
        end
    end
end

% interactive tarck display...
disp( ['Number of recorded particle tracks = ', num2str(currtracks)] );
track = input('Enter no. of track to display (or zero to exit):  ');
while track ~= 0
    figure;
    subplot(3, 1, 1);
    clear xplot yplot;
    for f=1:nframes(track)
        xplot(f) = xp(track,f);
        yplot(f) = yp(track,f);
    end
    plot(xplot, yplot, 'r');
```

```
257     title( ['Particle Track No. ', num2str(track)] );
258     xlabel('X (pix)');  ylabel('y (pix)');
259     axis( [0 2352 0 832] )
260     clear xplot yplot;
261     subplot(3, 1, 2);
262     for f=1:nframes(track)
263         xplot(f) = xp(track,f);
264         yplot(f) = up(track,f);
265     end
266     plot(xplot, yplot, '--g');
267     xlim ( [0 2352] );
268     title('u velocity along track');
269     xlabel('(solid = fluid, dashed = particle)');  ylabel('u (m/s)');
270     clear xplot yplot;
271     hold on;
272     for f=1:nframes(track)
273         xplot(f) = xp(track,f);
274         yplot(f) = uf(track,f);
275     end
276     plot(xplot, yplot, 'g');
277     clear xplot yplot;
278     hold off;
279     subplot(3, 1, 3);
280     for f=1:nframes(track)
281         xplot(f) = xp(track,f);
282         yplot(f) = vp(track,f);
283     end
284     plot(xplot, yplot, '--b');
285     xlim ( [0 2352] );
286     title('v velocity along track');
287     xlabel('(solid = fluid, dashed = particle)');  ylabel('v (m/s)');
288     clear xplot yplot;
289     hold on;
290     for f=1:nframes(track)
291         xplot(f) = xp(track,f);
292         yplot(f) = vf(track,f);
293     end
294     plot(xplot, yplot, 'b');
295     clear xplot yplot;
296     hold off;
297
298     figure;
299     subplot(3, 1, 1);
300     clear xplot yplot;
301     for f=1:nframes(track)
302         xplot(f) = xp(track,f);
303         yplot(f) = yp(track,f);
```

```
    end
    plot(xplot, yplot, 'r');
    title( ['Particle Track No. ', num2str(track)] );
    xlabel('X (pix)');  ylabel('y (pix)');
    axis( [0 2352 0 832] )
    clear xplot yplot;
    subplot(3, 1, 2);
    for f=1:nframes(track)
        xplot(f) = xp(track,f);
        yplot(f) = udashf(track,f);
    end
    plot(xplot, yplot, 'g');
    xlim ( [0 2352] );
    title('Fluid velocity perturbation along track');
    xlabel('(solid = u'', dashed = v''))');  ylabel('u'', v'' (m/s)');
    clear xplot yplot;
    hold on;
    for f=1:nframes(track)
        xplot(f) = xp(track,f);
        yplot(f) = vdashf(track,f);
    end
        plot(xplot, yplot, '--g');
        clear xplot yplot;
        hold off;
        subplot(3, 1, 3);
    for f=1:nframes(track)
        xplot(f) = xp(track,f);
        yplot(f) = quadrant(track,f);
    end
    plot(xplot, yplot, 'b');
    xlim ( [0 2352] );  ylim( [0.5 4.5] );
    title('Quadrant number along track');
    xlabel('X (pix)');  ylabel('Quadrant');
    clear xplot yplot;

    disp( ['Number of recorded particle tracks = ', num2str(currtracks)] );
    track = input('Enter no. of track to display (or zero to exit):  ');
end
```

References

Abe, H., Kawamura, H. and Choi, H. (2004), 'Very large-scale structures and their effects on the wall shear-stress fluctuations in a turbulent channel flow up to Re $_\theta$ = 640', *J. Fluid Mech.* **126**, 835–843.

Adrian, R. J. (1984), 'Scattering particle characteristics and their effect on pulsed laser measurements of fluid flow: Speckle velocimetry vs. particle image velocimetry', *Appl. Opt.* **23**, 1690–1691.

Adrian, R. J. (1991), 'Particle-imaging techniques for experimental fluid mechanics', *Ann. Rev. Fluid Mech.* **23**, 261–304.

Adrian, R. J. (2005), 'Twenty years of particle image velocimetry', *Exp. Fluids* **39**, 159–169.

Adrian, R. J. (2007), 'Hairpin vortex organization in wall turbulence', *Phys. Fluids* **19**, 041301.

Adrian, R. J., Christensen, K. T. and Liu, Z. C. (2000), 'Analysis and interpretation of instantaneous turbulent velocity fields', *Exp. Fluids* **29**, 275–290.

Adrian, R. J., Meinhart, C. D. and Tomkins, C. D. (2000), 'Vortex organization in the outer region of the turbulent boundary layer', *J. Fluid Mech.* **422**, 1–54.

Adrian, R. J. and Westerweel, J. (2011), *Particle Image Velocimetry*, Cambridge University Press.

Aliseda, A., Cartellier, A., Hainaux, F. and Lasheras, J. C. (2002), 'Effect of preferential concentration on the settling velocity of heavy particles in homogenous turbulence', *J. Fluid Mech.* **468**, 77–105.

Balachandar, S. and Eaton, J. K. (2010), 'Turbulent dispersed multiphase flow', *Ann. Rev. Fluid Mech.* **42**, 447–464.

Bandyopadhyay, P. R. (1980), 'Large structure with a characteristic upstream interface in turbulent boundary layer', *Phys. Fluids* **23**, 2326–2327.

Bandyopadhyay, P. R. and Hussain, A. K. M. F. (1984), 'The coupling between scales in shear flows', *Phys. Fluids* **27(9)**, 2221–2228.

Barnet, D. O. and Bentley, H. T. (1974), Statistical bias of individual realization laser velocimetry, *in* 'Proc. 2nd Int. Workshop on Laser Velocimetry', Purdue, pp. 428–444.

Bell, W. A. (1986), Spectral analysis of laser velocimeter data with the slotted correlation method, *in* '4th Joint Fluid Mechanics, Plasma Dynamics and Laser Conference', Atlanta, GA, USA, pp. B1–B13.

Bigillon, F. and Garcia, M. H. (2002), 'Exploratory study of flow-particle interaction using Particle Image Velocimetry', *HMEM Estes Park, Colorado, USA* .

Borowsky, J. and Wei, T. (2006), 'Simultaneous velocimetry/accelerometry measurements in turbulent two-phase pipe flow', *Exp. Fluids* **41**, 13–20.

Buchhave, P., George Jr., W. K. and Lumley, J. L. (1979), 'The measurement of turbulence with the laser Doppler anemometer', *Ann. Rev. Fluid Mech.* **11**, 442–503.

Chetelat, O. and Kim, K. C. (2002), 'Design of a particle image velocimetry objective maximising the image signal-to-noise ratio', *Meas. Sci. Technol.* **13**, 667–682.

Christensen, K. T. and Adrian, R. J. (2001), 'Statistical evidence of hairpin vortex packets in wall turbulence', *J. Fluid Mech.* **431**, 433–443.

Chung, D. and McKeon, B. J. (2010), 'Large-eddy simulation of large-scale structures in long channel flow', *J. Fluid Mech.* **694**, 100–130.

Clauser, F. H. (1956), 'The turbulent boundary layer', *Adv. Appl. Mech.* **4**, 1–51.

Cleaver, J. W. and Yates, B. (1975), 'A sub-layer model for the deposition of particles from a turbulent flow', *Chem. Eng. Sci.* **30**, 983âĂŞ992.

Crowe, C. T. (1982), 'Review: Numerical models for dilute gas-particle flows', *J. Fluids Eng.* **104**, 297–303.

Crowe, C. T. (2000), 'On models for turbulence modulation in fluid-particle flows', *Int. J. Multiphase Flow* **26**, 719–727.

Crowe, C. T., Sommerfeld, M. and Tsuji, Y. (1998), *Multiphase flows with droplets and particles*, CRC Press, Boca Raton, Fla.

Del Álamo, J. C., Jiménez, J., Zandonade, P. and Moser, P. D. (2004), 'Scaling of the energy spectra of turbulent channels', *J. Fluid Mech.* **500**, 135–144.

Dennis, D. J. C. and Nickels, T. B. (2011*a*), 'Experimental measurement of large-scale three-dimensional structures in a turbulent boundary layer. Part 1. Vortex packets', *J. Fluid Mech.* **673**, 180–217.

Dennis, D. J. C. and Nickels, T. B. (2011*b*), 'Experimental measurement of large-scale three-dimensional structures in a turbulent boundary layer. Part 2. Long structures', *J. Fluid Mech.* **673**, 218–244.

Doorne, C. W. H. V. (2004), Stereoscopic PIV on transition of pipe flow, PhD thesis, Delft Univeristy of Technology, The Netherlands.

Elghobashi, S. (1994), 'Theory of cross-correlation analysis of PIV images', *Appl. Sci. Res.* **52**, 309–329.

Elsinga, G. E. and Westerweel, J. (2012), 'Tomographic-PIV measurement of the flow around a zigzag boundary layer trip', *Exp. Fluids* **52**, 865–876.

Ganapathisubramani, B., Lakshminarasimhan, K. and Clemens, N. T. (2008), 'Investigation of three-dimensional structure of fine scales in a turbulent jet by using cinematographic sterescopic particle image velocimetry', *J. Fluid Mech.* **598**, 141–175.

Ganapathisubramani, B., Longmire, E. K. and Marusic, I. (2003), 'Characteristics of vortex packets in turbulent boundary layers', *J. Fluid Mech.* **478**, 35–46.

Geraschenko, S., Sharp, N. S., Neuscamman, S. and Warhaft, Z. (2008), 'Lagrangian measurements of inertial particle accelerations in a turbulent boundary layer', *J. Fluid Mech.* **2008**, 255–281.

Guala, M., Hommema, S. and Adrian, R. J. (2006), 'Large-scale and very-large-scale motions in turbulent pipe flow', *J. Fluid Mech.* **554**, 521–542.

Guingo, M. and Minier, J. P. (2008), 'A stochastic model of coherent strutures for particle deposition in turbulent flows', *Phys. Fluids* **20**, 053303.

Hambleton, W., Hutchins, N. and Marusic, I. (2006), 'Simultaneous orthogonal plane PIV measurements in a turbulent boundary layer', *J. Fluid Mech.* **560**, 53–64.

Head, M. R. and Bandyopadhyay, P. (1981), 'New aspect of turbulent boundary-layer structure', *J. Fluid Mech.* **107**, 297–337.

Hetsroni, G. (1998), 'Particle-turbulence interaction.', *Int. J. Multiphase Flow* **15**, 735–746.

Hösel, W. and Rodi, W. (1977), 'New biasing elimination method for laser-Doppler-velocimeter counter processing', *Rev. Sci. Instrum.* **48**, 910–919.

Huang, T. S. (1981), *Two-Dimensional Digital Signal Processing II*, Springer-Verlag, Berlin.

Hutchins, N. and Marusic, I. (2007*a*), 'Evidence of very long meandering streamwise structures in the logarithmic region of turbulent boundary layers', *J. Fluid Mech.* **579**, 1–28.

Hutchins, N. and Marusic, I. (2007*b*), 'Large-scale influences in near-wall turbulence', *Philos. Trans. R. Soc. Lond. A.* **365**, 647–664.

Hutchins, N., Nickels, T. B., Marusic, I. and Chong, M. S. (2009), 'Hot-wire spatial resolution issues in wall-bounded turbulence', *J. Fluid Mech.* **635**, 103–136.

Jeong, J. and Hussain, F. (1995), 'On the identification of a vortex', *J. Fluid Mech.* **285**, 69–94.

Jiménez, J. and Pinelli, A. (1999), 'The autonomous cycle of near-wall turbulence', *J. Fluid Mech.* **389**, 335–359.

Jin, C., Potts, I. and Reeks, M. W. (2015), 'A simple stochastic quadrant model for the transport and deposition of particles in turbulent boundary layers', *Phys. Fluids* **27**, 053305.

Kaftori, D., Hetsroni, G. and Banerjee, S. (1995*a*), 'Particle behaviour in the turbulent boundary layer. I. Motion, deposition and entrainment', *Phys. Fluids* **7**, 1095–1106.

Kaftori, D., Hetsroni, G. and Banerjee, S. (1995*b*), 'Particle behaviour in the turbulent boundary layer. II. Velocity and distribution profiles.', *Phys. Fluids* **7**, 1107–1121.

Kaftori, D., Hetsroni, G. and Banerjee, S. (1998), 'The effect of particles on wall turbulence.', *Int. J. Multiphase Flow* **24**, 359–386.

Kallio, G. A. and Reeks, M. W. (1989), 'A numerical simulation of particle deposition in turbulent boundary layers', *Int. J. Multiphase Flow* **15**, 433–446.

Keane, R. D. and Adrian, R. J. (1990), 'Optimization of particle image velocimeters. Part I: Double-pulsed systems', *Meas. Sci. Technol.* **1**, 1202–1215.

Khalitov, D. A. and Longmire, E. K. (2002), 'Simulataneous two-phase PIV by two-parameter phase discrimination', *Exp. Fluids* **32**, 252–268.

Kholmyansky, M., Moriconi, L. and Tsinober, A. (2007), 'Large-scale intermittency in the atmospheric boundary layer', *Phys. Rev. E.* **76**, 026307.

Kiger, K. T. and Pan, C. (2000), 'PIV technique for the simultaneous measurement of dilute two-phase flows', *J. Fluids Eng.* **122**, 811–818.

Kiger, K. T. and Pan, C. (2002), 'Suspension and turbulence modification effects of solid particulates on a horizontal turbulent channel flow', *J. Turbul.* **1**, 1–21.

Kim, K. C. and Adrian, R. J. (1999), 'Very large-scale motion in the outer layer', *Phys. Fluids* **11**, 417–422.

Kline, S. J., Reynolds, W. C., Schraub, F. A. and Runstadler, P. W. (1967), 'The structure of turbulent boundary layers', *J. Fluid Mech.* **30**, 741–773.

Kline, S. J. and Robinson, S. K. (1989), *Quasi-coherent structures in the turbulent boundary layer. I- Status report on a community-wide summary of data, Near-wall turbulence*, Hemisphere Publishing Corp., New York.

Kovasnay, L. S. G., Kibens, V. and Blackwelder, R. F. (1970), 'Large-scale motion in the intermittent region of a turbulent bounday layer', *J. Fluid Mech.* **41**, 283–326.

Kulick, J. D., Fessler, J. R. and Eaton, J. K. (1994), 'Particle response and turbulence modification in fully developed channel flow', *J. Fluid Mech.* **277**, 109.

Landreth, C. C. and Adrian, R. J. (1990), 'Impingement of a low Reynolds number turbulent circular jet onto a flat plate at normal incidence', *Exp. Fluids* **9**, 74–84.

Laughlin, D. K. M. and Tiederman, W. G. (1973), 'Biasing correction for individual realization of laser anemometry measurements in turbulent flows', *Phys. Fluids* **16**, 2082–2088.

Lee, J. H. and Sung, H. J. (2011), 'Very-large-scale motions in a turbulent boundary layer', *J. Fluid Mech.* **673**, 80–120.

Lee, J. and Lee, C. (2015), 'Modification of particle-laden near-wall turbulence: Effect of Stokes number', *Phys. Fluids* **27**, 023303.

Lelouvetel, J., Bigillon, F., Doppler, D., Vinkovic, I. and Champagne, J. Y. (2009), 'Experimental investigation of ejections and sweeps involved in particle suspension', *Water Resour. Res.* **45**, W02416.

Li, Y., McLaughlin, J. B., Kontomaris, K. and Portela, L. (2001), 'Numerical simulation of particle-laden turbulent channel flow', *Phys. Fluids* **13**, 2957.

Liu, Y. H. and Agarwal, J. K. (1974), 'Experimental observation of aerosol deposition in turbulent flow', *J. Aerosol Science* **5**, 145–148.

Liu, Z. C., Landreth, C. C., Adrian, R. J. and Hanratty, T. J. (1991), 'High resolution measurement of turbulent structure in a channel with particle image velocimetry', *Exp. Fluids* **10**, 301–312.

Longmire, E. K., Ganapathisubramani, B., Marusic, I. and Urness, T. (2001), Structure identification and analysis in turbulent boundary layers by stereo PIV, *in* 'Proc. 4th Intl. Symp. on Particle Image Velocimetry, PIV'01 Paper 1093', Gottingen, Germany.

Lourenço, L. and Krothapalli, A. (1986), 'The role of photographic parameters in laser speckle of particle image displacement velocimetry', *Exp. Fluids* **5**, 29–32.

Lourenço, L., Krothapalli, A. and Smith, C. A. (1989), *Particle Image Velocimetry*, Advances in Fluid Mechanics Measurments, Springer-Verlag, Berlin.

Marchioli, C. and Soldati, A. (2002), 'Mechanisms for partical transfer and segregation in a turbulent boundary layer', *J. Fluid Mech.* **468**, 283–315.

Marchioli, C., Soldati, A., Kuerten, J. G. M., Archen, B., Tanière, A., Goldensoph, G., Squires, K. D., Cargnelutti, M. F. and Portela, L. M. (2008), 'Statistics of particle dispersion in direct numerical simulations of wall-bounded turbulence: result of an international collaborative benchmark test', *Int. J. Multiphase Flow* **34**, 879–893.

Marusic, I. (2001), 'On the role of large scale structures in wall turbulence', *Phys. Fluids* **13**, 735–743.

Marusic, I. and Hutchins, N. (2008), 'Study of the log-layer structure in wall turbulence over a very large range of Reynold number', *Flow Turbul. Combust.* **81**, 115–130.

Mathis, R., Hutchins, N. and Marusic, I. (2009), 'Large-scale amplitude modulation of the small-scale structures of turbulent boundary layers', *J. Fluid Mech.* **628**, 311–337.

Mclean, I. R. (1990), The near-wall eddy structure in an equilibrium turbulent boundary layer, PhD thesis, University of Southern California, USA.

Mei, R., Adrian, R. J. and Hanratty, T. J. (1991), 'Particle dispersion in isotropic turbulence under Stokes drag and Basset force with gravitational settling', *J. Fluid Mech.* **225**, 481–495.

Monty, J., Steward, J., Williams, R. and Chong, M. (2007), 'Large-scale features in turbulent pipe and channel flows', *J. Fluid Mech.* **589**, 147–156.

Mosser, R. D., Kim, J. and Mansour, N. N. (1999), 'Direct numerical simulation of turbulent channel flow up to $\mathrm{Re}_\tau = 590$', *Phys. Fluids* **11**, 943–5.

Munson, B. R., Young, D. F. and Ohiishi, T. H. (2002), *Fundamentals of Fluid Mechanics*, John Wiley and Sons, Inc.

Nakagawa, H. and Nezu, I. (1981), 'Structure of space-time correlations of bursting phenomena in an open-channel flow', *J. Fluid Mech.* **104**, 1–43.

Nezu, I. and Nakagawa, H. (1993), *Turbulence in open-channel flows*, A. A. Balkema, Rotterdam, Brookfield.

Nezu, I. and Rodi, W. (1986), 'Open-channel flow measurements with laser doppler anemometer', *J. Hydraulic Eng., ASCE* **112**, 335–355.

Niño, Y. and Garcia, M. H. (1996), 'Experiments on particle-turbulence interactions in the near-wall region of an open channel flow: Implication for sediment transport', *J. Fluid Mech.* **326**, 285–319.

Pan, Y. and Banerjee, S. (1996), 'Numerical simulation of particle interactions with wall turbulence', *Phys. Fluids* **8**, 2733.

Papavergos, P. G. and Hedley, A. B. (1984), 'Particle deposition behaviour from turbulent flows', *Chem. Eng. Research and Design* **62**, 275–295.

Raffel, M., Willert, C., Wereley, S. and Kompenhans, J. (1998), *Particle Image Velocimetry: A Practical Guide*, Berlin: Springer.

Rashidi, M., Hetsroni, G. and Banerjee, S. (1990), 'Particle-turbulence interaction in a boundary layer', *Int. J. Multiphase Flow* **16**, 935–949.

Righetti, M. and Romano, G. P. (2004), 'Particle-fluid interactions in a plane near-wall turbulent flow', *J. Fluid Mech.* **505**, 93–121.

Robinson, S. K. (1991), 'Coherent motions in the turbulent boundary layer', *Ann. Rev. Fluid Mech.* **23**, 601–639.

Robinson, S. K., Kline, S. J. and Spalart, P. R. (1989), Quasi-coherent structures in the turbulent boundary layer. Part II: verification and new information from a numerically simulated flat-plate boundary layer, *in* 'Kline SJ; Afgan NH (ed) Near Wall Turbulence, Proceedings of Zaric Memorial Conference, New York, Hemisphere', pp. 218–247.

Rogers, C. B. and Eaton, J. K. (1991), 'The effect of small particles on fluid turbulence in a flat-plate, turbulent boundary layer in air', *Phys. Fluids* **3**, 928–937.

Schiller, L. and Newmann, A. (1933), 'A drag coefficient correlation', *Zeitschrift des Vereins Deutscher Ingenieure* **77**, 318–320.

Schlatter, P. (2010), *Vortical and large-scale structures in a turbulent boundary layer*, Poster, Linné FLOW Centre, KTH Mechanics, Stockholm, Sweden.

Schlatter, P. and Örlü, R. (2010), 'Assessment of direct numerical simulation data of turbulent boundary layers', *J. Fluid Mech.* **659**, 116–126.

Schoppa, W. and Hussain, F. (2002), 'Coherent structure generation in near-wall turbulence', *Ann. Rev. Fluid Mech.* **129**, 27–54.

Schröder, A., Geisler, R., Staack, K., Elsinga, G. E., Scarano, F., Wieneke, B., Henning, A., Poelma, C. and Westerweel, J. (2011), 'Eulerian and Lagrangian views of turbulent boundary layer flow using time-resolved tomographic PIV', *Exp. Fluids* **50**, 1071–1091.

Smith, A. J. and Metzler, S. P. (1983), 'The characteristics of low-speed streaks in the near-wall region of a turbulent boundary layer', *J. Fluid Mech.* **129**, 27–54.

Smith, C. R. (1984), A synthesized model of the near-wall behaviour in turbulent boundary layers, *in* 'Proc. 8th Symp. on Turbulence (eds. G.K. Patterson & J. L. Zakin)', Univeristy of Missouri (Rolla), pp. 299–327.

Soldati, A. (2005), 'Particles turbulent interactions in boundary layers', *Z. Agnew. Math. Mech.* **85**, 683–699.

Soldati, A. and Marchioli, C. (2009), 'Physics and modeling of turbulent particle deposition and entrainment: review of systematic study', *Int. J. Multiphase Flow* **35**, 827–839.

Sreenivasan, K. R. (1985), 'On the fine scale intermittency of turbulence', *J. Fluid Mech.* **151**, 81–103.

Theodorsen, T. (1952), Mechanism of turbulence, *in* 'Proc. 2nd International Midwestern Conference on Fluid Mech.', Ohio State University, Columbus, pp. 1–19.

Tomkins, C. D. and Adrian, R. J. (2003), 'Spanwise structure and scale growth in turbulent boundary layers', *J. Fluid Mech.* **490**, 37–74.

Toschi, F. and Bodenschatz, E. (2009), 'Lagrangian properties of particles in turbulence', *Ann. Rev. Fluid Mech.* **41**, 375–404.

Townsend, A. A. (1956), *The structure of turbulent shear flow*, Cambridge University Press, Cambridge, Vol. 1.

Townsend, A. A. (1976), *Structure of turbulent boundary layer*, Cambridge University Press, Cambridge, Vol. 2.

Tsuji, Y. and Morikawa, Y. (1982), 'LDV measurements of an air-solid two-phase flow in a horizontal pipe', *J. Fluid Mech.* **120**, 385–409.

Van Hout, R. (2011), 'Time-resolved PIV measurements of the interaction of polystyrene beads with near-wall-coherent structures in a turbulent channel flow', *Int. J. Multiphase Flows* **37**, 346–357.

Wang, L. P. and Maxey, M. R. (1993), 'Settling velocity and concentration distribution of heavy particles in homogenous isotropic turbulence', *J. Fluid Mech.* **568**, 27–68.

Wark, C. E., Naguib, A. M. and Robinson, S. K. (1991), Scaling of spanwise length scales in a turbulent boundary layer., *in* 'AAIA - paper 91-0235', 29th Aerospace Sciences Meeting, Nevada.

Wells, M. R. and Stocks, D. E. (1983), 'The effects of crossing trajectories on the dispersion of particles in a turbulent flow', *J. Fluid Mech.* **136**, 31–62.

Westerweel, J. (1993), Digital particle image velocimetry - theory and application, PhD thesis, Delft Univeristy of Technology, The Netherlands.

Willert, C. E. and Gharib, M. (1991), 'Digital particle image velocimetry', *Exp. Fluids* **10**, 181–193.

Willmarth, W. W. and Lu, S. S. (1972), 'Structure of the Reynold stress near the wall', *J. Fluid Mech.* **55**, 65–92.

Wu, X. and Christensen, K. T. (2006), 'Population trends of spanwise vortices in wall turbulence', *J. Fluid Mech.* **568**, 55–76.

Wu, X. and Moin, P. (2009), 'Direct numerical simulation of turbulence in a nominally zero-pressure-gradient flat-plate boundary layer', *J. Fluid Mech.* **630**, 5–41.

Yamamoto, Y., Potthoff, M., Tanaka, T., Kajishima, T. and Tsuji, Y. (2001), 'Large-eddy simulation of turbulent gas-particle flow in a vertical channel: Effect of considering inter-particle collisions', *J. Fluid Mech.* **442**, 303.

Yang, T. S. and Shy, S. S. (2005), 'Two-way interaction between solid particles and homogenous air turbulence: particle settling rate and turbulence modification measurements', *J. Fluid Mech.* **526**, 171–216.

Yudine, M. I. (1959), 'Physical considerations on heavy-particle diffusion', *Adv. Geophys.* **6**, 185–191.

Zanoun, E., Durst, F. and Nagib, H. (2003), 'Evaluating the law of the wall in two-dimensional fully developed channel flows', *Phys. Fluids* **15**, 3079–3089.

Zhou, J., Adrian, R. J., Balachandar, S. and Kendall, T. M. (1999), 'Mechanisms for generating coherent packets of hairpin vortices in channel flow', *J. Fluid Mech.* **387**, 353–396.